AD NUMBER

AD488164

NEW LIMITATION CHANGE

TO

Approved for public release, distribution unlimited

FROM

Distribution authorized to U.S. Gov't. agencies only; Administrative/Operational Use; 9 Jun 1966. Other requests shall be referred to Office of Civil Defense, Ofc. of the Sec. of Army, Div. for Research, Washington, DC. 20310.

AUTHORITY

OCD D/A ltr, 24 May 1971

USNRDL-R&L-177
9 June 1966

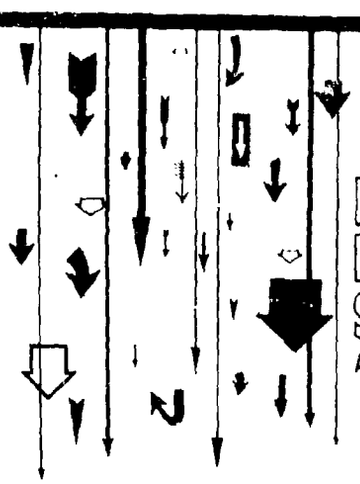

FALLOUT PHENOMENA SYMPOSIUM

APRIL 12-14, 1966

OFFICE OF CIVIL DEFENSE

DEFENSE ATOMIC SUPPORT AGENCY

PROCEEDINGS / PART 1

U.S. NAVAL
RADIOLOGICAL DEFENSE LABORATORY
SAN FRANCISCO, CALIFORNIA

DISCLAIMER NOTICE

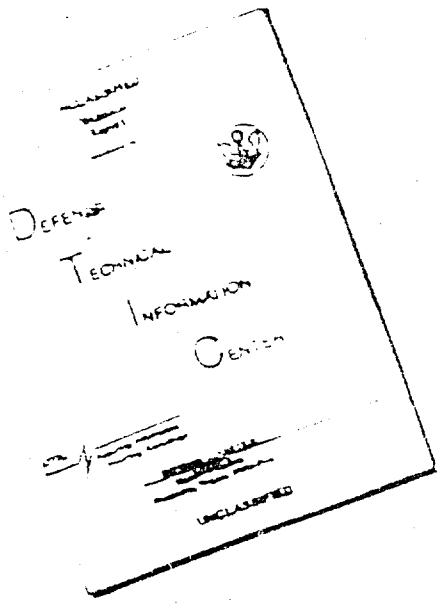

THIS DOCUMENT IS BEST QUALITY AVAILABLE. THE COPY FURNISHED TO DTIC CONTAINED A SIGNIFICANT NUMBER OF PAGES WHICH DO NOT REPRODUCE LEGIBLY.

PROCEEDINGS/PART 1

FALLOUT PHENOMENA SYMPOSIUM

APRIL 12-14, 1966

Sponsored by

DEFENSE ATOMIC SUPPORT AGENCY

OFFICE OF CIVIL DEFENSE

at

THE NAVAL POSTGRADUATE SCHOOL
Monterey, Calif.

Technical Assistance by
THE TECHNICAL MANAGEMENT OFFICE

US NAVAL RADIOLOGICAL DEFENSE LABORATORY
SAN FRANCISCO, CALIFORNIA

BLANK PAGE

FOREWORD

During April 12-14, 1966 a Fallout Phenomena Symposium, co-sponsored by the Office of Civil Defense and the Defense Atomic Support Agency, and developed by the Technical Management Office of the U.S. Naval Radiological Defense Laboratory, was held at the Naval Postgraduate School. During the first two days twenty-three papers were presented in four sessions covering the main aspects of the subject field. On the third day, four Working Groups each composed of the speakers in the session and representatives of the sponsoring agencies under the guidance of the session chairman, convened to consider the current status and future requirements of the particle formation, cloud development and particle circulation, transport and deposition, and radiation fields subject areas. The conclusions of the Working Groups were summarized in brief reports.

These proceedings are published as a record of the papers presented and the Working Group reports, for the benefit of those who attended the Symposium, and for other interested scientists. Because of the nature of the material covered, some of the papers were classified. These papers will be published in a separate classified document under the same title (Part II). Dr. I. J. Russell's paper entitled "Fallout Models and Their Parametric Inputs" is not included in either of these volumes, but will be published separately at a later date.

S. Z. Mikhail
Editor

PREFACE

By agreement between the Department of the Navy and the Office of Civil Defense, the U.S. Naval Radiological Defense Laboratory provides technical advisory services for specific areas of the OCD research program. In addition to recommending annual research programs, monitoring and reviewing research progress, and evaluating research proposals, such technical advisory services include efforts to promote the exchange and examination of pertinent information and consequently, includes development of appropriate scientific symposia. It is in this capacity that the USNRDL assisted in the planning and development of the OCD/DASA Fallout Phenomena Symposium.

AGENDA

Tuesday, April 12, 1966

Registration	0800-0830
Introduction	0830-0900
Welcome	E.J. O'Donnell, RADM, USN
Area Familiarization	C.E. Menneken
Technical Arrangements	P.E. Zigman
DASA Mission	J.W. Cane, LCDR, USN
OCD Objectives	J.C. Greene

SESSION ONE - PARTICLE FORMATION

Approx. Time: 0900-1200

Chairman

G.A. Cowan, Los Alamos Scientific Lab

Title	Speaker
Cloud Chemistry of Fallout Formation	J. Norman General Atomic
Experimental Determination of Input for the Prediction of Fractionation Effects	E.C. Freiling U.S. NavRadDefLab
Distribution of Individual Radionuclides as Functions of Fallout Particle Size	R.E. Heft Lawrence Radiation Lab
Fractionation of Induced Products in Subsurface Events	W.J. Auth, Major, USAF McClellan Central Lab
Simulated Fallout	G.F. Rynders Lawrence Radiation Lab
Physical and Radiochemical Characteristics of Particles From Air and Ground Bursts	M.W. Nathans Tracerlab

SESSION TWO - CLOUD DEVELOPMENT, PARTICLE CIRCULATION

Approx. Time: 1330-1630

Chairman

R.R. Rapp, RAND Corporation

Title	Speaker
Some Analytical Methods Leading to a Determination of the Approximate Velocity Field of the Fireball	J.W. McKee G.E. Tempo
Early Fireball Phenomena	H.L. Brode The RAND Corporation
Studies of Nuclear Cloud Rise and Growth	H.G. Norment Tech Ops Research
Cloud Expansion and Fallout Arrival Characteristics	O.S. Yu Stanford Research Institute
The Energy Cycle and the Energy Cascade of the Atomic Cloud	I.O. Huebsch U.S. NavRadDefLab

Wednesday, April 13, 1966

SESSION THREE - TRANSPORT AND DEPOSITION

Approx. Time: 0830-1200

Chairman

L. Machta, Air Resources Lab

Title	Speaker
Comparison of Nuclear Fallout Models	M. Polan Ford Instrument Co.
Transport and Output Processor Modules for the DOD Fallout Prediction System	T.W. Schwenke Tech Ops Research
Transport and Deposition Anomalies	E.C. Evans, III U.S. NavRadDefLab
The DOD Land Fallout Prediction System	R.C. Tompkins U.S. ArmNucDefLab
Fallout Models and Their Parametric Inputs	I.J. Russell Boston College

SESSION FOUR - RADIATION FIELDS

Approx. Time: 1330-1700

Chairman

L.V. Spencer, National Bureau of Standards
Ottawa University

Title	Speaker
Predictions of Some Radiation Properties of Unfractionated and Fractionated Fallout Fields	G.R. Crocker U.S. NavRadDefLab
Neutron Induced Activity	J.M. Ferguson U.S. NavRadDefLab
Gamma Ray Fields Above Rough Contaminated Surface	R.R. Soule U.S. NavRadDefLab
Disintegration Rate Multipliers in Beta-Emitter Dose Calculations	S.L. Brown Stanford Research Institute
Characteristics of the Gamma-Ray Environment Produced by Fallout Fields	R.L. French Radiation Research Assoc
Intensity--Activity Relations for Shot Small Boy	P.D. LaRiviere, O.S-K Yu, and C.F. Miller Stanford Research Institute
Radiological Model System Calculations	C.F. Miller and P.D. LaRiviere Stanford Research Institute

Thursday, April 14, 1966

Meeting of the Working Groups

CONTENTS

Page

FOREWORD i

PREFACE ii

AGENDA iii

INTRODUCTION 1

Technical Arrangements - P. E. Zigman 2
DASA Mission - J. W. Cane 5
OCD Objectives in Fallout Research - J. C. Greene 7

SESSION ONE - PARTICLE FORMATION 11

Cloud Chemistry of Fallout Formation -
J. Norman and P. Winchell 12

Experimental Determination of Input for the Prediction of Fractionation Effects -
E. C. Freiling 55

Simulation of Particulate Fallout -
G. F. Rynders 75

SESSION TWO - CLOUD DEVELOPMENT-PARTICLE CIRCULATION 97

Some Analytical Methods Leading to a Determination of the Approximate Velocity Field of the Fireball -
J. W. McKee. 98

The Energy Cycle and the Energy Cascade of the Atomic Cloud -
I. O Huebsch 129

SESSION THREE - TRANSPORT AND DEPOSITION 181

Comparison of Nuclear Fallout Models -
M. Polan 182

Transport and Output Processor Modules for the DOD Fallout Prediction System -
T. W. Schwenke 215

SESSION FOUR - RADIATION FIELDS

Approx. Time: 1330-1700

Chairman

L.V. Spencer, National Bureau of Standards
Ottawa University

Title	Speaker
Predictions of Some Radiation Properties of Unfractionated and Fractionated Fallout Fields	G.R. Crocker U.S. NavRadDefLab
Neutron Induced Activity	J.M. Ferguson U.S. NavRadDefLab
Gamma Ray Fields Above Rough Contaminated Surface	R.R. Soule U.S. NavRadDefLab
Disintegration Rate Multipliers in Beta-Emitter Dose Calculations	S.L. Brown Stanford Research Institute
Characteristics of the Gamma-Ray Environment Produced by Fallout Fields	R.L. French Radiation Research Assoc
Intensity--Activity Relations for Shot Small Boy	P.D. LaRiviere, O.S-K Yu, and C.F. Miller Stanford Research Institute
Radiological Model System Calculations	C.F. Miller and P.D. LaRiviere Stanford Research Institute

Thursday, April 14, 1966

Meeting of the Working Groups

CONTENTS

	Page
FOREWORD	i
PREFACE	ii
AGENDA	iii
INTRODUCTION	1
Technical Arrangements - P. E. Zigman	2
DASA Mission - J. W. Cane	5
OCD Objectives in Fallout Research - J. C. Greene	7
SESSION ONE - PARTICLE FORMATION	11
Cloud Chemistry of Fallout Formation - J. Norman and P. Winchell	12
Experimental Determination of Input for the Prediction of Fractionation Effects - E. C. Freiling	55
Simulation of Particulate Fallout - G. F. Rynders	75
SESSION TWO - CLOUD DEVELOPMENT-PARTICLE CIRCULATION	97
Some Analytical Methods Leading to a Determination of the Approximate Velocity Field of the Fireball - J. W. McKee	98
The Energy Cycle and the Energy Cascade of the Atomic Cloud - I. O Huebsch	129
SESSION THREE - TRANSPORT AND DEPOSITION	181
Comparison of Nuclear Fallout Models - M. Polan	182
Transport and Output Processor Modules for the DOD Fallout Prediction System - T. W. Schwenke	215

Differences in Transport and Deposition of Close-In and Intermediate Fallout -
E. C. Evans, III and C. A Young 236

The DOD Land Fallout Prediction System -
R. C. Tompkins 291

SESSION FOUR - RADIATION FIELDS 301

Predictions of Some Radiation Properties of Unfractionated and Fractionated Fallout Fields -
G. R. Crocker. 302

Gamma Ray Fields Above Rough Contaminated Surfaces -
R. R. Soule 318

Disintegration Rate Multipliers in Beta Emitter Dose Calculations -
S. L. Brown 337

Characteristics of the Gamma-Ray Environment Produced by Fallout Fields -
R. L. French 357

Intensity--Activity Relations for Shot Small Boy -
P. D. LaRiviere, S-K Yu and C. F. Miller 403

Introduction to Long-Term Biological Effects of Nuclear War -
C. F. Miller and P. D. LaRiviere 438

SUMMARIES AND RECOMMENDATIONS OF THE WORKING GROUPS 451

Session One - Particle Formation 452

Session Two - Cloud Development, Particle Circulation 460

Session Three - Transport and Deposition 463

Session Four - Radiation Fields 467

LIST OF ATTENDEES 475

INTRODUCTION

TECHNICAL ARRANGEMENTS

P. E. Zigman
U. S. Naval Radiological Defense Laboratory
San Francisco, California

On behalf of the Naval Radiological Defense Laboratory I would like to welcome you to this symposium dealing with nuclear fallout. NRDL's Commanding Officer, Captain Campbell, and our Scientific Director, Dr. Cooper, have requested that I convey their pleasure and appreciation for your willingness to attend and participate.

In the time available to me I would like to comment on three items. The first is directed to the objectives of this conference and how these can be met. The second is the planned conduct of the meeting. Finally, our intentions regarding publication of the record.

The conference will be concerned with three obviously inter-related aspects of fallout -- its formation, its transport and deposition, and its emission of ionizing radiation. A significant fraction of the U.S. scientists knowledgeable in these particular fields is present. You may be interested in learning that the over 120 attendees present represent 35 organizations involved in fallout and related research.

It is earnestly hoped that all of you will contribute to the conference objectives which have been described as

1. General examination of each subject area
2. Review, and through exchange of current information, definition of the present state of knowledge in each area
3. Development of information to specify necessary and desirable future research

The last, in one sense, is the objective. It is the desired end product of providing to the Office of Civil Defense and the Defense Atomic Support Agency guidance and recommendations for research which should be carried out to satisfy their requirements.

Real satisfaction of the objectives depends completely upon the extent to which each of you contribute your experience, knowledge and opinions. Little is accomplished in a meeting of this sort unless there is this active interchange.

This symposium will be carried out in two distinct parts.

The first part will consist of four open sessions held today and tomorrow. A total of 23 prepared papers will be delivered. After each, time will be available for questions and comments.

On the fourteenth, each of the session chairmen, the individuals who made presentations in his session and representatives of OCD and DASA will assemble as a Working Group. For the most part their discussions will be restricted to their session subject area -- such as particle development or radiation fields. This will be a serious, formal attempt to arrive at conclusions concerning the symposium objectives to define the current status of research and knowledge and to characterize required future efforts. Unless there are very good reasons to the contrary it is planned to restrict the Working Group meetings to the individuals noted above; it is felt that only through such limited attendance will there be fruitful, directed discussions. The deliberations of the working groups are to be summarized in brief state-of-the art reports. These reports will be published as part of the record of the symposium.

NRDL would very much like to assemble and publish a record of the symposium no later than June 30, 66. The record is planned to include the presentations and, as noted, the Working Group reports. To date we have received drafts of 10 of the 23 scheduled papers. To accomplish publication at the desired date it will be necessary to receive the remaining papers and the initial drafts of the Working Group reports no later than April 19. We view this as a final cut-off date and earnestly solicit your cooperation in this regard. If it is at all feasible, NRDL will publish an unclassified document containing most of the material and accompany this with a supplementary classified report.

Thank you for your attention.

At this time I would like to introduce Lt. Commander Jack Cane, DASA Project Officer for Fallout and Residual Radiation.

DASA MISSION

J. W. Cane
Defense Atomic Support Agency
Washington, D.C.

Good Morning Gentlemen:

I would like to welcome you, on behalf of DASA, to this symposium. I was personally gratified by the response to invitations. This symposium was originally intended to be an exchange of views between OCD and DASA Contractors, but it soon became apparent that the attendance should not be limited to them, and we are pleased at the great interest shown in this meeting.

The DASA mission is to support the Secretary of Defense, Joint Chiefs of Staff, Services and others as appropriate in nuclear weapons matters. Primary staff supervision comes from JCS while DDR&E has cognizance over our RDT&E programs. In addition, ATSD (AE) supervises certain of our logistics, safety and liaison activities. We are the DOD Coordinator for research in the effects of nuclear weapons, and we respond to requirements of the Services for effects information. This boils down to the following with regard to fallout research: We sponsor research activity which we in coordination with the services feel to be necessary to enable one to adequately assess the fallout hazard as it affects military operations and strategic plans. Our current program is at a focus. We are completing the first version of the DOD land fallout prediction system this year. You will hear more about this later in the symposium. We expect this model to provide all users with the type of information they need, but also, and just as important for this group, we expect tests of this model to tell us what effects are the most significant contributors to fallout prediction, so that with these results we can go ahead and simplify the model in those areas where tests show it is advisable, and do more research in those areas where

we need more complete knowledge. So, the results of future tests of the completed model will determine the direction of our effort. This is the reason for my earlier remark about our program coming to a focus.

In addition to the DOD fallout prediction system, we have in final stages of completion prediction codes for underwater and water surface bursts and for fast-neutron activation of soil materials. We are proceeding with publication of DASA 1215, the five-volume compilation of fallout data from past shots. We also have a pilot program of post facto cloud filter analysis, of which you will hear more later.

Before yielding the floor to Mr. Greene, may I leave two thoughts with you: First, please remember we are allotting 1/2 day for each session and discussion in order to be finished in two days; second, I am looking forward to a most interesting symposium. In this connection may I borrow from John Milton the following quotation to keep our sessions in perspective: "Where there is much desire to learn there of necessity will be much arguing, much writing, many opinions; for opinion in good men is but knowledge in the making."

OCD OBJECTIVES IN FALLOUT RESEARCH

J. C. Greene
Office of Civil Defense
Washington, D. C.

The objectives of the fallout studies sponsored by the Office of Civil Defense are very broad. In one way or another, almost anything relating to fallout has a civil defense implication. Because of this breadth of interest, let me first narrow it a bit by identifying general areas in which our interests are minimal.

OCD has little interest in tactical-sized weapons. This includes yields below perhaps 100 KT. In a strategic attack on this country, the weapons, unfortunately, seem likely to be much more powerful. The Russians claim they have bombs of the 100-megaton variety.

We have only minor interest in deep-water, surface, or sub-surface bursts, even of megaton size. Although such bursts might occur in sea battles, or as a result of aiming errors or aborts, or through defensive action, the hazard posed to the civilian population seems to be small compared to the fallout hazard from land-surface detonations. Megaton bursts in rivers or on lake or coastal harbors likely would produce fallout similar to that in the land-surface burst case.

We have little interest in underground bursts. In a strategic nuclear attack on this country, there seems to be no easy way to get a weapon very far underground nor, for that matter, any particular benefit from doing so.

Any of the above, i.e., small-weapon or sea or underground bursts, may be of considerable concern to the military. A battlefield commander would have a grave concern about how much fallout to expect from a tactical weapon and where it will go. The Navy would have real interest in the fallout characteristcs of an anti-submarine detonation, and the

demolition expert of necessity must consider the underground event.

On the other hand, there are areas of interest to civil defense that are of only minor concern to the military. As examples, civil defense must consider both short- and long-term food and water contamination problems, especially iodine-131 and strontium-90. The effects of beta and gamma radiation on both wild and domestic plants and animals, and the subsequent consequences to the food supply and to the ecology may be very important. The longer-range somatic and genetic effects of heavy and low-level exposures to external- and internal-radiation sources must be considered in developing shelter plans and exposure-control doctrine for civil defense emergency operations teams.

In brief, the civil defense interests as we see them can be summarized under the following categories: Fallout Patterns, and the Physical, Radiological and Chemical Properties of Fallout. I don't mean to imply that these categories are inclusive -- or independent -- they are not.

1. Fallout Patterns. Civil defense needs to know the probable characteristics of fallout patterns (especially the gamma dose rates as a function of time, distance, and direction) resulting from the detonation of high-yield nuclear weapons, considering such factors as height of burst, weapon design, type of soil, and meteorology. It is through use of "models" of such fallout patterns in analyzing hypothetical attacks that the requirements for fallout shelters are determined in terms of quantity, quality (protection factor), and distribution.

2. Radiological Properties of Fallout. Civil defense needs to predict radiological properties of the fallout in order to evaluate such factors as shielding requirements, decay characteristics (e.g., probable shelter stay time), decontamination requirements, and radiological instrument characteristics.

3. Physical Properties of Fallout. The physical properties of fallout must be taken into consideration in planning fallout decontamination, i.e., mass and particle-size distribution of material to be moved. The physical properties also relate to requirements for filters in ventilation systems, the settling

rates of fallout in water-supply systems, and relocation due to wind, rain, or traffic.

4. Chemical Properties of Fallout. The chemical property of fallout of most concern to civil defense is its solubility. Solubility determines such things as the dissolution of individual radionuclides in water supplies, the biological availability of the fallout (i.e., plant and animal uptake) and the amount of radioactivity that would remain behind after a contaminated street had been flushed free of fallout particles by water hosing.

The National Civil Defense Program has as its central element, the protection of the civil population against the effects of fallout. It is obvious that the best possible understanding of the fallout threat is needed if this protection is to be effective and is to be achieved at the least possible cost.

BLANK PAGE

SESSION ONE

PARTICLE FORMATION

CLOUD CHEMISTRY OF FALLOUT FORMATION*

J. Norman and P. Winchell
General Atomic, San Diego, California

ABSTRACT

The fallout model presented by C. F. Miller to account for fractionation of fission products during fallout formation has been reconsidered to include the glassy nature of fallout particles from a general land surface detonation. The occurrence of glass formation requires the use of temperature-variable condensed state diffusion coefficients in place of "go/no-go" diffusion represented by a soil fusion temperature in order to amply describe fission product absorption.

In describing fission product absorption according to this diffusivity-condensation model, fallout formation is assumed to be governed by equilibria established at the gas-surface interfaces, the rate of cooling of the cloud, and the rate of diffusion of adsorbed fission products into the central portions of the fallout particles. Using this model to make calculations appears to be quite reasonable, and examples of such calculations are included. In these calculations, however, cloud effects that will cause particle stirring, cloud radiation-field chemical effects, and agglomeration are not considered. Also, the cloud is considered to be homogeneous.

In this Laboratory, measurements have been made of some of the gaseous fission product-molten silicate equilibria. Measurements of some fission product diffusion coefficients in these silicates have also been made. These fission product properties are being studied for several compositions of silicate glasses in an attempt to evaluate the composition parameter.

An electron microprobe is being used to investigate elemental distributions in fallout particles from various land surface detonations. These studies, while generally confirming model hypotheses, point out the existence of inhomogeneities and accretion phenomena that are not yet part of any calculational system.

*Research sponsored by the Office of Civil Defense, Office of the Secretary of the Army, through the Technical Management Office, U.S. Naval Radiological Defense Laboratory.

MODEL STUDIES

Since the observation of fractionation of fission products in fallout formation,[1] it has been realized that fission products differ considerably from one another in their behavior at early times after a nuclear detonation. This has been attributed to a difference in the chemistry of the individual fission product elements. Fission products whose precursors form particularly volatile species in an oxygen-rich atmosphere are found in fallout generally to a degree that would seem to indicate different primary total fission yields than fission products whose precursors are easily condensed in the same atmosphere. Miller[2] explained this phenomenon by relating the absorption of a fission product to the thermodynamics of volatilization of appropriate fission product oxides, fire ball parameters, and a "freezing temperature" of the fallout droplets. In this model, fission product absorption is governed by equilibrium thermodynamics down to the "freezing temperature" of the soil. At this point, further fission product sorption is treated as adsorption. In general, this model exhibits reasonable agreement with observed fractionation of fission products. It also yields an estimate of the quantity of surface-adsorbed fission products, which can be translated into a quantity of biologically active fission products.

While Miller's "freezing point" model provides a degree of realism not encountered in strictly physical models, its premises are somewhat unrealistic. Specifically, the assumption of "go/no-go" condensed state diffusion is inadequate for silicate soil fallout both above and below any reasonable "freezing temperature." In the first place, "molten" silicates in the region just above their "freezing temperatures" are generally viscous liquids which have associated with them rather low mobilities (diffusivities) of their component species. As a result,

above the "freezing temperature," liquid silicate fallout particles will not be uniformly loaded with fission products but will exhibit a considerable radial concentration gradient, except for the least volatile fission product oxides, in all but the largest particles. It is also true of molton silicates that they tend to form glasses on cooling. A glass, of course, is a supercooled liquid whose viscosity has become so high that the tendency toward crystallization has become essentially negligible. Diffusivity in a glass, as a first-order description, can be considered an extension of diffusivity in the corresponding molten silicate. Therefore, the system behaves as if no phase transition of any kind has occurred. This means that not only is the assumption of homogeneity above a "freezing temperature" inadequate, but the assumption of strictly surface adsorption occurring after the "freezing temperature" has been reached is also questionable. Indeed, the very smallest fallout particles may absorb fission product oxides essentially homogeneously at temperatures lower than the "freezing temperature."

The use of temperature-dependent diffusivities in place of the "freezing temperature" is thus a natural step in describing fission product sorption in silicate fallout particle formation. For this extension of the chemical model, sorption of fission products is deemed to occur by a homogeneous gas phase coming to equilibrium with the surface of all fallout particles. The adsorbed fission products then diffuse into the assumed nonconvecting fallout particles. These processes occur in a temperature-time field associated with the nuclear detonation.

In order to illustrate this condensation-diffusion model, a parametric study of the variables involved in the model was made. The parameters investigated were weapon yield, diffusion coefficient, activation energy for diffusion, fallout particle radius, Henry's Law constant (a ratio of partial pressure to solution concentration), enthalpy associated with Henry's Law constant, initial fission product pressure, and relative quantities of fission product and soil associated with the

cloud. Each of these parameters enters into the calculation at a given temperature of the average concentration and/or diffusion profile of a fission product in a fallout particle.

Concentration-independent diffusion in spherical particles as given by Carslaw and Jaeger[3] is assumed to govern the penetration of the condensed fission product into the silicate. The diffusion coefficient, D, is related to the average concentration, $\bar{C}$, and the surface concentration, C_0, by the following equation:

$$\frac{C_0 - \bar{C}}{C_0} = \frac{6}{\pi^2} \sum_{n=1}^{\infty} \frac{1}{n^2} e^{-(\pi^2 n^2 Dt/R^2)} , \qquad (1)$$

where R is the radius of the spherical particle and t is the diffusion time. The diffusion coefficient and the Henry's Law constant are assumed to follow Arrhenius and Clausius-Clapeyron temperature dependencies, respectively. For the purpose of this investigation, the silicate is considered nonvolatile. The thermal history of a nuclear event is approximated in the following manner. Cooling rates are calculated at 2300°, 2100°, 1900°, 1700°, 1500°, 1300°, and 1100°K from an equation given by Freiling, Crocker, and Adams.[4] At each temperature the calculated cooling rate is used to estimate the time required for a particle to cool from 100° hotter to 100° cooler than the selected temperature. In this treatment the particle is assumed to reside at that temperature for this time and then discontinuously cool 200°C. That is, the cooling process is taken as a stepped function which, while it is far from the actual situation, appears to exhibit in a not too greatly distorted manner most of the features of the cooling phenomenology associated with fallout formation.

To permit consideration of the first-order effects of the system parameters, a set of reference values for these parameters has been chosen. Some values were selected with the aim of being realistic and some with the aim of keeping the evaluation of system behavior simple.

The reference conditions and the investigated first-order variations of these values are given in Table 1. A first-order variation of one of the reference values is studied by changing the value in question and retaining the rest of the reference conditions.

The first parameter considered here is weapon size. While weapon size will undoubtedly affect some of the other parameters listed, such as the comparative amounts of fission product and soil and the initial fission product pressure, the only effect considered in the weapon size variation is the effect on the cooling rate of the system. The other suggested effects will be considered separate parameters.

A relation between cooling rates for different yield events can be easily derived by means of the following cooling rate scaling equation presented by Freiling:[4]

$$-\frac{dT}{dt} \sim 3 \times 10^{-11} W^{-0.3} T^4 \quad , \tag{2}$$

where -dT/dt is the cooling rate (°K/sec) and W is the yield (KT). The ratio of residence times for a given temperature range, dT, is given by the ratio of yields to the 0.3 power:

$$\frac{dt_1}{dt_2} = \left(\frac{W_1}{W_2}\right)^{0.3} \quad . \tag{3}$$

Thus, a 100-fold increase in yield results in a residence time increase of a factor of approximately 4. (The effect of this change in weapon size on the distribution of fission products in a particle is the same as a factor of 4 increase in diffusivity or a factor of 2 decrease in particle size. However, this effect is not particularly noteworthy.) Thus, retarding the rate of cooling by increasing the size of the nuclear event has only a minor effect on fission product distribution in fallout. This effect is shown in Fig. 1, where the standard-conditions profiles are compared with the 10-MT variation, and is compared in Fig. 2 with larger

Table 1

Parameter Description for Formation of Fallout Simulation

PARAMETER	REFERENCE CONDITIONS	VARIATIONS
WEAPON SIZE (COOLING RATE), KILOTONS	100	10,000
DIFFUSION COEFFICIENT AT 1673°K, CM^2/SEC	10^{-7}	10^{-5}, 10^{-9}
ENERGY OF ACTIVATION FOR DIFFUSION $[-dR\ln(D)/d(1/T)]$, KCAL/MOLE	100	50
PARTICLE RADIUS, CM	10^{-2}	10^{-3}
RELATIVE QUANTITIES OF FISSION PRODUCT AND SOIL*	<0.1 ABSORBED AT 1100°K	0.2 ABSORBED AT 2100°K 0.1 ABSORBED AT 1700°K
HENRY'S LAW CONSTANT (P/C) AT 1673°K (ATM)	1	10^{+2}
ENTHALPY OF THE HENRY'S LAW CONSTANT $[-dR\ln(P/C)/d(1/T)]$, KCAL/MOLE	-80	-40
INITIAL FISSION PRODUCT PARTIAL PRESSURE, ATM	10^{-10}	10^{-12}

* CALCULATED IN FRACTION ABSORBED TERMS UNDER REFERENCE CONDITIONS FOR EASE OF MODEL HANDLING

effects caused by either changes in diffusivity (10^{-7} to 10^{-5} cm^2/sec at 1673°K) or particle size (10^{-2} to 10^{-3} cm).

In these and subsequently introduced figures, the concentration profiles at each of the temperature steps are presented. The high concentration envelope of these reported profiles may be considered the resulting concentration profile of a cold fallout particle. Since the volume of the outer 10% of the radius shell of a sphere is 1000 times the volume of the inner 10% of the shell, the high surface concentrations shown are an even more important contribution to the total activity of the particle than is at first apparent from the figures.

The particle radius and diffusivity parameters are intimately related according to Eq. (1) and will be considered together. The effects of decreasing the particle size or increasing the diffusivity are shown in Fig. 2. Under the reference conditions, the earliest major effects of diffusion limitation of absorption appear at 1900°K and 1500°K, respectively, for particles with a radius of 10^{-2} and 10^{-3} cm. A large particle thus gets out of equilibrium with the accompanying gas cloud at higher temperatures than does a smaller particle. This is sufficient reason to expect large particles to carry less than their share, on a volume basis, of volatile fission products.

Another related effect is that of variation in the temperature coefficient of diffusion. For different silicates in the CaO-Al_2O_3-SiO_2 system, the authors have reported activation energies associated with diffusion of radioantimony of 120 to 60 kcal/mole.[5] In Fig. 3, the effect of changing the reference activation energy from 100 to 50 kcal/mole is shown. This effect is quite similar to that measured in the CaO-Al_2O_3-SiO_2 system. Figure 3 shows a very pronounced lengthening of the temperature range where diffusion-limited absorption is apparent for the described parametric change. Even at the highest temperature studied (2300°K), diffusion limitation is important in the case of the 50 kcal/mole activation energy; and at the lowest temperatures, penetration of

the fission product is still a few microns and thus the fission product deposited at 1100°K is probably not all effectively on the leachable surface.

The results of the parametric studies discussed thus far strongly point out that the variation of absorption with diffusion parameters--principally properties of the soil constituting the major portion of a fallout particle--is quite important in describing fission product absorption. Another factor to be considered is the effect of chemistry between the surface of the fallout particle and the gas-phase interface.

Figure 4 illustrates the effects of changes in the partial pressure of a fission product and in the Henry's Law constant, simplified here to mean the partial pressure of a fission product divided by its equilibrium surface concentration in the silicate. This figure is rather uninteresting, as only axis translations are involved. While the effect of a first-order change in either parameter (shown here) suggests only a proportional difference, the effect of second-order (parametric interaction) changes makes these quantities important with regard to distribution of the fission product in fallout. In particular, the interaction of this axis translating effect with changes in the relative amounts of fission product and soil is important.

An examination of changes in the temperature coefficient of the Henry's Law constant, illustrated in Fig. 5, is also not very revealing. The major effect noted in changing to the lower enthalpy is the compression of the axis. This does affect the diffusion profile somewhat, as can be seen by the envelopes of the two sets of curves, but is only likely to be important as it interacts with the relative amounts of fission product and soil. Thus, the effect of changing this temperature coefficient seems relatively uninteresting except as it changes the absorption level at which depletion of the gas phase could set in.

One of the most interesting system parameters is the relative amounts of fission product and soil, given here by the quantity of fission

product absorbed at a particular temperature and set of conditions. In Fig. 6, this effect is demonstrated for three levels of absorption. Consider the case of a highly absorbed fission product. The Henry's Law constant, as defined, will be quite small, which means that the fission product will be almost totally absorbed before low enough temperatures are reached for a diffusion profile to be apparent. The concentration profile then would look like either the 2100° or 2300°K profile translated to the proper surface concentrations. In Fig. 6, the situation for a fission product which is 20% absorbed at 2100°K is also demonstrated. This type of profile shows clearly what may be expected for absorption of a slightly "fractionable" fission product in silicates during fallout formation. The curves representing 10% absorption at 1700°K would be representative of a more volatile fission product element, and the reference conditions curves would be representative of a very volatile fission product element. It is thus apparent that this cloud depletion cutoff of absorption is one of the major factors determining how important diffusivities are in describing the distribution of a fission product within a fallout particle and among fallout particles.

A degree of realism can be assigned to the parameters used in this study. The weapon sizes chosen certainly can be considered typical. Diffusion coefficients in the CaO-Al_2O_3-SiO_2 system for all of the elements studied have been between 10^{-8} and 10^{-7} cm^2/sec at 1673°K. Activation energies for diffusion between 46 and 130 kcal/mole have been measured. Particle radii of 10 to 100 microns would seem to be in a very important range. An estimated Henry's Law constant around unity at 1673°K has been a criterion used in selecting "fractionable" fission products. The Henry's Law constant temperature coefficient range selected encompasses the experimental values reported for cesium and molybdenum. Fission product partial pressures of 10^{-10} atm are in line with estimates by Miller.[2] While the low amount of fission product absorbed at 1100°K used as a measure of comparative amounts of fission product and soil is

probably quite atypical, the amounts absorbed given in the variations seem very reasonable values for real systems.

The parametric study thus suggests that there should be concentration gradients of volatile fission products in fallout and that limitation of fission product absorption in fallout by condensed state diffusion should be expected. Since completion of this study, an effort has been made to submit the proposed model to a computer program. While this initially seemed a rather formidable task, it has been reduced to a reasonable problem. The mathematical system includes time-temperature stepping, Henry's Law constants, diffusion coefficients, detonation models, and a mass balance equation relating the total amount of a nuclide in the cloud to the amounts of this nuclide in the gas phase and in the particles of various sizes through an analytically determinable surface concentration of the nuclide. By stepping the temperature and decaying the nuclides, a similar but more complicated analytical determination of an increment to the surface concentration can be made. This stepping calculation then is performed for the nuclide until the diffusion process essentially ceases. This calculational system can be carried out through a nuclide chain in order to incorporate into the model elemental transmutation effects. In this way, it seems feasible to make calculations describing the chemistry of fallout formation according to a condensation-diffusion mode.

For this model experimental values of Henry's Law constants and diffusion coefficients are necessary. Thus, a large portion of the present studies has consisted of an experimental program to investigate the absorption and diffusion of fission product elements into silicate matrices from oxygen-rich atmospheres.

VAPORIZATION STUDIES

For the vaporization studies, it was necessary to select a silicate matrix as a simulant of a basic fallout particle matrix. The $CaO-Al_2O_3-SiO_2$ system was chosen for the following reasons. It has a liquid range which is adequate (eutectic melts at 1450°K). The elements making up this system are very common soil ingredients. Experimentally, this system is easier to work with than sodium, potassium, or iron soils because there is no problem with volatile components or variable valence states. The working composition ranges are shown in Fig. 7.

Studies of Henry's Law constant performed at General Atomic[5] have included measurements of vaporization thermodynamics of the elements cesium, rubidium, molybdenum, tellurium, ruthenium, antimony, iodine, and indium from silicate melts. These studies have been made either by equilibrating samples with certain pressures of these elements and measuring uptake or by using the transpiration method. In both cases, essentially the same experimental apparatus (illustrated in Fig. 8) is used. A silicate solution containing a radioactively tagged element to be studied is placed in the bottom of a platinum tube. While this melt is held at high temperature, a gas is flowed between the walls of the melt-containing platinum tube and an inner platinum tube. In the space between the melt and the bottom of the inner tube, the gas picks up the vapor of a fission product dissolved in the melt. The gas is then sampled by passing it through a capillary in the bottom of the inner tube. The amount of fission product transpired through the orifice can be related to the partial pressure of the fission product in the vapor phase. If the solution is dilute enough, this pressure and the solution concentration of the fission product should be a measure of the Henry's Law constant for this element in this system.

Typical transpiration data are shown in Fig. 9. These data follow the formula described by Merten[6] to account for diffusional flow as well as slug transport of a transpired species through a capillary:

$$K = \frac{Vp}{1 - e^{-V}} \quad , \qquad (4)$$

where p is the partial pressure of the transpired species; V equals the gas flow rate times the capillary length, λ, divided by the quantity of the species diffusion coefficient, D, times the capillary cross-sectional area, A; and K is the mass flow rate times λ/DA times the gas constant, R, times the temperature divided by the molecular weight. When V becomes small, K approaches p; and when V becomes large, K approaches Vp. From the type of data shown in Fig. 9, the value of p can readily be extracted. The low flow rates necessary for gas phase saturation in these transpiration studies are noteworthy. Indeed, transpiration studies of this type yield thermodynamic equilibrium data and constitute the most accurate type of data that the authors have achieved.

Much of the data presented here has been obtained from equilibration studies performed in the same apparatus. In these studies, samples are hung in the chamber above the silicate melt and allowed to come to equilibrium with the gases above the melt. The gas composition in this region is determined by transpiration techniques, and sample composition is determined directly after quenching and dismantling of the system. In this way, Henry's Law constants are derived. The major problem with this method is that it has not been possible to quench rapidly enough to preclude transfer of fission product between the melt and the samples during cooling.

The results obtained from the transpiration and equilibration studies are summarized in Fig. 10. Only the 55 equivalent-% silicate points for cesium and rubidium were determined by the transpiration method. (Also, heats of vaporization of cesium and rubidium from this melt have been established as 79 and 81 kcal/mole, respectively, using the transpiration method.) The other cesium and rubidium points are equilibration data corrected to force agreement between the transpiration and equilibration data at the 55 equivalent-% silicate points. For both elements the equilibration data showed somewhat higher loadings than the transpiration data.

The equilibration data for the other elements studied probably are not as reliable as the cesium and rubidium data. The antimony and ruthenium data may be questionable because of platinum absorption of these metals from an oxygen atmosphere. The antimony data also are suspect because of formation of a gas phase polymer (Sb_4O_6) and must be corrected to the monomer (SbO) to apply in fallout situations. The tellurium and iodine data appear to be valid; however, because of sensitivity problems they must be considered less reliable than the cesium and rubidium data. The iodine dimer, I_2, also constitutes a problem. The molybdenum data are good, but they too suffer from the presence of gas phase polymers (Mo_3O_9 and Mo_2O_6). A correction for the effect of polymers in these systems can be and has been made.[7]

In general, these data show that there can be a considerable solution nonideality correction for fission product oxides in silicates. It is also apparent that the correction may vary with the silicate employed. Only ruthenium and tellurium, which would not be expected to interact strongly with silicates, gave pressures within a factor of 100 of the ideal solution values presented by Miller.[2]

As mentioned above, there has been some difficulty in interpreting the cesium and rubidium vaporization data, the main problem being that the vapor pressures of these species are found to be insensitive to oxygen pressure. If these species vaporize as the elements and are dissolved as monovalent positive ions, there should be a dependence on oxygen pressure, namely,

$$Cs^{+} + \frac{1}{2}\,O = \rightleftharpoons Cs(g) + \frac{1}{4}\,O_2(g) \quad . \tag{5}$$

For this reason, mass spectrometric studies of the vaporization of Cs_2O and Rb_2O have been made. In these studies it was found that contrary to previous information in the literature, evaporating species included Cs_2O, Cs_2O_2, and Rb_2O. Thermodynamic stabilities have been determined for these oxides. This discovery makes it easy to believe that the

presence of some gaseous mixed oxide can be responsible for the lack of dependence on oxygen pressure. Since the activity of cesium in the silicate melt is quite low, it does not appear that the volatile species are themselves the dimeric-type oxides. A cursory mass spectrometer search for the species vaporizing from the silicate is planned.

DIFFUSION OF RADIONUCLIDES IN MOLTEN SILICATES

Since diffusion-limited transport is considered one of the important parameters in fallout formation, part of the present studies has been concerned with trace-level chemical diffusion of tagged fission product elements in molten matrices which were chosen from the CaO-Al_2O_3-SiO_2 ternary. In some cases, radionuclides were purchased from Oak Ridge National Laboratory and then were introduced into the vitreous matrices. In other cases, carrier nuclides were incorporated in the matrices and subsequently activated in General Atomic's TRIGA reactor. In all cases, the diffusant was initially homogeneously distributed in the glasses at, or below, the 1% level.

Two methods were employed to investigate transport in these media. One technique, called the plane-source technique,[8] utilizes platinum capillaries containing a matrix which is overlayed with a small amount of the same substance containing the radiotracer. After this couple is annealed at a known temperature for a known period, the sample is sectioned, and the resulting concentration gradient defines the diffusivity. The alternative method, which to the authors' knowledge is unique in such studies, is called the vaporization technique.[5] It involves vaporization of the radionuclide from a bead of glass which is both contained by and heated by a platinum ring which is a resistance element. In this case, the sample is pumped in a high-vacuum system with the jacket kept cold. The isothermal rate loss of the radionuclide defines the diffusivity.

Both approaches have been used extensively at General Atomic, and for five different nuclides, they yield data which agree within the uncertainties of the techniques. The vaporization technique has added virtue in that it provides precise energies of activation with a single sample, and that it has greater utility and simplicity here than the plane-source technique. An example of concentration-gradient data obtained with the plane-source technique is shown in Fig. 11, and an example of isothermal rate loss data obtained with the vaporization technique is shown in Fig. 12. Results from an activation energy study performed with the vaporization technique are plotted in Fig. 13. On a statistical basis, both techniques provide the same data. The two methods are compared in Fig. 14, which is an Arrhenius plot of antimony diffusion data in the 1450°K, eutectic $CaO-Al_2O_3-SiO_2$ system. The overall uncertainty in the diffusivity is roughly 50%, which is not a standard deviation but includes temperature and matrix uncertainties.

Thus far, studies of the transport of nine radionuclides in the 1450°K $CaO-Al_2O_3-SiO_2$ eutectic have been completed. Also, a composition-dependence study was carried out for antimony diffusing in six different compositions of the $CaO-Al_2O_3-SiO_2$ ternary. As demonstrated by the vaporization technique, Arrhenius's Law may be used to describe the data. The diffusion equation may be written

$$\log_{10} D = A - \frac{B}{T} \quad , \tag{6}$$

where D is in cm^2/sec and T is in °K. In the language of Eyring's formulation, B is proportional to the energy of activation and A is proportional to the sum of a "constant" and the entropy of activation.

The results for the nine species diffusing in the 1450°K, eutectic matrix are summarized in Table 2. This table shows the wide range of values obtained for A and B, the corresponding range of activation energies being 46 to 94 kcal/mole. It is also apparent from Table 2 that a reasonable correlation exists between A and B. This correlation,

Table 2

Activation Energies and Entropies for Diffusion in $CaO-Al_2O_3-SiO_2$ Eutectic Between 1215° and 1950°K

SPECIES	A	B X 10^{-3}
Cs	5.57	20.5
Rb	4.27	18.2
K	3.80	17.1
In	3.57	18.3
Te	3.30	15.6
Sn	2.49	15.7
Sb	2.10	14.1
Mo	0.94	12.5
Na	0.14	10.0

which is shown in Fig. 15, is evidently a special case of a general correlation between A and B for diffusion in molten silicates. The authors have compiled a set of more than 100 A, B data points for diffusion of many different nuclides in many different silicate matrices. The resulting A:B correlation is surprisingly good. This can be considered an example of the compensation law in kinetics which has been observed in many different systems. Rüetschi[9] has discussed this compensation law. Its importance to fallout considerations is that if A (or B) is known, or can be predicted, then a statistically reasonable value of B (or A) can be obtained, and the thermal behavior of the diffusivity is thus definable. At this point, to our knowledge, there is no rule which affords a prediction of individual values of either A or B. For the four alkali metals in Table 2, a good correlation is found between A (or B) and the reciprocal ionic radius (see Fig. 16). Indeed, the values of A and B were predicted successfully for potassium prior to initiation of the experiments involving potassium. One would thus expect that the reciprocal ionic radius would enter into any prediction for the behavior of multiply charged species. Work in this area is still in progress at General Atomic.

Matrix effects upon the diffusivity of radionuclides are expected to be of major importance in the diffusion of radionuclides in molten silicates. A preliminary study has been carried out to determine the dependence of antimony diffusion on compositional changes within the CaO-Al_2O_3-SiO_2 ternary. Six matrices were prepared which had a constant CaO:Al_2O_3 ratio and a changing CaO:SiO_2 ratio. These glasses were homogeneously doped with radioantimony, and the transport of this nuclide was studied using the vaporization technique. The results are shown in Table 3.

From Table 3, the A:B correlation may be observed. Also, the very strong dependence of both A and B on SiO_2 content is obvious. Figure 17 illustrates the change in activation energy ($E^* = 4.575$ B) with SiO_2

Table 3

Comparison of Antimony Diffusion Data with Composition of $CaO-Al_2O_3-SiO_2$ Melt

SiO_2 (EQUIV. %)	A	$B \times 10^{-3}$	NO. POINTS	TEMP RANGE (°K)
34	7.39	22.3	5	1587 - 1748
45	8.90	24.5	8	1613 - 1779
50	4.72	17.5	4	1672 - 1824
55	2.10	14.1	25	1215 - 1866
59	4.55	19.2	4	1739 - 1852
63	9.32	27.8	7	1739 - 1866

concentration. This result is not yet understood, and further studies of this kind are being made. A similar dependence of the diffusion coefficient on SiO_2 content is also evident. Further studies in this area should reveal how to estimate diffusivities for use in the proposed model.

ELECTRON MICROPROBE STUDIES OF FALLOUT PARTICLES

Electron microprobe studies of silicate fallout particles have yielded results which support the condensation-diffusion model. While fission products were not present in these particles at a high enough concentration to be observed by electron microprobe techniques, other elements such as iron, potassium, silica, and lead were easily found.[5] The distribution of these elements as demonstrated by the microprobe was in line with what would be expected from diffusion control of fission product penetration.

As part of the electron microprobe studies, a fallout particle, which was oval in shape rather than spherical, was submitted to microprobe analysis. The results are illustrated in Fig. 18. Pictures (a) and (b) are photomicrographs of the sectioned particle. On the right end of the particle is a portion of a square raster burned into the plastic surrounding the particle. This raster is located where focused exciting electrons were swept over the particle (and mounting plastic), giving rise to the characteristic X-rays which tell what quantity of an element is present at any spot swept on the raster. Pictures (c), (d), (e), (f), (g), and (h) are raster pictures, in which the concentration of an element on the face of the sectioned fallout particle is directly related to the brightness of the microprobe picture. Bright areas in the electron backscatter picture, (c), suggest high molecular weight material. Microprobe picture (d) suggests that the dark area of the fallout particle in the electron backscatter picture was high in silicon. Picture (e) shows potassium to be reasonably uniformly distributed, except

in the high-silica region. Picture (f) shows a similar situation for iron, except that there seems to be somewhat more segregation. Picture (g) shows that titanium is highly segregated along the silica inclusion border, and picture (h) shows that lead is bordering the particle and the silica inclusion. The SiO_2 inclusion lead border suggests that the fallout particle has accreted the silica inclusion. Further investigation of this lead border reveals that it exhibits a diffusion gradient as demonstrated in Fig. 19. That is, the lead concentration falls off continuously from the surface of the particle toward its interior.

The formation of this particle might be reconstructed from Figs. 18 and 19 as follows. A lead-coated, unmelted silica-titania particle was accreted by the main particle while it was quite fluid. This event was followed by the accretion of a molten, iron potassium-silicate particle which was also coated with lead. This happened when the particle was viscous enough so that it did not fully spheroidize. The lack of potassium gradient suggests that the particle was not heated to a high enough temperature to lose its potassium and pick it back up with a resulting concentration gradient. Since the iron could come from the tower or the soil, its history cannot be well defined. However, iron seems to be more concentrated near the surface than in the central portions of the particle. On the other hand, lead is presumably not a major soil contaminant, and must have been sorbed by the particle from the vapor state. It does show condensation-diffusion model phenomena.

Other particles from the same shot generally showed the same characteristics--lead borders, surface iron, large silica inclusions, and evidence of agglomeration (usually to a much lesser degree, however). While the particles investigated normally had diameters in the millimeter region, at least one particle (attached to a large particle) was only a tenth this size. This particle, shown in Fig. 20, exhibited features much like those described previously--a lead border and high iron concentration near the surface. This particle even shows evidence of the accretion of a smaller lead-coated iron particle.

Microprobe studies have also been made on particles from a seeded coral shot. High-iron, black, spherical particles from this shot show crystallization phenomena rather than diffusion phenomena. These particles thus might better fit the Miller model of fission product sorption governed by freezing phenomena. However, the most interesting information obtained from these particles is the large degree of nonhomogeneity associated with the seeding elements titanium, zirconium, silicon, barium, potassium, aluminum, and sulfur. These seeding elements range in concentration from not detectable to a few percent from particle to particle and element to element. They are distributed to a highly variable degree of homogeneity within a particle. Sometimes a spot or two of an element is found, usually near the surface; other times a major phase is homogeneously loaded with an element.

CONCLUSIONS

Microprobe studies, diffusion studies, vaporization studies, and calculations all support the premise of this paper that a model incorporating condensed state diffusion with equilibrium thermodynamic fission product absorption on the surface layers of silicate fallout particles is superior to the "freezing point" model for describing the phenomenological behavior of fission products in silicate fallout formation. The implementation of this model is strongly recommended, even though it does not encompass all the relevant phenomena in describing the distribution of fission products in fallout particles.

REFERENCES

1. Freiling, E. C., "Fractionation I. High-Yield Surface Burst Correlation," Naval Radiological Defense Laboratory Report USNRDL-TR-385, October 29, 1959. 40 p.

2. Miller, C. F., "Fallout and Radiological Countermeasures," Stanford Research Institute Project No. IM-4021.

3. Carslaw, H. S., and J. C. Jaeger, Conduction of Heat in Solids, 2d ed., Clarendon Press, Oxford, 1959.

4. Freiling, E. C., G. R. Crocker, and C. E. Adams, "Nuclear Debris Formation," Naval Radiological Defense Laboratory Reviews and Lectures No. 151, December 1964.

5. Norman, J., et al., "Fallout Studies, Cloud Chemistry," General Atomic Report GA-6094, January 1965.

6. Merten, U., "Diffusion Effects in the Transpiration Method of Vapor Pressure Measurement," J. Phys. Chem. 63, 443-45 (1959).

7. Norman, J., "Fission Product Volatilities from a Silicate Matrix," General Atomic Report GA-7058, April 1966.

8. Yang, L., and M. T. Simnad, "Measurement of Diffusivity in Liquid Systems" in Physiochemical Measurements at High Temperatures, J. O'M. Bockris, J. L. White, and J. D. Mackenzie (eds.), Academic Press, Inc., New York, 1959.

9. Ruetschi, P., "The Relation between Frequency Factor and Activation Energy (Compensation Law)," Z. Phys. Chem. 14, 277-91 (1958).

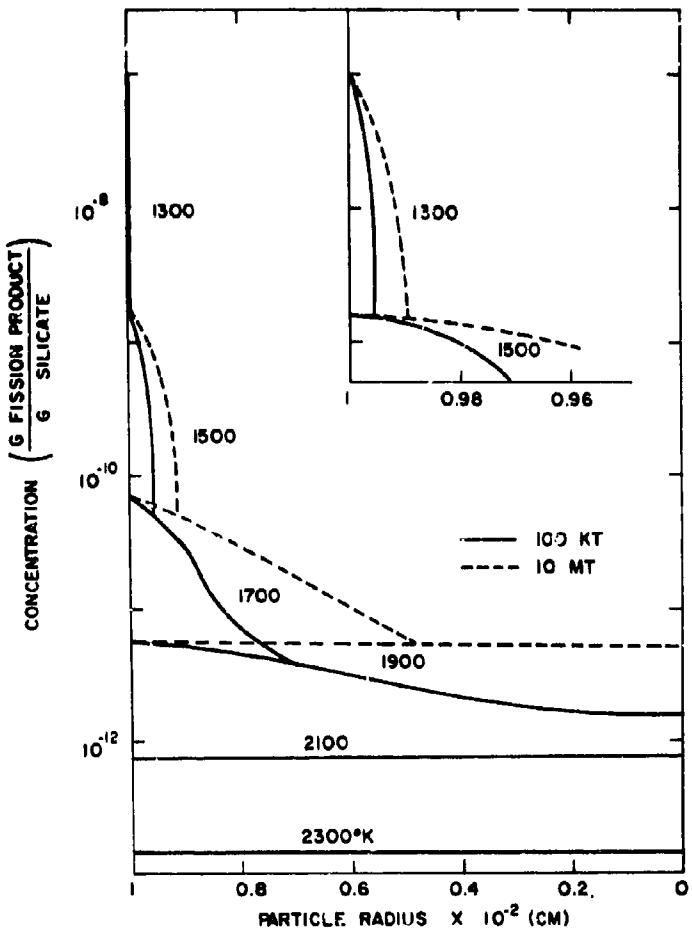

Fig. 1. Profile Variation with Weapon Size

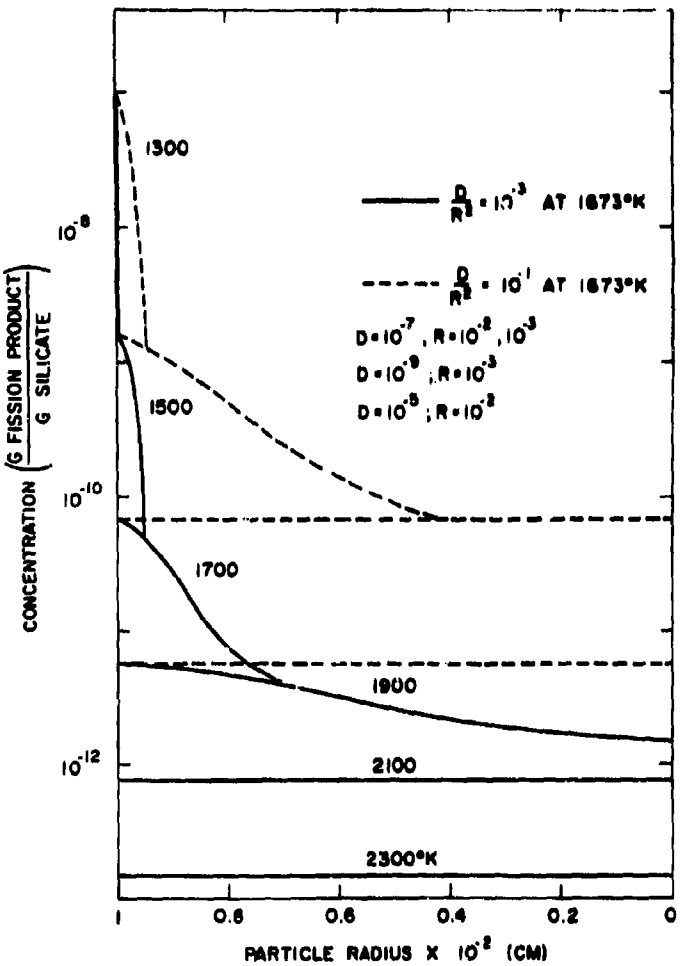

Fig. 2. Profile Variation with Diffusion Coefficient or Particle Radius

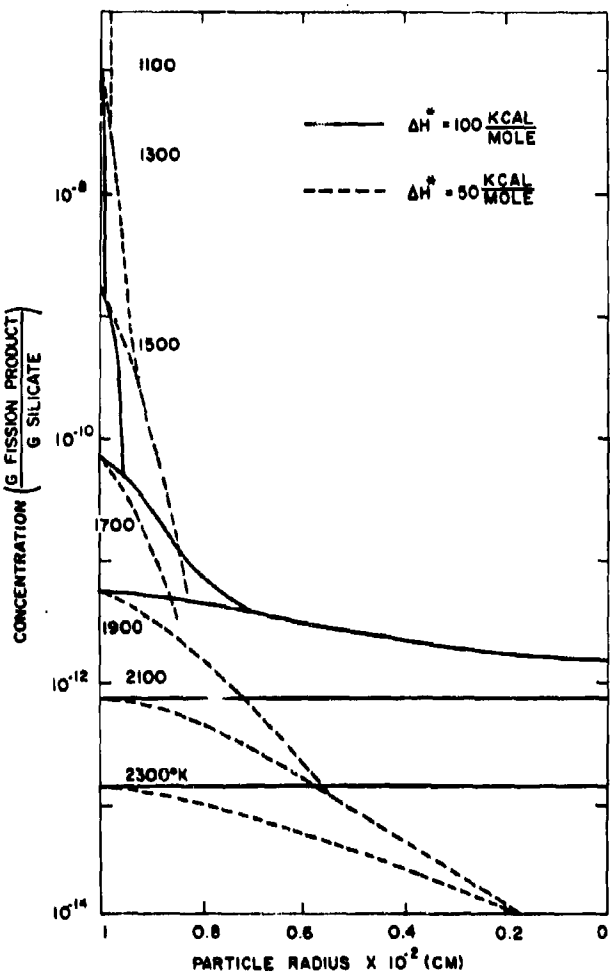

Fig. 3. Profile Variation with Heat of Activation of Diffusion

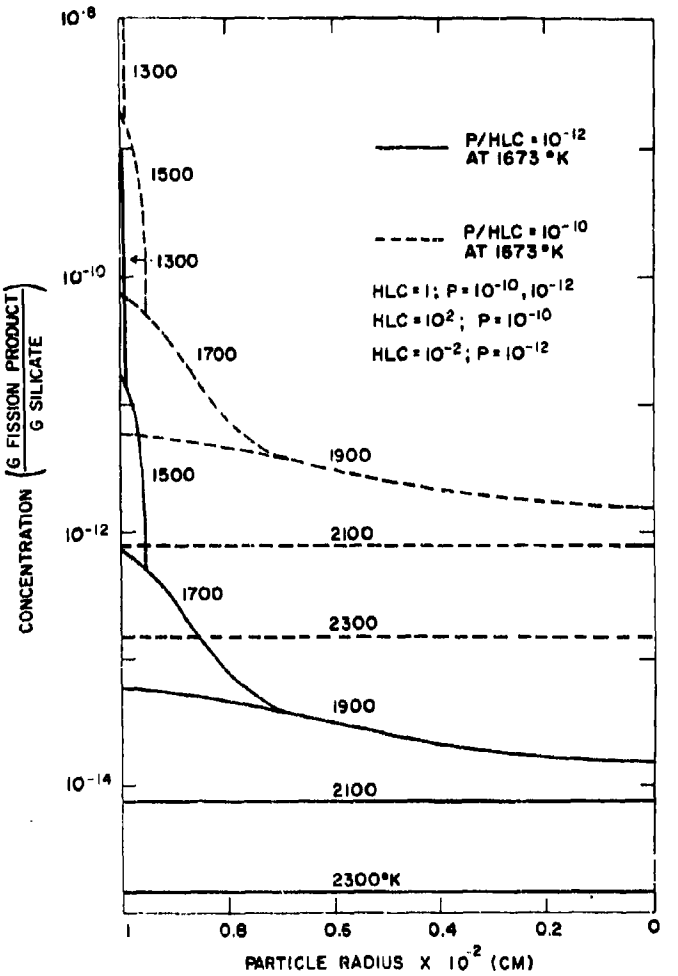

Fig. 4. Profile Variation with Henry's Law Constant (HLC, atm^{-1}) or Fission Product Pressure (P, atm)

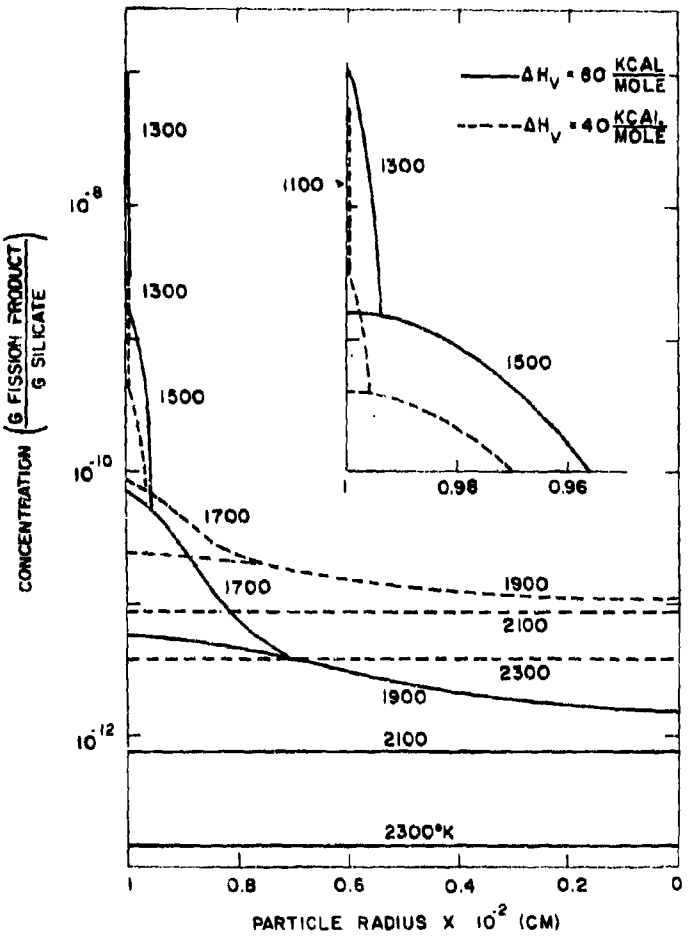

Fig. 5. Profile Variation with Heat of Vaporization (Temperature Coefficient of the Henry's Law Constant)

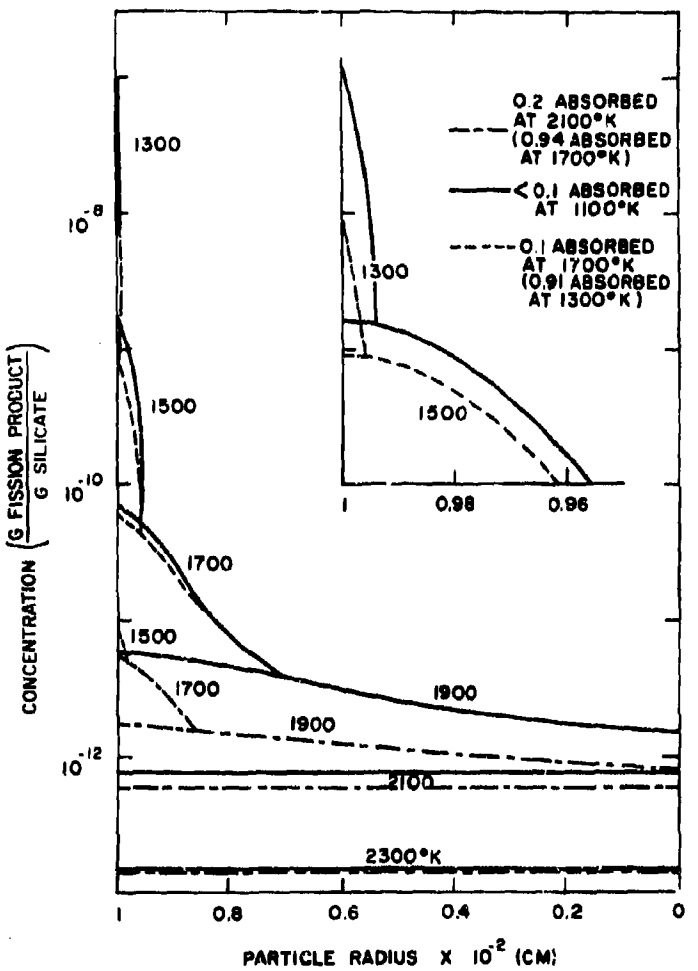

Fig. 6. Profile Variation with Degree of Fission Product Absorption in Molten or Glassy Soil

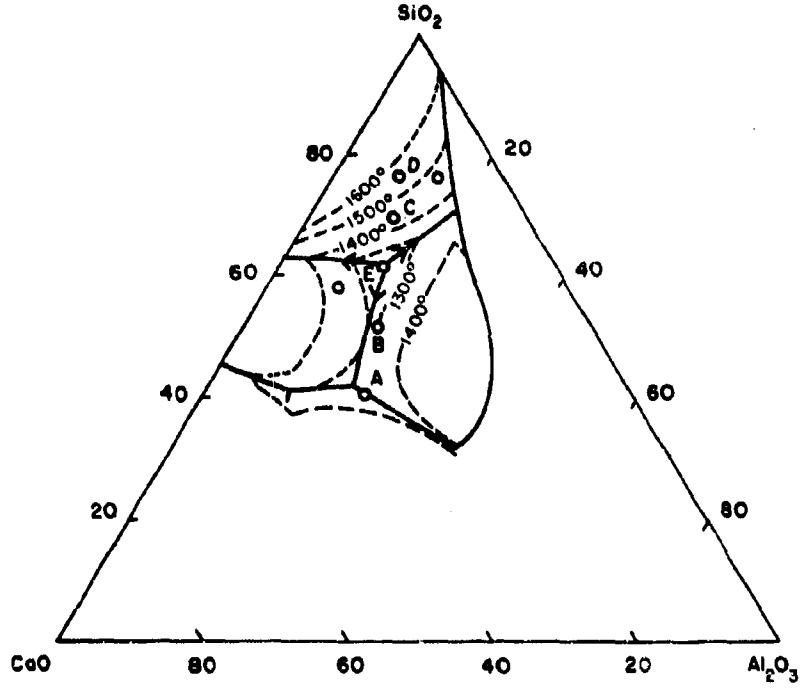

Fig. 7. Liquidus Surface Diagram of $CaO-Al_2O_3-SiO_2$ (Temperature in °C)

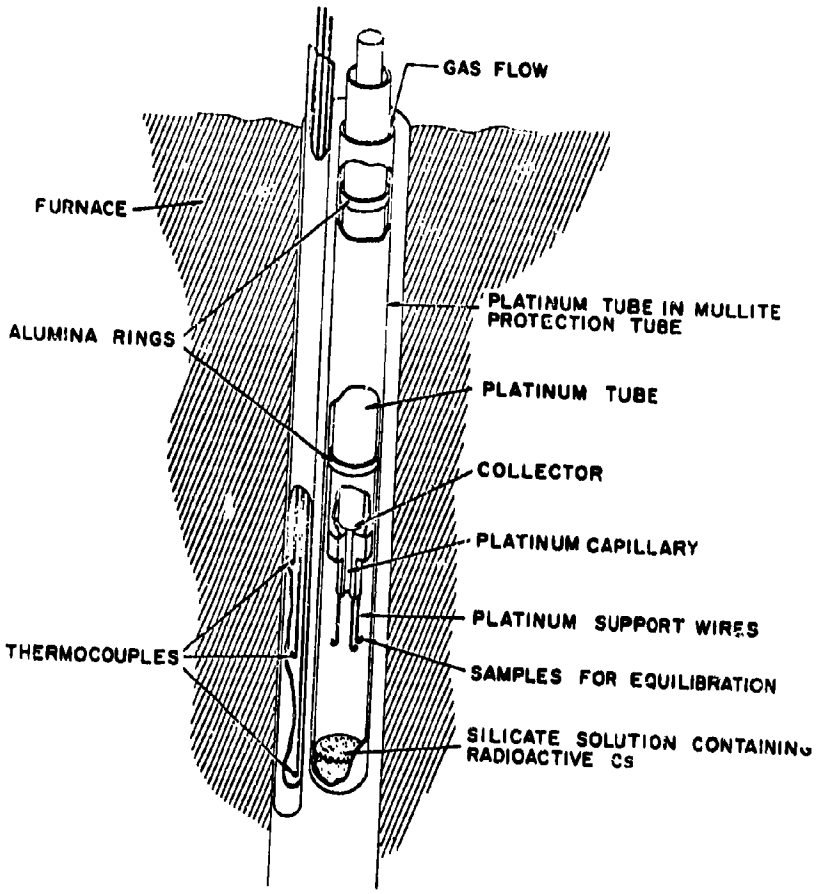

Fig. 8. Equilibration Apparatus

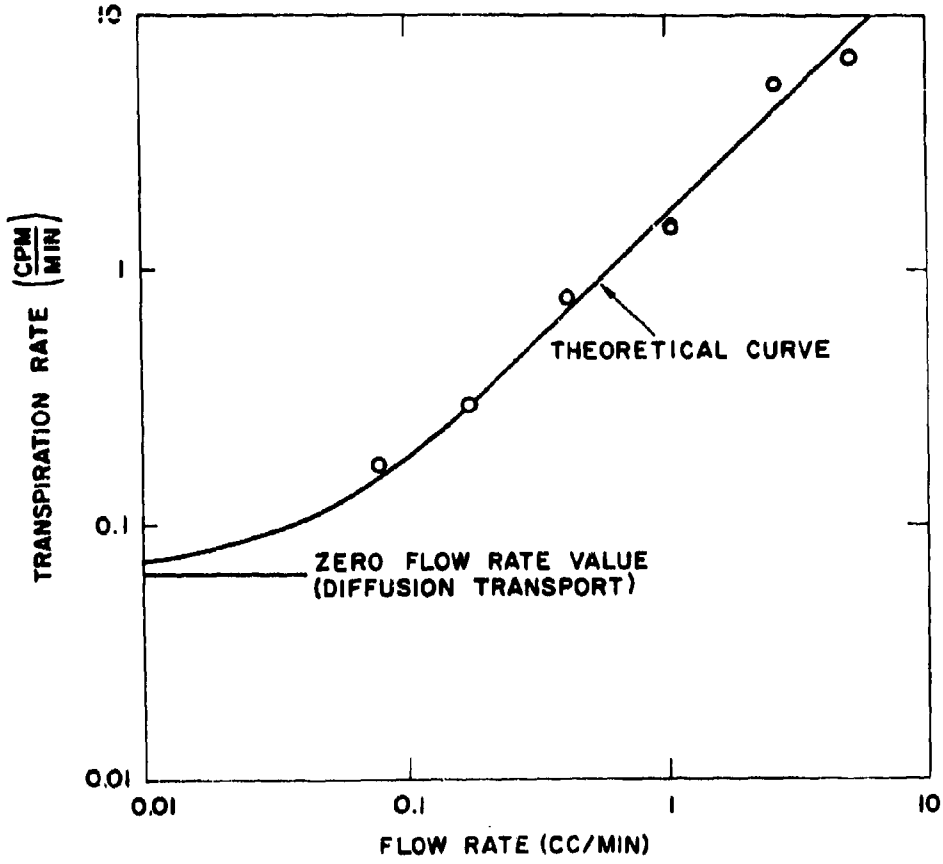

Fig. 9. Rubidium Transport as a Function of Oxygen Flow Rate

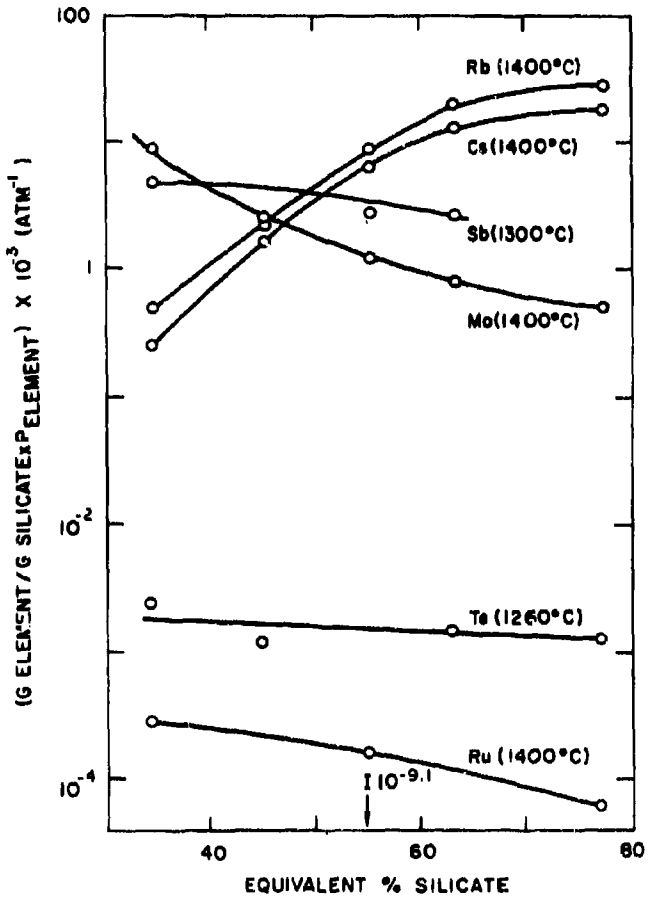

Fig. 10. Absorptions per Atmosphere for Cesium, Rubidium, Antimony, Molybdenum, Tellurium, and Rubidium in $CaO-Al_2O_3-SiO_2$ Samples; Mole Fraction Ratio $3CaO/Al_2O_3 = 0.98 \pm 0.05$

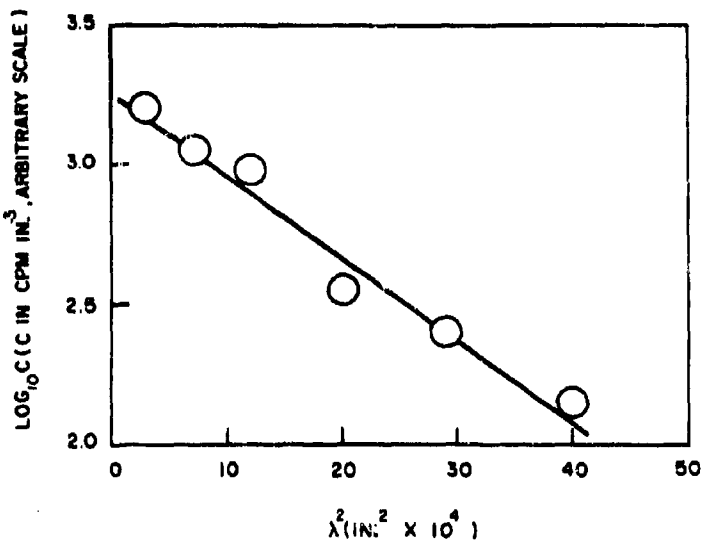

Fig. 11. Example of Data from the Plane-Source Technique for Radiotin Transport in the 1450°K Eutectic of the $CaO-Al_2O_3-SiO_2$ Ternary at 1858°K

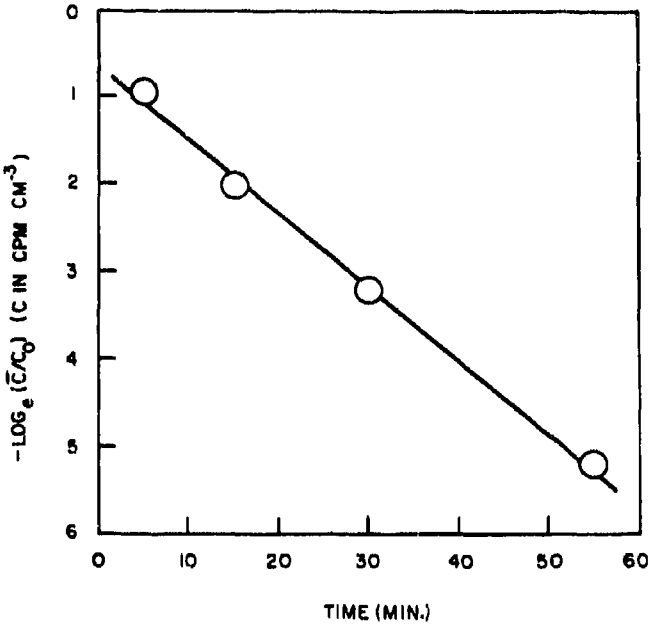

Fig. 12. Example of Data from the Vaporization Technique for Radiorubidium Transport in the 1450°K Eutectic of the $CaO-Al_2O_3-SiO_2$ Ternary at 1722°K

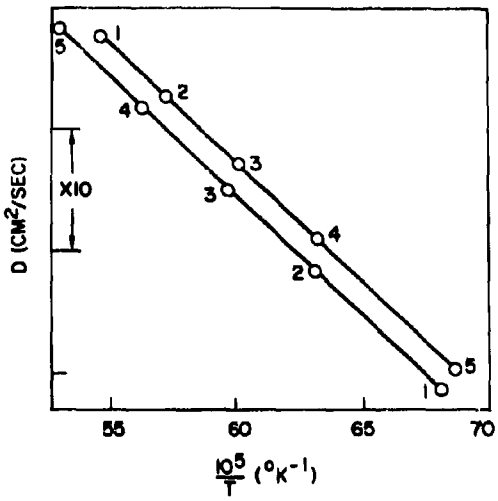

Fig. 13. Temperature Dependence of Diffusion Coefficient of Radiocesium in Two $CaO-Al_2O_3-SiO_2$ Samples of Identical Composition but with Different Radii (Points Are Numbered According to Order of Experiments)

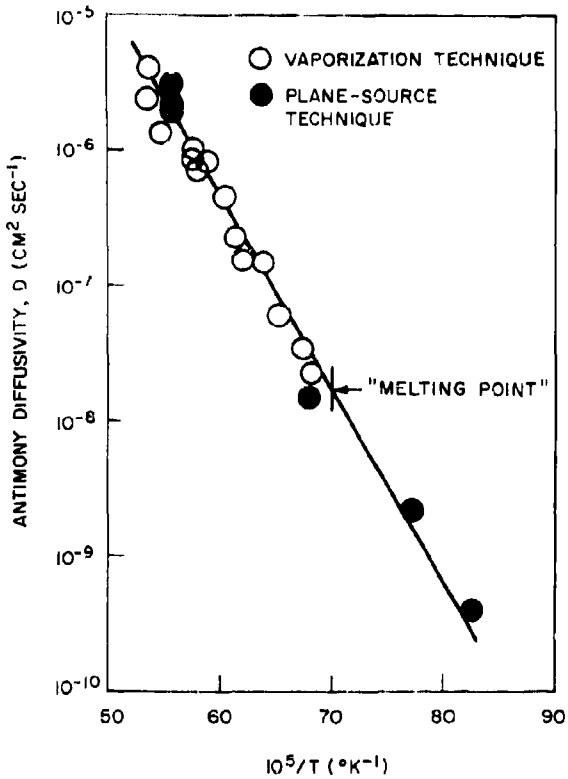

Fig. 14. Diffusivity of Radioantimony in Matrix E as a Function of Reciprocal Temperature

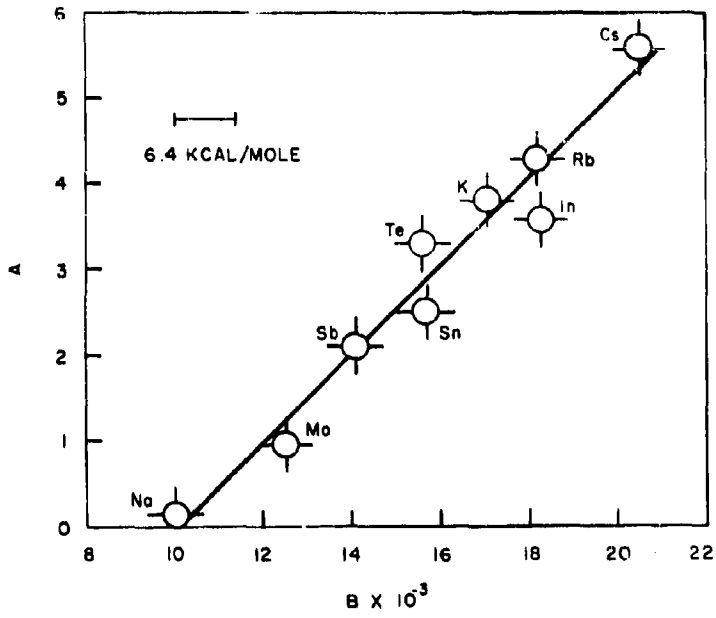

Fig. 15. Correlation Between the Coefficients in the Diffusion Equation, $\log_{10} D = A-(B/T)$, for Diffusion of Radionuclides in the 1450°K Eutectic of the $CaO-Al_2O_3-SiO_2$ Ternary

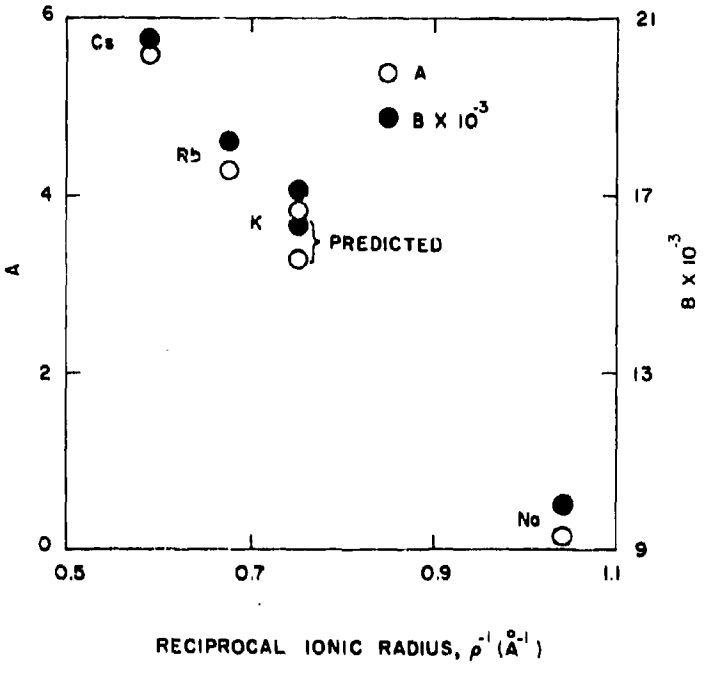

Fig. 16. Correlation of Coefficients in the Diffusion Equation, $\log_{10} D = A-(B/T)$, with Reciprocal Ionic Radius for Diffusion of Cesium, Rubidium, Potassium, and Sodium in Molten Eutectic $CaO-Al_2O_3-SiO_2$

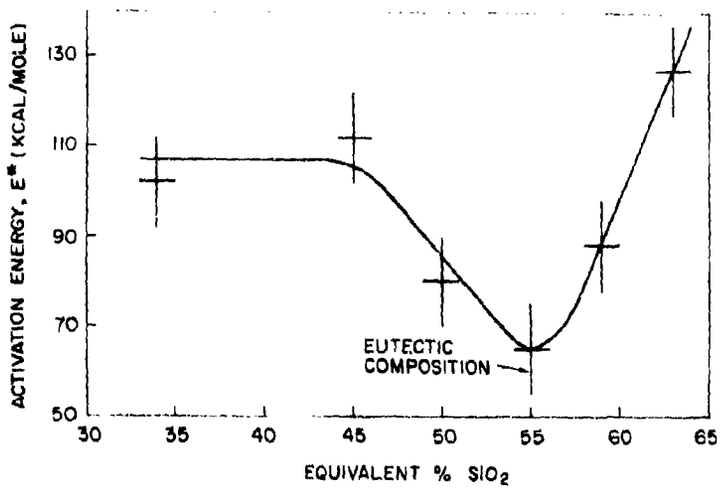

Fig. 17. Composition Dependence of Activation Energy, E*, for Diffusion of Radioantimony in Molten $CaO-Al_2O_3-SiO_2$ Glasses

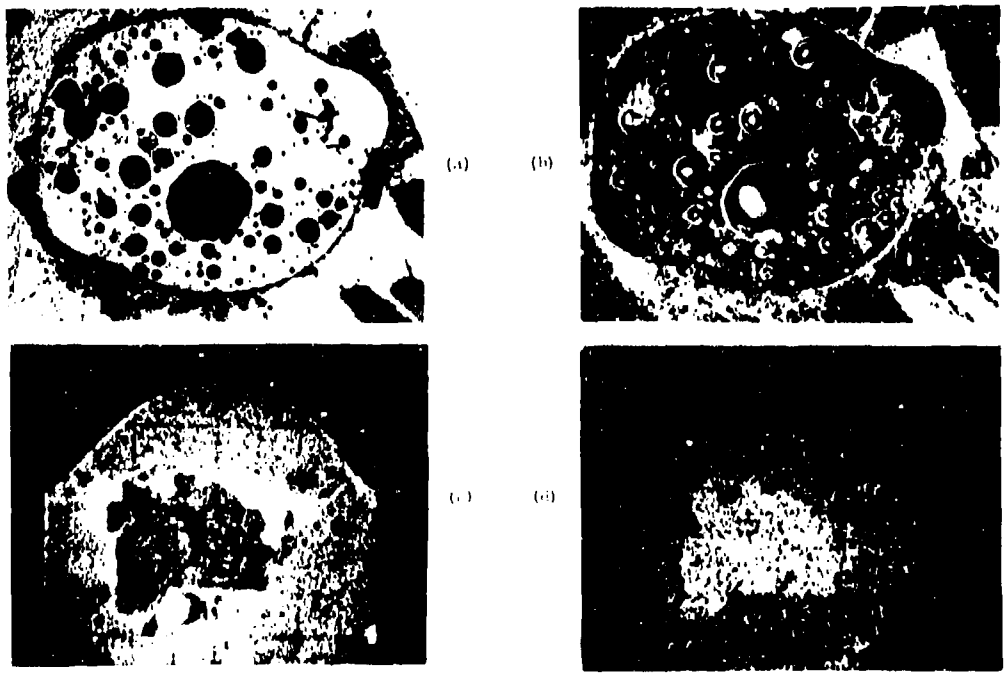

Fig. 18. Microprobe Studies of a Fallout Particle: (a) Light Field Photomicrograph; (b) Dark Field Photomicrograph; (c) Electron Backscatter Intensity Picture; (d) Silicon K_α Intensity Picture of a Feature

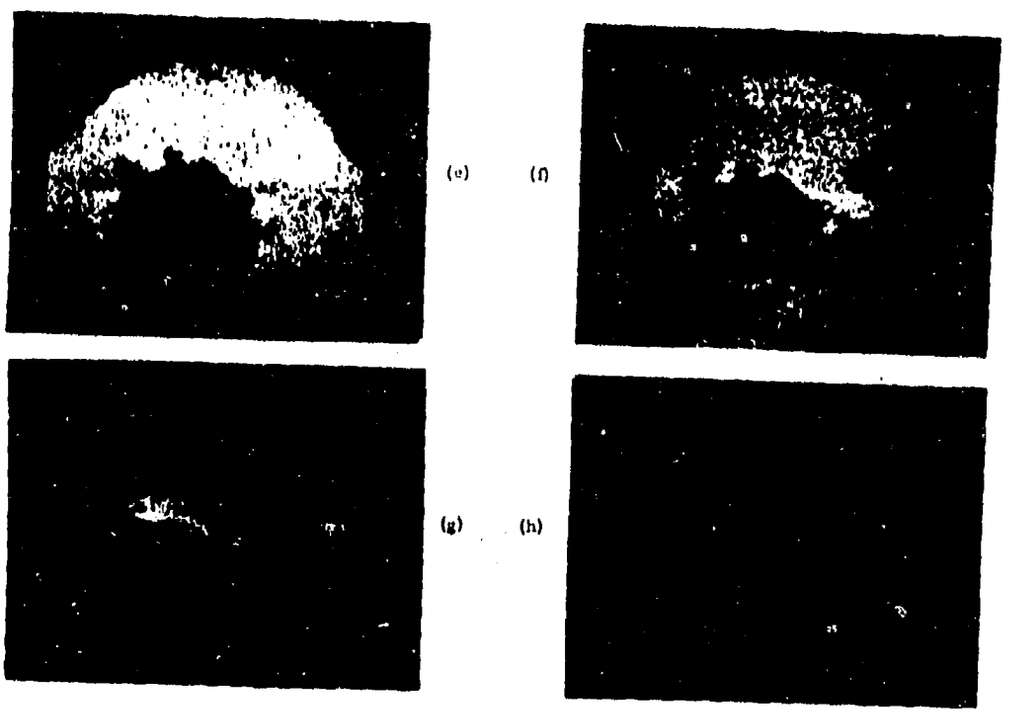

Fig. 18 (continued). (e) Potassium K_α Intensity Picture of this Feature; (f) Iron K_α Intensity Picture of this Feature; (g) Titanium K_α Intensity Picture of this Feature; (h) Lead M_α Intensity Picture of this Feature

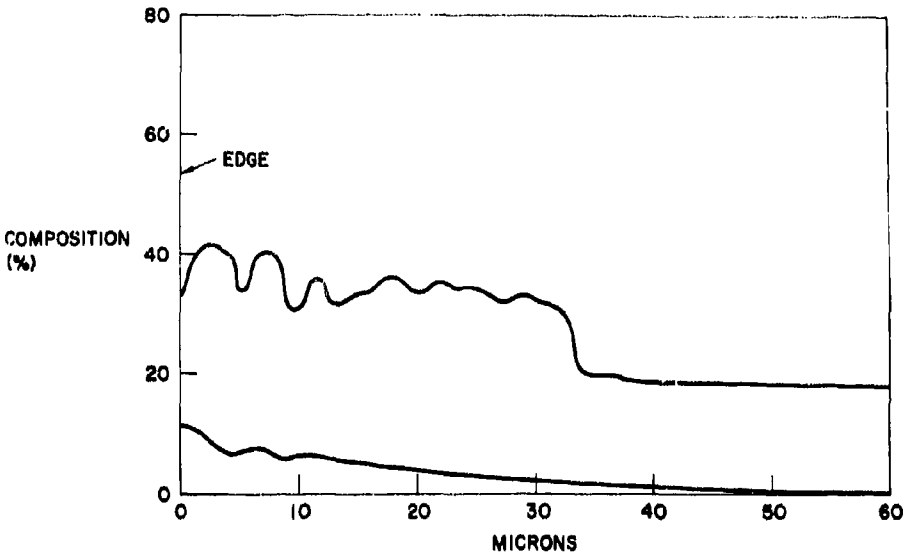

Fig. 19. Microprobe Traces Following Lead and Iron Concentrations from the Surface of a Fallout Particle

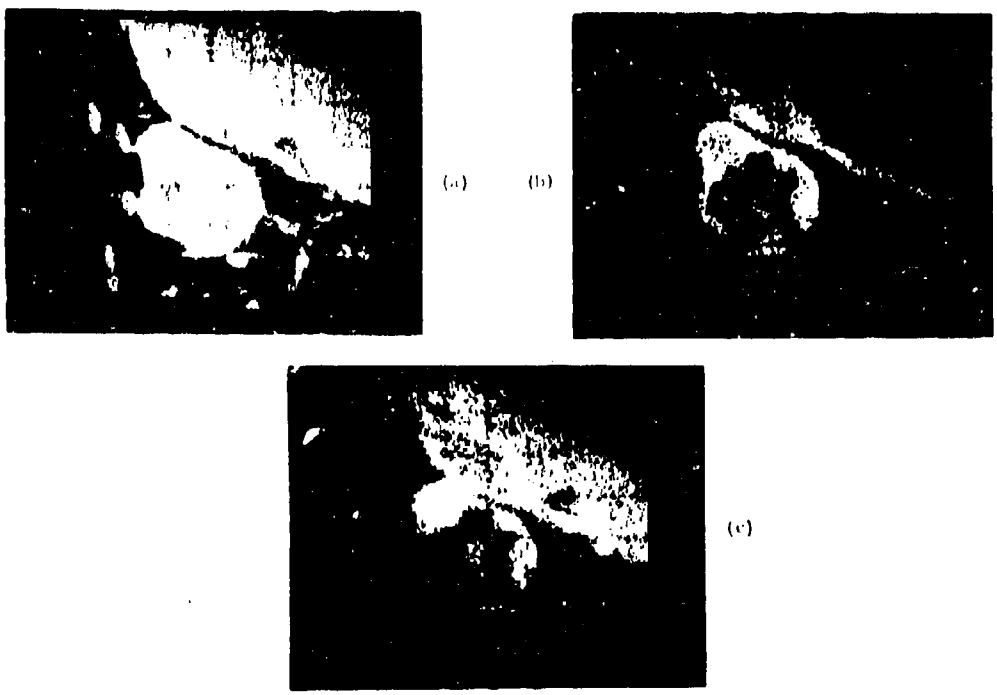

Fig. 20. Microprobe Studies of Another Fallout Particle; (a) Electron Backscatter Intensity Picture of a Feature; (b) Lead M_α Intensity Picture of this Feature; (c) Iron K_α Intensity Picture of this Feature

EXPERIMENTAL DETERMINATION OF INPUT FOR THE PREDICTION OF FRACTIONATION EFFECTS

E. C. Freiling
U.S. Naval Radiological Defense Laboratory
San Francisco, California

ABSTRACT

The lack of uniformity in radiochemical composition among samples of nuclear debris produces a concomitant variation in many properties of interest: the partition of radionuclides among local, tropospheric, and stratospheric fallout, the exposure rate from deposited debris, the variation of this rate with shielding and rainwater leaching, and the availability of individual nuclides to the biosphere. The recognition of the importance of these effects has produced a demand for increasing sophistication in the methods of predicting them. Our work at NRDL is presently concerned with the theoretical development of a kinetic method for the prediction of fractionation effects and the simultaneous measurement of required kinetic and thermodynamic input data.

Using a two-temperature furnace of special design, the rates of condensation of MoO_3 vapor on calcium ferrite, sodium silicate, calcium aluminum silicate eutectic, and clay loam have been measured. Experiments were performed at 1400°C in dry air at partial pressures of $5x10^{-7}$ to $5x10^{-4}$ atm. of MoO_3. Uptake for spherical particles was determined as a function of time and particle diameter. Both rate and mechanism of uptake were found to vary markedly with substrate composition.

INTRODUCTION

The ability to realistically predict nuclear weapons effects is of universally recognized importance to the national security. Also recognized is the fact that the effects of residual radiation have long been among the most difficult to treat satisfactorily. This difficulty is due partly to the complexity of these effects, partly to their inadequate documentation, and partly to the extreme variability of the debris. In the case of land-surface bursts, initial attempts to handle fallout prediction began by distributing an appropriate quantity of activity (usually in terms of an eventual exposure rate) among particles of varying kinematic properties. After assigning some initial spatial distribution to these particles, rise, fall and transport mechanisms were employed in various degrees of detail to bring them to earth. Numerous prediction schemes were devised, and although each was established to give reasonable predictions for at least one known case, comparison of the predictions made by these schemes for other cases were found to be dishearteningly different. Eventually and gradually it has been realized that a different approach is called for.

One sensible, alternative approach to this problem is through the breakdown of the overall prediction scheme into modules (e.g., a particle-formation module, a cloud-rise module, a transport module, etc.) and submodules which can be evaluated individually for both validity and influence and refined as necessary to obtain the confidence levels required. At NRDL we have been using this kind of approach. The efforts of the Physical Chemistry Branch have been directed toward a particle-formation module.

Figure 1 shows a schematic diagram of the processes which occur in particle formation. Our ability to predict the properties of fallout

particles theoretically will depend upon our ability to handle the processes shown here. The efforts of Glenn Crocker have brought the treatment of the nuclear properties to a point of refinement commensurate with the available data. Laboratory studies by Charlie Adams, Jack Quan and Bill Balkwell are now being directed toward the condensation of radioactive species on primary particles. Ian Huebsch is helping us to tackle coagulation and scavenging effects.

This paper concerns the work of Adams, Quan and Balkwell. Although their investigations are still in early stages, they have already turned up significant and not generally expected features of the condensation process. Their findings represent a firm and decisive step on the road to putting the study of fallout formation on a scientific basis.

PRELIMINARY INVESTIGATIONS

The apparatus used for these studies is shown schematically in Figure 2. It consists mainly of a two-temperature furnace constructed from gas-tight aluminum oxide tubing and lined with platinum foil. The high-temperature zone at the top is wound with Pt-10%Rh wire and the low temperature zone at the middle and bottom is wound with Kanthal wire.

When conducting a run, the top and bottom furnace zones are first heated to the proper temperature, the vapor source (in this case radioactive MoO_3) is inserted through the bottom into the low temperature zone, the flow of dry air is begun (60ml/min) and the system is allowed to equilibrate for several hours. The partial pressure of the MoO_3 in the apparatus is determined by weighing the MoO_3 source before and after each series of runs and measuring the volume of carrier gas that has passed through the apparatus.

The samples whose uptake of MoO_3 is to be studied are suspended from a platinum wire hook, preheated in a flame, and then lowered axially through the hole at the furnace top into the high-temperature zone.

After the desired exposure the sample is quickly withdrawn, quenched in air, and the amount of MoO_3 uptake determined by radioactive counting. In the preliminary runs, samples consisted of molten calcium ferrite, molten loam or molten sodium silicate and were suspended in flat, round trays.

Figure 4 shows the resul s obtained by this method as a graph of rate of uptake vs. partial pressure of MoO_3. It can be seen that the three materials show considerable variation in the rate at which they take up MoO_3 vapor.

The calcium ferrite, which is both the most fluid and the most reactive with MoO_3, takes up the vapor the fastest. For this substance the sticking coefficient (defined in Reference 1 as the dimensionless ratio of the amount taken up to the number of impacts calculated by kinetic theory) in the linear region is 6.9×10^{-4}. The less fluid sodium silicate has a coefficient of 2.2×10^{-4} while the viscous clay loam has a coefficient of 0.3×10^{-4}. The questions now arise as to what is the significance of these low sticking coefficients and how are they related to the actual mechanism of condensation. Preliminary to describing the conclusions we have reached, some theoretical background on this subject is appropriate.

BACKGROUND

The condensation of fission-product vapors on substrate material is a case of complex heterogeneous kinetics. Figure 3 shows the various courses that can be taken by a molecule impinging on a surface. These have been dealt with previously in some detail.[2] In the present paper we will confine discussion to the gross features.

From a simplified viewpoint the steps in condensation can be visualized as (1) diffusion through the vapor to the particle surface, (2) condensation at the surface, (3) diffusion into the particle and

(4) eventual equilibrium between vapor and condensate. The relative rates at which particles of different size condense fission products and eventually distribute them will depend upon the relative dominance of these steps.

If the first three steps all proceed rapidly and reversibly, equilibrium will be achieved and the radionuclides will distribute themselves among the available particles in proportion to the cube of their diameters, provided the particles are large enough that surface effects can be neglected.

If condensation is reversible but the slowness of one particular step (called the rate-determining step) controls the rate of attaining equilibrium, the rate of uptake will be proportional to some power of the particle diameter. If particle diffusion is slower than either vapor diffusion or surface condensation, the particles will take up the vapor at rates proportional to their surfaces. If condensation ceases long before equilibrium is reached in any particle, the resulting distribution among particles will go as the square of the diameter. A somewhat greater degree of achieving equilibrium would result in the smaller particles becoming equilibrated with the vapor while the larger ones remained unsaturated.

If condensation at the surface were rate determining, particles would again take up vapors at rates proportional to their surfaces; again an early cessation of the reaction would leave a surface distribution; again, if the reaction were reversible, the smallest particles would achieve equilibrium first.

If vapor diffusion were rate determining, particles much larger than the mean free path of the condensing molecules would assimilate fission products as the first power of their diameters. Particles much smaller than a mean free path would assimilate fission products as the second power of their diameters. As before, the smaller particles would get the closer to equilibrium.

Table 1 summarizes these considerations and shows also the dependence of uptake upon time for different rate-determining steps. Here it is seen that the time required to reach a given concentration depends upon the mechanism: it is proportional to the diameter for surface-condensation control but to the diameter squared for particle-diffusion control. This fact, too, can be used as a criterion in referring the nature of the rate-determining step.

At this point we should not anticipate that every fission product-substrate combination would be governed by the same mechanism, or even that each situation will be a clear cut case of government by a single slow step. Control may pass gradually from one step to another with changes in temperature, particle size, etc.

Table 1

Functional Dependence of Deposition Properties on Time (t) and Particle Diameter (x) for Different Rate-Controlling Steps (Spherical particles far from equilibrium)

Property	Rate-Controlling Step			
	Diffusion in Vapor		Condensation at the Surface	Diffusion in the Particle
	$x \gg \lambda$[a]	$x \ll \lambda$		
Rate of Uptake	x	x^2	x^2	$\frac{x^2}{\sqrt{t}}$
Amount Taken up	xt	x^2t	x^2t	$x^2\sqrt{t}$
Average Concentration	$\frac{t}{x^2}$	$\frac{t}{x}$	$\frac{t}{x}$	$\frac{\sqrt{t}}{x}$
Time to Reach a Given Concentration	x^2	x	x	x^2

[a] λ = mean free path of condensing molecule

MECHANISM

To determine the significance of the observed sticking coefficients and the mechanisms responsible, a series of experiments was designed to gather data which would use the relations of Table 1 to distinguish between rate-determining steps. These experiments measured the rate of uptake by pendant drops of molten substrate supported by Pt wire loops. Drop diameter varied from 0.16 to 0.5cm. The substrates used were calcium ferrite, sodium silicate and clay loam, as before. For intercomparison of results with the General Atomic group, calcium aluminum silicate was added to the list. Runs were conducted at 1387°C using about 6 to 7×10^{-6}atm. of MoO_3 in dry air.

Figures 5 and 6 show the results obtained with calcium ferrite and clay loam, respectively, as graphs of uptake vs. time. Results obtained with the other materials were intermediate between these two extremes.

The rate of MoO_3 uptake by the fluid calcium ferrite particles are seen to be independent of time, indicating that the rate-controlling step is either surface reaction or vapor diffusion. The high affinity of CaO for MoO_3 suggests that the latter is more likely.

The rate of MoO_3 uptake by the viscous clay loam is time-dependent, as were the results obtained with sodium silicate and calcium aluminum silicate eutectic. These observations suggest that diffusion in the particle is rate controlling for the siliceous substrates.

A further test of these indications can be obtained by studying the rate of uptake as a function of drop size. This is shown for calcium ferrite in Figure 7. Here, the rate of uptake is plotted both against the diameter x and against x^2. The linear relation to the diameter shows that diffusion in the air, rather than reaction at the surface, is rate controlling. This conclusion is in accord with the physical and chemical properties of the calcium ferrite.

Figure 8 shows the results for the clay loam. Here, the amount of uptake is plotted against x^2t, $x^2\sqrt{t}$ and xt for each particle. Only the curve against $x^2\sqrt{t}$ is linear, supporting the previous indication that diffusion in the particle is rate determining. This support is clearer for the smaller particles and is in accord with the high viscosity of this material.

The results obtained for the other two substances are not as clear cut, although in each case the graphs for the smallest particle again indicate that particle diffusion is rate controlling. Graphs for the larger sizes are ambiguous.

Figure 9 compares the amount of uptake of MoO_3 for all four substances as a function of particle size. Next to calcium ferrite, calcium aluminum silicate eutectic takes up MoO_3 the most rapidly. Sodium silicate is seen to approximate more closely the behavior of the clay loam.

One sample of clay loam and one of calcium aluminum silicate were allowed to take up MoO_3 until saturation was reached. The final amounts taken up were 0.18 and 0.98 weight percent (0.12 and 0.43 mole percent) respectively. These correspond in turn to Henry's Law constants of 5.1×10^{-3} and 1.4×10^{-3}atm. The latter agrees with the value 10^{-3}-10^{-4}atm. reported by Norman.[3] The value for the clay loam is based on an assumed molecular weight of 92.5 and is for illustrative purposes only. This equilibrium data allowed diffusion constants to be calculated. Depending upon the data chosen these varied from 5×10^{-9} to 9×10^{-9}cm^2/sec for the clay loam and 4×10^{-9} to 12×10^{-9}cm^2/sec for the eutectic. The latter value is some forty times lower than that reported by Norman.[3] The discrepancy and range indicate that in our case uptake by the eutectic is not completely controlled by particle diffusion.

CONCLUSION

If the rate-controlling steps observed here hold for the conditions under which particles are formed in Nevada and Eniwetok, these results have considerable practical significance. To the already impressive list of known differences between Nevada and Eniwetok surface shots (viz., yield, soil melting point, soil boiling point, chemical affinity) they add the difference of mechanism of condensation for at least one fission product element. Attendant to this possibility is the awareness that added caution is necessary when extrapolating results from one soil to another, particularly when so many difficulties in fallout prediction, past and present, can be traced to one or another unwarranted extrapolation.

There is some slight evidence that such a difference in mechanisms may hold under actual shot conditions. Russell[4] has pointed out that, in the 5 to 50-μ range of active particles from Bravo, Sr^{89} was incorporated as the 1.4 power of the diameter and Mo^{99} as the 1.8 power, while in undifferentiated Johnie Boy debris these powers were 2.0 and 2.8 respectively. Of course, the behavior we have observed would be more appropriately applied to Ru and Rh activities, but the differences mentioned by Russell are at least cause for concern.

Further studies are necessary to determine whether these results hold at the lower vapor pressures, smaller particle sizes and higher temperatures prevailing in fallout formation. Table 2 shows some of the effects that changes in conditions may produce. Also necessary are observations on the effect of water vapor, comparison of ambiguous cases with theoretical equations, and comparison of apparently clear cut cases to measured diffusion constants.

In closing it is appropriate to paraphrase the words of G. N. Lewis and M. Randall in their classic treatise on thermodynamics: "Let this (work) be dedicated to the (fallout scientists) of the newer generation, who will not wish to reject all inferences from conjecture or surmise,

but who will not care to speculate concerning that which may be surely known."

Table 2

Effect of Change in Conditions on Relative Importance of Processes and on Final Distribution

Change	Effect on Processes	Effect on Rate of Approach to Equilibrium
Increase Temperature	Speed up all processes. Decrease relative importance of diffusion in the particle.	Increase
Decrease Partial Pressure	Decrease relative importance of diffusion in the particle.	None if not controlled by particle diffusion
Shorten Exposure	Increase relative importance of diffusion in the particle.	Decrease
Increase Irreversibility	Increase relative importance of diffusion through the vapor.	Decrease
Decrease Particle Diameter	Increase relative importance of diffusion through the vapor.	Increase
Increase Turbulance	Decrease relative importance of diffusion through the vapor.	Increase if controlled by vapor diffusion

ACKNOWLEDGEMENT

This work was carried out under joint sponsorship of the Defense Atomic Support Agency and the U.S. Atomic Energy Commission. Laboratory work was performed by Messrs. J. T. Quan and W. R. Balkwell under the direction of C. E. Adams. The capable assistance of Mr. Adams in preparing this paper is gratefully acknowledged.

REFERENCES

1. J. P. Hirth and G. M. Pound, "Condensation and Evaporation. Nucleation and Growth Kinetics." Volume 11 of "Progress in Materials Science," B. Chalmers, Ed., Pergamon Press, MacMillan, New York, 1963.

2. E. C. Freiling, G. R. Crocker and C. E. Adams, "Nuclear-debris Formation," p. 1 of "Radioactive Fallout from Nuclear Weapons Tests," Proceedings of the Second Conference, 3-6 November 1964, A. W. Klement, Jr., Ed., USAEC Division of Technical Information, November 1965.

3. J. H. Norman, et al., "Fallout Studies--Cloud Chemistry," Final Report, GA 6094, 29 January 1965.

4. I. J. Russell, private communication.

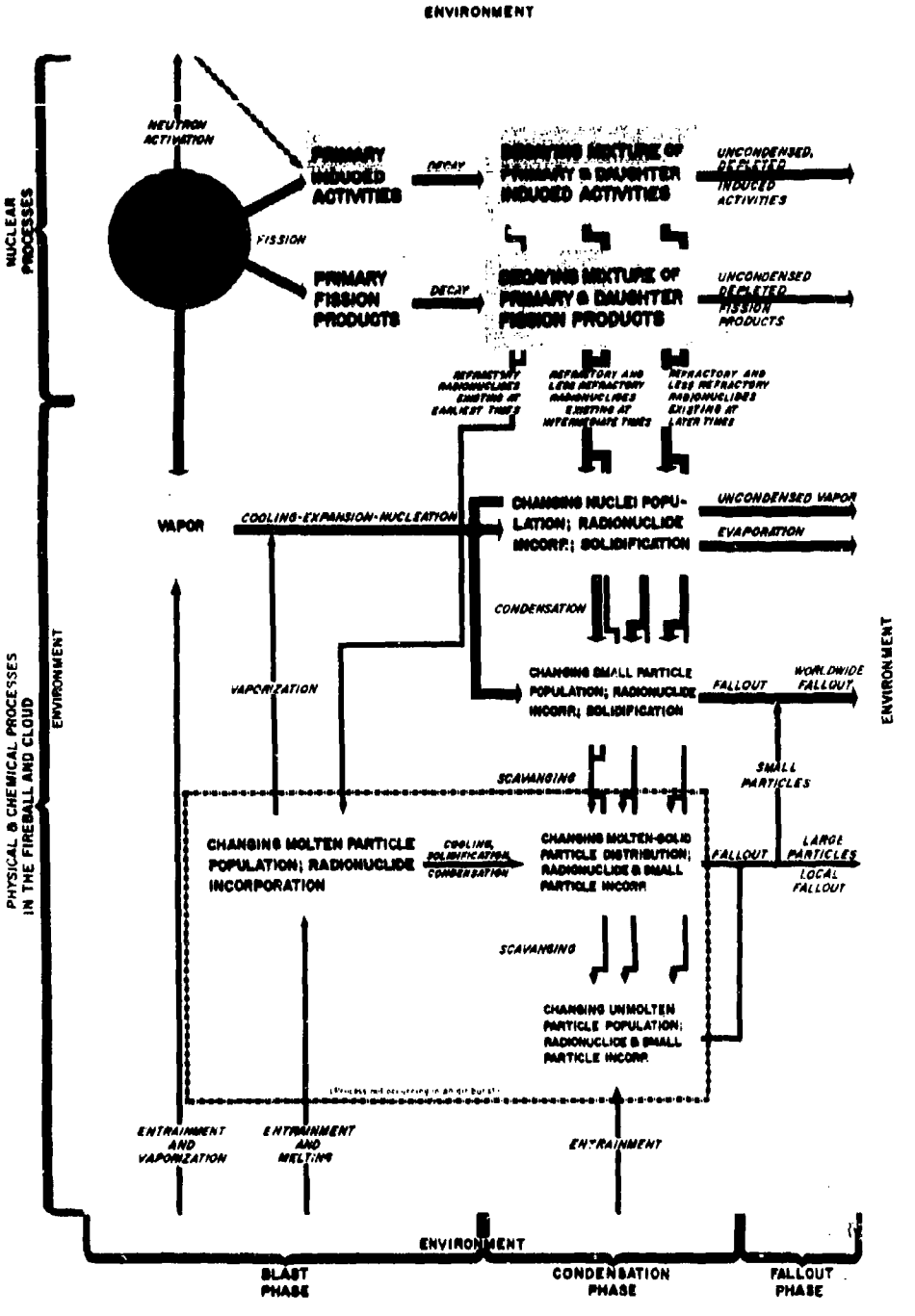

Fig. 1. Fallout-Formation Processes in Air and Surface Bursts

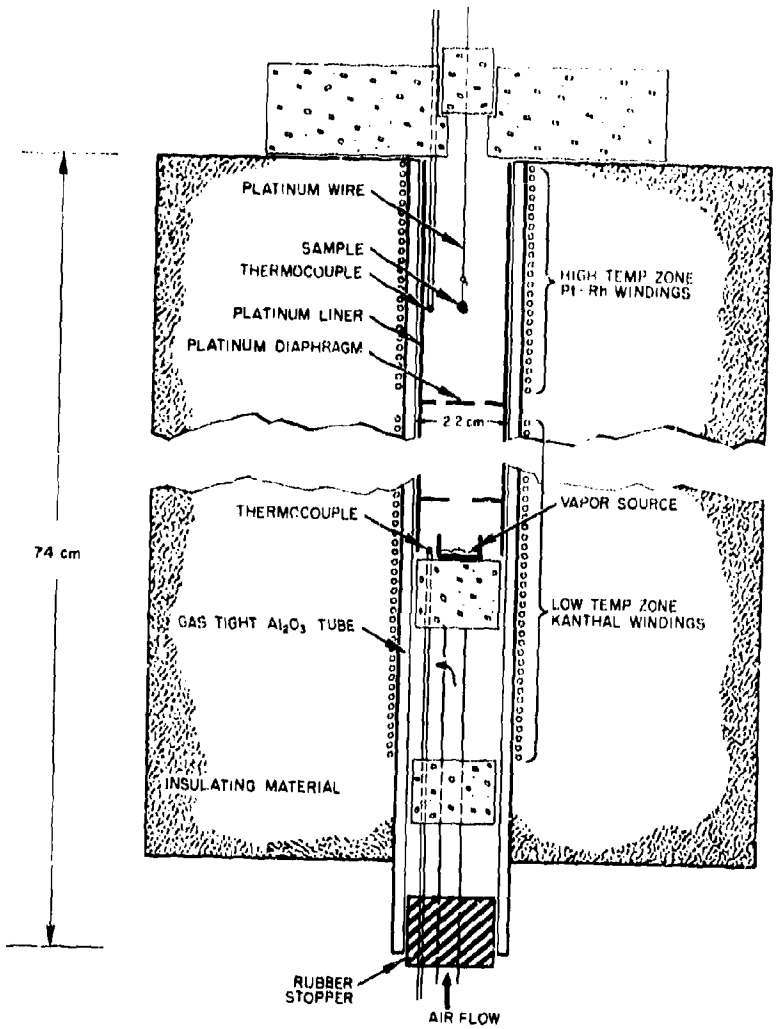

Fig. 2. Two-Temperature Furnace

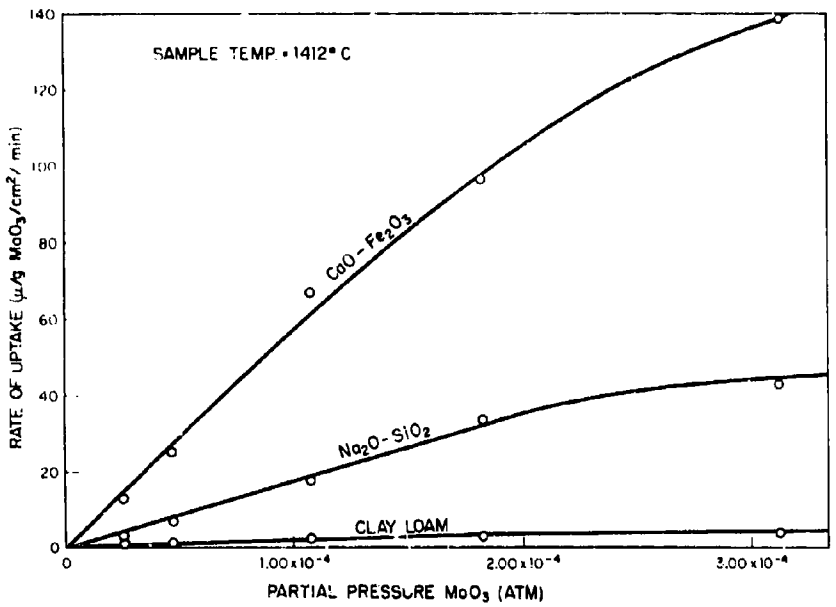

Fig. 3. Results of Preliminary Investigations

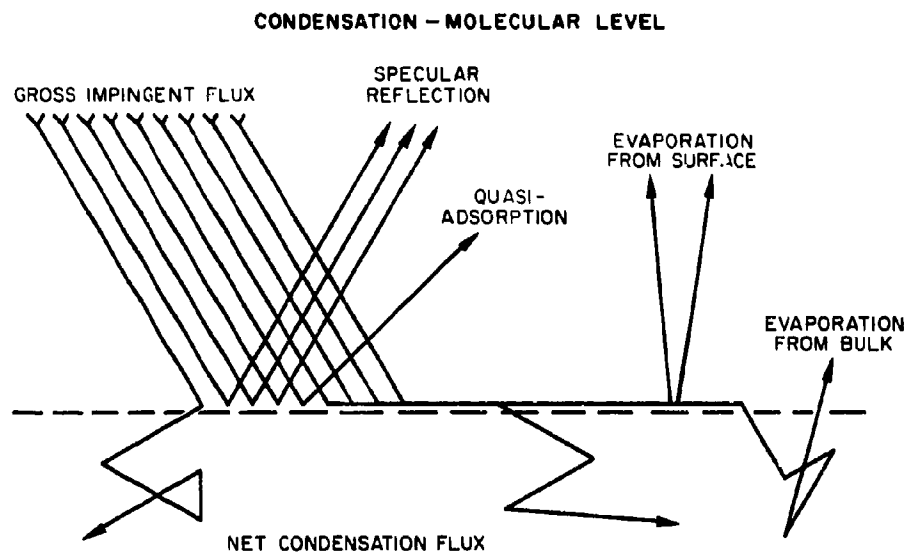

Fig. 4. Possible Steps that Can be Taken by a Molecule Impinging on a Surface

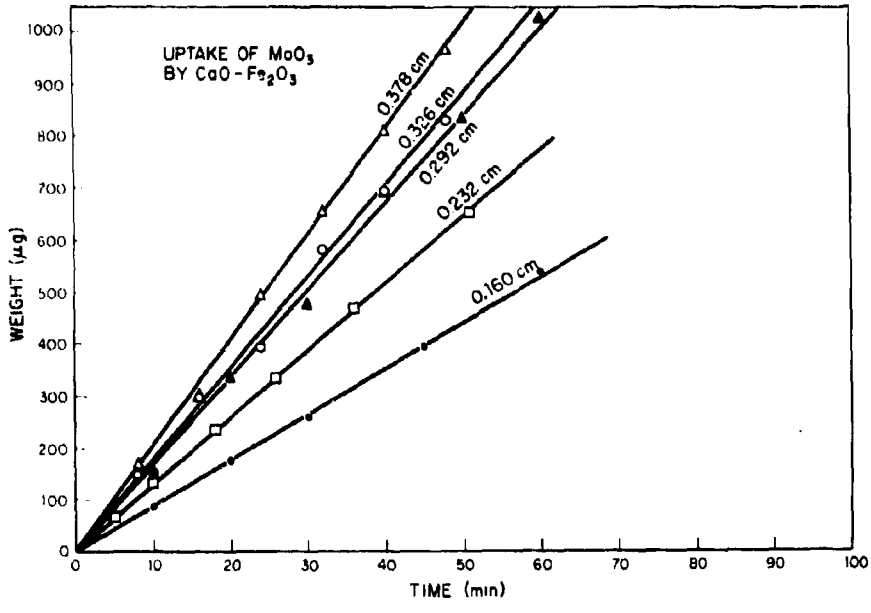

Fig. 5. MoO_3 Uptake vs. Time: $CaO-Fe_2O_3$

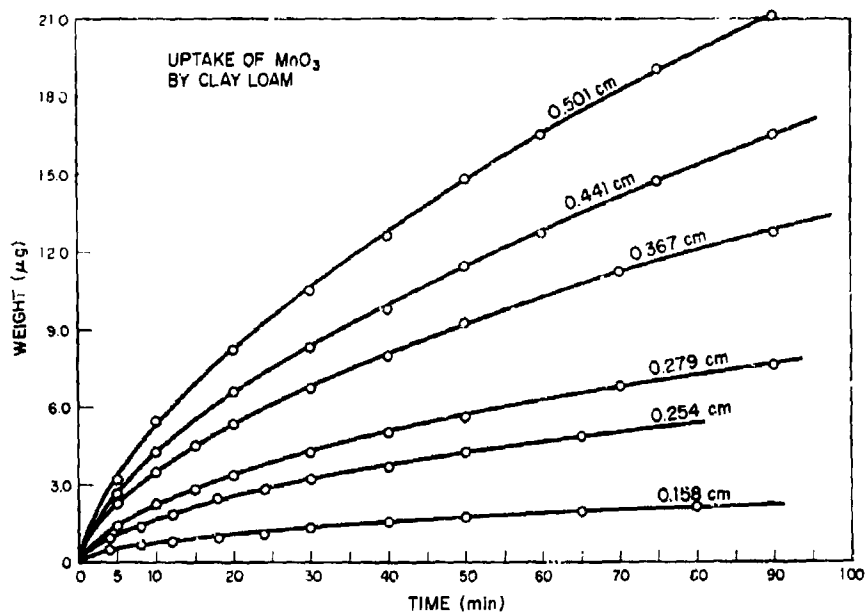

Fig. 6. MoO_3 Uptake vs. Time: Clay Loam

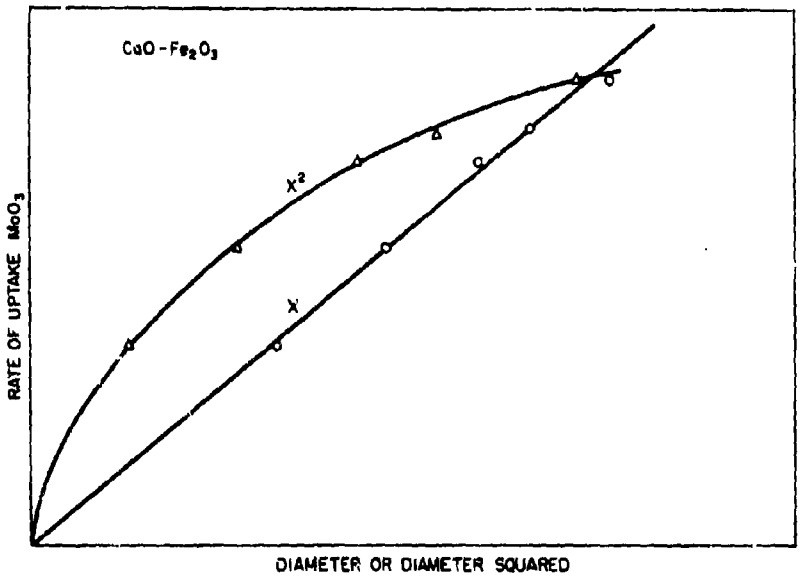

Fig. 7. Rate of MoO_3 Uptake vs. Size: $CaO-Fe_2O_3$

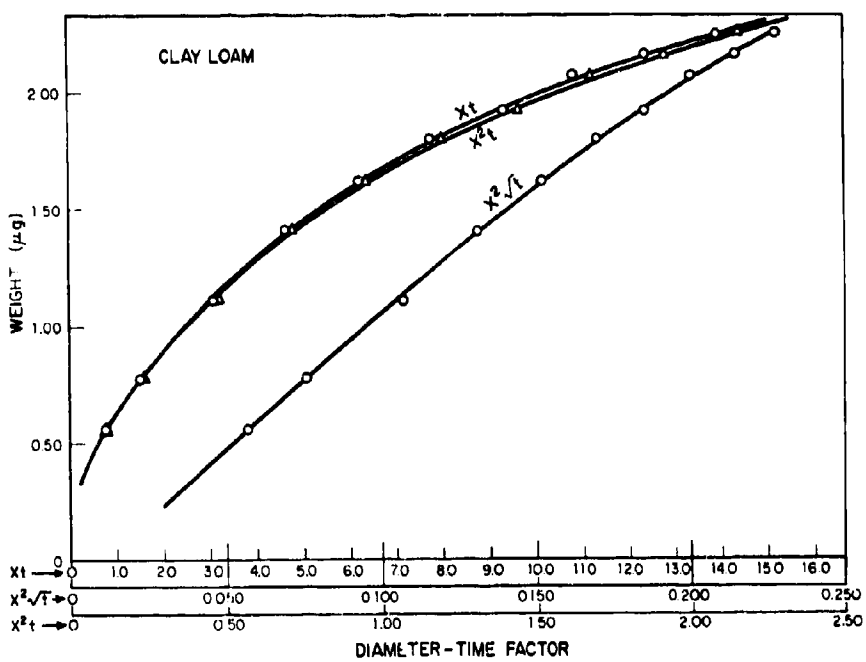

Fig. 8. MoO_3 Uptake vs. Size and Time: Clay Loam

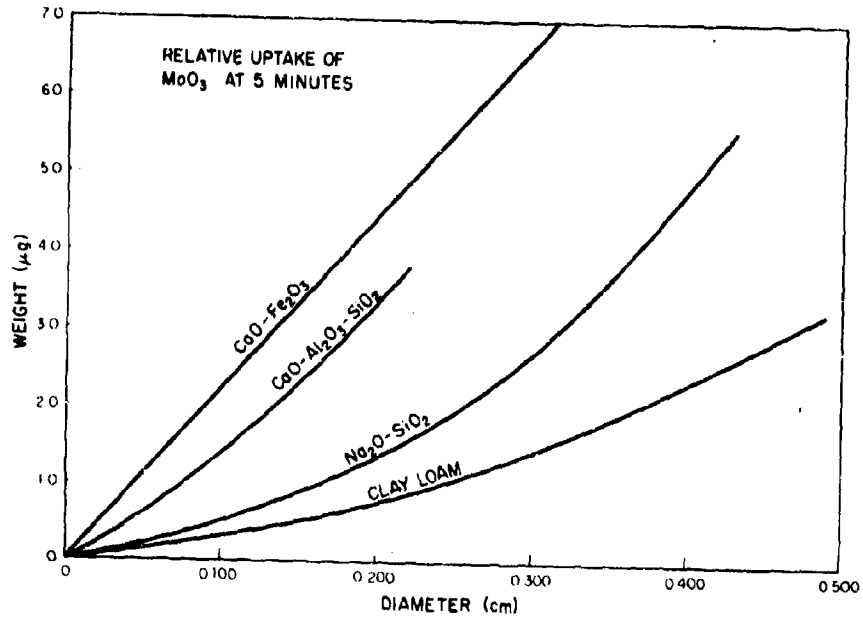

Fig. 9. MoO_3 Uptnke vs. Size

SIMULATION OF PARTICULATE FALLOUT*

G. F. Rynders
University of California, Lawrence Radiation Laboratory
Livermore, California

ABSTRACT

A radio-frequency induction plasma generator is being used to obtain chemical reactions similar to those encountered in a nuclear explosion. Thermal plasmas produced by this technique range in temperature from 4,000 to 20,000°K, and offer high enthalpic input and freedom from container contamination. While material fed into the plasma may not reach these temperatures, the more refractory oxides can be vaporized completely. Reactions of interest generally occur below 3000°K. In this system, completely enclosed for better control of the environment, gas-gas and/or gas-liquid reactions are studied by variation of parameters such as average particle size, feed rate, residence time, and power input. For a monodisperse system of particles fed, a bimodal distribution of particles results. The larger particles result from melting of the original particles (a consequence of short residence time); their shape is controlled by surface tension. They may be solid or hollow, crystalline or glassy. Some of the hollow spheres have internal negative crystals. Particles condensed from vapor are sub-micron in size because of the short quench time which limits growth. Both types of particles are similar to those found in nuclear explosion debris. The report also gives a description of equipment and a discussion of the relationship of the experimental parameters to those expected in formation of fallout.

* Work performed under the auspices of the U.S. Atomic Energy Commission.

I. INTRODUCTION

In the fireball of a nuclear explosion, very high temperatures are produced in which material exists in the atomic and ionized states. The condensation processes responsible for determining the physical and chemical nature of fallout, however, occur at temperatures less than about 3,000°K. A number of working models have been proposed to explain the mechanism of fallout formation and its distribution.[1,2,3] These models, primarily based on radiochemical and microscopic studies of fallout, are handicapped by a lack of kinetic and thermodynamic data. Experimental data of the type carried out by Adams and Quan[4] at NRDL and at General Atomics[5] is needed for incorporation into these models.

In the present work, an experiemental approach has been taken to simulate some of the chemical processes which may occur during the formation of fallout in the later stages of the fireball. The laboratory plasma provides a convenient means of heating materials to high temperatures without contaminating the container. While material being fed into the torch may not reach the plasma temperatures, enough heat may be transferred to melt and to vaporize the most refractory oxides. A primary factor in this transfer is the "residence time" which in this study is of the order of tens of milliseconds. The rapid heating and quenching effect experienced by particles in the plasma has an obvious analogy to that occurring in the fireball.

Laboratory plasmas have been used in a number of applications to study high-temperature reactions. Kana'an and Margrave[6] have presented a review of current work which includes use of plasmas as spectroscopic excitation sources, ablation studies, crystal synthesis, spheroidization of materials, application of refractory coatings, and chemical processing. The radio-frequency induction method was chosen for our work to eliminate electrode contamination problems and to permit the use of reactive gases.

An investigation of the characteristics of a plasma produced by a radio-frequency induction generator shows that temperatures between 4,000 and 20,000°K may be attained.[7,8] For torches operating at one atmosphere, local thermal equilibrium is found to exist with the gases of the more common types, that is, temperatures are found to be equal for electrons, ions, and atoms, within short distances. The common gases are found to be nearly completely dissociated. The plasma is considered to be "optically thin,"[9] i.e., transparent in many areas of the spectrum. Many new lines appear in the spectra from forbidden transitions, not usually observed.

II. EXPERIMENTAL

Figure 1 shows an argon plasma operating at a plate power of 7.5 kW or about 88 kcal/mole, and having an average temperature of about 12,000°K. This does not imply a uniformity of temperature within the fireball. Once the plasma has been initiated, conduction takes place in the outer skin of the plasma, and this skin is surrounded by a cooler region between it and the walls of the fused silica container. The gradient to the center of the plasma region may be steep or flat, depending upon the turbulence in the system. It is convenient to express the energy in the system in terms of its enthalpy. The efficiency for conversion of electrical energy from the generator to energy in the plasma is estimated to be about 45 percent of the plate power of the oscillator tube.

The power supply is a variable-frequency (4 to 15 MHz), 20-kW induction generator unit manufactured by the Forrest Electronics Company. In Figure 2, the generator with accessory equipment is shown. A powder feeder supplies a sized fraction of particles to the plasma. The melted or vaporized material is then collected in the lower part of the apparatus, either by sedimentation or electrostatic precipitation. A final membrane filter and exhaust pump completes the system. A diluent gas is added in the collector to lower the mean temperature in the chamber. Total flow

through the system is fixed at 51 liters/min. Since the position of the torch is fixed, provision is made for x, y and z movement of the collector assembly. In addition, the lower part of the assembly is hinged for rotation out of the chamber for cleaning. The electrostatic precipitator is lined with a 0.125-mm-thick, stainless steel removable liner. A 25-kV half-wave rectified power supply is connected to the precipitator. The feeder, torch, and collector assembly form a closed system so that the environmental atmosphere controls the degree of oxidation of the reaction products. Although the gases are presently exhausted, provision can be readily made to scavenge particular gases of interest. The reactor portion of the system is sealed in chamber apart from the generator, utility supply chamber, and the outside. Thus, contamination would be contained in the event of rupture of the torch walls.

To obtain meaningful results, it was felt necessary to feed particulate material at a known constant and reproducible rate. A number of commercial feed units were evaluated and found to be unsatisfactory for the purpose. A screw-feed device was therefore designed by us to deliver particles between 20 and 150 microns in diameter at a rate ranging from 1/2 to 2 g/min (e.g., alumina with a true density of 3.95). Up to the present time, feeding of fine powders in our system has been limited to this size range. It is also possible to inject solutions and gases, such as H_2O, CO_2 and SO_2, into the plasma.

III. ANALYTICAL TECHNIQUES

The techniques used in characterizing the particles produced are those used for obtaining particle-size distributions and those describing the physico-chemical nature of the individual particles, i.e., chemical phase, structure and morphology. Optical microscopy, with both reflected and transmitted light, is used to analyze the larger particles, i.e., those above a few microns in diameter. To observe spheroidized particles in polished thin sections, we have experimented with the use of soft glasses

for mounting. For the sub-micron particles, the electron microscope is necessary for observation of the character and size.

To obtain the size distribution, a Zeiss particle size analyzer has been used. The particles, suitably dispersed on a slide, are photographed and a print is made. The size of the individual particles are matched with the area of a circular spot of light whose size is related to a particular channel in a counting device. As each particle is matched, a foot switch actuates a counter and perforates the print, thus indicating the particle has been counted. This technique was chosen for its utility to both light and electron microscopy.

The centrifuge technique as described by Whitby[10] and manufactured by the Mines Safety Appliances Co. is expected to be useful for concentration purposes as well as analyses. Micro-mesh sieves are being used for separations down to 5 microns. Other techniques, such as x-ray diffraction, radioactive counting and autoradiography, will also be needed as the program develops.

IV. RESULTS AND DISCUSSION

Most of the work thus far has concentrated on the development of the system-torch, particle feeder, and collector. In the course of this work particles have been obtained in exploratory experiments, but an organized study of their formation processes has not been started. Since aluminum oxide is readily obtainable, much of the work has been done with this material. Other materials, such as basalt, granite, tuff and sandstone, have been passed through the torch. Results of several of these experiments will be discussed.

If the residence time of the particle in the plasma is short and the particles are large, the particles melt without appreciable vaporization. The volume of the resulting spheres is only slightly less than in the initial material. Vaporization from the surface and subsequent condensation results in the formation of small spherical particles which are collected in the electrostatic precipitator. If smaller particles are introduced, complete vaporization may take place.

Figure 3 shows alumina particles spheroidized in an argon plasma with an enthalpy of 32 kcal/mole of argon. Initial polycrystalline particles, averaging 70 microns in diameter, were fed at the rate of 0.4 g/min. Of the large particles recovered, about 95 percent were found to be spheroidized. This percentage is primarily a function of torch design and plasma heat content. It can be nearly 100 percent. Many of the resulting spheres contained voids. Surfaces show thermal etching as well as excessive surface shrinkage effects. Closer examination of the particles shows several distinct types. Two crystalline phases - alpha, the high-temperature form and theta, a form usually associated as an intermediate phase - are obtained in the dehydration of the hydroxide. Three different types of spheres have the alpha form; the spheres of the theta form have a rectilinear void structure. As collected, the particles show a high degree of strain and require annealing to obtain the characteristic indices of refraction. Since the crystallites are small and polycrystalline, only average optical values were obtained.

The particles shown in Figure 3 were obviously not chosen for the lack of defects, but to show the character of a specimen that is particularly difficult to mount and manipulate. In addition, the presence of a multiphase reaction product is also of interest.

Several rock types have been crushed and fed through the system. All these particles ranged in diameter between 70 and 130 microns. A typical sample of basalt is shown in Figure 4. To bring out the character of the rock samples, they were photographed under crossed polarizers with a first-order red plate. The high absorption of the ferromagnesian minerals may be observed. After the material was passed through an argon plasma, the resulting particles were nearly completely spheroidized. Figure 5 shows the spheres, as collected. The individual grains have melted and may be separated for analysis. Figure 6 shows spheres obtained from granite. Figure 7 shows spheres obtained from tuff. Figure 8 is the sample of crushed sandstone rock before spheroidizing. The large

grains are primarily quartz, stained with iron and titanium. However, some terminated crystal clumps of calcite may also be observed. The small particles are fragments of the calcite broken up during the sieving process. Spheres resulting from this material may be seen in Figure 9.

Rocks containing phases with gaseous decomposition products tend to have more hollow spheres, as is the case with granite, tuff and sandstone. The shape and relative amount of voids in the spheres differ appreciably. In experiments with alumina, voids having internal faces were observed. For those materials which crystallize readily, such as alumina, the resulting spheres are crystalline. In the case of the silicate minerals, the molten liquids tend to be more viscous, and glassy spheres result. Annealing is required to relieve the strains introduced during cooling.

Hollow sphere formation has been observed by others and has been the subject of some discussion. The solubility of oxides in high-temperature gases, viz., water vapor, has received appreciable concern in recent years, but little effort has been placed in obtaining an understanding of the solubility of gases in liquid oxides. Meyer[11] has pointed out that hollow spheres are more readily formed in high enthalpic plasmas containing nitrogen. Particle porosity increased with residence time in the plasma. He has concluded that the solubility of nitrogen is a chemical process which reverses itself at lower temperatures to release nitrogen and inflates the liquid particles to hollow spheres. Some evidence is also given for excess aluminum remaining in the particles. Diamond and Dragoo[12] have observed that molten alumina picks up water and releases it when cooled. However, these latter investigators did not observe the same effect with other common gases, including nitrogen. It has also been observed that the presence of small amounts of water in liquid silicates decreases the viscosity of the melts.

The rate at which various materials absorb heat in passing through the plasma is of interest in obtaining a value for the peak temperature of liquid particles. An important parameter is the residence time. Meyer[11]

has pointed out that with argon and argon/nitrogen mixtures, the ease of melting is not related to the melting point of the compound, but appears to result from a catalytic recombination effect similar to that found in the atomic hydrogen torch. Marynowski, Halden and Farley[13] have also examined the various methods of heat transfer.

For the material vaporized in the plasma, condensation occurs with the formation of extremely fine particles. For the alumina experiment discussed previously, the material collected in the electrostatic precipitator appears as spherical particles, or nearly so, ranging in size from 0.01 to 0.10 microns. Figure 10 shows a collection of such particles. The particles occur in aggregates that may be several microns in size. Some of the particles appear to have hexagonal faces. The presence of highly charged particles in the atmosphere of the "tail flame" of the plasma provides ready nucleation of material from the vapor. X-ray diffraction patterns indicate the material to be alpha alumina, which is hexagonal.

Long and Tiechner[14] observed that an interaction occurred between particles that were passed through a flame a second time to obtain an increased average particle size. In the present work, this growth effect has not been observed. There appears to be little interaction between particles when they are above say 50 microns, at least for the material concentrations examined.

V. SUMMARY

A closed system in which a radio-frequency induction plasma is used for heating material introduced in particulate form, together with a particle collection system, has been constructed. Particles obtained from the system show some similarities with those obtained from fallout produced from nuclear explosions. Because of the control which may be exercised in producing the particles, it is expected that this experimental

approach will be useful in understanding some chemical processes taking place during the cooling of a nuclear fireball.

ACKNOWLEDGMENTS

Acknowledgment is extended to Dr. Larry Schwartz, Al Loethen, Jack Wells, and Willa Wadliegh for the assistance given in obtaining a working system, specimen preparation and electron microscopy.

REFERENCES

1. Worldwide Effects of Atomic Weapons, Project Sunshine, Rand Corporation R-251-AEC (Amended), August 6, 1953.

2. C. F. Miller, "Fallout and Radiological Measures," Vol. I, Stanford Research Project No. IM-4021, January, 1963.

3. E. C. Freiling, "Fractionation in Surface Bursts," Radioactive Fallout from Nuclear Weapons Tests, Conference at Germantown, Maryland, November 15-17, 1961, pp. 25-46.

4. C. E. Adams and J. T. Quan, "Development of a High-Temperature Isopiestic Technique," U.S. Naval Radiological Defense Laboratory, USNRDL-TR-823, January 19, 1965.

5. J. H. Norman, P. Winchell, W. E. Bell and A. B. Riedinger, "Fallout Studies, Cloud Chemistry, Final Report," General Atomics Division of General Dynamics, Report GA-6094, January 29, 1965.

6. A. S. Kana'an and J. L. Margrave, "Chemical Reactions in Electric Discharges," Advances in Inorganic Chemistry, Vol. 6, Academic Press, New York, 1964, pp. 143-206.

7. T. B. Reed, "Induction-Coupled Plasma Torch," J. Appl. Phys. 32, 821-824 (1961).

8. C. W. Marynowski and A. G. Monroe, "RF Generation of Thermal Plasmas," in High Temperature Technology, Proc. Intern. Symp. High-Temperature Technology, Butterworths, Washington, 1964, pp. 67-83, 525-540.

9. H. N. Olsen, "Thermal and Electric Properties of an Argon Plasma," Phys. Fluids 2, 614-623 (1959).

10. K. T. Whitby, "A Rapid General Purpose Centrifuge Sedimentation Method for Measurement of Size Distribution of Small Particles, Part I and II," Heating, Piping, Air Conditioning 61, 449 (1955).

11. H. Meyer, "Fusion of Powders in a Plasma Jet," UCRL-Trans-1135 (L) Oct. 1964, transl. from Ber. Deut. Keram. Ges. 41, 112-119 (1964).

12. J. J. Diamond and A. L. Dragoo, "The Solubility of Water Vapor in Molten Alumina," Thermal Imaging Techniques, edited by P. E. Glaser and R. F. Walker, Plenum Press, New York, 1964, pp. 225-228.

13. C. W. Marynowski, F. A. Halden, and E. P. Farley, "Variables in Plasma Spraying," Electrochem. Tech. 3, 109-115 (1965).

14. J. Long and S. J. Tiechner, "Elaboration dans la Flamme Oxyhydrique du Bioxide de Titane en Particules Spheriques Homodispersées," Rev. Hautes Temp. Refractaires 2, 47-54 (1965).

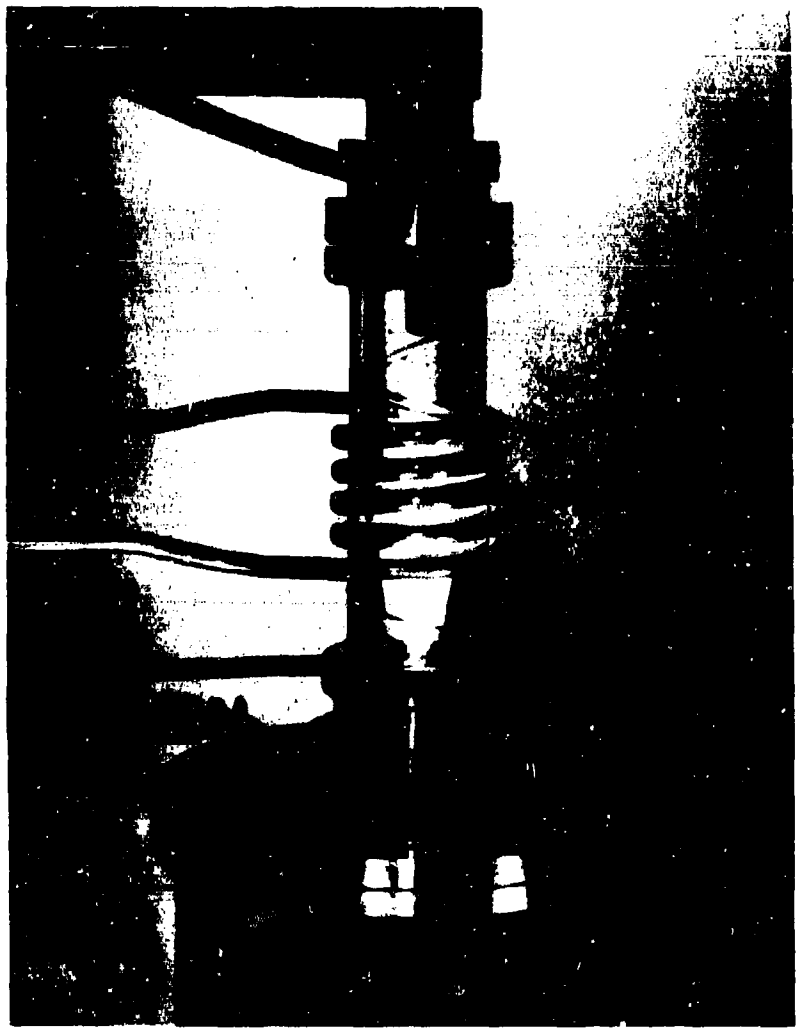

Fig. 1. Argon Plasma at ~ 53 kcal/mole; Generated at 5 MHz

Fig. 2. High-Frequency Induction Plasma Fallout-Simulation Apparatus

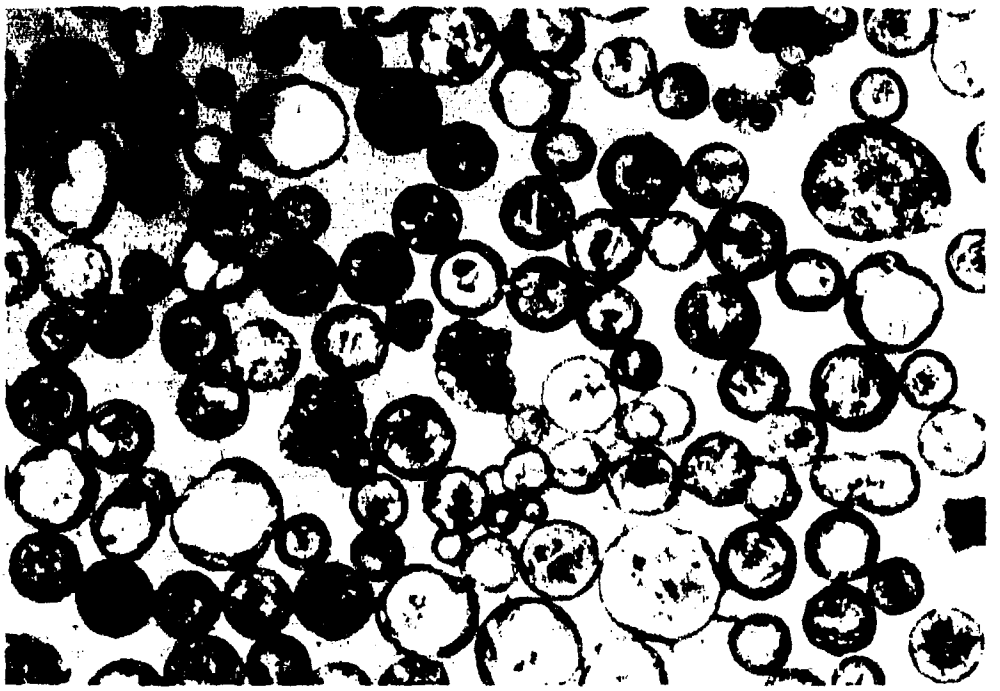

Fig. 3. Alumina Spheroidized in an Argon Plasma with an Enthalpy of 32 kcal/mole. Photomicrograph was Taken in Transmitted Light with Crossed Polarizers Through a Thin Section (~35μ) Mounted in Glass. (Magnification 200×)

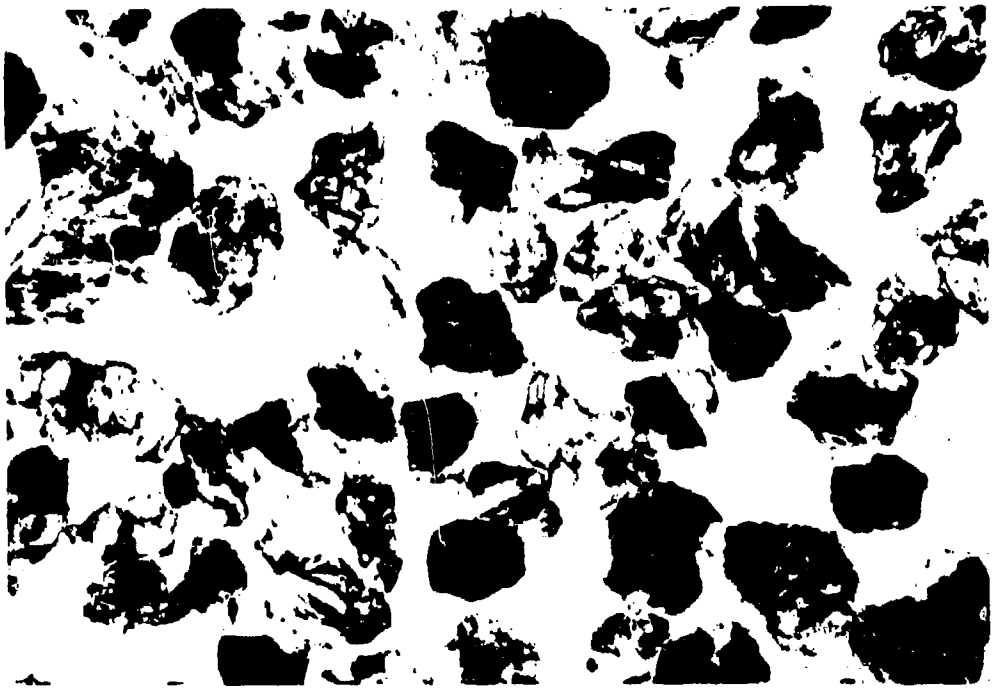

Fig. 4. Particles of Crushed Basalt Before Spheroidizing. Photomicrograph was Taken with Transmitted Light with Crossed Polarizers and First-Order Red Plate. (Magnification 150×)

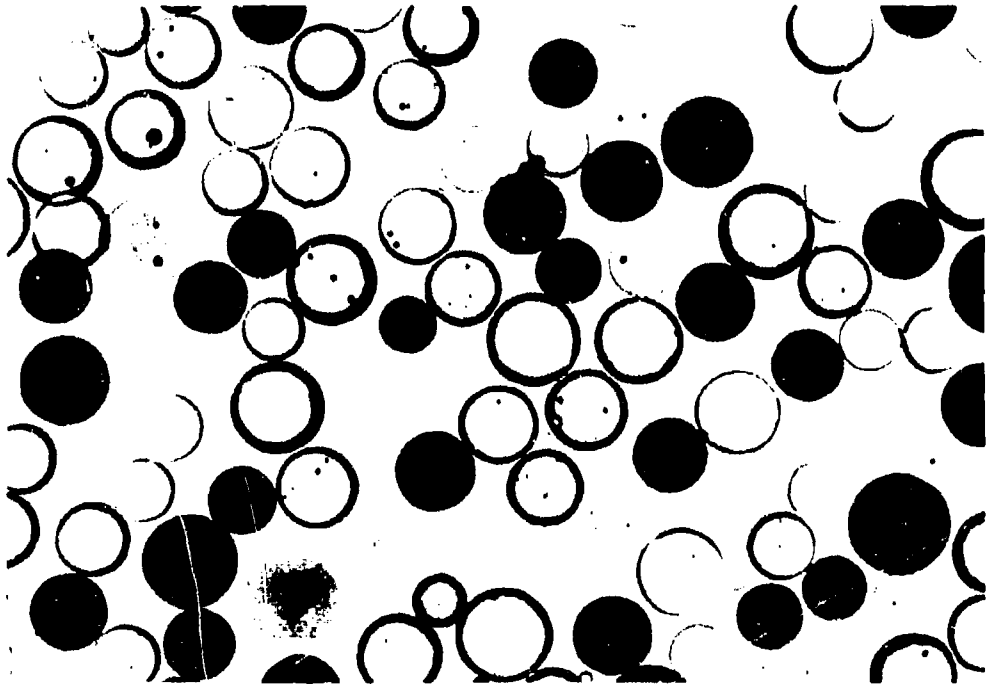

Fig. 5. Basalt Particles Spheroidized in an Argon Plasma at 40 kcal/mole Argon. Photomicrograph was Taken in an Immersion Oil (n = 1.56). (Magnification 150×)

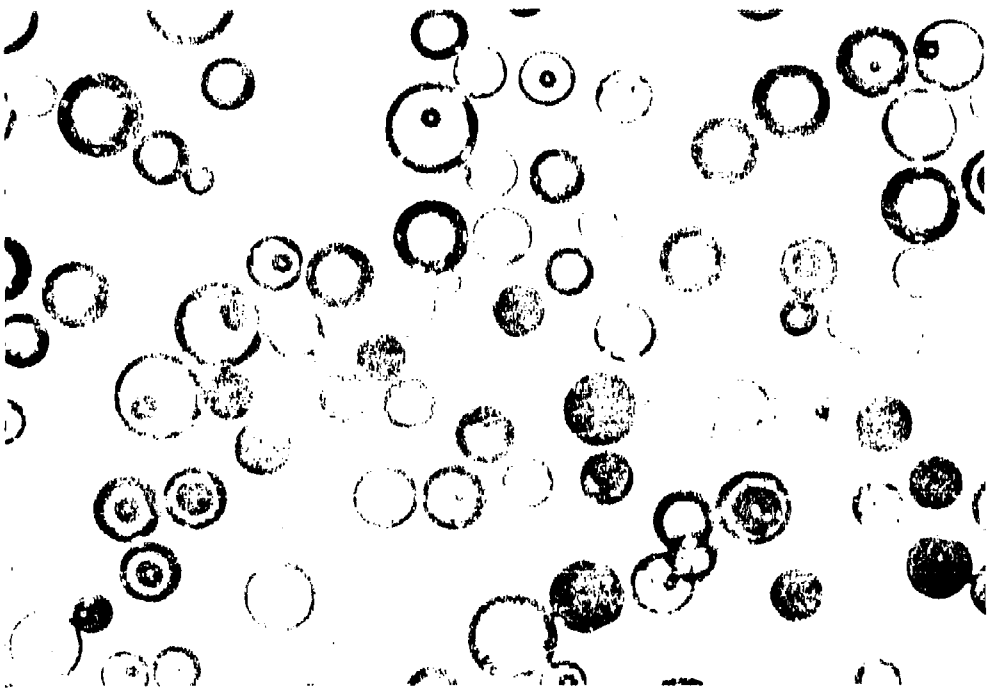

Fig. 6. Granite Particles Spheroidized in an Argon Plasma (64 kcal/mole Argon). Photomicrograph was Taken in an Immersion Oil (n = 1.60) with Transmitted Light. (Magnification 150×)

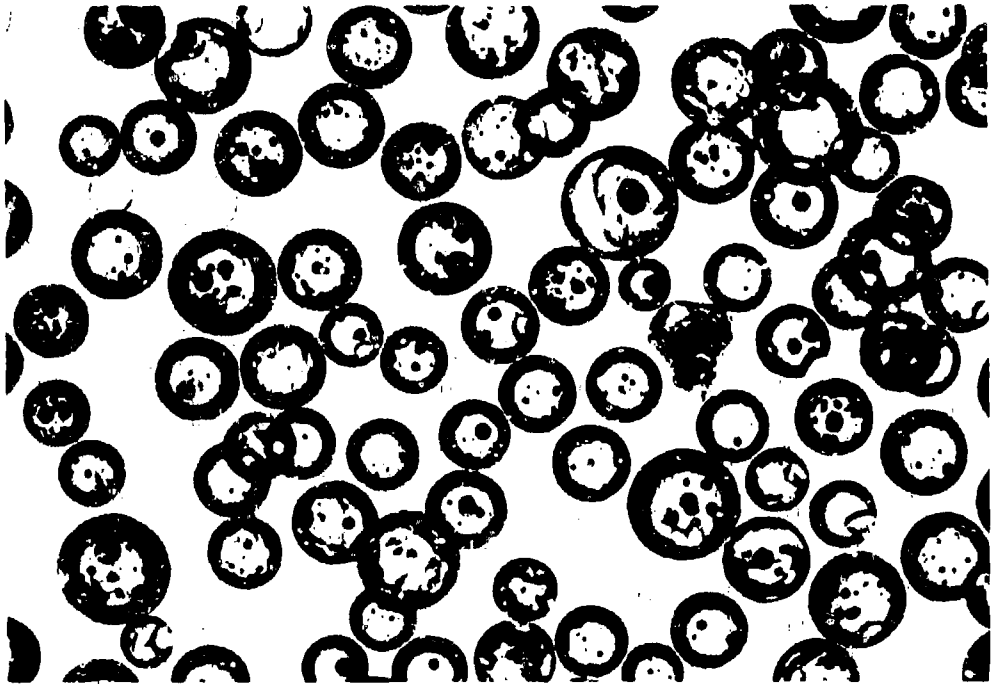

Fig. 7. Tuff Particles Spheroidized in an Argon Plasma (41 kcal/mole Argon). Photomicrograph was Taken in an Immersion Oil (n = 1.56). (Magnification 150×)

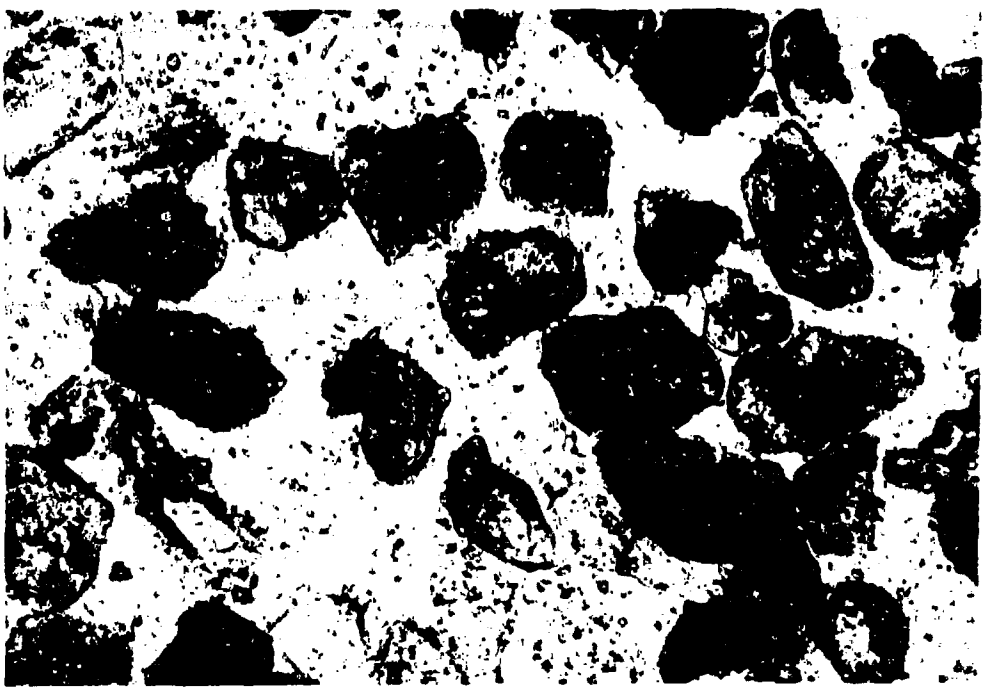

Fig. 8. Sandstone Particles Before Spheroidizing. Photomicrograph was Taken Using an Immersion Oil (n = 1.56) with Transmitted Light, Crossed Polarizers and a First-Order Red Plate. (Magnification 150×)

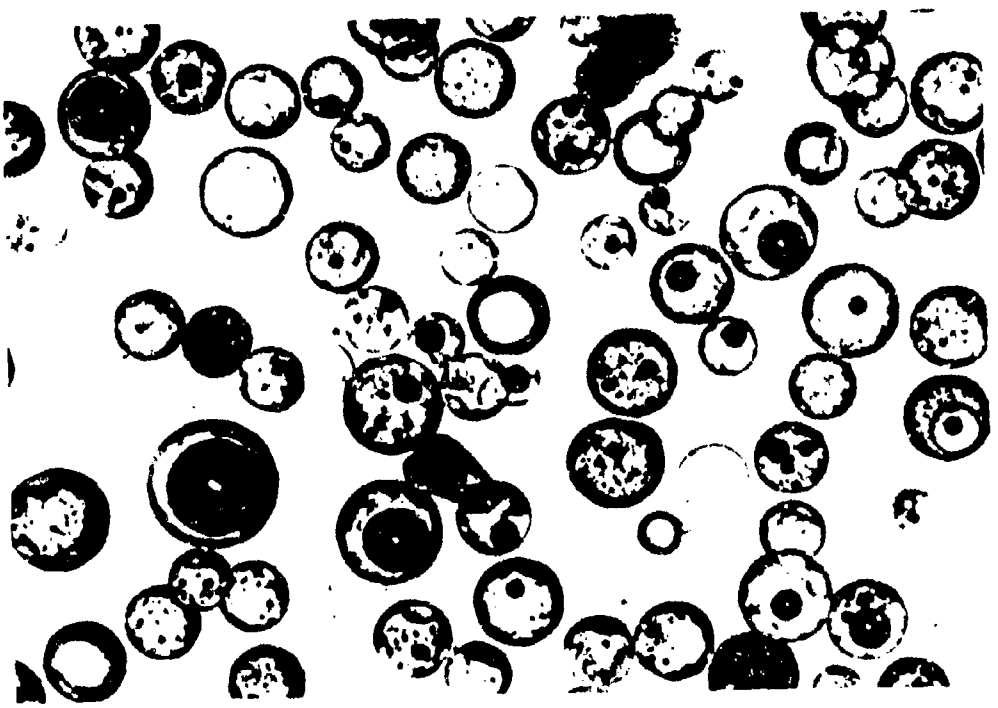

Fig. 9. Sandstone Particles Spheroidized in an Argon Plasma (43 kcal/mole Argon). Photomicrograph Was Taken Using an Immersion Oil (n = 1.56) with Transmitted Light and Green Filter. (Magnification 150×)

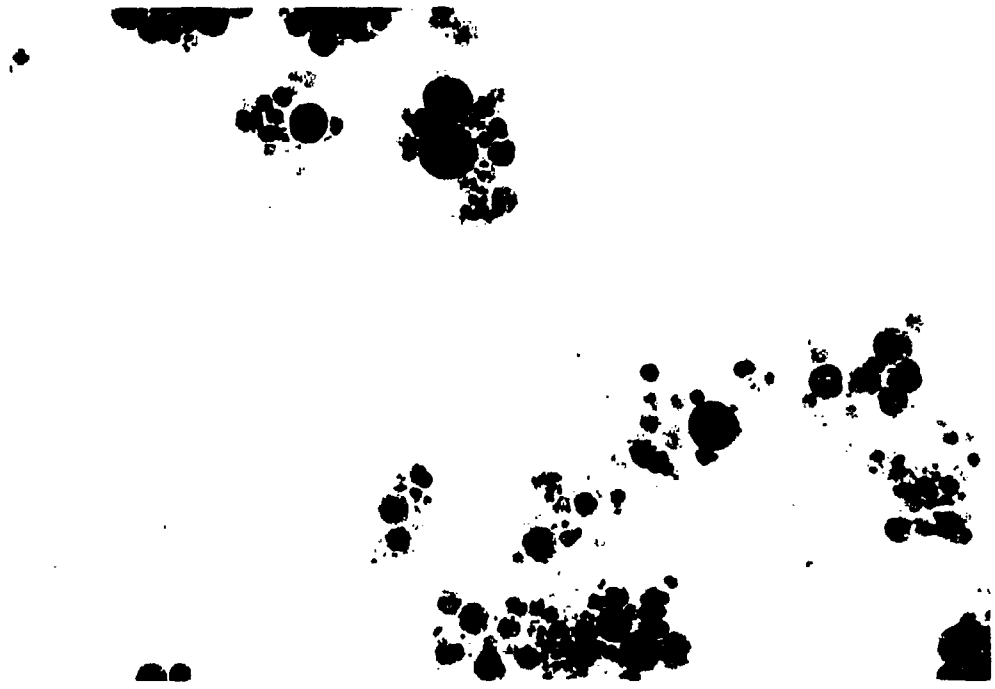

Fig. 10. Electron Micrograph of Vapor Deposited Alumina Particles Collected on the Walls of an Electrostatic Precipitor after Vaporization in Argon Plasma. (Magnification 106,000×)

BLANK PAGE

SESSION TWO

CLOUD DEVELOPMENT - PARTICLE CIRCULATION

SOME ANALYTICAL METHODS LEADING TO A DETERMINATION OF THE APPROXIMATE VELOCITY FIELD OF THE FIREBALL

J. W. McKee
General Electric-Tempo
Santa Barbara, California

ABSTRACT

The application of Moyal's method in fluid mechanics to determine the velocity field of the fireball is described. The equations of change are Fourier transformed and the momentum equation in wave-vector space is shown to segregate into two equations which may be uncoupled under some conditions. The convolution integrals which arise from the non-linear terms after Fourier transformation are approximated by the value of the integrand which corresponds to non-linear coupling between the largest eddies and the eddies of all other sizes. It is shown that the resulting term is responsible for translation of the space coordinates in a manner which depends on the initial conditions. The translation effect allows a convenient description of the motion and temperature distribution in a moving frame of reference. For the case of an initial velocity in the upward direction only, the translational velocity may be identified with the rise velocity of the fireball.

A set of initial conditions is used to show the character of the solutions which may be obtained. The solutions are examined and their limitations are discussed.

INTRODUCTION

The objective of this paper is to discuss the processes within the fireball and cloud of a nuclear explosion which are important in determining the distribution of debris, temperature, and velocity. The problem may be approached from many points of view, some of which are:

(1) Correlation of test information to develop empirical expressions for average temperature, rise velocity and fireball radius.[1,2]

(2) Development of computer programs[3,4,5] for the calculation of fireball and cloud characteristics.

(3) Simplified theoretical studies of the governing equations and the associated concepts involving, for example, buoyant effects, mixing, turbulence, and diffusion.[6,7,8]

(4) Theoretical studies of the fundamental properties of turbulence starting with isotropic flow.[9,10,11,12]

This paper adopts the point of view of Item 3 above in which the equations of change are examined for the information they contain, are simplified and solved for several cases which may bear on the problem of predicting fallout. Throughout the analysis a series of assumptions is invoked to continuously simplify the problem in a way which may preserve the main mechanisms of the dynamics and still allows solutions to be obtained which display some features of the problem.

In an important paper Moyal[9] demonstrates the methodology by which two types of velocity spectra may be segregated. The resulting equations are tractable if the assumption is made that the largest eddies in the flow dominate the non-linear terms.

In this paper the convolution integrals which arise from the non-linear terms in the momentum equation are approximated by the value of the integrand which corresponds to non-linear coupling between the largest eddies and the eddies of all other sizes. It is shown that the resulting

term is responsible for translation of the space coordinates in a manner which depends on the initial conditions. The translation effect allows a convenient description of the motion and temperature distribution in a moving frame of reference. For the case of an initial velocity which has a net momentum transfer upward, the translational velocity may be identified with the rise velocity of the fireball.

O. M. Phillips[13] has shown that if the net linear momentum of the fluid is non-zero in a viscous fluid in the final stages of decay of turbulence, the motion develops into a kind of vortex ring similar to the solutions found in this report. The inclusion of part of the non-linear term as carried out here provides a translation of the ring through the fluid which depends on the initial conditions. The theory of vortex rings in an inviscid fluid due to Lamb and to Hill are reviewed by Turner.[14]

The work reported here is an extension of the theory of turbulence* in the final period of decay to include a translating, viscous vortex ring. The theoretical description of the viscous vortex ring has not, in the past, included the translation effect. The theory of the inviscid vortex ring has included translation but does not predict expansion of the ring.

The plan of the paper is as follows: First, the equations of change are Fourier-transformed and the momentum equation linearized. Second, solutions for the velocity spectra are obtained which consist of the particular integral which includes the effect of the buoyant forces and solutions of the homogeneous equations which do not include the effect of the buoyant forces. The spectra of velocity are inverted back into physical space for selected initial conditions. A type of motion corresponding to formation of a translating torus is found to be a special case of a more general motion.

*The use of the word turbulence here is dependent on the use of sufficiently complex initial conditions that during decay the flow appears "turbulent."

THE EQUATIONS OF MOTION, HEAT TRANSFER, AND STATE IN PHYSICAL SPACE

The problem is specified in terms of the conservation of mass, momentum, energy, and the equation of state using the dependent variables s, π_p, and θ where $s = \ell n(\rho/\rho_o)$, $\pi_p = \ell n(p/p_o)$, $\theta = \ell n(T/T_o)$ and the velocity, $\vec{v} = (v_1, v_2, v_3)$ of the fluid. The subscript zero corresponds to any convenient time-independent reference condition and ρ, p, and T are the density, pressure and temperature at any point $\vec{x}' = (x_1', x_2', x_3')$ and any time t'. We specify a body force per unit mass of g' in the negative x_3' direction.

$$\frac{\partial s}{\partial t'} + \frac{\partial v_j}{\partial x_j'} = -v_j \frac{\partial s}{\partial x_j'} \tag{1}$$

$$\frac{\partial v_i}{\partial t'} - \nu\nabla^2 v_i - \frac{1}{3}\nu \frac{\partial}{\partial x_i'}\left(\frac{\partial v_j}{\partial x_j'}\right) + \frac{a'^2}{\gamma}\frac{\partial \pi_p}{\partial x_i'} = -v_j \frac{\partial v_i}{\partial x_j'} - g'\delta_{i3} \tag{2}$$

$$\frac{\partial \theta}{\partial t'} - \eta\nabla^2\theta - \frac{(\gamma-1)}{\gamma}\frac{\partial \pi_p}{\partial t'} = -v_j \frac{\partial \theta}{\partial x_j'} + \frac{(\gamma-1)}{\gamma} v_j \frac{\partial \pi_p}{\partial x_j'} + \frac{\nu}{c_p T}$$

$$\left[\frac{1}{2}\left(\frac{\partial v_i}{\partial x_j'} + \frac{\partial v_j}{\partial x_i'}\right)^2 - \frac{2}{3}\left(\frac{\partial v_j}{\partial x_j'}\right)^2\right] \tag{3}$$

$$\pi_p = s + \theta \tag{4}$$

The summation convention is used in these equations and throughout this report. In the order given, the equations represent the conservation of mass, momentum, and energy and the equation of state. The quantities ν, η are the kinematic viscosity and thermal diffusivity of the fluid, respectively. The quantities a', γ, c_p are the velocity of sound, ratio of specific heats, and the specific heat at constant pressure of the fluid,

respectively. The quantity δ_{i3} is equal to unity if i = 3 and zero otherwise. In performing the following analysis we make the assumption that the quantities ν, η, a', γ and c_p are constant at their values corresponding to an average condition within the fireball.

In many problems involving the late-time fireball, with low Mach number rise rate, the term in braces on the right-hand side of Equation (3), representing the effect of viscous dissipation on the temperature, is small compared to the other terms and may be disregarded. This does not imply that viscous dissipation is neglected insofar as it is the ultimate energy sink in the smallest eddies. It is simply not considered to influence the temperature measurably.

In addition, the equation of state represents a perfect gas and we therefore assume that the effect of chemical reactions within the fluid plays a negligible role. This contributes to inaccuracy of the solutions when the temperature is above, say 2000°K at most altitudes.

It is implicitly assumed in writing the above equations that the flow behaves according to continuum mechanics.

We have also assumed that the fireball is small compared to distances over which the Earth's gravitational field changes by a significant amount.

The late-time fireball is characterized by a relatively uniform pressure at a given altitude. This concept of "pressure equilibrium," though it is probably not completely valid, will be employed to simplify the equations. This assumption requires that the pressure everywhere in the fireball is equal to that which occurs in an undisturbed atmosphere. This requires that

$$\frac{\partial \pi_p}{\partial x_1} = \frac{\partial \pi_p}{\partial x_2} = 0 \, , \, \frac{\partial_p}{\partial t} = 0 \qquad (5)$$

Let b_3 be the buoyant force per unit mass

$$b_3 = -\frac{a'^2}{\gamma}\frac{\partial \pi_p}{\partial x_3} - g = g'\left(\frac{T}{T_0} - 1\right) = g'(e^{\theta} - 1)$$

where T_0 is the ambient temperature in the vicinity of the fireball.

If θ is restricted to values much less than one, then

$$b_3 = g'\theta \tag{6}$$

If H' is the scale height of pressure in the atmosphere, we have

$$\frac{\partial \pi_p}{\partial x_3'} = -\frac{1}{H'} \tag{7}$$

If Equations (5), (6) and (7) are employed in the momentum and energy equations these become

$$\frac{\partial v_i}{\partial t'} - \nu\nabla^2 v_i - \frac{1}{3}\nu\frac{\partial}{\partial x_i'}\frac{\partial v_j}{\partial x_j'} = -v_j\frac{\partial v_i}{\partial x_j'} + b_3\delta_{i3} \tag{8}$$

$$\frac{\partial \theta}{\partial t'} - \eta\nabla^2\theta = -v_j\frac{\partial \theta}{\partial x_j'} - \frac{\gamma-1}{\gamma}v_3/H' \tag{9}$$

Equations (1) and (4) remain unchanged. Equations (1), (4), (8) and (9) are the basic set which will be discussed in this paper.

THE NON-DIMENSIONAL EQUATIONS IN WAVE-VECTOR SPACE

Following the work of Moyal the set of Equations (1), (4), (8) and (9) is transformed into wave-vector space in accordance with the following relation

$$v_i = \int e^{+i\vec{k}\cdot\vec{x}'} \, dZ_i \tag{10}$$

The quantity dZ_i is the Fourier spectra of the velocity in the i direction. Similarly, we define formally the quantities dS, dP, and dQ as follows:

$$s = \int e^{+i\vec{k}\cdot\vec{x}'} \, dS, \; \pi_p = \int e^{+i\vec{k}\cdot\vec{x}'} \, dP, \; \theta = \int e^{+i\vec{k}\cdot\vec{x}'} \, dQ$$

The integrals are taken over all of wave-vector space. We follow the notation used by Moyal,[9] and Batchelor[12] and others where the velocity spectra are shown as differentials and the velocities are formally written as Stieltjes integrals of the spectra. A rigorous analysis of this usage has been published by Wiener.[15]

The magnitude of the vector $\vec{k} = (k_1, k_2, k_3)$ can be loosely considered as an inverse measure of eddy size in the sense that 2π/eddy length in the i direction approximately equals k_i. The transformation into wave-vector space thus brings together, into a small volume in this space, all eddies in the flow of a given size and shape independent of where they may occur in physical space. The largest eddies in the flow are transformed so that they reside near the origin in wave-vector space, while the smallest eddies occupy regions far from the origin in that space. Energy is considered to start with the largest eddies near the origin and flows outward toward the region occupied by the smallest eddies where, by the action of viscosity, it is eventually dissipated as heat. In this manner energy is removed from the gross motion of the fluid as the eddies

are reduced in size and reappear more remote from the origin. This process cannot continue indefinitely without supplying energy to the flow, mainly to the largest eddies. The role of the body force per unit mass in Equation (2) is to supply this energy from the gravitational field. This concept will be used later in an attempt to reduce to manageable form, the convolution integrals which will soon appear.

The transformation is straightforward and the approximate non-dimensional equations in wave-vector space are

$$\frac{\partial}{\partial t}\, dS + iRek_j dZ_j = -iRe\int k'_j dZ_j\ (k'-k)\ dS(k') \tag{11}$$

$$\frac{\partial}{\partial t}\, dZ_i + k^2 dZ_i + \frac{1}{3}\, k_i k_j dZ_j = -iRe\int k'_j dZ_j (k'-k) dZ_i(k') + gdQ\delta_{i3} \tag{12}$$

$$\frac{\partial}{\partial t}\, dQ + \frac{\eta}{\nu}\, k^2 dQ = -iRe\int k'_j dZ_j (k'-k) dQ(k') - Re\left(\frac{\gamma-1}{\gamma}\right)\frac{dZ_3}{H} \tag{13}$$

$$dP = dS + dQ \tag{14}$$

Adding Equations (11) and (13) we have a useful auxiliary equation

$$\gamma\,\frac{\eta}{\nu}\, k^2 dQ + i\gamma Rek_j dZ_j = \frac{Re}{H}\, dZ_3 \tag{15}$$

To obtain Equation (15) we have made use of Equations (5) and (7). In these equations a typical length in the flow, r_0, is taken as the unit of length; a typical velocity, v_0, becomes the unit of velocity. The Reynolds number, Re, is given by $r_0 v_0/\nu$. The unit of time becomes r_0^2/ν, and $g' = gr_0^2/v_0\nu$. Therefore, all quantities in the set of equations immediately above are non-dimensional, including k which is measured in units of $1/r_0$.

DECOMPOSITION OF THE VELOCITY

Moyal has shown that the component of the vector $d\vec{Z}$ in wave-vector space which is parallel to the vector $\vec{k}$ is associated with compression waves and random noise (irrotational flow). The components of $d\vec{Z}$ which are transverse to $\vec{k}$ are associated with the eddy turbulence (solenoidal flow). In order to segregate these two kinds of motion, following Moyal, we define dZ_k as the component of dZ along k and $dZ_i^{(t)}$ as the ith component of $d\vec{Z}^{(t)}$ a vector transverse to $\vec{k}$. This may be written

$$dZ_i = dZ_i^{(t)} + \frac{k_i}{k} dZ_k \tag{16}$$

Note that $k_j dZ_j = k dZ_k$ and $k_j dZ_j^{(t)} \equiv 0$.

If we define the quantity $dC_i(X)$ by

$$dC_i(X) = -iRe \int_{k'} k'_j dZ_j(k'-k) dX_i(k')$$

then we have

$$dC_i(X) = dC_i^{(t)}(X) + \frac{k_i}{k} dC_k(X)$$

where dX is any one of the spectra.

If Equation (16) is substituted into Equation (12) and both sides are multiplied by k_i/k, the result is

$$\frac{\partial}{\partial t} dZ_k + \frac{4}{3} k^2 dZ_k = dC_k(Z) + g dQ\, k_3/k \tag{17}$$

If Equation (12) is multiplied by $(\delta_{ij} - k_i k_j/k^2)$, the result is

$$\frac{\partial}{\partial t} dZ_j^{(t)} + k^2\, dZ_j^{(t)} = dC_j^{(t)}(Z) + g dQ(\delta_{3j} - k_3 k_j/k^2) \tag{18}$$

The quantity $\delta_{ij} - k_i k_j/k^2$ is called the projection operator and has the property of converting a vector in k-space into components normal to $\vec{k}$. That is, if $\vec{A}_j$ is a vector in wave number space, the vector $\vec{A}_i$ is normal to $\vec{k}$ when

$$\vec{A}_i = \vec{A}_j(\delta_{ij} - k_i k_j/k^2)$$

We now have two equations which result from the original momentum equation. One of these equations governs the behavior of the spectra of the irrotational velocity [Equation (17)]; the other governs the behavior of the spectra of solenoidal velocity [Equation (18)].

LINEARIZATION OF THE MOMENTUM EQUATION

The non-linear effects represented by the convolution integrals will be partially taken into account by assuming that the largest eddies in the flow (those for which k = 0) are the principal agents in the convective process. It is possible to decompose the convolution integrals into the following form:

$$\int k_e' \, dZ_e(k'-k) \, dZ_j(k') \left(\delta_{ij} - \frac{k_i k_j}{k^2}\right) = \int_{k' \neq k} k_e' \, dZ_e(k'-k) dZ_j(k')$$

$$\cdot \left(\delta_{ij} - \frac{k_i k_j}{k^2}\right) + k_e \, dZ_e(0) \, dZ_i^{(t)}(k)$$

and

$$\int k_e' \, dZ_e(k'-k) \, dZ_j(k') k_j/k = \int_{k' \neq k} k_e' \, dZ_e(k'-k) \, dZ_j(k') k_j/k$$

$$+ k_e \, dZ_e(0) \, dZ_k(k)$$

where we have used the relations $dZ_i^{(t)}(k) = (\delta_{ij} - k_i k_j/k^2) \, dZ_j(k)$ and $k_i dZ_i = k \, dZ_k$.

The last term on the right in these equations represents the non-linear interaction of the largest eddies with the eddies of all other sizes and is the part of the integral which corresponds to the spherical shell in wave-vector space for which $k' = k$. The non-linear effects associated with the first term on the right-hand side are disregarded for the present study.

The equations for the spectra of velocity become

$$\frac{\partial}{\partial t} dZ_i^{(t)} + k^2 dZ_i^{(t)} = -iRek_e dZ_e(0)dZ_i^{(t)}(k) + gdQ(\delta_{i3}-k_3k_i/k^2) \quad (19)$$

$$\frac{\partial}{\partial t} dZ_k + \frac{4}{3} k^2 dZ_k = -iRek_e dZ_e(0)dZ_k(k) + gdQ\, k_3/k \quad (20)$$

The time dependence of the quantity $k_e\, dZ_e(0)$ is found by letting $k = 0$ in the above equations

$$\frac{\partial}{\partial t} dZ_i^{(t)}(0) = gdQ(0) \;,\; i = 1,\, 2 \;;\; \frac{\partial}{\partial t} dZ_3^{(t)}(0) = 0$$

$$\frac{\partial}{\partial t} dZ_k(0) = gdQ(0)$$

The equations immediately above may be integrated to give

$$dZ_i^{(t)}(0,t) = dZ_i^{(t)}(0,0) + (1-\delta_{i3})\, g\int_0^t [dQ(0,t)]dt$$

$$dZ_k(0,t) = dZ_k(0,0) + g\int_0^t [dQ(0,t)]dt$$

This shows the increased spectral component corresponding to the largest eddies caused by the buoyant forces.

The resulting equations for the spectra of the solenoidal velocity are linear (the relation $k_e\, dZ_e = k dZ_k$ has been used again).

$$\frac{\partial}{\partial t} dZ_i^{(t)} + [k^2 + iRek\, dZ_k(0,0)]\, dZ_i^{(t)} = gdQ(\delta_{is} - k_s k_i/k^2) \qquad (21)$$

The equation for the spectra of the irrotational velocity is identical except that the term k^2 is replaced by $4k^2/3$ and the projection operator is replaced by k_s/k.

The solutions for the homogeneous equations are

$$dZ_i^{(t)}(k,t) = dZ_i^{(t)}(k,0) e^{-k^2 t} \exp[-iRek\, dZ_k(0,0)t] \qquad (22)$$

$$dZ_k(k,t) = dZ_k(k,0) e^{-\frac{4}{3}k^2 t} \exp[-iRek\, dZ_k(0,0)t] \qquad (23)$$

Note that $dZ_i^{(t)}(k,0) = (\delta_{ij} - k_i k_j/k^2) dZ_j(k,0)$, and $k\, dZ_k(k,0) = k_j dZ_j(k,0)$.

The velocity spectra obtained from the homogeneous equations are, from Equation (16)

$$dZ_i(k,t) = dZ_i^{(t)}(k,t) + (k_i/k) dZ_k(k,t)$$

$$= dZ_j(k,0) \exp[-iRek_j\, dZ_j(0,0)t] \cdot$$

$$\left[(\delta_{ij} k^2 - k_i k_j) \frac{e^{-k^2 t}}{k^2} + k_i k_j \frac{e^{-\frac{4}{3}k^2 t}}{k^2} \right] \qquad (24)$$

The first factor involving the exponential translates the resulting inversion in physical space so that each x_j is replaced by $x_j - Re dZ_j(0,0)t$. The coordinate system in which the motion is most conveniently described

is one which is moving with non-dimensional velocity $dZ_j(0,0)$ in each of the x_j directions. The factors $\delta_{ij}k^2-k_ik_j$ and k_ik_j become differential operators on the inverse of the functions $dZ_j(k,0)e^{-k^2t}/k^2$ and $dZ_j(k,0)e^{-\frac{4}{3}k^2t}/k^2$. As will be shown later, for certain initial conditions, the differential operators cause vortex and torus (or "smoke ring") formation.

If Equations (13) and (15) are combined, the energy equation becomes*

$$\frac{\partial}{\partial t}\, dQ + \gamma\,\frac{\eta}{\nu}\,k^2\, dQ \;=\; -iRek_j\, dZ_j(0,0)dQ - i(\gamma-1)Rek_j\, dZ_j \qquad (25)$$

with solution

$$dQ(k,t) \;=\; \exp\left(-iVt - \gamma\,\frac{\eta}{\nu}\,k^2t\right)\left\{dQ(k,0) - i(\gamma-1)Re\int_0^t k_j\,dZ_j(k,t')\right.$$

$$\left.\exp\left[+iVt' + \gamma\,\frac{\eta}{\nu}\,k^2t'\right]\,dt'\right\}$$

where we have defined V by

$$V \;=\; Rek_j\, dZ_j(0,0)$$

From Equation (24) with the translating term as a factor we have

$$k_j dZ_j(k,t) \;=\; k_j dZ_j(k,0)e^{-\frac{4}{3}k^2t}\exp(-iVt)$$

*Attempts to solve the continuity equation for density yielded integrals which could not be evaluated analytically.

so that

$$dQ(k,t) = \exp(-iVt)\left\{ dQ(k,0)e^{-\gamma \frac{\eta}{\nu} k^2 t} - i \frac{(\gamma-1)Rek_j dZ_j(k,0)}{\left(\gamma \frac{\eta}{\nu} - \frac{4}{3}\right) k^2} \right.$$

$$\left. \cdot \left[\exp\left(-\frac{4}{3} k^2 t\right) - \exp\left(-\gamma \frac{\eta}{\nu} k^2 t\right)\right]\right\} \qquad (26)$$

To insure compatible initial conditions of velocity and temperature we use Equation (15) in the form

$$dQ(k,0) = \frac{Re}{\gamma \frac{\eta}{\nu} k^2}\left[\frac{dZ_3(k,0)}{H} - i\gamma k_j\, dZ_j(k,0)\right] \qquad (27)$$

substituting into Equation (26) we have for the spectrum of the temperature function

$$dQ(k,t) = RedZ_j(k,0)\exp(-iVt)\left\{\left[\frac{Pr}{\gamma H} - iPrk_j + \frac{i(\gamma-1)k_j}{\left(\frac{\gamma}{Pr} - \frac{4}{3}\right)}\right]\right.$$

$$\left. \frac{e^{-\gamma \frac{k^2 t}{Pr}}}{k^2} - \frac{i(\gamma-1)k_j}{\left(\frac{\gamma}{Pr} - \frac{4}{3}\right)} \frac{e^{-\frac{4}{3}k^2 t}}{k^2}\right\} \qquad (28)$$

where $Pr = \nu/\eta$, the Prandtl number.

Again, the term exp(-iVt) indicates that a moving coordinate system is the convenient frame of reference for a description of the temperature.

This will be inverted in a later section for a specific initial velocity distribution.

The density function may be found directly from the temperature function and the equation of state.

The solution of the homogeneous equations corresponds to the case where the buoyant force term and the non-linear convective terms have decayed to small values. This is characteristic of very late-time conditions.

At earlier times when the buoyant force term is important, the momentum and energy equations are coupled through this term as well as through the non-linear convective terms (which cause "dilution") and the terms which correspond to adiabatic expansion.

The non-linear term causes reduction of the temperature by convection of cooler air into the fireball which dilutes the hot air in the original x-ray fireball. Studies of photographs indicate that this air enters the fireball predominately at the bottom. This term can be treated approximately by first considering that only velocities in the upward direction convect significant amounts of air into the fireball. The non-linear term is approximated by the following relation

$$v_j \frac{\partial \theta}{\partial x_j} \cong v_3 \frac{\partial \theta}{\partial x_3} \cong \lambda \theta \, v_R$$

where v_R is the fireball rise velocity, λ is the fraction of the rise velocity which is effective in convecting cooler air into the fireball, and θ is the change in θ over a distance r_0. When the convolution integral in Equation (13) is replaced and the other approximations are made, we have

$$\frac{\partial}{\partial t} dQ + \frac{\eta}{\nu} k^2 dQ + Re \, \lambda \, v_R \, dQ = -Re \, c \, dZ_3 \qquad (29)$$

The linear set of equations which describe the case when buoyant forces are important are

$$\left[\frac{\partial}{\partial t} + k^2 + iRek_e \, dZ_e(0,0) \right] dZ_i^{(t)} = g \, dQ(P_{i3}) \qquad (30)$$

$$\left[\frac{\partial}{\partial t} + \frac{4}{3}\,k^2 + iRek_e\, dZ_e(0,0)\right] dZ_k = g\, dQ\, \frac{k_3}{k} \qquad (31)$$

$$\left[\frac{\partial}{\partial t} + \frac{\eta}{\nu}\,k^2 + Re\,\lambda\, v_R\right] dQ = -Re\, c\, dZ_3 \qquad (32)$$

where

$$c = \frac{\gamma-1}{\gamma H}$$

The rise velocity is assumed to be constant during this phase of the motion which agrees with a large body of experimental data.

These equations may be solved by the methods described in Appendix A of Reference 6.

QUANTITATIVE FEATURES OF THE SOLUTIONS

SOLUTIONS FOR THE VERY LATE-TIME MOTION AND TEMPERATURE

Selection of Initial Conditions

We assume that the initial motion can be represented by a single component of velocity in the z (or x_3) direction. The upward initial velocity is assumed to follow a Gaussian distribution so that the initial conditions are

$$v_3(\vec{x},0) = v_{30}\, e^{-r^2/4b}\,,\quad v_1(\vec{x},0) = v_2(\vec{x},0) = 0 \qquad (33)$$

where v_{30} is the upward velocity at the center and b is a parameter governing the rate at which the velocity reduces toward the edge of the fireball. The origin of the stationary coordinate system now requires definition and is taken at the center of the fireball at t = 0. The

quantities r and b are non-dimensional.* When $r = 2\sqrt{b}$ the velocity has dropped by a factor of e below its value at the center of the fireball. Transformation of the initial conditions gives

$$dZ_3(k,0) = v_{30}\left(\frac{b}{\pi}\right)^{3/2} e^{-k^2 b} \tag{34}$$

$$dZ_3(0,0) = v_{30}\left(\frac{b}{\pi}\right)^{3/2} \tag{35}$$

The Velocity Field

The inversion of Equation (24) with the initial conditions specified above in a frame of reference moving upward with non-dimensional velocity $v_{30}(b/\pi)^{3/2}$ is (see Appendix C, Ref. 6)

$$v_i(\vec{x},t) = -2\sqrt{\pi}\, v_{30}\, b^{3/2}\left[\left(\delta_{i3}\nabla^2 - \frac{\partial^2}{\partial x_i \partial x_3}\right)\frac{1}{r}\,\mathrm{erf}\,\frac{r}{2\sqrt{t+b}}\right.$$

$$\left. + \frac{\partial^2}{\partial x_i \partial x_3}\,\frac{1}{r}\,\mathrm{erf}\,\frac{r}{2\sqrt{\frac{4}{3}\,t+b}}\right] \tag{36}$$

The moving frame of reference is introduced as a convenience resulting from the factor $\exp[-iRek_j dZ_j(0,0)]$ in the original transform of the velocity. The velocity itself is measured relative to a stationary observer since the effect of the exponential factor is simply to replace x_i by $x_i - Re\,dZ_i(0,0)$ in evaluating the magnitude of the velocity. An observer on the moving coordinate system will measure an upward velocity which is less than the value given by Equation (38) by an amount $v_{30}(b/\pi)^{3/2}$.

*Normally we will choose b = 1/4 so that the velocity has reduced by a factor e when r = 1.

Performing the differentiation the velocity in the $x_i (i = 1,2)$ direction is

$$v_i(\vec{x},t) = 2\sqrt{\pi}\, v_{30}\, \frac{x_i x_3}{r^5}\, b^{3/2} \left[T\left(\frac{r}{\tau_1}\right) - T\left(\frac{r}{\tau_2}\right)\right] \qquad (37)$$

where

$$T(u) = u^2\, \mathrm{erf}''\, u - 3u\, \mathrm{erf}'\, u + 3\, \mathrm{erf}\, u$$

$$\tau_1 = 2\sqrt{t+b}$$

$$\tau_2 = 2\sqrt{4t/3+b}$$

$$\frac{\partial}{\partial u}\, \mathrm{erf}\, u = \mathrm{erf}'\, u\,, \quad \frac{\partial}{\partial u}\, \mathrm{erf}'\, u = \mathrm{erf}''\, u$$

The radial velocity in any horizontal plane is given by

$$v_\rho = (v_1^2 + v_2^2)^{1/2}$$

$$= 2\sqrt{\pi}\, v_{30}\, \frac{x_3 \rho}{r^5}\, b^{3/2} \left[T\left(\frac{r}{\tau_1}\right) - T\left(\frac{r}{\tau_2}\right)\right] \qquad (38)$$

where

$$\rho = (x_1^2 + x_2^2)^{1/2}$$

The velocity in the x_3 direction is

$$v_3(\vec{x},t) = -2\sqrt{\pi}\, v_{30}\, b^{3/2} \left\{ \frac{\rho^2}{r^5}\, T\left(\frac{r}{\tau_1}\right) + \frac{x_3^2}{r^5}\, T\left(\frac{r}{\tau_2}\right) + \frac{1}{r^3}\left[2S\left(\frac{r}{\tau_1}\right) + S\left(\frac{r}{\tau_2}\right)\right]\right\} - v_{30}\left(\frac{b}{\pi}\right)^{3/2} \qquad (39)$$

where

$$S(u) = u\,\mathrm{erf}'\,u - \mathrm{erf}\,u$$

The functions T(u) and S(u) are displayed vs u in Table 1. Note that as $t \to 0$, $\tau_1 \to \tau_2 = \tau$, and we have

$$v_1(\vec{x},0) = v_2(\vec{x},0) = 0\,, \quad t \quad 0$$

$$v_3(\vec{x},0) = -2\sqrt{\pi}\, v_{30}\, b^{3/2}\, \frac{1}{\tau^2 r}\, \mathrm{erf}''\, \frac{r}{\tau}\,, \quad t \to 0$$

The derivatives of the error function are

$$\mathrm{erf}'\,u = \frac{2}{\sqrt{\pi}}\, e^{-u^2}$$

$$\mathrm{erf}''\,u = \frac{4u}{\sqrt{\pi}}\, e^{-u^2}$$

yielding

$$v_3(\vec{x},0) = v_{30}\, e^{-r^2/4b}$$

The initial conditions have been recovered at $t = 0$.

The horizontal radial velocity v_ρ given by Equation (38) is seen to change signs as we move from above to below the origin of the moving coordinate system. It is zero on the vertical axis and on the horizontal plane through the moving origin. It rapidly approaches zero as $r \to \infty$.

The vertical velocity has a more complex dependence on time and the space coordinates. In the moving frame of reference it is symmetrical about the plane $x_3 = 0$, positive near the vertical axis, and negative

far from the axis for small values of time. As time increases it reduces in value near the vertical axis and increases at values of ρ which are increasingly large.

Table 1.

Numerical Values of the Functions T and S

U	T(U)	S(U)
0	0	0
0.1	$3.84171\ 10^{-6}$	$-7.46049\ 10^{-4}$
0.2	$2.74908\ 10^{-4}$	$-5.87369\ 10^{-3}$
0.3	$2.05179\ 10^{-3}$	$-1.92466\ 10^{-2}$
0.4	$8.24533\ 10^{-3}$	$-4.37742\ 10^{-2}$
0.5	$2.36258\ 10^{-2}$	$-8.11072\ 10^{-2}$
0.6	$5.44369\ 10^{-2}$	-0.131509
0.7	0.107508	-0.193908
0.8	0.189068	-0.266111
0.9	0.303536	-0.345136
1.0	0.452562	-0.427592
1.1	0.634522	-0.510077
1.2	0.844559	-0.5895
1.4	1.31703	-0.729767
1.6	1.79576	-0.836782
1.8	2.21318	-0.909545
2.0	2.53129	-0.953988
2.2	2.74552	-0.978508
2.4	2.87403	-0.990778
2.6	2.94311	-0.996363
2.8	2.97654	-0.998681
3.0	2.99116	-0.99956
3.5	3.000	-1.000

Temperature Distribution

If we continue to employ an initial upward velocity which is a Gaussian distribution in space about the center of the early fireball, the temperature spectra is given by

$$dQ(k,t) = \mathrm{Re}\ v_{30}(b/\pi)^{3/2} \exp(-i\ Vt) \left\{ \left[\frac{Pr}{\gamma H} - i\ Pr\ k_3 + \frac{i(\gamma-1)k_3}{\left(\frac{\gamma}{Pr} - \frac{4}{3}\right)} \right] \right.$$

$$\left. \frac{e^{-\left(\frac{\gamma}{Pr}\ t+b\right)k^2}}{k^2} - \left[\frac{i(\gamma-1)k_3}{\left(\frac{\gamma}{Pr}\right) - \frac{4}{3}} \right] \frac{e^{-\left(\frac{4}{3}\ t+b\right)k^2}}{k^2} \right\} \qquad (40)$$

where $Pr = \nu/\eta$, the Prandtl number ($\cong 0.7$ for air). The factor $\exp(-iVt)$ translates the resulting inversion so that x_3 is replaced by $x_3 - \mathrm{Re}\ dZ_3(0,0)t$ and again the coordinate system offering the greatest utility is one moving upward with uniform non-dimensional velocity $\mathrm{Re}\ dZ_3(0,0) = \mathrm{Re}\ v_{30}(b/\pi)^{3/2}$. If the spectra of temperature is inverted and expressed in this system the result is (Appendix C, Ref. 6)

$$\theta = 8\sqrt{\pi}\ v_{30}\ b^{3/2}\ \mathrm{Re} \left[\frac{Pr}{\gamma H} \frac{1}{r} \mathrm{erf} \frac{r}{2\sqrt{\frac{\gamma}{Pr}\ t+b}} - \frac{1 - \frac{4Pr}{3}}{\frac{\gamma}{Pr} - \frac{4}{3}} \frac{\partial}{\partial x_3} \right.$$

$$\left. \left(\frac{1}{r} \mathrm{erf} \frac{r}{2\sqrt{\frac{\gamma}{Pr}\ t+b}} \right) - \frac{(\gamma-1)}{\frac{\gamma}{Pr} - \frac{4}{3}} \frac{\partial}{\partial x_3} \left(\frac{1}{r} \mathrm{erf} \frac{r}{2\sqrt{4t/3+b}} \right) \right] \qquad (41)$$

Performing the differentiation yields

$$\theta = 8\sqrt{\pi}\ v_{30}\ b^{3/2}\ \mathrm{Re} \left\{ \frac{Pr}{\gamma Hr} \mathrm{erf} \frac{r}{\tau_A} - \frac{x_3}{\left(\frac{\gamma}{Pr} - \frac{4}{3}\right) r^3} \right.$$

$$\left. \left[\left(1 - \frac{4Pr}{3}\right) S\left(\frac{r}{\tau_A}\right) + (\gamma-1)\ S\left(\frac{r}{\tau_B}\right) \right] \right\} \qquad (42)$$

where

$$\tau_A = 2\sqrt{\frac{\gamma}{Pr}\ t+b}$$

$$\tau_B = 2\sqrt{\frac{4}{3}\ t+b}$$

and, as before,

$$S(u) = u\ \mathrm{erf}'\ u - \mathrm{erf}\ u$$

If we let b = 1/4, the length scale is established such that the initial velocity drops by a factor e at a distance r_0 from the center of the fireball.

To establish the velocity scale, let t = 0, r → 0 and note that erf x → $2x/\sqrt{\pi}$, x small. This yields

$$\theta = 2\,\frac{v_{30}\,RePr}{\gamma H \tau_A}$$

from Equation (42) for b = 1/4. Define θ_{oc} as the value of θ at t = 0, r = 0 (at the center of the fireball) so that

$$\theta_{oc} = \frac{2v_{30}\,RePr}{\gamma H}$$

Substituting into Equation (42) to remove the Reynolds number, velocity product

$$\theta = \frac{\sqrt{\pi}}{2}\,\theta_{oc}\left\{\frac{1}{r}\,\mathrm{erf}\,\frac{r}{\tau_A} - \frac{x_3\gamma H}{\left(\gamma - \frac{4Pr}{3}\right)r^3}\left[\left(1 - \frac{4Pr}{3}\right)S\left(\frac{r}{\tau_A}\right)\right.\right.$$

$$\left.\left. + (\gamma-1)\,S\left(\frac{r}{\tau_B}\right)\right]\right\} \qquad (43)$$

Along the horizontal midplane $x_3 = 0$ the temperature function is

$$\theta = \frac{\sqrt{\pi}}{2\rho}\,\theta_{oc}\,\mathrm{erf}\left(\frac{\rho}{2\sqrt{2t+1/4}}\right)$$

where we have taken $\gamma = 1.4$, $Pr = 0.7$ and $\rho = (x_1^2 + x_2^2)^{1/2}$.

For small values of $\rho/2\sqrt{2t+1/4}$ the temperature for $x_3 = 0$ is

$$\theta \cong \theta_{oc}/2\sqrt{2t+1/4}$$

giving (using $e^{\theta} = T/T_o$)

$$\frac{T}{T_o} = \left(\frac{T_{oc}}{T_o}\right)^{\frac{1}{\sqrt{8t+1}}}$$

Note that T_o is the temperature of the ambient atmosphere.

MOTION IN A VISCOUS, TRANSLATING VORTEX RING

Consider the motion found by Phillips[13] for an incompressible viscous vortex ring which is caused to translate by the non-linear inertia terms as discussed in the preceding sections. His results are for a stationary ring and an incompressible fluid. They can be obtained from the results found here by dropping those parts of the solutions involving (r/τ_2) in Equation (38). We shall retain the translating term in the spectra although it does not enter explicitly into the results for velocity; it is simply understood that the coordinates are measured from a moving frame of reference. We find for the moving torus

$$v_\rho = 2\sqrt{\pi}\, v_{3c}\, b^{3/2}\, \frac{x_3\rho}{r^5}\, T\left(\frac{r}{\tau_1}\right) \qquad (44)$$

$$v_3 = -2\sqrt{\pi}\, v_{30}\, b^{3/2} \left[\frac{\rho^2}{r^5} T\left(\frac{r}{\tau_1}\right) + \frac{2}{r^3} S\left(\frac{r}{\tau_1}\right) \right] \qquad (45)$$

where

$$\tau_1 = 2\sqrt{t+b}$$

Using Table 1 for the values of the functions T and S we find that the development of the torus with time is as shown in Figure 1. The upward velocity in the plane $x_3 = 0$ and the radial velocity in the plane $x_3 = 1$ are shown. The point $\rho \cong 1.0$ is the smallest value of ρ for which the velocity is downward. The radial motion of this point at which the velocity is downward varies as $\rho = 2\sqrt{t+b}$ and the torus appears to be developed by the time $t \cong 0.1$. The streamlines[13] for this motion are circles centered on the ρ axis at increasingly larger values of ρ as time increases.

If initial conditions are chosen so that the fireball is initially expanding then a component of irrotational velocity is introduced. The motion then has streamlines which are spirals and the debris will tend to be concentrated in the torus.

DISCUSSION

The velocity and temperature distributions and their spectra obtained in the previous sections result from an extension of the theory of turbulence for the final period of decay. The extension is brought into the theory by including that part of the non-linear terms which corresponds to coupling of the largest eddies with eddies of all other sizes. The resulting linearization, which is carried out in wave-vector space, has the effect of translating the space coordinates in the prescription of the velocity and temperature in a wave-like manner depending upon the velocity of the largest eddies in the initial motion. The resulting translational velocity is to be identified with the rise

velocity of the fireball if the initial motion has only an upward component. A convenient coordinate system for describing the motion and temperature in the case of more general initial conditions is one which is moving in the direction of the velocity of the largest eddies in the initial motion.

The principal limitations of the solutions found in this paper may be summarized as follows:

1. The influence of the non-linear terms is only partially included. This does not allow the convective processes to exert sufficient influence, particularly on the temperature distribution. For very late-time motion the error introduced by linearization may be small, however.
2. When the buoyant force term is included the spectra become difficult to Fourier transform because of the complicated integrals involved.
3. The assumption of constant kinematic viscosity is a limiting factor except at very late times.

The form of the solutions obtained in this report have suggested an approach to the problem of fireball mixing involving the use of Hermite functions. Employing a Gaussian distribution of upward velocity as the initial condition, the solutions found are expressed in terms of the error function and its derivatives. These derivatives, as well as the initial conditions, may be written as Hermite functions which have several properties which may be useful in obtaining solutions of the fundamental equations.[16] For example, the Fourier transform of a Hermite function is also a Hermite function, convolution integrals involving Hermite functions may be performed analytically, a series of Hermite functions is capable of expressing a wide range of generalized functions.[17]

Another alternative approach and one which is usually employed in the general theory is to determine relationships among the various statistical features of the dynamics, such as correlation coefficients, but to include better approximations to the governing equations. Since

no direct data exist on correlation coefficients within the fireball, the spectra of velocity and temperature were felt to be more useful for our purpose.

ACKNOWLEDGMENT

Some of the work reported here was performed in collaboration with Dr. Charles Dolph, Professor of Mathematics at the University of Michigan and Consultant to the General Electric Company. Informative discussions have been held with several members of the Tempo staff including R. W. Hendrick, Jr., T. J. Barrett, W. S. Knapp, and G. Rohringer. This work has been supported by the Advanced Research Project Agency under Contract AF 19(628)-4210.

LIST OF SYMBOLS

a	velocity of sound
$a(k)$	$= k^2 + i\,\mathrm{Re}\,K\,dZ_k(0,0)$
b	initial condition index
g	acceleration of gravity
γ	ratio of specific heats
H	scale height in the atmosphere
i	$= \sqrt{-1}$
k	Fourier mode index (modulus of wave vector)
η	thermal diffusivity
λ	entrainment parameter
ν	kinematic viscosity
p	pressure
Pr	Prandtl number
π_p	pressure function $(= \ell n\ p/p_o)$
r	radial coordinate in spherical system or typical length
Re	Reynold's number
ρ	density or radial coordinate in cylindrical system
dQ	Fourier transform of temperature function
dS	Fourier transform of density function
s	density function $(= \ell n\ \rho/\rho_o)$
T	absolute temperature

t	time
θ	temperature function ($= \ell n\ T/T_o$)
v_i	i-th component of velocity
x_i	space coordinate in rectangular system
dZ_i	Fourier spectra of i-th component of velocity

Subscripts

AD	denotes adiabatic expansion
D	denotes dilution
k	denotes component of the spectra of velocity along the wave vector k
0	denotes reference conditions far from the fireball, initial conditions or denotes typical values of velocity and length in the flow field
oc	denotes conditions at fireball center at t = 0
i	denotes vector component (i = 1, 2, 3)
p	denotes particular integral
s	denotes stabilization time

Superscripts

prime	denotes dimensional variable
$(t)'$	denotes part of velocity spectra transverse to wave vector

REFERENCES

1. Knapp, W. S. et al, Electromagnetic Blackout Handbook, Second Edition, Vol. 1 and 2, DASA 1580, RM 64TMP-44, General Electric Company, Santa Barbara, California, 15 December 1964 (Secret-Restricted Data).

2. Barrett, T. J. et al, Low-Altitude Fireball Phenomenology, R 63 TMP-38, General Electric, Tempo, October 1963 (Secret-Restricted Data).

3. Nawrocki, E. A., Theoretical Calculations of Late Phenomenology, BlueGill, Air Force Weapons Laboratory, AFWL-TR-65-154, October 1965 (Secret-Restricted Data).

4. Torrey, M. D., and M. R. Rubin, Study of Bomb Debris Effects, Technical Operations Research, TO-B 64-10, 14 February 1964 (Unclassified).

5. Culbertson, J. B., Buoyant Fireball Rise, General Electric, Tempo, TMP-47266, October 1965 (Secret-Restricted Data).

6. McKee, J. W. and C. L. Dolph, A Theory of Compressible Viscous Flow with Applications to Late-Time Fireball Mixing, RM 65TMP-4, General Electric, Tempo, January 1965 (Unclassified).

7. Morton, B. R., G. Taylor and J. S. Turner, "Turbulent Gravitational Convection from Maintained and Instantaneous Sources," Proc. Roy. Soc., London A, 234 (1956), pp. 1-23.

8. Deissler, R. G., "Turbulence in the Presence of a Vertical Body Force and Temperature Gradient," J. Geophys. Res. 67 (1962), p. 3049.

9. Moyal, J. E., "The Spectra of Turbulence in a Compressible Fluid; Eddy Turbulence, and Random Noise," Proc. Camb. Phil. Soc. 48, (1952) p. 329.

10. Hopf, E., "Statistical Hydromechanics and Functional Calculus," J. Ratl. Mech. Anal., I (1952), p. 87.

11. Lewis, R. M. and R. H. Kraichnan, "A Space-Time Functional Formalism for Turbulence, Comm. Pure and Appl. Math, Vol. XV (1962), p. 397.

12. Batchelor, G. K., The Theory of Homogeneous Turbulence, Cambridge University Press, Cambridge, 1960.

13. Phillips, O. M., "The Final Period of Decay of Non-Homogeneous Turbulence," Proc. Camb. Phil. Soc. 52 (1956) p. 135.

14. Turner, J. S., "The Dynamics of Spheroidal Masses of Buoyant Fluid," J. of Fluid Mech. 19 (1964) p. 481.

15. Wiener, N., "Generalized Harmonic Analysis," Acta Math 55, 1930, pp. 117-258.

16. Korevaar, J., "Pansions and the Theory of Fourier Transforms," Trans. Am. Math. Soc. 91 (1959) p. 53.

17. Widlund, O., "On the Expansion of Generalized Functions in Series of Hermite Functions," Trans. of the Roy. Inst. of Tech., Stockholm, Pure and Appl. Math. and Physics 16, No. 173 (1961).

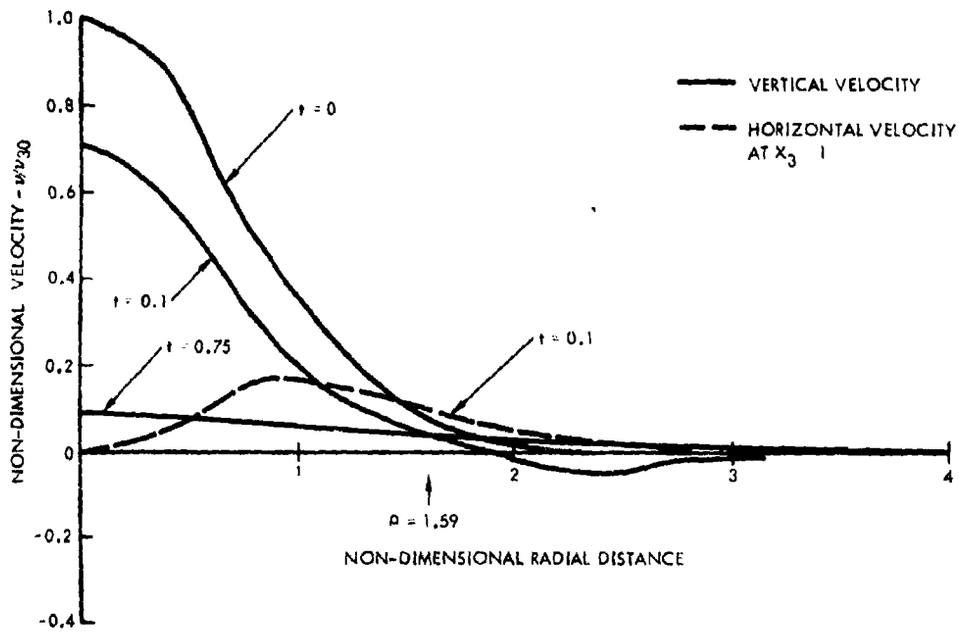

Fig. 1. Translating Vortex Ring Development and Decay

THE ENERGY CYCLE AND THE ENERGY CASCADE OF THE ATOMIC CLOUD*

I. O. Huebsch
U.S. Naval Radiological Defense Laboratory
San Francisco, California

ABSTRACT

The difficulties of calculating fluid motion and particle trajectories in the atomic cloud are so great that we resign ourselves to a parcel-model description of the cloud. Such a model specifies only average values of cloud temperature, rate of rise, turbulence intensity, particle concentration, etc., as functions of time.

In the present atomic cloud model,

(1) Turbulent energy is produced from kinetic energy of rise by

  (a) Eddy-viscous drag,

  (b) Inelastic-collision, momentum-conserving entrainment of ambient air.

(2) Turbulent energy is dissipated to heat at a rate independent of fluid viscosity.

The model can be represented as an energy cycle between kinetic energy of rise, turbulent kinetic energy, enthalpy and potential energy.

Various results now follow from the cloud model and turbulent similarity theory.

The energy associated with any eddy size in the turbulent energy cascade can be specified.

If toroidal circulation is to be represented by a classical vortex ring superimposed on the parcel-model cloud, the vortex ring can be considered the largest eddy in the turbulent spectrum, containing a fixed fraction of the turbulent energy.

---

*This work was sponsored by the Defense Atomic Support Agency

Alternately, the cloud circulation, as a function of time, can be calculated directly from the model adapting Kelvin's theorem. This calculation does not require the superimposed vortex. The resulting estimates of the circulation are obtained without recourse to, but are in general agreement with, measurements of atomic cloud films.

Attempts have been made to calculate the effect of toroidal circulation on particle dispersion from the cloud using laminar flow methods. This dispersion can instead be represented as due to turbulent diffusion, using the calculated dissipation rate as the governing parameter. Diffusion coefficients and concentration gradients are derived from turbulent similarity theory. The resulting dispersion rate is shown to be small compared with that due to gravitational fallout rate indicating that dispersion induced by circulation or turbulence can be ignored.

1. INTRODUCTION

1.1 Background

One of the striking features of nuclear explosions is the vortex ring and/or "toroidal circulation" in the rising, intensely turbulent atomic cloud. It has been suggested that particles of different sizes in the cloud follow the motion of the fluid circulation to different extents, so that the circulation influences the dispersion of particles from the cloud (by a sort of centrifuging process) and thus the distribution of radioactive fallout in the air and on the ground. Calculation of the fluid motion and of the particle trajectories by classical hydrodynamic methods presents both theoretical and computational difficulties, not yet overcome. These difficulties arise largely from the turbulent character of the flow in and around the cloud.

1.2 Objectives

The purposes of this paper are

1. To present a revision of a previously published[1] entraining-parcel model of the atomic cloud, allowing, as before, for transfer of kinetic energy of cloud rise to turbulence by eddy-viscosity, and also for

   (a) additional transfer of kinetic energy of rise to turbulence by the inelastic-collision, momentum-conserving entrainment process, so that total energy is conserved, and

   (b) transfer of energy from turbulence to heat.

2. To discuss the energy cycle of the atomic cloud which is implicit in this model.

3. To discuss attempts to superimpose a classical vortex motion on a parcel-method cloud, and to show how such attempts can at least be made consistent with the energy balance of the cloud, and how cloud circulation can be estimated without use of the superimposed vortex.

4. To show how the particle-dispersive effect attributed to fluid circulation can be represented as due to turbulent diffusion consistent with the parcel method, and to estimate the relative importance of diffusive and gravitational dispersion of particles from the cloud.

1.3 Approach

The principal tool used in the present study is the revised version[2] of the entraining-parcel model of the atomic cloud. This model was originally developed for water-surface bursts but is also applicable to air bursts, since in both cases, the mass fraction of condensed matter is small. The model can further be applied to land-surface bursts provided the mass and size distribution of condensed matter at start of cloud rise are specified.

The present development of the original model is largely inspired by turbulence theory, especially by the concept of the energy cascade and the theory of local similarity, or similarity of small eddies.[3] Therefore, the relevant parts of turbulence theory are reviewed in this report (Sec. 3).

2. MODELS OF THE ATOMIC CLOUD

Calculations of the behavior of the atomic cloud have been made by a number of investigators using different approaches, often patterned after studies of cumulus clouds or of the rise of hot gases from fires and factory chimneys.

Possible models of cloud behavior can be divided into those using (1) local methods and (2) parcel methods.

2.1 Local Methods

In a "local" method, the flow conditions in the cloud and surrounding atmosphere are described by a set of partial differential equations (Navier-Stokes equations) giving local values of velocity, temperature, etc., as functions of time. For numerical computation, the partial differential equations are replaced by a set of ordinary differential equations at each point of a grid or mesh of points covering the flow region. Some beginnings using this treatment have been made[5,6] for developing cumulus clouds, making the assumption that temperature differences between cloud and atmosphere are small relative to absolute temperature, and using an eddy viscosity in the Navier-Stokes equations. The values of velocity, etc., computed represent time averages, not the instantaneous values which are subject to turbulent fluctuations.

Eddy-viscosity is needed in the equations used for computation because molecular viscosity (ordinary viscosity) operates to convert the energy of only the smallest eddies of a turbulent flow into heat. It can be shown (see for instance, Section 3.1.5) that the ratio of the size of the smallest eddies, λ_o, to the overall flow dimensions, ℓ, for one-dimensional flow, is

$$\frac{\lambda_o}{\ell} = Re^{-3/4}$$

where Re is the Reynolds number of the flow. Such a flow could be pictured as containing a row of ℓ/λ_o such eddies, (on which are superimposed larger eddies) and so having $Re^{3/4}$ degrees of freedom. Then the mesh for a two-dimensional calculation must have $Re^{3/2}$ points, so that numerical computation is out of the question when Re is large. The eddy viscosity is used to blur together small eddies, and thus reduce the

number of degrees of freedom of the flow problem, and the required number of mesh points, to where numerical computation is possible.

No local-method computation has yet been carried out for atomic clouds. Even for cumulus clouds, the original two-dimensional array of mesh points (in an axisymmetric finite-difference calculation) is rapidly distorted. For atomic clouds, this distortion would be accompanied by extreme temperature gradients, so that heat conduction could not be neglected. Presumably, an eddy conductivity would be required as well as eddy viscosity. Altogether, one is inclined to question the use of eddy transport coefficients, to calculate mean local conditions at the extremely high Reynolds numbers ($\sim 10^{10}$) of these intensely turbulent flows. In any case, the attempt has not yet been made.

2.2 Parcel Methods

In a parcel method, the cloud is treated as a whole, as if all parts of it had the same properties. Temperature, velocity, etc., are represented by average values for the whole cloud. Pressure is taken as equal to ambient pressure at the altitude of the center of the cloud. Thus a parcel method is a simple, cheap substitute for a local method. But it is far more amenable to numerical computation. And with a few enlightened assumptions, a parcel method can give a wide variety of information, including an estimate of particle dispersion by toroidal circulation (simulated by turbulent diffusion, see Sec. 5).

2.3 The TR-741 Atomic Cloud Model, Revised

An atomic cloud model, using an entraining parcel method has been developed at this Laboratory.[1] This model, (referred to as the TR-741 model) was particularly designed for sea-water-surface nuclear explosions. The model treats the cloud gas as a mixture of air and water vapor and allows for the release of latent heat by water vapor condensation. The key assumptions in this model are:

1. The effective rate of flow of ambient air into the cloud (entrainment) per unit surface area is equal to the product of a constant, λ, a characteristic velocity, v, and the ratio of cloud density to ambient density, ρ/ρ_e.
2. Cloud rise is retarded by both entrainment and an apparent eddy-viscous force, directly proportional to the same characteristic velocity and inversely proportional to the density ratio. (This is formally equivalent to a drag coefficient.)
3. The kinetic energy of rise corresponding to the momentum lost by eddy viscosity is converted into kinetic energy of turbulence, which remains in the cloud.
4. The characteristic velocity, v, is the greater of absolute rate of cloud rise, u, and average velocity of turbulence, $\sqrt{2E}$. Thus entrainment does not necessarily end when cloud rise ends, but continues as a turbulent diffusion.
5. In accelerating from rest to its maximum velocity, the cloud must set in motion a volume of ambient air equal to one half the initial cloud volume. Because of this "virtual mass" the acceleration is always less than twice that of gravity.

No provision was made in this model for transformation of turbulent energy into heat. Not only does such transformation actually take place, but also it may affect the formation of fallout particles through the mechanism of turbulent coagulation.[4] The rate of this transformation, the so-called "dissipation rate," ε, is found both theoretically and experimentally to be proportional to the cube of a large scale turbulent velocity divided by a large scale length, ℓ (see Section 3, Turbulence). Therefore, we now add one assumption to the cloud model.

6. Turbulent energy is dissipated at a rate proportional to the cube of the average velocity of turbulence divided by a characteristic length. The average velocity of turbulence is defined as $\sqrt{2E}$ where E is the turbulent energy per unit mass. The characteristic length used is the vertical radius of the cloud.

It was not previously noted that in entrainment of stationary ambient air with conservation of momentum, kinetic energy is lost, i.e., entrainment is an inelastic-collision process. The proof is as follows:

The rate of change of cloud momentum per unit mass, u, (i.e., velocity) with time, t, due to entrainment, is

$$\frac{du}{dt} = -u \frac{1}{m} \frac{dm}{dt} \qquad (2.3.1)$$

The corresponding change in kinetic energy per unit mass is

$$u \frac{du}{dt} = \frac{d(u^2/2)}{dt} = -2 \left(\frac{u^2}{2}\right) \frac{1}{m} \frac{dm}{dt} \qquad (2.3.2)$$

whereas, if total kinetic energy is conserved, then for a small change in velocity and mass

$$\frac{1}{2} mu^2 = \frac{1}{2} (m+dm) (u+du)^2$$

$$\frac{d(u^2/2)}{dt} = -\frac{u^2}{2} \frac{1}{m} \frac{dm}{dt} \qquad (2.3.3)$$

Entrainment, then, results in a loss of total kinetic energy, at a rate, per unit mass, of $\frac{u^2}{2} \frac{1}{m} \frac{dm}{dt}$. The law of conservation of total energy and the concept of turbulent energy already used suggest the following assumption:

7. The kinetic energy of rise lost in the inelastic-collision, momentum-conserving entrainment process, remains in the cloud as turbulent energy.

A simplified version of the essential equations is given below, neglecting the effects of the 2-gas mixture, latent heat release, initial virtual mass and condensed-water mass fraction of the cloud. These effects are considered in the full set of equations used in computation. (See Refs. 1 and 2.)

$$\underline{\text{Mass}}: \quad \frac{1}{m}\frac{dm}{dt} = \frac{S}{V}\lambda v \qquad (2.3.4)$$

where m = mass

t = time

S = cloud surface area

V = cloud volume

λ = dimensionless entrainment constant

v = characteristic velocity of entrainment

$$\underline{\text{Momentum}}: \quad \frac{du}{dt} = \left(\frac{T}{T_e} - 1\right) g - \left(\frac{2k_2 v}{\ell}\frac{T}{T_e} + \frac{1}{m}\frac{dm}{dt}\right) u \qquad (2.3.5)$$

where u = rate of rise

T = cloud temperature

T_e = environment temperature

g = acceleration of gravity

k_2 = dimensionless drag or eddy viscosity constant

ℓ = a characteristic length of the cloud

$$\underline{\text{Temperature}}: \quad \frac{dT}{dt} = -\frac{g}{c_p}\frac{T}{T_e} u - (T-T_e)\frac{1}{m}\frac{dm}{dt} + \frac{\varepsilon}{c_p} \qquad (2.3.6)$$

where c_p = specific heat of air

Turbulent kinetic energy donsity:

$$\frac{dE}{dt} = 2k_2 \frac{T}{T_e}\frac{v}{\ell} u^2 + \frac{u^2}{2}\frac{1}{m}\frac{dm}{dt} - E\frac{1}{m}\frac{dm}{dt} - \varepsilon \qquad (2.3.7)$$

where E = turbulent energy per unit mass

The term $\frac{u^2}{2}\frac{1}{m}\frac{dm}{dt}$ compensates for the loss of kinetic energy of rise in entrainment (assumption 7). Thus, some turbulent energy is produced even in the absence of eddy viscosity, i.e., even if $k_2 = 0$.

Environment temperature, T_e, is a specified function of height, z, which is given by

$$u = \frac{dz}{dt} \tag{2.3.8}$$

Dissipation rate is given by

$$\varepsilon = k_3 (2E)^{3/2}/\ell \tag{2.3.9}$$

where k_3 is a dimensionless constant.

Cloud form is a sphere (initially tangent to sea level, say in the case of a surface burst) until the top (not the center, as in TR-741) reaches the tropopause and a horizontally expanding spheroid thereafter. The vertical radius of the spheroid is fixed as the sphere's radius at the tropopause. The cloud volume and surface area can then be calculated from the perfect gas law using the assumption of pressure equilibrium. The model actually uses a differential equation for volume, so that the gas law is available as a cross-check.

The characteristic length, ℓ, is taken as the (vertical) radius of the cloud. The characteristic velocity, v, is taken as max ($|u|, \sqrt{2E}$).

The equations have been programmed for machine computation, and the computations give predictions for rate of rise, cloud size, final cloud height and the late horizontal expansion of high yield clouds, in general agreement with observations of atomic clouds. Late horizontal expansion had not previously been predicted by a cloud model.

In this paper, numerical examples are based on the results of computations for two standard cases, namely 20 KT and 5 MT sea surface bursts

in a tropical atmosphere. The computer printouts are given in Ref. 2. Since the exact numerical values do not affect the discussion in the remainder of this paper only some representative results are given here. Figure 2.1 gives cloud size and height vs time for the two yields mentioned. The time and height at which water vapor condensation begins is indicated. Figure 2.2 gives turbulent energy dissipation rate per unit mass, ε, in m^2/sec^3, i.e., watts/kg, for the two cases mentioned and also for a 0.1 KT burst.

2.4 The Energy Cycle of the Atomic Cloud

If the momentum equation (2.3.5) is multiplied by u, the temperature equation (2.3.6) by c_p and the height equation (2.3.8) by g, then with the turbulent energy equation (2.3.7) they form a set of four energy equations whose terms have the indicated meanings.

Kinetic energy, KE

$$\frac{du^2/2}{dt} =$$

gain from H	loss to PE i.e., work done lifting cloud	eddy-viscous loss to turbulence	inelastic-collision loss to turbulence	dilution by entrainment	
$= \frac{T}{T_e} gu$	$- gu$	$- 2k_2 \frac{v}{\ell} \frac{T}{T_e} u^2$	$- \frac{u^2}{2} \frac{1}{m} \frac{dm}{dt}$	$- \frac{u^2}{2} \frac{1}{m} \frac{dm}{dt}$	(2.4.1)

Enthalpy, H

		loss to KE	gain from TE i.e., dissipation, viscous heating	dilution by entrainment	
$c_p \frac{dT}{dt}$	$= \frac{dH}{dt} =$	$- \frac{T}{T_e} gu$	$+ k_3 \frac{(2E)^{3/2}}{\ell}$	$- c_p (T-T_e) \frac{1}{m} \frac{dm}{dt}$	(2.4.2)

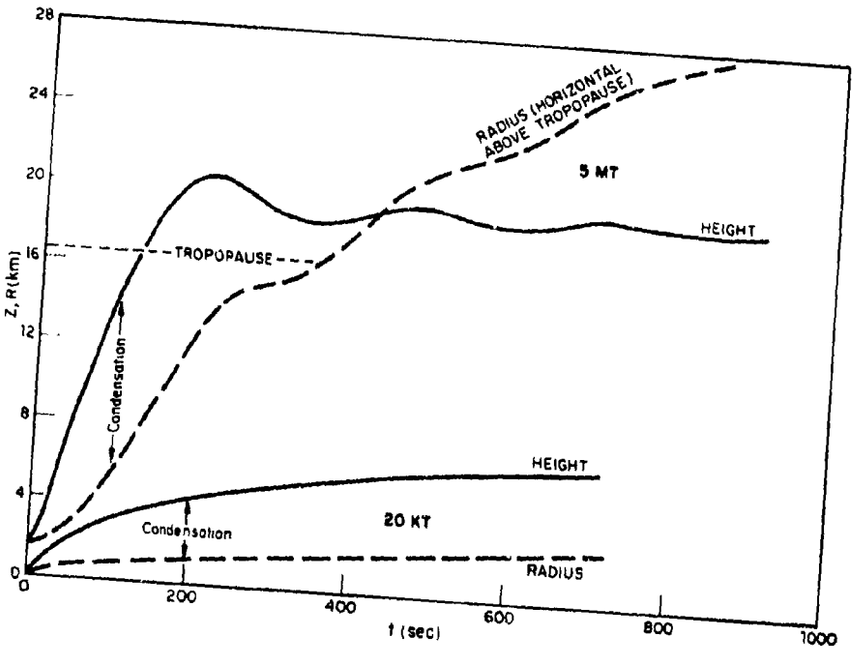

Fig. 2.1. Cloud (Center) Height Z, Radius R vs Time t

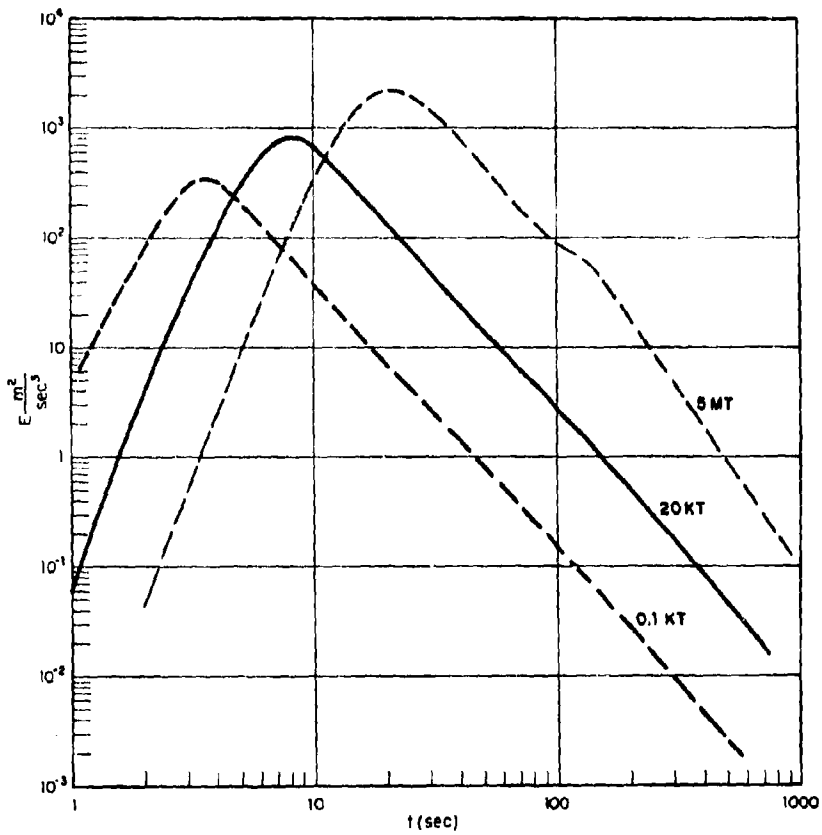

Fig. 2.2. Dissipation Rate ε vs Time t

Turbulent energy, TE

	gain from KE by eddy viscosity		gain from KE by inelastic-collision entrainment		dissipation loss to H		dilution by entrainment

$$\frac{dE}{dt} = 2k_2 \frac{v}{\ell} \frac{T}{T_e} u^2 + \frac{u^2}{2} \frac{1}{m} \frac{dm}{dt} - k_3 \frac{(2E)^{3/2}}{\ell} - E \frac{1}{m} \frac{dm}{dt} \qquad (2.4.3)$$

Potential energy, PE

	gain from KE

$$g \frac{dz}{dt} = gu \qquad (2.4.4)$$

Kinetic energy here means energy of directed motion of the cloud, $u^2/2$, turbulent energy, E, is actually kinetic energy of randomly moving lumps of fluid within the cloud. See Sec. 3.1.1. Adding the four equations gives an equation for total energy per unit mass

$$\frac{d}{dt} (u^2/2 + c_p T + E + gz) = - \frac{1}{m} \frac{dm}{dt} (u^2/2 + c_p(T-T_e) + E) \qquad (2.4.5)$$

The dimensionless constants k_2 and k_3 do not appear in the total energy equation; they only affect the rate of transfer between different forms of energy.

The present cloud model, then, is based on conservation of mass and energy, and the equations for velocity (or momentum or kinetic energy), temperature (or enthalpy), turbulent energy and height can be considered merely rules for energy transformation. These rules imply an energy cycle which may be diagrammed as follows. The heavier arrows indicate the usual direction of transfer (when $T > T_e$ and $u > 0$)

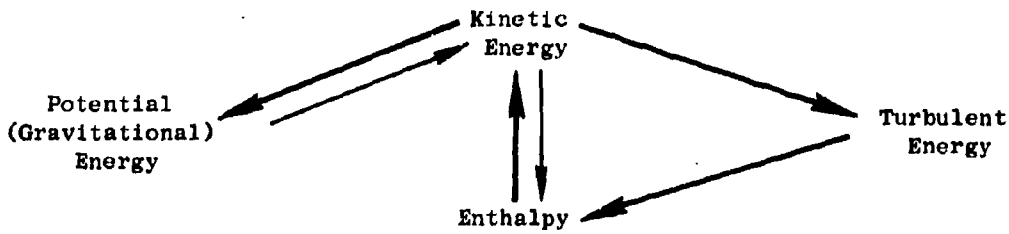

The energy flow through turbulence is always in the same direction; this part of the cycle is intrinsically irreversible. The novelty in this model is the use of turbulence as a delay line between kinetic energy of rise and heat. Although momentum is lost by drag or eddy viscosity, kinetic energy is not lost but rather transformed.

Because of entrainment, the cloud cannot be treated as a closed system, with constant total energy per unit mass, except under special atmospheric conditions. To examine change in total cloud energy (not per unit mass) all mass should be referred to the same datum, although the mass was entrained at different altitudes and temperatures (at different potential energies and enthalpies). As a datum, we use sea level, $z = 0$, with the corresponding ambient temperature, $T_e = T_{eo}$.

Multiplying Equation (2.4.5) by m and rearranging terms, the rate of change of total energy relative to this datum is

$$\frac{d}{dt}\left[m(u^2/2 + c_p(T-T_{eo}) + E + gz)\right] = \frac{dm}{dt}\left[(T_e + gz/c_p)-T_{eo}\right]c_p \qquad (2.4.6)$$

Now $T_e + gz/c_p$ is the potential temperature of the atmosphere at altitude z, (the temperature air at the given altitude would have if compressed adiabatically to sea level pressure), so that total cloud energy, referred to sea level, increases with altitude in proportion to the excess of potential temperature over sea level temperature. We can now sketch a total-energy cycle for the cloud, referred to the sea level datum. (See Fig. 2.3.)

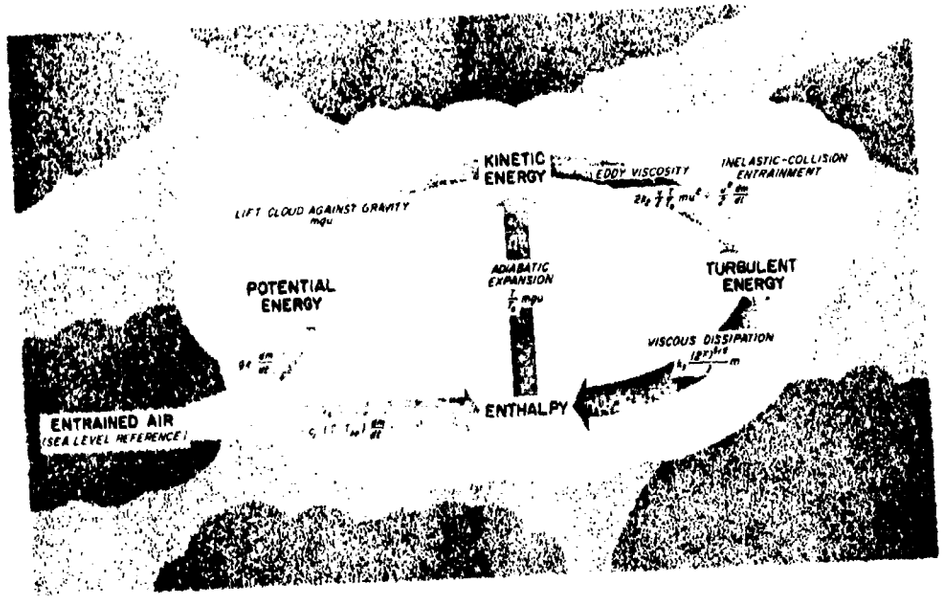

Fig. 2.3. Total Energy Cycle for the Rising Atomic Cloud

In an adiabatic atmosphere (one in which potential temperature does not vary with altitude), we have

$$T_e = T_{eo} - gz/c_p$$

so that, substituting in Equation (2.4.6),

$$\frac{d}{dt}\left[m(u^2/2 + E + c_p(T-T_{eo}) + gz)\right] = 0 \qquad (2.4.7)$$

i.e., total energy, referred to sea level, is constant.

3. TURBULENCE IN THE ATOMIC CLOUD

3.1 Theoretical Background

Turbulent motion of a fluid has by definition a fluctuating, random nature in time and space. This nature has suggested Fourier analysis of velocity components (and other fluctuating properties) into a spectrum of motions of various length scales, or "eddy sizes." We shall be concerned mostly with small eddies.*

3.1.1 The Energy Cascade

The kinetic energy of a large scale, intensely turbulent flow is supposed to be transmitted from the overall flow to the largest eddies (turbulent motions) and through a cascade of successively smaller eddies* to an approximate minimum eddy size, and finally, to be dissipated by viscosity to heat (molecular motions). This idea dates back at least to L. F. Richardson, c.1920. The cascade picture suggests that eddies sufficiently far along the cascade may be independent of large-scale flow conditions, and leads to the equilibrium hypothesis. (See next section.)

*'Small eddy' is used. . .as a concise term for a Fourier component belonging to a small length scale, or large wave number.(3)

3.1.2 The Equilibrium Hypothesis

During the transfer of energy to smaller and smaller eddies, the direction of motion becomes random and the concentration of energy in particular eddy sizes (wave lengths) is smoothed out by transfer to neighboring sizes. Information on eddy orientation is lost during energy transmission, so to speak. Thus, small scale turbulence is homogeneous and isotropic even though the largest eddies (such as the vortex ring of an atomic cloud) are not. The motions at different small length scales are similar in the sense that they differ only by scale factors which are independent of large scale flow conditions. Eddies of these sizes are said to be in the equilibrium range. This is "Kolmogorov's hypothesis": "the small scale components of turbulence are approximately in statistical equilibrium."[3] Equivalent names for this hypothesis are: theory of "local similarity," of "universal equilibrium," or of "similarity of small eddies." Kolmogorov's hypothesis applies only to very high Reynolds-number flows ($Re > 10^6$) such as a rising atomic cloud.

While sufficiently small eddies are independent of large scale flow, all except very small eddies are independent of fluid viscosity. This latter independence leads to the principle of Reynolds-number similarity (Ref. 5, Sec. 5.4):

> "Geometrically similar flows are similar at all sufficiently high Reynolds numbers. The aspects of the motion that are excluded from the similarity are quite simply those that occur at low Reynolds numbers, i.e., those in which viscous forces are comparable with inertial and pressure forces."

This principle is applied in the cloud model, for instance, in the choice of characteristic length involved in momentum and energy transfer. This length is scaled to cloud size, independent of fluid viscosity. It is used again in developing a theory of turbulent-diffusive dispersion of particles from the cloud. (Sec. 5.) Note that the principle of Reynolds-number similarity is a statement about large-scale conditions, while that of local similarity is a statement about small-scale conditions.

The equilibrium range of the eddy spectrum is independent of overall flow dimensions and thus of energy input by large eddies at one end of the spectrum. Furthermore, for extremely large Reynolds numbers[6] as in atomic cloud turbulence, the larger-eddy part of this equilibrium range, called the "inertial sub-range"[3] is also independent of viscous dissipation by the smallest eddies (the "dissipation range") at the other end of the spectrum. The existence of the "inertial range" or "sub-range" is sometimes[6] called "Kolmogorov's second hypothesis." Dimensional analysis, applied to the inertial and dissipation ranges, predicts the velocity, energy, etc., at each wave length, λ, or wave number, k, (reciprocal of wave length). See Sec. 3.1.3.

For a quasi-steady fluid flow, the rate of energy dissipation per unit mass, ε, by the smallest eddies, is equal to the rate of energy transmission through the spectrum from the large eddies, (energy-input) to the smallest, dissipative eddies. That is, if λ is an eddy size much smaller than the maximum flow dimensions, and somewhat larger than the minimum eddy size, λ_o, then the rate of energy transmission past λ is equal to ε. (The size range of λ might be about $10\lambda_o < \lambda \leq \ell/10$, but see Sec. 3.1.4.) A quasi-steady fluid flow is one in which the response time of the energy spectrum at a given small-eddy wave number is small compared with the time scale of changes in the overall flow.

The dissipation rate, ε, is determined by large-scale flow conditions, although it is the smallest eddies which actually dissipate kinetic energy to heat. At this largest scale of the flow, the Reynolds number is extremely large and viscosity is of negligible importance. Then, using dimensional analysis, ε must have the form

$$\varepsilon \sim u^3/\ell$$

where u and ℓ are a large scale velocity and length, respectively, since these are the only large scale quantities out of which a dissipation rate

(power per unit mass, or length^2/time^3) can be formed. Here and later, the symbol ~ means "proportional to and of the order of magnitude of."

Writing

$$\varepsilon \sim u^3/\ell \sim \ell u(u/\ell)^2$$

it is seen that ℓu has the dimensions of kinematic viscosity, and u/ℓ has the dimensions of shear. Just as molecular kinematic viscosity is proportional to the product of molecular speed and mean free path, an eddy viscosity can be defined:

$$\nu_{turb} \sim u\ell$$

Then we can write

$$\varepsilon \sim \nu_{turb} (u/\ell)^2$$

in analogy to the dissipation rate in laminar viscous flow, whose form is $\nu \left(\frac{\partial u}{\partial y}\right)^2$ where y is a coordinate perpendicular to u.

3.1.3 Small Scale Turbulence Parameters

The smallest eddy size, λ_o, the "Kolmogorov microscale," can depend only on (molecular) kinematic viscosity and on ε, so that again by dimensional analysis,

$$\lambda_o \sim (\nu^3/\varepsilon)^{1/4}$$

(The constant of proportionality in these relations is usually of order unity.) Thus, the microscale is only weakly dependent (to the -1/4 power on dissipation rate. It is typically of order 1 mm in severe atmospheric storms, where $\varepsilon \sim u^3/\ell \sim 10^3 cm^2/sec^3$ or exceptionally, $\varepsilon \sim 10^4$ (see for instance, Ref. 7). Even if $\varepsilon \sim 10^6$ or 10^7, as seems possible in a

megaton atomic cloud, (see Fig. 2.2) ν_o is not much less – say .3 mm = 300 μ, since at the high temperature and/or low density of atomic clouds, the value of ν will be greater than at standard temperature and pressure. (See Sec. 3.2.3). Further predictions of characteristic quantities in the inertial and dissipation ranges are readily derived (as in Refs. 4 and 8) and are listed here (Table 3.1).

3.1.4 Approximations to the Energy Spectrum

It has been suggested[9] that for very high Reynolds numbers the inertial range can be extended over the entire spectrum, from the largest wave lengths, ℓ, to the microscale, λ_o.

3.1.5 The Degrees of Freedom of a Turbulent Flow

Associated with any eddy size, λ, there is a "spectral Reynolds number" $Re_\lambda = \frac{\lambda v_\lambda}{\nu}$.

From Table 3.1, substituting $\varepsilon \sim u^3/\ell$,

$$Re_\lambda \sim \frac{\varepsilon^{1/3}\lambda^{4/3}}{\nu} \sim \frac{u\ell}{\nu}\left(\frac{\lambda^{4/3}}{\ell^{4/3}}\right) = Re\left(\frac{\lambda}{\ell}\right)^{4/3}$$

where Re refers to the overall flow. Since for $\lambda = \lambda_o$, $Re_\lambda = 1$, the ratio of size of largest to smallest eddies is of order $Re^{3/4}$.

Taking the largest eddies as of nearly the same size as the overall flow, there are then $Re^{3/4}$ independent microscale eddies, or degrees of freedom. In a three dimensional flow there are then $Re^{9/4}$ independent eddies, or degrees of freedom. This suggests the problems associated with numerical computation of turbulent flows. (See Sec. 2.1.)

3.2 Estimates of Atomic Cloud Turbulence

In this discussion, reference is made to the revised TR-741 cloud model for numerical estimates of characteristics of explosion clouds.

Table 3.1

Small Scale Turbulence Parameters

RANGE	INERTIAL	MICROSCALE	VISCOUS
Parameter Length, λ	$\lambda > \lambda_o$	$\lambda_o = \left(\frac{\nu^3}{\varepsilon}\right)^{1/4}$	$\lambda < \lambda_o$
Velocity, v_λ	$(\varepsilon\lambda)^{1/3} = v_o \left(\frac{\lambda}{\lambda_o}\right)^{1/3}$	$v_o = (\varepsilon\nu)^{1/4}$	$\frac{\lambda}{t_o} = \lambda \frac{v_o}{\lambda_o}$
Time, $t_\lambda = \frac{\lambda}{v_\lambda}$	$\left(\frac{\lambda^2}{\varepsilon}\right)^{1/3} = t_o \left(\frac{\lambda}{\lambda_o}\right)^{2/3}$	$t_o = \left(\frac{\nu}{\varepsilon}\right)^{1/2} = \frac{\lambda_o}{v_o}$	t_o
Acceleration, $a_\lambda = \frac{v_\lambda}{t_\lambda}$	$\left(\frac{\varepsilon^2}{\lambda}\right)^{1/3} = \frac{v_o}{t_o}\left(\frac{\lambda_o}{\lambda}\right)^{1/3}$	$a_o = \frac{v_o}{t_o} = \left(\frac{\varepsilon^3}{\nu}\right)^{1/4} = \left(\frac{\varepsilon^2}{\lambda_o}\right)^{1/3}$	$\frac{v_\lambda}{t_o} = \frac{\lambda}{t_o^2} = \frac{\lambda}{\lambda_o}\frac{v_o}{t_o}$
Shear Rate, $\frac{v_\lambda}{\lambda} = \frac{1}{t_\lambda}$	$\left(\frac{\varepsilon}{\lambda^2}\right)^{1/3} = \frac{1}{t_o}\left(\frac{\lambda_o}{\lambda}\right)^{2/3}$	$\frac{1}{t_o} = \frac{v_o}{\lambda_o} = \left(\frac{\varepsilon}{\nu}\right)^{1/2}$	$\frac{1}{t_o}$

Table 3.1

Small Scale Turbulence Parameters (Continued)

RANGE	INERTIAL	MICROSCALE	VISCOUS
Energy Per Unit Wave Length,	S A M E A S A C C E L E R A T I O N		
Energy Per Unit Wave Number, $\mathcal{E}(k)$	$\mathcal{E}^{2/3}\, k^{-5/3}$	$\mathcal{E}(1/\lambda_o) = (\mathcal{E}\nu^5)^{1/4} = \frac{\nu^2}{\lambda_o} = (\mathcal{E}^2\lambda_o^5)^{1/3}$	$\frac{\lambda^3 v_o^2}{\lambda_o^2} = \frac{\nu^2}{\lambda_o}\left(\frac{\lambda}{\lambda_o}\right)^3 = \mathcal{E}(1/\lambda_o)\left(\frac{\lambda}{\lambda_o}\right)^3$
Reynolds Number, $Re_\lambda = \frac{\lambda v_\lambda}{\nu}$	$\frac{\lambda^{4/3}\mathcal{E}^{1/3}}{\nu} = \left(\frac{\lambda}{\lambda_o}\right)^{4/3} > 1$	1	$\left(\frac{\lambda}{\lambda_o}\right)^2 < 1$

3.2.1 Scales and Reynolds Numbers

As a large scale characteristic length for calculating Reynolds number we use cloud diameter. The size of the largest eddies (such as the vortex ring cross section), used as a length scale for energy dissipation rate, $\varepsilon \sim u^3/\ell$, is less than this diameter, but we assume that ℓ is a constant fraction of cloud diameter. For the corresponding characteristic velocity, u, we use the "velocity of turbulence," $\sqrt{2E}$.

In the early part of cloud rise (up to about 60 sec. for 5 MT), the cloud is much hotter than the environment. This leads to different values for "external" and "internal" Reynolds numbers.

$$R_{ext} = \frac{u\ell\rho_e}{\mu_e} \quad ; \quad R_{int} = \frac{u\ell\rho}{\mu}$$

Here, u and ℓ are appropriate velocity and length scales. Since, for a perfect gas

$$\frac{\rho}{\rho_e} \simeq \frac{T_e}{T} \quad \text{and} \quad \frac{\mu}{\mu_e} \simeq \left(\frac{T}{T_e}\right)^{1/2} \quad , \quad \text{then} \quad \frac{R_{ext}}{R_{int}} = \left(\frac{T}{T_e}\right)^{3/2} \quad .$$

It is R_{int} that is of interest in cloud turbulence. Although calculated turbulence velocities are high — of the same order as rate of rise — the Mach number of turbulence is (even for a 5 MT shot) ever more than 1/3 because of the higher speed of sound in the hot cloud than in the cold environment. Thus, compressible-flow effects can be neglected.

3.2.2 The Turbulent Spectrum of the Cloud

Since atomic-cloud Reynolds numbers are extremely high (for a 5 MT cloud, Re $\sim 10^{10}$ from 30 to 600 sec. after burst) one can certainly assume homogeneity and isotropy of small eddies. Homogeneity is also consistent with the "parcel" cloud method. Because of the high Reynolds number we

can also, with some confidence, extend the inertial range to nearly the entire spectrum from the microscale to almost the largest eddies. (Sec. 3.1.4.)

Because the atomic cloud is not in a steady state, there is difficulty in defining the dissipation rate, ε. The rate of "loss" (dilution) of energy per unit mass due to entrainment may be larger than viscous loss (i.e., $\frac{E}{m}\frac{dm}{dt} > \varepsilon$), and the flux of energy from its source in the large eddies to the viscous sink is actually neither independent of time nor of eddy size. Nevertheless, we propose to neglect any distorting effect of entrainment on the spectrum and estimate turbulence parameters quasi-statically at each time of interest on the basis of E and ℓ. That is, we treat the turbulence as "quasi-steady" as defined in Sec. 3.1. This treatment is justified if the characteristic time of change of E, say $\left[\frac{1}{E}\left|\frac{dE}{dt}\right|\right]^{-1}$ is much greater than the "local transfer time"[9] of energy flow through the spectrum, $\tau(k) = [k^3 \varepsilon(k)]^{-1/2}$.

There are several possible choices for $\frac{dE}{dt}$:

(1) the total derivative (net rate of change) of E. This cannot be used at some early times, (for instance, near 22 sec. in Table 2.1) as it is nearly zero because increase of E by generation of turbulence and decrease by dissipation and entrainment nearly cancel;

(2) the generation rate, $2k_2 \frac{T}{Te}\frac{v}{\ell} u^3 + \frac{1}{m}\frac{dm}{dt}\frac{u^2}{2}$

(3) the dissipation rate, $\varepsilon = k_3 \frac{(2E)^{3/2}}{\ell}$

The characteristic time $\left(\frac{1}{E}\frac{dE}{dt}\right)^{-1}$, calculated using each of these choices for $\frac{dE}{dt}$, has been compared with the local transfer time, for the 5 MT cloud computation. For the local transfer time, τ, we use a characteristic time based on similarity theory (Table 3.1). $\tau = (\varepsilon k^2)^{-1/3} = (\lambda^2/\varepsilon)^{1/3}$.

It is found that for typical inertial-range wavelengths (up to 10 meters), τ is much smaller than $\left[\frac{1}{E}\frac{dE}{dt}\right]^{-1}$ so that the equilibrium treatment

of small scale turbulence is justified for the atomic cloud. We might say that if the local transfer time is small compared with the characteristic time, turbulent energy is flowing through the eddy spectrum like an incompressible fluid.

4. VORTEX MOTION IN THE CLOUD

Pictures of atomic clouds often show a vortex ring of hot incandescent gas within the rising cloud and also, even at later times when the gas is no longer incandescent, a general toroidal circulation of the cloud boundary. These phenomena appear more clearly in air bursts than surface blasts. Surface material in and around the cloud may diminish their visibility or actually interfere with their occurrence, say by mass loading of the circulating gas. We will generally refer to these phenomena as "toroidal circulation," restricting "vortex ring" to its classical hydrodynamic meaning. The reasons for interest in the circulation are (1) that it may affect cloud rise and expansion and especially (2) its effect on particle dispersion from the cloud.

4.1 The Pasted Vortex

Atomic cloud vortex models proposed to date consist of an assumed classical vortex flow superimposed, or "pasted," on a parcel method cloud, without regard even to conservation of energy, much less to whether the resulting "pseudo-local" velocities satisfy the time-averaged Navier-Stokes equations. Since the streamlines thus drawn in the cloud are intended to represent average flow directions in the intensely turbulent cloud, the time of averaging must be long compared with cloud rise. The time of averaging then, should be just shorter than the periods of the largest eddies, i.e., of the vortex ring. Actually, the local velocities can represent only one solution to the equation of motion, that for steady motion in an infinite homogeneous, non-viscous, incompressible medium; the vortex, however, is being superimposed on radically different conditions.

If the pasted vortex is to be used, it is necessary to specify first the vortex form and then its numerical parameters. The two extremes of vortex structure[10] are Hill's spherical vortex, in which the entire moving spherical fluid body is the vortex, and a thin ring vortex, which constitutes only a small part of the traveling fluid volume. The use of Hill's vortex has been suggested for cumulus cloud elements.[11] Observations of atomic clouds indicate that the thin ring is more appropriate than the spherical vortex, (and that early in cloud rise, the ring cross-section radius is not more than 1/10 of the cloud radius).

Given the general ring vortex form, its numerical parameters can be obtained either empirically or theoretically. The flow is completely determined by specifying ring radius, vortex core cross-section radius, and circulation (line integral of velocity around a closed circuit through the ring). If cross-section radius is very small, i.e., a thin ring vortex, then local velocities outside the core are completely determined by ring radius and circulation. Alternatively, a number of local values of velocity can be used to determine the vortex parameters and the flow structure.

4.1.1 Specification of Vortex Parameters by the Cloud Model.

The vortex ring is certainly the largest, most permanent eddy in the turbulent atomic cloud. In fact, the vortex ring might be pictured as the flywheel maintaining the cascade of energy to smaller eddies in the turbulent spectrum (see, for instance, Hinze,[6] Sec. 3.5) even after the end of cloud rise, when no more energy is supplied to turbulence. This energy supply picture is compatible with the late horizontal cloud expansion. Now we propose that the transfer of energy from mean motion to turbulence begins with the generation of the vortex, and that the vortex ring be allocated a fixed fraction of the total turbulent energy density E, say 0.2^6 or 0.25^3. This proposal is suggested by Hinze's statement:[6]

"In the fully developed state it is not the largest eddies that will have the maximum kinetic energy, but the eddies in a higher-wave number range. The range of the energy spectrum where the eddies make the main contribution to the total kinetic energy of turbulence will be called the range of the energy-containing eddies. . . . Though the more permanent largest eddies contain much less energy than the energy-containing eddies, their energy is by no means negligibly small and may still amount to as much as 20 percent of the total kinetic energy."

We can now outline a procedure for specifying vortex parameters using our cloud model. Our three input parameters will be rate of cloud rise, u, cloud radius, r, and rotational (vortex) energy, 0.2mE, where m is cloud mass.

The total energy of a thin-ring vortex flow is[10]

$$T = \frac{\kappa^2 \rho \bar{\omega}_o}{2} \left(\ell n \frac{8\bar{\omega}_o}{a} - \frac{7}{4} \right) \tag{4.1}$$

Here we use Lamb's[10] notation: κ is circulation, $\bar{\omega}_o$ is the radius of the vortex ring, a is the cross-section (vortex core) radius.

This energy consists, (we suppose) of kinetic energy of rise of the cloud, $\frac{1}{2}$ mu^2, and rotational energy, 0.2mE. Then the energy equation becomes

$$\frac{1}{2} mu^2 + 0.2mE = \frac{\kappa^2 \rho \bar{\omega}_o}{2} \left(\ell n \frac{8\bar{\omega}_o}{a} - \frac{7}{4} \right) \tag{4.2}$$

The velocity of translation of the vortex is

$$u = \frac{\kappa}{4\pi\bar{\omega}_o} \left(\ell n \frac{8\bar{\omega}_o}{a} - \frac{1}{4} \right) \tag{4.3}$$

The radius of the cloud is related to the radius of the vortex ring by the fact that the stream function[10] equals zero at the boundary of the "cloud," that is, at the boundary of the fluid which is carried along

with the vortex ring. This relation gives a third equation (Lamb,[10] Sec. 161, Equation 11) so that κ, a, and $\bar{\omega}_o$ can be found. The algebra of the solution is involved and only numerical solutions for κ, a, and $\bar{\omega}_o$ can be obtained explicitly. In any case, for a thin ring the stream function can be given in terms of κ, $\bar{\omega}_o$ and u, without using a, which does not affect velocities outside the core.

For purposes of illustration, we take a simplified case. Set $\bar{\omega}_o$ = 3/5 r as indicated by Figure 3 of Reference 12. Treat the cloud as spherical, so that $\rho = m/(\frac{4}{3}\pi r^3)$ and drop the second term in parenthesis in Equations (4.2) and (4.3) since $\bar{\omega}_o >> a$. Then, dividing the energy equation (4.2) by the velocity equation (4.3) and substituting the given values of $\bar{\omega}_o$ and ρ,

$$\kappa = 1.85r \frac{u^2/2 + 0.2E}{u} \tag{4.4}$$

Until nearly the end of cloud rise, $u^2/2 > 0.2E$ so that approximately

$$\kappa = ru \tag{4.5}$$

This result[13] can be obtained directly by dimensional analysis: if κ depends only on r and u, it must have the form of Equation (4.5).

Values of circulation calculated from Equations (4.4) and (4.5) for our standard 20 KT case are rather lower at early times (5 to 10 sec) than comparable values estimated from cloud films.[12, 14] Now, at very early times, ambient air is several times as dense as the cloud and circulation is changing rapidly, so that the use of classical vortex theory is on especially shaky ground. However, it is reasonable that if circulation is due to the drag of the ambient air on the cloud, it should be proportional to the density ratio $\rho_e/\rho = T/T_e$, like the eddy-viscous momentum loss rate in the momentum equation (Sec. 2.3). An appropriate formula would then be

$$\kappa = ruT/T_c \qquad (4.6)$$

No theoretical consistency with Equations (4.1) - (4.3) can be claimed for Equation (4.6): the latter is offered as an intuitive value for circulation in a situation where attempts to use formulas from classical vortex theory seem particularly remote from reality.

Table 4.1 gives values of κ calculated from Equations (4.4), (4.5), and (4.6), for several times of interest using data from our standard 20 KT and 5 MT computations. The values are of the same order of magnitude as the widely scattered estimates from cloud films[12,14] which are for different yields and generally earlier times. Our conclusion is that if one wishes to superimpose an assumed vortex ring on a parcel-method cloud model, one may as well derive vortex parameters from the model itself as from film observations. Not only is laborious film measurement avoided, but, at least for Equations (4.4) and (4.5), the vortex velocity and energy are now compatible with those of the cloud.

4.2 Use of Kelvin's Theorem to Estimate Rate of Change of Cloud Circulation

The equations for the classical vortex ring are derived assuming steady incompressible flow. Under such circumstances, circulation is constant, hence it is illogical to claim that the rate of change of circulation can be obtained by differentiating Equation (4.4) or (4.5). An expression for rate of change of circulation* $\frac{d\Gamma}{dt}$, can be obtained more consistently from a consequence of Kelvin's equation.[15]

$$\frac{d\Gamma}{dt} = \frac{d}{dt} \oint \vec{v} \cdot d\vec{x} = \oint \vec{a} \cdot d\vec{x} \qquad (4.7)$$

*The symbol Γ is used here for circulation to conform with Ref. 15, while in Section 4.1 the symbol κ was used to conform with Ref. 10.

TABLE 4.1

VORTEX CIRCULATION CALCULATED FROM CLOUD MODEL

Time	Radius	Rate of Rise	Turbulent Energy Density	Temperature Ratio	Circulation, Λ(m^2/sec)		
(sec.)	r(m)	u(m/sec)	E(m^2/sec^2)	$T/T_e = \rho_e/\rho$	Eq (4.4) $1.85 \frac{r}{u}(\frac{u^2}{2} + 0.2E)$	Eq (4.5) ru	Eq (4.6) ruT/T_e
W = 5 MT (from Table 2.1)							
20	$1.8x10^3$	$1.8x10^2$	$4.1x10^4$	5.3	$4.5x10^5$	$3.2x10^5$	$1.7x10^6$
30	2.1	1.6	3.4	3.0	4.8	3.3	$9.9x10^5$
60	3.2	1.2	1.5	1.5	5.0	3.8	5.7
80	3.9	1.1	1.1	1.3	5.3	4.1	5.3
W = 20 KT (from Table 2.2)							
5	$2.4x10^2$	61.	$2.8x10^3$	7.7	$1.8x10^4$	$1.5x10^4$	$1.2x10^5$
10	2.7	62.	5.4	3.6	2.5	1.7	$6.1x10^4$
15	3.1	51.	3.3	2.1	2.2	1.6	3.4
30	4.4	34.	1.2	1.2	2.0	1.5	1.8

where $\vec{v}$ is velocity, $\vec{a}$ is acceleration, $\vec{dx}$ is a line element and the integral is taken around a circuit moving with the fluid, i.e., consisting of the same fluid particles. Writing the equation of motion as

$$\vec{a} = -\frac{1}{\rho} \nabla p$$

the rate of change of circulation around the circuit is

$$\frac{d\Gamma}{dt} = -\oint \frac{1}{\rho} dp \qquad (4.8)$$

To calculate cloud circulation, we take a rectangular circuit in a vertical plane through the cloud axis. As indicated in the following diagram, the circuit extends vertically from below the bottom to above the top of the cloud, and horizontally from the axis to well out in the ambient air.

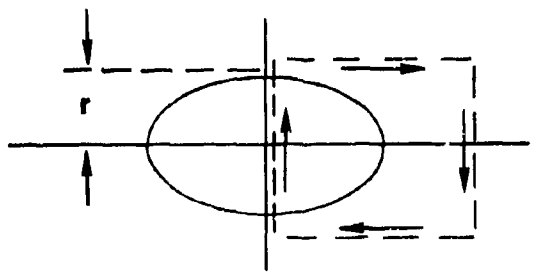

Now dp is zero along the horizontal parts of the circuit. Furthermore, the parts of the upward vertical path outside the cloud are exactly cancelled by the corresponding parts of the downward path at the same altitudes so that the only possible non-zero contribution to the line integral is from the remaining vertical parts, i.e., between the top

and bottom of the cloud, a distance $\Delta z = 2r$. On each of these two vertical parts, take an average value of specific volume, namely, $1/\rho$ inside and $1/\rho_e$ outside the cloud, and using the hydrostatic law, replace dp by $-\rho_e g dz$. On the upward path, the change in p is then $-\rho_e g \Delta z = -2\rho_e g r$ and similarly on the downward path (pressures inside and outside being equal) so that

$$\frac{d\Gamma}{dt} = -\left[-\frac{2r}{\rho}\rho_e g + \frac{2r}{\rho_e}\rho_e g\right] = 2rg\left(\frac{\rho_e}{\rho} - 1\right) \qquad (4.9)$$

Note that the cloud need not be spherical; it is only its vertical extent, 2r, that matters.

The foregoing derivation makes no allowance for decrease of circulation due to (1) eddy viscosity or (2) entrainment. Inclusion of these two effects violates, respectively, the (1) ideal-fluid and (2) closed-streamline assumptions of Kelvin's theorem. Nevertheless, we offer a way to allow for these effects on circulation. Substitute in Equation (4.7) the value of acceleration given by the momentum Equation (2.3.5) and integrate around the same circuit as before. The entrainment rate is taken at zero on the part of the circuit outside the cloud. The resulting rate of change of circulation is

$$\frac{d\Gamma}{dt} = 2r\left[\left(\frac{\rho_e}{\rho} - 1\right) g - \left(\frac{\rho_o}{\rho} - 1\right)\frac{2k_2 v}{\ell} u - \frac{1}{m}\frac{dm}{dt} u\right] \qquad (4.10)$$

The first term in the brackets on the right side of this equation is the ideal-fluid term, corresponding to Equation (4.9). The second and third terms represent the effect of eddy-viscosity and entrainment respectively. In this heuristic derivation, it seems a worse abuse of hydrodynamic theory to introduce entrainment across streamlines than

eddy viscosity. Figure 4.1 gives numerical values of circulation from a hand integration of Equation 4.10 with and without the entrainment term, using data from our standard 20 KT and 5 MT computations.

It is seen in Fig. 4.1 that circulation attains nearly its maximum value early in cloud rise, at about the time of maximum rate of rise. The time of rapid increase in circulation can be associated with the formation of a vortex ring from the initial spherical cloud. This picture is reinforced if the entrainment term is omitted - no entrained mass crosses the surface of the initial cloud even though this surface is deformed from sphere to toroid.

The values of circulation are somewhat larger than those obtained with the "pasted vortex" (Table 4.1). Since the present "Kelvin" method of calculating circulation requires neither any particular, assumed vortex form, nor steady-state flow, it is more consistent with the physical conditions of the atomic cloud. The resulting values of circulation therefore inspire somewhat more confidence than those in Table 4.1.

5. TURBULENT DIFFUSION OF PARTICLES

If particles escape from the atomic cloud by centrifugal force as well as gravity, due to "centrifugal throwout" from the toroidal circulation of the fluid, then the concentration of these particles, immediately after leaving the cloud, would vary with distance from the axis of the rising cloud. Their distribution, projected on the ground, would increase with distance from the projected cloud center, while if particles escaped under gravity alone, the distribution would be nearly uniform over the projected cloud area. The intense turbulence of the cloud suggests treating any non-gravitational dispersion of particles as a turbulent diffusion. How do particles "really" get out of the cloud? Perhaps the question is meaningless. We propose to use the

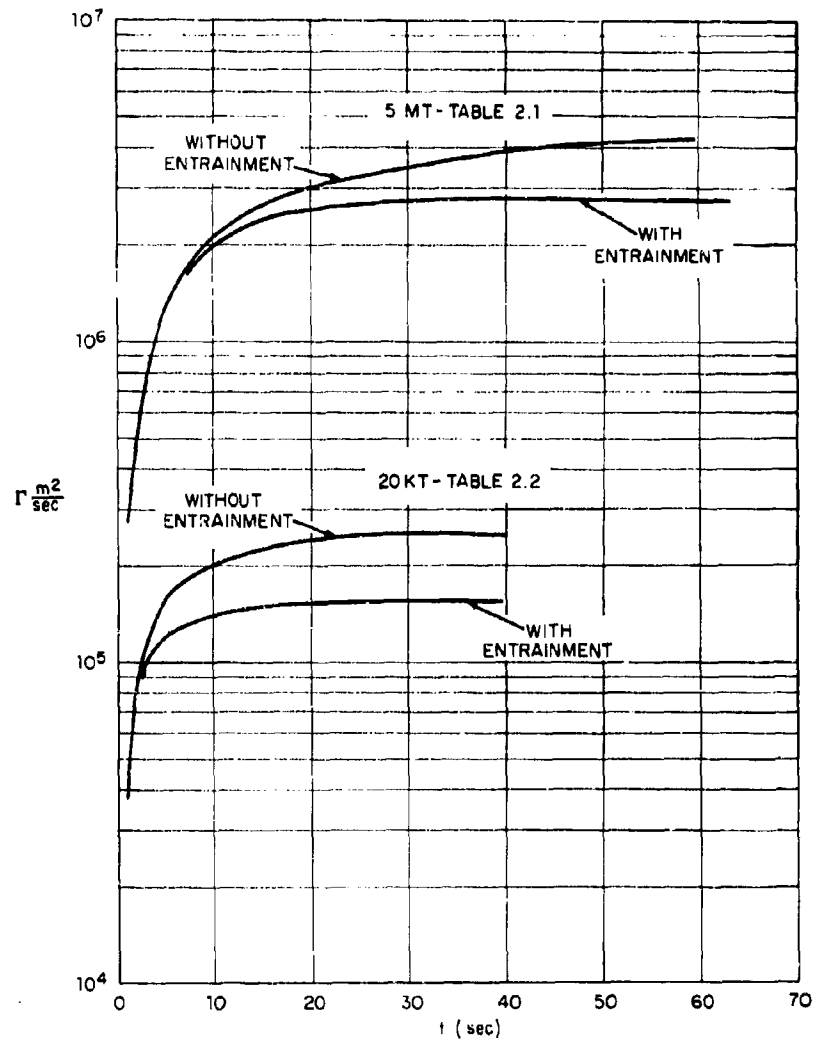

Fig. 4.1. Circulation Γ vs Time t

language of turbulence, as more appropriate than that of laminar flow, to model non-gravitational dispersion.

5.1 Geometrical Effect of Turbulent Diffusion

Suppose turbulent diffusion of particles is uniform over the spheroidal cloud surface (a sphere before the cloud top has reached the tropopause; an oblate spheroid thereafter). Only radial diffusion causes dispersion of particles from the cloud. Dispersion of particles out through the upper surface of the cloud can be neglected since particles so dispersed are either recaptured by the rising cloud or fall back into the cloud after end of rise. Therefore, only dispersion through the lower surface need be considered.

If particle flux density, I_o, is uniform over the cloud surface, then its projection, I, on a horizontal plane varies with radial distance, x, for the projected cloud center as the ratio of arc length on a cross section through the vertical axis, ds, to projected arc length, dx. If y is the vertical coordinate, then $ds = \sqrt{(dx)^2 + (dy)^2}$ so that for a spheroid whose vertical cross section has the equation $\frac{x^2}{a^2} + \frac{y^2}{b^2} = 1$, we have

$$\frac{ds}{dx} = \sqrt{\frac{1-(x^2/a^2)(1-b^2/a^2)}{1-x^2/a^2}}$$

Since the projected flux density is proportional to $\frac{ds}{dx}$, it becomes infinite below the periphery of the cloud, x = a, (neglecting diffusion in the atmosphere, wind, etc.). A more realistic approach is to divide the projection into say five concentric rings whose mid-radii are x/a = 0.1, 0.3, 0.5, 0.7, 0.9. The corresponding relative projected flux densities $\frac{ds}{dx}$ are, for a sphere, 1.01, 1.05, 1.15, 1.40, 2.29 and for a 2/1 ellipsoid (such as our 5 MT cloud at 140 seconds) 1.00, 1.01, 1.04, 1.11, 1.44.

The total projected flux is equal to the flux density integrated over rings of area 2π x dx, and equal to the total flux through the lower half of the cloud. For a spherical cloud of radius, R = a = b,* the demonstration is particularly simple:

$$\text{Total projected flux} = \int_0^R I(X) \cdot 2\pi x \, dx = I_0 \int_0^R \frac{ds}{dx} \cdot 2\pi x \, dx$$

$$= 2\pi I_0 \int_0^R \frac{x}{\sqrt{1-x^2/R^2}} \, dx = 2\pi R^2 I_0 = \text{total flux}$$

5.2 Turbulent Diffusion Coefficients

Turbulent diffusion coefficients as a function of particle size, have been determined in a study[4] of relative motion and coagulation of particles in a turbulent gas, which is being applied to the atomic cloud.

The derivation of the diffusion coefficients and other particle parameters uses the similarity theory of turbulence and was suggested by a remark of V. G. Levich[8] that for any size particle there is a minimum size eddy which just contains the particle during a turbulent fluctuation. (Exception: Small particles below a certain size are contained by all, even microscale eddies.) Mean particle speed relative to fluid is a maximum for this eddy size, since turbulent velocity increases with eddy size (see Table 3.1).

By analogy with the molecular diffusion coefficient in kinetic theory, the turbulent diffusion coefficient is defined as the product of the mean free path and the speed, relative to the fluid, of the particle. The table of diffusion coefficients and other parameters[4] is reproduced here. As indicated in the table, there are four flow

* The symbol R is used for cloud radius in this section to distinguish it from particle radius, r.

regimes, which apply to particles of increasing size, reading from left to right. The mean speed of the particle relative to the fluid in the first, microscale regime is equivalent to that given by Levich[8].

In each of the other three regimes, the speed, q, is given by

$$q^3 \sim \frac{r\varepsilon\rho_p}{C_D\rho}$$

where drag coefficient C_D is a specified function of Reynolds number, $Re = \frac{2rq}{\nu}$. This equation for q was derived by Levich for the case C_D = constant, and derived in Ref. (4) without this restriction.

In these three regimes, the forms $C_D = 24/Re$ (Stokes' law), $C_D = 24\ Re^{-3/4}$ (empirical) and C_D = constant were used, respectively.

The relaxation time, τ, in each of the four regimes is given by $\tau \sim \frac{r\rho_p}{C_D q\rho}$ where Stokes' law is used for C_D in both of the first two regimes. Here ρ_p is particle density.

The mean free path is $q\tau$, which equals the minimum containing eddy size for all but the smallest particles. The turbulent diffusion coefficient is $q^2\tau$. For the smallest particles, contained by all eddies, the turbulent diffusion coefficient is less than the molecular diffusion coefficient, taken as nearly equal to kinematic viscosity.

Note that with increasing particle size, i.e., moving from left to right in Table 5.1, kinematic viscosity becomes ever less important, appearing to smaller absolute powers when the microscales λ_o, v_o, t_o (Table 3.1) are expressed in terms of ν and ε. Finally, in the extreme right column, ν does not appear at all, except in the Reynolds number. The expressions in this column, then, are pure inertial-range forms: they apply to interaction of particles with eddies so much larger than the microscale that the interaction parameters depend only

Table 5.1

Relative Velocity Parameters as a Function of Particle Size

TABLE RELATIVE VELOCITY PARAMETERS AS A FUNCTION OF PARTICLE SIZE

PARTICLE RADIUS, r	$r < \lambda_o\left(\frac{\rho_a}{\rho}\right)^{1/2} < r < \lambda_a\left(\frac{\rho_a}{\rho}\right)^{1/4} < r < \sim 20\lambda_o\left(\frac{\rho_a}{\rho}\right)^{1/4} < r$					
FLOW REGIME	STOKES' LAW		Stokes – Inertial	EMPIRICAL FORMS		CONSTANT DRAG COEFFICIENT
	Microscale					
MEAN RELATIVE SPEED, q	$v_o\left(\frac{r}{\lambda_o}\right)^2\frac{\rho}{\rho_a} < v_o = (\varepsilon\nu)^{1/4} < v_o\frac{r}{\lambda_o}\left(\frac{\rho}{\rho_a}\right)^{1/2} < v_o\left(\frac{\rho}{\rho_a}\right)^{1/4} < v_o\left(\frac{r}{\lambda_o}\right)^{2/3}\left(\frac{\rho}{\rho_a}\right)^{1/6} < \sim 3v_o\left(\frac{\rho}{\rho_a}\right)^{1/4} < v_o\left(\frac{r}{\lambda_o}\right)^{1/3}\left(\frac{\rho}{\rho_a}\right)^{1/3} = (\varepsilon r\frac{\rho}{\rho_a})^{1/3}$					
MINIMUM CONTAINING EDDY SIZE	$\lambda_o = \lambda_o = \left(\frac{\nu^3}{\varepsilon}\right)^{1/4} < \lambda_o\left(\frac{r}{\lambda_o}\right)^2\left(\frac{\rho}{\rho_a}\right)^{3/4} < \lambda_o\left(\frac{\rho}{\rho_a}\right)^{3/4} < \lambda_o\left(\frac{r}{\lambda_o}\right)^{2/3}\left(\frac{\rho}{\rho_a}\right)^{1/2} < \sim 25\lambda_o\left(\frac{\rho}{\rho_a}\right)^{3/4} < \lambda_o\left(\frac{r}{\lambda_o}\right)\frac{\rho}{\rho_a} = r\frac{\rho}{\rho_a}$					
RELAXATION TIME	$t_o\left(\frac{r}{\lambda_o}\right)^2\frac{\rho}{\rho_a} < t_o = \left(\frac{\nu}{\varepsilon}\right)^{1/2} < t_o\left(\frac{r}{\lambda_o}\right)^2\frac{\rho}{\rho_a} < t_o\left(\frac{\rho}{\rho_a}\right)^{1/2} < t_o\left(\frac{r}{\lambda_o}\right)^{4/3}\left(\frac{\rho}{\rho_a}\right)^{1/3} < \sim 10t_o\left(\frac{\rho}{\rho_a}\right)^{1/2} < t_o\left(\frac{r}{\lambda_o}\right)^{2/3}\left(\frac{\rho}{\rho_a}\right)^{2/3} = \left(\frac{r^2}{\varepsilon}\right)^{1/3}\left(\frac{\rho}{\rho_a}\right)^{2/3}$					
TURBULENT DIFFUSION COEFFICIENT	$\nu\left(\frac{r}{\lambda_o}\right)^4\left(\frac{\rho}{\rho_a}\right)^3 < v_o\lambda_o = \nu < \nu\left(\frac{r}{\lambda_o}\right)^4\left(\frac{\rho}{\rho_a}\right)^2 < \nu\frac{\rho}{\rho_a} < \nu\left(\frac{r}{\lambda_o}\right)^{4/3}\left(\frac{\rho}{\rho_a}\right)^{1/3} < \sim 100\nu\frac{\rho}{\rho_a} < \nu\left(\frac{r}{\lambda_o}\right)^{1/3}\left(\frac{\rho}{\rho_a}\right)^{1/3} = (\nu^2\varepsilon)^{1/3}\left(\frac{\rho}{\rho_a}\right)^{1/3}$					
REYNOLDS NUMBER, $Re \sim qr/\nu$	$\left(\frac{r}{\lambda_o}\right)^3\frac{\rho}{\rho_a} < \left(\frac{\rho_a}{\rho}\right)^{1/2} < \left(\frac{r}{\lambda_o}\right)^2\left(\frac{\rho}{\rho_a}\right)^{1/2} < 1 < \left(\frac{r}{\lambda_o}\right)^{1/3}\left(\frac{\rho}{\rho_a}\right)^{1/6} < \sim 200 < \left(\frac{r}{\lambda_o}\right)^{1/3}\left(\frac{\rho}{\rho_a}\right)^{1/3}$					

NOTES

- Numerical Constants Are Omitted Or Order-Of-Magnitude
- $C_D \sim Re^{-3/4}$ Is Used As A Representative Empirical Form
- $Re = 200$ Is Given As An Empirical, Approximate Bound
- ρ Is Particle Density, ρ_a Is Gas Density
- Parameter Value In Shaded Columns Correspond To Limits Of Each Particle Size Range
- Parameter Value Between Shaded Columns Are Functions Of Particle Radius In The Corresponding Size Range

on the dissipation rate, for a given value of the ratio of particle density to fluid density.

5.3 Turbulent-Diffusive Flux of Particles

The flux of particles through a unit area of cloud surface equals the diffusion coefficient times the concentration gradient (as for any transport process). The gradient has the units of concentration per unit length. This length is taken as proportional to the cloud radius (vertical radius when the cloud is an ellipsoid). This is the same characteristic length used in the cloud-model equations, Section 2.3. That is, the principle of Reynolds-number similarity, (Sec. 3.1) is again used here: since we are dealing with a turbulent process, the length is independent of fluid, (molecular) viscosity, or diffusivity. This principle may not apply to the smallest particles mentioned above, governed by molecular diffusion, but their diffusion rate, and falling rate, are extremely small.

The flux through a unit area of cloud surface, then, is

$$I_0 = k_4 D \frac{n}{\ell} \tag{5.3.1}$$

where n and D are the concentration and diffusion coefficient of particles of the given size, and k_4 is a dimensionless constant. The value of k_4 is not specified, but by analogy with the other turbulent transfer coefficients involving ℓ, in the cloud equations, Section 2.3, we estimate that

$$.10 \leq k_4 \leq .25.$$

The flux through the lower half of the cloud is then

$$\Phi_t = \frac{S}{2} k_4 D \frac{n}{\ell} \qquad (5.3.2)$$

where S is cloud surface area.

5.4 Gravitational vs Turbulent-Diffusive Dispersion of Particles

The total gravitational flux equals horizontal projected cloud area times particle concentration (assumed uniform in the cloud) times particle falling rate, p.

$$\Phi_g = \pi R^2 np \qquad (5.4.1)$$

For a spherical cloud, $S = 4\pi R^2$ and, substituting this in Equation (5.3.2)

$$\frac{\Phi_t}{\Phi_g} = k_4 \frac{2D}{Rp} \qquad (5.4.2)$$

so the larger the cloud, the less important particle dispersion due to turbulent particle diffusion becomes, relative to gravitational dispersion. The turbulent diffusion coefficient for a given particle size increases with turbulent energy dissipation rate, and, therefore, with yield and finally with radius, R, but such dependence does not significantly alter the relative importance of turbulent and gravitational dispersion established above.

5.4.1 Large Particles

Consider now particles of radius, r, so large that their drag coefficient, C_D, in gravitational fall is constant. Then

$$p = \frac{8}{3}\frac{rg}{C_D}\frac{\rho_p}{\rho}^{1/2} \qquad (5.4.3)$$

where ρ_p and ρ are particle and fluid density, and $(\rho_p-\rho)/\rho \sim \rho_p/\rho$. Such particles are so large that they are also in a constant drag coefficient regime with respect to intensely turbulent motion, (i.e., at high dissipation rates). Then (see Table 5.1) the particle Reynolds number is over 200 and

$$D = \varepsilon^{1/3} r^{4/3} \left(\frac{\rho_p}{\rho}\right)^{4/3} \qquad (5.4.4)$$

so that taking $\sqrt{1.5C_D}\sim 1$, (as is approximately valid for such Reynolds numbers) and substituting Equations (5.4.3) and (5.4.4) in Equation (5.4.2)

$$\frac{\Phi_t}{\Phi_g} \sim k_4 \left(r\frac{\rho_p}{\rho}\right)^{5/6} \frac{\varepsilon^{1/3}}{Rg^{1/2}} \qquad (5.4.5)$$

Figure 5.1 is a plot of the flux ratio, Equation (5.4.5), omitting the factor k_4 and using our 20 KT and 5 MT computations. In this plot, particle radius is taken as 1000 microns (a large fallout particle) and density as 2.2 gm/cm^3. The dashed lines are the result of multiplying the calculated flux ratio by the ratio of ambient to cloud density as if the concentration gradient were steeper by this factor. Some intuitive arguments to support the introduction of this factor were given in Ref. 1. It is seen that even with this factor the flux ratio is generally small and decreases with increasing yield. Its peak value would exceed unity for yields under 1 KT, but only for a very few seconds,

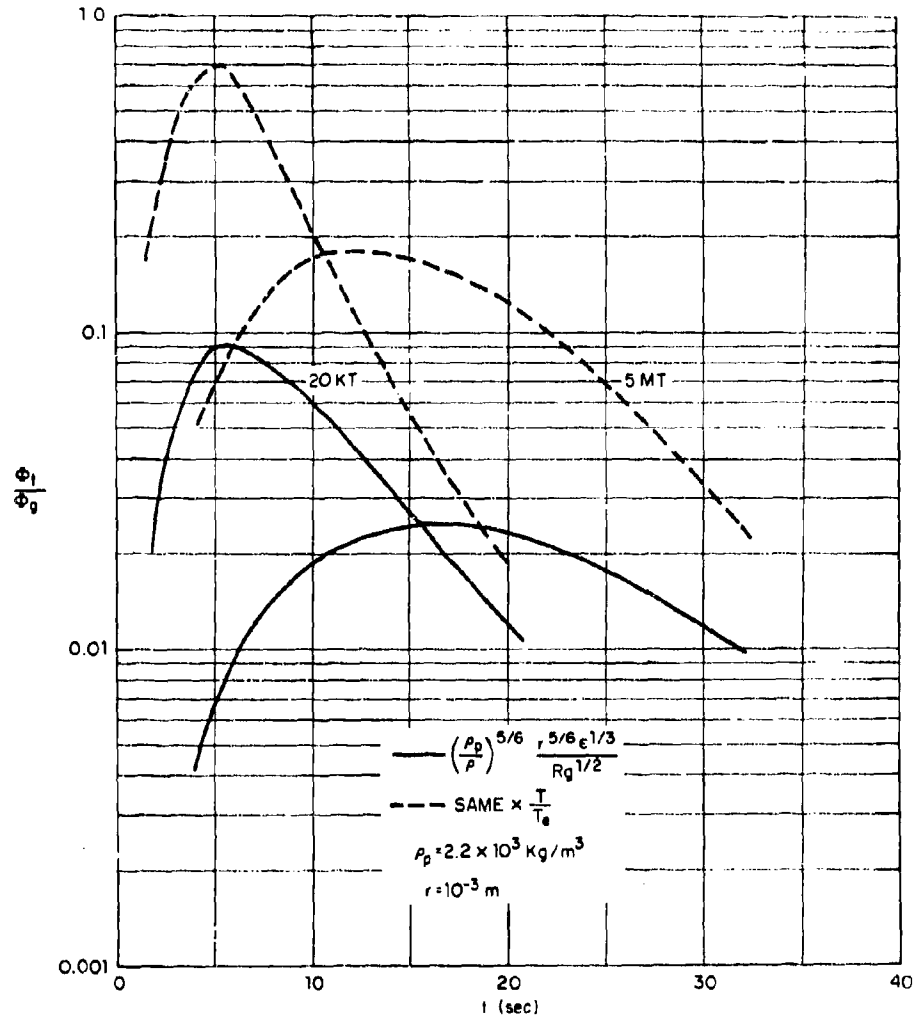

Fig. 5.1. Turbulent to Gravitational Flux Ratio Φ_t/Φ_g vs time t, for Large Particles

corresponding to the short duration of intense turbulence at such low yields.

Another instructive formulation of the flux ratio is as follows: For a spherical cloud, from Equation (2.3.9)

$$\varepsilon = k_3 \, (2E)^{3/2}/R$$

and early in cloud rise the velocity of turbulence, $\sqrt{2E}$, does not much exceed rate of rise, u, so that

$$\sqrt{2E} \sim u$$

and also $k_3^{1/3}$ is of order unity,

$$k_3^{1/3} \sim 1$$

Making these three substitutions in Equation (5.4.5),

$$\frac{\Phi_t}{\Phi_g} \sim k_4 \left(\frac{r}{R} \frac{\rho_p}{\rho} \right)^{5/6} \frac{u}{(gR)^{1/2}} \qquad (5.4.6)$$

But the Froude number of the cloud, or ratio of inertial to gravitational forces, is

$$Fr = u^2/gR$$

and these forces are nearly in balance during the "steady" rise of the cloud, i.e., Fr~1 as is roughly confirmed by the first page of Table 2.1.

Substituting $Fr = u^2/gR = 1$ in Equation (5.4.6)

$$\frac{\Phi_t}{\Phi_g} \sim k_4 \left(\frac{r}{R} \frac{\rho_p}{\rho} \right)^{5/6} \tag{5.4.7}$$

from which it is evident, since $k_4 < 1$ and $\rho_p/\rho \sim 10^4$, that an improbably large particle size, $r > 10^{-4}R$, is required for turbulent dispersion to be dominant.

5.4.2 Small Particles

The largest particles to whose motion Stokes' law can be applied are of radius $r \sim \lambda_o (\rho/\rho_p)^{1/4}$. These particles are at the upper limit of the "Stokes-inertial" size range.

Using the same 5 MT computation, the viscosity of air, μ, and the definition of kinematic viscosity, $\nu = \mu/\rho$, the microscale $\lambda_o = (\nu^3/\varepsilon)^{1/4}$ is of order 300 microns, and the limiting size $r \sim \lambda_o (\rho/\rho_p)^{1/4}$ is about 30 microns. The diffusion coefficient at this upper limit is

$$D = \nu \frac{\rho_p}{\rho} \tag{5.4.8}$$

while the falling rate for such particles is given by Stokes' law,

$$p = \frac{2}{9} \frac{r^2 g}{\nu} \frac{\rho_p}{\rho} \tag{5.4.9}$$

where again $(\rho_p - \rho)/\rho \sim \rho_p/\rho$. Then the flux ratio, substituting $r \sim \lambda_o (\rho/\rho_p)^{1/4}$, and Equations (5.4.8) and (5.4.9) in Equation (5.4.2) is

$$\frac{\Phi_t}{\Phi_g} \sim 9k_4 \frac{\nu^2}{Rg\lambda_o^2} \left(\frac{\rho}{\rho_p}\right)^{1/2} \tag{5.4.10}$$

Now we use the fact that (Sec. 3.1.5) $\lambda_o \sim \ell Re^{-3/4}$ and for the large-scale length, ℓ, take cloud radius, R. Using also the definition of Reynolds number $Re \sim uR/\nu$, Equation (5.4.10) becomes

$$\frac{\Phi_t}{\Phi_g} \sim 9k_4 \frac{u^2}{RgRe^{1/2}} \left(\frac{\rho}{\rho_p}\right)^{1/2} \tag{5.4.11}$$

As in Sec. (5.4.1), we substitute the value of the Froude number, $u^2/gR = Fr \sim 1$ in Equation (5.4.11) giving for the ratio of turbulent-diffusive to gravitational flux of small particles,

$$\frac{\Phi_t}{\Phi_g} \sim 9 \frac{k_4}{Re^{1/2}} \left(\frac{\rho}{\rho_p}\right)^{1/2} \tag{5.4.12}$$

Now even for a low yield cloud (say 20 KT) $Re \sim 10^7$, while $(\rho_p/\rho) \sim 10^4$, so that $\Phi_t/\Phi_g \sim 10^{-3/2}$, i.e., this ratio is small. To be sure, for these small particles gravitational dispersion is itself quite slow.

6. SUMMARY

A revised version of the TR-741 cloud model has been presented which takes into account the decay of turbulent energy to heat. The rate of this decay per unit mass, the turbulent energy dissipation rate, is the governing parameter for small scale turbulent motions. The model is shown to imply an atomic cloud energy cycle.

If toroidal circulation in the atomic cloud is to be represented by a classical vortex ring flow superimposed on the parcel-model cloud, then the vortex parameters, in particular the circulation, may be estimated from the cloud model by taking vortex rotational energy as a given fraction of the turbulent energy, consistent with conservation of energy and with turbulence theory. Alternately, cloud circulation as a function of time may be calculated directly from the model by adapting Kelvin's theorem. This approach is more consistent with atomic cloud conditions since it does not require any assumed steady-state vortex form.

Finally, it is proposed that the centrifugal throwout of particles by the vortex flow be represented by a turbulent-diffusive dispersion. For both large and small particles, the rate of this turbulent-diffusive dispersion is shown to be small compared with the rate of gravitational fallout.

LIST OF SYMBOLS

a	horizontal semi-axis of cloud, or acceleration, or vortex cross-section radius
b	vertical semi-axis of cloud
C_D	drag coefficient
c_p	specific heat of gas at constant pressure
D	turbulent diffusion coefficient
E	turbulent kinetic energy per unit mass
$\mathcal{E}(k)$	turbulent kinetic energy per unit mass per unit wave number
Fr	Froude number
g	acceleration of gravity
H	enthalpy
I_o	turbulent-diffusive particle flux density
I	horizontal projection of I_o
k_2	empirical constant (in eddy viscosity)
k_3	empirical constant (in dissipation rate)
k_4	empirical constant in turbulent diffusion
k	wave number $1/\lambda$
ℓ	characteristic large-scale length
m	mass of cloud
n	concentration of particles of a given size
p	pressure, or particle falling rate

R	cloud radius
Re	Reynolds number
r	radius of cloud, or particle radius
S	surface area of cloud
s	curvilinear coordinate
T	temperature, or vortex energy
t	time
u	vertical velocity, or large-scale velocity
V	volume of cloud
v	characteristic velocity, $v = \max(\lvert u \rvert, \sqrt{2E})$; or turbulent velocity
W	total explosion energy (kilotons)
y	length coordinate
z	vertical coordinate
Γ	circulation
ϵ	energy dissipation rate per unit mass
κ	vortex circulation
λ	empirical constant (in entrainment rate) or eddy size
μ	viscosity
ν	kinematic viscosity (μ/ρ_a)
ρ	density
τ	relaxation time of accelerated particle, or local transfer time of turbulent energy

$\bar{\omega}_o$ radial coordinate of vortex ring

Φ total particle flux

SUBSCRIPTS

a air (dry air)

e ambient (environment) conditions

g gravitational

o Kolmogorov microscale values; or initial values

p particle, or constant pressure

t turbulent

λ values for eddies of size λ

REFERENCES

(all unclassified)

1. Huebsch, I. O., Development of a Water-Surface-Burst Fallout Model: The Rise and Expansion of the Atomic Cloud, USNRDL-TR-741, 23 Apr 64, (AD-441 983).

2. Huebsch, I. O., Turbulence, Toroidal Circulation and Dispersion of Fallout Particles from the Rising Atomic Cloud, USNRDL technical report to be published.

3. Batchelor, G. K., The Theory of Homogeneous Turbulence, Cambridge U. Press, 1953.

4. Huebsch, I. O., Relative Motion and Coagulation of Particles in a Turbulent Gas, USNRDL technical report to be published.

5. Townsend, A. A., The Structure of Turbulent Shear Flow, Cambridge U. Press, 1956.

6. Hinze, J. O., Turbulence, New York, McGraw-Hill, 1959.

7. Rhyne, R. H. and Steiner, R., Power Spectral Measurement of Atmospheric Turbulence in Severe Storms and Cumulus Clouds, NASA-TN-D-2469, Oct 1964.

8. Levich, V. G., Physico-chemical Hydrodynamics, Prentice-Hall, Inc., 1962.

9. Corrsin, S., "Outline of Some Topics in Homogeneous Turbulent Flow", J. Geophys. Res., 64, 2134, 1959.

10. Lamb, H., Hydrodynamics, 6th Edition, Cambridge U. Press, 1932.

11. Levine, Joseph, "Spherical Vortex Theory of Bubble-like Motion in Cumulus Clouds", J. Meteor., 16, 653-662, 1959.

12. Norment, H. G., Research on Circulation in Nuclear Clouds, Technical Operations Research, TO-B 63-102, December 1963.

13. Turner, J. S., "Buoyant Vortex Rings", Proc. Roy. Soc., A, 239, 61, 1957.

14. Norment, H. G., Research on Circulation in Nuclear Clouds, II, Summary of Final Report, Technical Operations Research, TO-B 64-102A, 1 Nov 1964, (AD-464 482).

15. Serrin, J., "Mathematical Principles of Classical Fluid Mechanics" in S. Fluegge, ed., Encyclopedia of Physics, vol. VIII/I, Berlin, Springer-Verlag, 1959.

SESSION THREE

TRANSPORT AND DEPOSITION

COMPARISON OF NUCLEAR FALLOUT MODELS*

M. Polan
Ford Instrument Company
Long Island City, N.Y.

ABSTRACT

The fallout prediction models presented at the 1962 USNRDL-DASA Fallout Symposium will be discussed. They include those developed or used by the following agencies: RAND Corp. (simplified version), Weapon Systems Evaluation Group, Defense Intelligence Agency, National Resource Evaluation Center (Dusty III), NRDL (D and Miller-Anderson), Ford Instrument Co. (T), Technical Operations Research, University of California Civil Defense Research Project and Lawrence Radiation Laboratory (Dr. Knox's and Dr. Shelton's), U.S. Army, U.S. Navy (RADFO), U.S. Weather Bureau, Sandia Corp. (Dropsy), AN/GMQ-18, AN/GMQ-21, and U.S. Army Signal Corps, most of which are currently considered valid.

The models simulate the transport and deposition of fallout in one or the other of two ways:

1. A single effective fallout wind (EFW) is used to simulate the horizontal wind field, and the size and shape of the fallout contours are a function (explicit or implicit) of this EFW and the yield.

2. A multilayer wind field is used, the nuclear cloud is partitioned (by horizontal slicing and by grouping of particle sizes) into small elements (wafers), and the trajectory of each wafer is computed.

The EFW models are found to be suitable for use when computing-speed requirements outweigh the accuracy requirements (multiburst operations analysis and military field operations). The wafer models are found to be suitable when the requirements are reversed (in scientific, engineering, and military studies, including predicting fallout at nuclear test sites).

*Based on work performed for USNRDL under contract No. N228(62479)62185, Bureau of Ships Subproject SF 011 05 12, Task 0506.

The following model characteristics will be compared: the effects of initial burst conditions, the dimensions of the nuclear cloud at the start of transport, the distribution of radioactivity within the cloud, the activity-particle-size distributions, and the dose rate normalization factor. Fallout contours from various models will be compared and the variations discussed.

INTRODUCTION

I would like to acknowledge the assistance given us by some thirty people who have helped clarify our concepts of the models, who have provided us with valuable information not available in the published literature, and who have reviewed our analyses of their models. Rather than take the time to read such a list, I refer you to the report, where they are all listed, and extend a general and grateful "thank you" to all who are now present.

We will discuss a classification scheme for the nuclear fallout models, presented at the 1962 USNRDL-DASA Fallout Symposium, and we will compare some of their major characteristics. A detailed analysis of the fallout models will be available in a USNRDL-TRC publication currently being reviewed. Then, from an analysis of the homework predictions in progress, we will sample some features of the predicted patterns that should be of interest to both the developers of fallout models and the users of fallout predictions.

CLASSIFICATION OF THE MODELS

There are two classifications of fallout models, based on the methods used for calculating the transport and deposition of fallout. All models in one class use a single effective fallout wind (EFW) to simulate the horizontal wind field; all models in the other class use a multilayer wind field.

The EFW's are constant with altitude, and with one exception, are constant with time and downwind distance (DWD). However, there are enormous variations among the EFW's derived from a single wind sounding for the several models.

Most of the EFW models contain a submodel of some sort to predict the nuclear cloud. The shapes and dimensions of the predicted clouds vary considerably from model to model, as do also the spatial and particle-size distributions of activity within the clouds. The clouds in the EFW models are not partitioned into discrete elements; that is, the clouds are not sliced by horizontal planes nor are the particle size ranges divided into groups.

The shapes, sizes, and relative locations of fallout contours predicted by EFW models are very dependent on the physical assumptions and calculational techniques used in each particular model. In fact, the shapes of the contours are so dependent on these factors that it is frequently easy to identify the model used by examining the shape of a predicted fallout pattern.

SLIDE 1

The EFW models in the upper group have been programmed for digital computers. (The WSEG model is sometimes referred to as the Pugh-Galiano model; the DIA model was formerly called the AFIC model.) These models are suitable for large-scale nuclear attack problems; that is, for predicting fallout from large numbers of bursts distributed over large areas. Manual prediction techniques (slide rules, tables, graphs, nomographs) developed for these models represent their less important applications. The two models in the lower group are designed for manual solution under military field conditions, including ships at sea.

Only in the EFW models is there explicit consideration of crosswind shear. The exact definition of crosswind shear and the altitude layer for which it is calculated vary from model to model. However, the following may be considered a general definition of crosswind shear for the computer programmed EFW models. It is the change in speed of the wind components perpendicular to the EFW with altitude, in some cloud layer.

The RAND model contours are based on a zero crosswind shear. The WSEG and NREC (National Resource Evaluation Center) models accept the crosswind shear as an input, but NREC always uses one of four values that are dependent upon weapon yield and time of year. A typical crosswind shear was assumed in the development of the DIA model; it cannot be varied from prediction to prediction.

The equivalent general definition of crosswind shear for the lower group of models can be considered to be the angle subtended by a wind hodograph drawn for the winds between two significant cloud levels. In the Army model the contours occupy a downwind sector equal to this angle, using 40° as the minimum for the angle. In the RADFO model, this angle is used primarily to select the proper shape for the fallout contour.

The hotlines in the RAND, WSEG, DIA, and Army models are always straight lines, and the contours are always linearly symmetrical about the hotline. The NREC model produces a hotline that curves to reflect changes in the 500-mb wind with time and with location on the earth's surface, as well as the effects of the curvature of the earth. What is essentially the WSEG model is then applied to the curved hotline, with downwind distance measured along the hotline and crosswind distance perpendicular to it.

The RADFO model is the only EFW model that can produce contours that are not symmetric about some axis.

SLIDE 2

In all fallout models in the other class, the clouds are sliced by horizontal planes, and the slices are partitioned by particle-size grouping into wafers, which are also called discs and fallout increments. The wafer models are intended for use with multilayer wind fields rather than single EFW's. Inherently (at the cost of

increased computation time) they can predict more accurately and realistically shaped contours than can the EFW models.

The wafer models fall into three groups. First, there are those that are systematized as computer programs. The LRL-b model, presented by Dr. Knox in 1962, contains a barotropic atmospheric submodel for predicting the winds during fallout. The Civil Defense Research Project (CDRP) model is a special transport submodel that uses wind statistics representing several years of local wind records to estimate and reduce the error in the predicted landing point of each wafer. This transport submodel can be used with almost any cloud submodel.

The second group comprises the wafer models that are manually solved. The Technical Operations Research (TOR) model was developed for general or operations analysis studies, and the Signal Corps model was developed for military field use. However, manual predictions with wafer models are too time consuming for these applications, and EFW models are now used.

The LRL-h model (which was to have been presented by the late Dr. Shelton in 1962) and the U.S. Weather Bureau (USWB) model both use what we call fallout hodographs to simulate the transport of fallout. These are wind hodographs with lines drawn from ground zero through the wind vectors at the heights of the centers of the cloud slices. Each radial line is the locus of wafer centers from a particular cloud slice.

The third group consists of the wafer models that are the bases of special-purpose electronic computers. Dropsy is an analog computer used by Sandia Corporation to simulate transport of fallout. It requires inputs calculated from some cloud submodel. The model that was used in this computer has been programmed for a digital computer subsequent to the 1962 symposium.

The AN/GMQ-18 analog computer has been used during the past decade to study the effects of meterological parameters on fallout. The AN/GMQ-21 is a special-purpose digital computer design based on the Ford-T fallout model. It has never been built. It appears that the rapid growth in general-purpose digital computer technology has reduced the importance of special-purpose computers.

SLIDE 3

The models shown here contain a height-of-burst adjustment (HOBA) for elevated bursts; no adjustment of this sort is made in any of the other models. The HOBA enters into dose-rate calculations in the same manner as does the fission-to-total-yield fraction (F). That is, the dose-rate value for a surface burst is directly proportional to the product of the yield, the fission fraction, and the normalization factor (W·F·NF). For an elevated burst, the dose-rate value is directly proportional to the product: W·F·NF·HOBA.

Let us note some of the more obvious intermodel differences in the HOBA. In the Ford-T, NREC, and Signal Corps models, the HOBA is based on the ratio of the height of burst to the radius of the fireball (HOB/R), where the various expressions for R are as shown on the slide. This approach was also used in the USWB model until 1955, so it is shown here only for background. In the LRL-h model, the HOBA is based on the ratio of the depth of burst to the depth of the apparent crater (DOB/DAC). Graphs showing this ratio for various types of soil are available in LRL publications.

The 0.4 and 1/3 exponents of yield cause a 50% difference in fireball radius for a 1-MT yield. The difference decreases with lower yields and increases with higher yields. For HOB/R = 0.5 as computed by the several models, the resulting HOBA's range from 0.2 to 0.85.

With the next four slides we will compare the heights used for the top and the bottom of the cloud cap by the various models, for land-surface bursts at mean sea level.

SLIDES 4 and 5

This and the next slide (5) show the heights used for the top of the cloud cap as determined by the various models. That shown for the NRDL-D model is the cap-top height at the cessation of cloud rise. We see that for a 10-MT yield, the cap-top heights vary between approximately 64 and 115 kilofeet. For a 10-KT yield, the heights vary between 21 and 33 kilofeet.

SLIDES 6 and 7

This and the next slide (7) show the heights used for the bottom of the cloud cap. (The bottom of the whole cloud is used for clouds that have no stems.) These heights vary between 36 and 74 kilofeet for a 10-MT yield, and between 10 and 21 kilofeet for a 10-KT yield. Thus for both yields, a range of heights of approximately 2 to 1 is shown for the cap heights.

These intermodel variations in the height of the cloud cap must inevitably cause variations in the predicted fallout patterns. They indicate, too, that the applicable wind levels vary from model to model. It is possible that the variations in other model characteristics, such as particle-size distributions, settling-rate equations, and the like, exist in part to compensate for the variations in cap heights.

SLIDE 8

This and the next two slides (9,10) show the activity particle-size distributions used in the cloud submodels. In general, the higher the curve lies on the graph, the larger the mean logarithm of the particle diameter. The slope of the curve indicates the kurtosis of the distribution, with the smaller slopes or more horizontal curves representing the more peaked distributions. In the wafer models these distributions may be divided into as few as 3 or as many as 200 particle-size groups.

Activity-particle-size distributions used for the cloud caps are shown on this slide. The USWB(J-S) distribution has been made available since the 1962 Symposium. It was developed from Johnie Boy-Small Boy test data. The RAND model uses two distributions: the one shown represents 95% of the total cloud activity and is spread uniformly throughout the whole cloud. The NRDL-D distribution is used for the whole cloud; it is shown here for comparison.

SLIDE 9

This slide shows distributions used for the cloud stems. The RAND distribution shown here represents the remaining 5% of total cloud activity and is spread uniformly throughout the lower 1/5 of the cloud. The activity in this distribution is generally associated with particles larger than those used in the stems of the other models. This may be considered to compensate for the fact that the cloud has no stem, and thus there is no activity between the bottom of the cloud cap and the ground. The stem distributions shown for the other models all lie between the bottom of the cloud cap and the ground-zero surface. All stem distributions are associated with particles larger than those used in the cap distributions.

SLIDE 10

This slide shows activity-particle-size distributions used by the models that use only a single distribution for the whole cloud. Notice particularly the NRDL-D model coral and Nevada soil distributions. These two distributions were used in the only homework problem reply for two cases that differed only in the type of soil.

The Nevada soil distribution has a smaller mean but a larger standard deviation than the coral distribution. Note that in the distribution with the smaller mean, 14% of the activity is associated with particles greater than 700 microns in diameter, while in the

distribution with the larger mean only 7% of the activity is associated with the same very large particles. The effects of these two distributions will be shown shortly.

SLIDE 11

The vertical distributions of activity for a 20-KT land-surface burst at mean sea level are shown on this slide. Although the geometry of the LRL-h cloud is a right circular cylinder centered above ground zero, the activity is distributed in a typical mushroom shape. The Ford-T model shows that about 8% of the stem activity is locked onto the ground-zero site. For this yield, some of the wafers in the NRDL-D model have landed by the time the cloud has ceased to rise.

SLIDE 12

This slide shows the vertical distributions of activity for a 20-MT burst. Note that the greater part of the activity in the RAND and WSEG clouds is lower than it is in most of the other clouds. For a 20-MT burst, the lowest wafers in the NRDL-D cloud are still some 30 kilofeet above mean sea level at the time the cloud ceases to rise.

The activity is assumed to be constant along the wafer diameters in all wafer models except the Dropsy, in which the activity has a Gaussian distribution along the wafer diameters.

SLIDE 13

The normalization factors used in the various models are shown here. Models for which a numerical value is listed under Realistic Flat Terrain predict dose rates for 3-foot height above realistic flat terrain. The other models predict dose rates for a 3-foot height above an ideally smooth infinite plane.

RAND used a normalization factor (NF) of 1200 for the homework problems. The values of the shielding factors used in the DIA model

are still classified. For flat terrain, a value of (*) would be used, resulting in NF = (*) for realistic flat terrain.

Within each model, a predicted dose rate is directly proportional to the NF. However, the dose-rate levels predicted by the various models for the same conditions frequently do not show correspondence with the NF's used in the models.

SYMPOSIUM HOMEWORK PROBLEMS

SLIDE 14

The effective fallout winds used in the EFW model predictions are listed here. Dashes in the listing represent cases in which the yields were outside the yield range of the particular model. The conventional direction for winds is the direction from which the wind is blowing, measured clockwise from north. We derived the EFW's for the RADFO model by using the procedures given in ATP-25.

In Case I, the winds used as inputs to the EFW models varied in direction by nearly 90 degrees and in speed by a factor of approximately 5. The large variations in the EFW's have caused intermodel variations in the predicted contours that cannot be explained solely in terms of the contents of the models themselves.

The variations in the direction of the predicted contours are directly related to the variations in the directions of the EFW's. In some cases, the predominant effect of using a higher rather than a lower value for EFW speed is an increase in the size of all contours. In other cases, higher values of EFW speed cause a relative decrease in the size of contours for high dose-rate values and relative increase in the size of contours for low dose-rate values.

(*) Values omitted for security reasons.

SLIDE 15

This slide shows the dose rate normalized to H+1 hours (DR) as a function of downwind distance (DWD) for a 15-MT yield. The predicted contours with the highest DR values were obtained with the Signal Corps model, which used the lowest reported normalization factor (NF = 689). In the two NRDL predictions, the Nevada soil distribution yielded higher DR values close to ground zero and lower values at moderate distances from ground zero, than did the coral distribution. This was to be expected when one considers the combined effects of the means and standard deviations of these two distributions. At DWD's greater than 200 miles, both distributions produced essentially the same dose rates.

Little can be said about the AN/GMQ-18 analog computer predictions because we have been unable to obtain details concerning the cloud submodel it contains.

SLIDE 16

This slide shows infinite dose for a 1-MT yield as a function of DWD and the area enclosed by the contours. Surprisingly, it shows that the Ford-T model contours based on an NF = 900 enclose much larger areas than do the LRL-h model contours based on an NF = 2700. I suspect that the Army point agrees well with the other (wafer model) contours because the winds in this case contained large directional variations. I also suspect that this agreement may not occur in cases where the wind is more uniformly directed.

SLIDE 17

The dose-rate-contour-area characteristics for a 20-ton yield in vertically uniform 10-knot and 40-knot wind fields are compared here. The DIA 40-knot plot is slightly less steep than the 10-knot

plot, and all the DIA contour for the higher wind enclose larger areas than they do for the lower wind. The NRDL-D model produces higher dose rates close-in for the 10-knot wind than it does for the 40-knot wind, but there is only a slight decrease in contour-enclosed areas further downwind. The Ford-T model contour shows the effect of no cap wafers having landed within this DWD range.

SLIDE 18

This and the next slide (19) shows identical parameters for a 10-MT burst in a 10-knot and a 40-knot uniform wind field, respectively. This slide shows that the RAND and NRDL-D plots for the 10-knot wind field are very similar. The two models also coincide over parts of their range in the plots for the 40-knot wind field.

SLIDE 19

There is a tendency for the high dose-rate levels close to ground zero (within approximately 300 miles) for the 10-knot wind field to be completely missing in the plots for the 40-knot wind. There is also a tendency for areas within very low dose-rate contours to increase significantly in the case of the 40-knot wind. For example, the 5-roentgen/hour NRDL-D and DIA dose-rate contours for the 10-knot wind enclose areas of approximately 17,000 and 29,000 square miles, respectively. For the 40-knot wind, the areas are approximately 66,000 and 88,000 square miles for the same dose-rate level.

The homework predictions indicate that there are at least two additional problem areas yet to be tackled. The first is to define the upper limit of fallout. Some models always consider the activity locked in the crater to be the hottest point in the fallout field, and then show decreasing activity with downwind distance. Other models consider the only activity in the cloud to be fallout, and thus, as in the WSEG model, always predict the highest dose rates downwind of

ground zero. Still other models more or less leave inclusion of ground zero in the upwind ends of the contours to the judgment of the model user.

The second problem area is the errors introduced into the fallout predictions by the calculational techniques used. One example is the determination of the minimum number of wafers necessary to prevent severe distortion of contours. Homework predictions produced by the CDRP model show circles drawn around individual wafers. Plots from other models show several isolated contours for the same normalized-dose-rate value. Judging by our own experience in running fallout predictions with various numbers of wafers, these contour separations are due to misinterpretations resulting from the use of insufficient numbers of wafers. Even with the NRDL-D and Ford-T models, both of which use thousands of wafers, it is sometimes difficult to judge the locations of the contours. In some cases, changing the map scale for the predicted pattern produces a 2 to 1 change in the area enclosed by some contours.

EFW MODELS

1. Computer Programmed

   RAND, WSEG, NREC, DIA } multiburst operations analysis

2. Manual

   ARMY, RADFO } simple field predictions

Fig. 1. EFW Models

WAFER MODELS

1. Computer Programmed

   NRDL-D
   Ford-T
   LRL-b
   Miller-Anderson
   CDRP

2. Manual

   TOR
   Signal Corps

   LRL-h
   USWB

3. Electronic Systems

   Dropsy
   AN/GMQ - 18
   AN/GMQ - 21

Fig. 2. Wafer Models

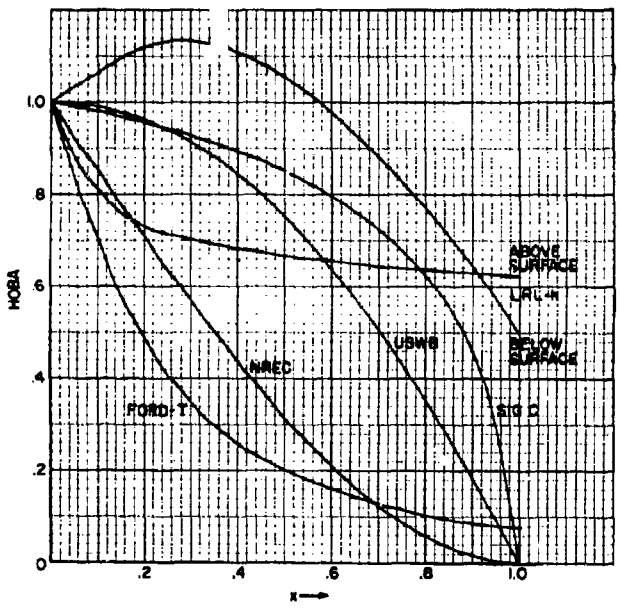

$x = HOB/R \begin{cases} R = 180\,W^{0.4}, \text{ NREC} \\ R = 180\,Wp^{1/3}, \text{ FORD-T} \\ R = 184\,W^{1/3}, \text{ USWB (pre-1955), SIG C} \end{cases}$

x = DOB/DAC FOR LRL-h

Fig. 3. Height-of-Burst Adjustments

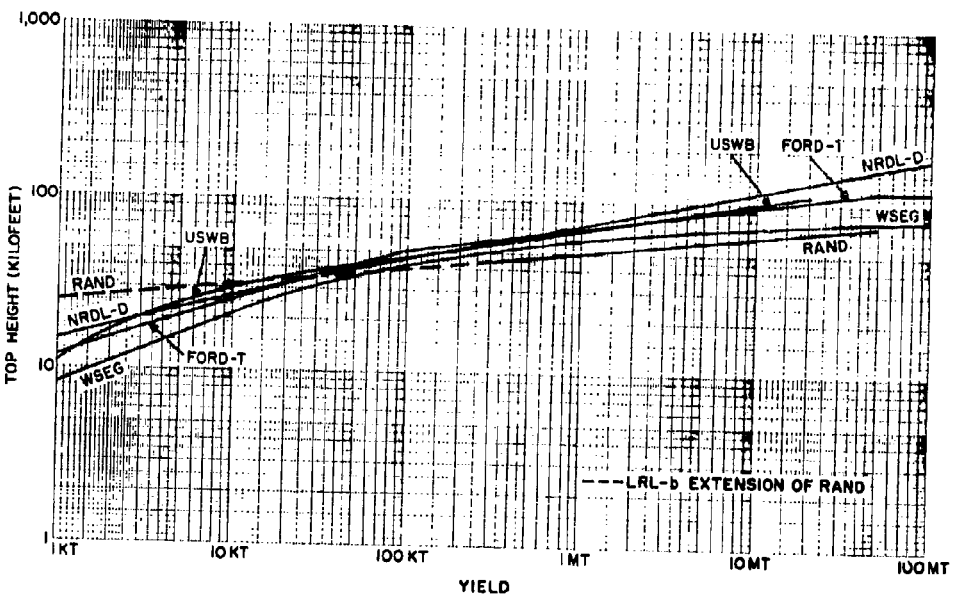

Fig. 4. Cap Top Heights

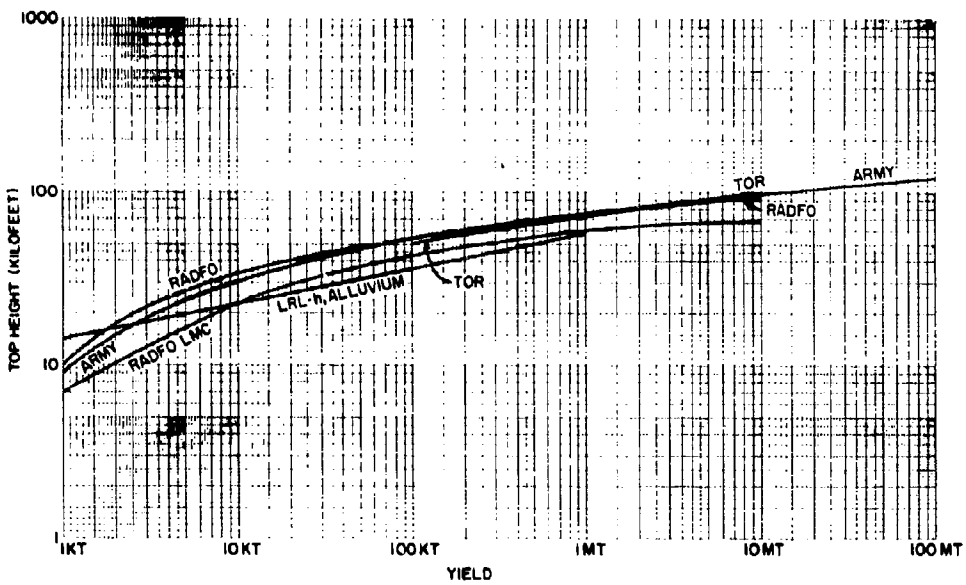

Fig. 5. Cap Top Heights
(2)

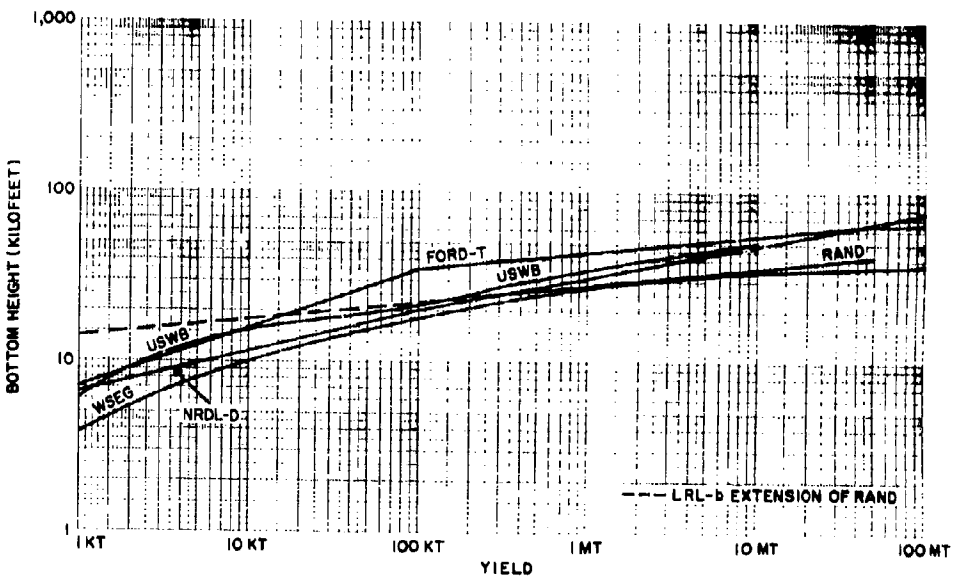

Fig. 6. Cap Bottom Heights

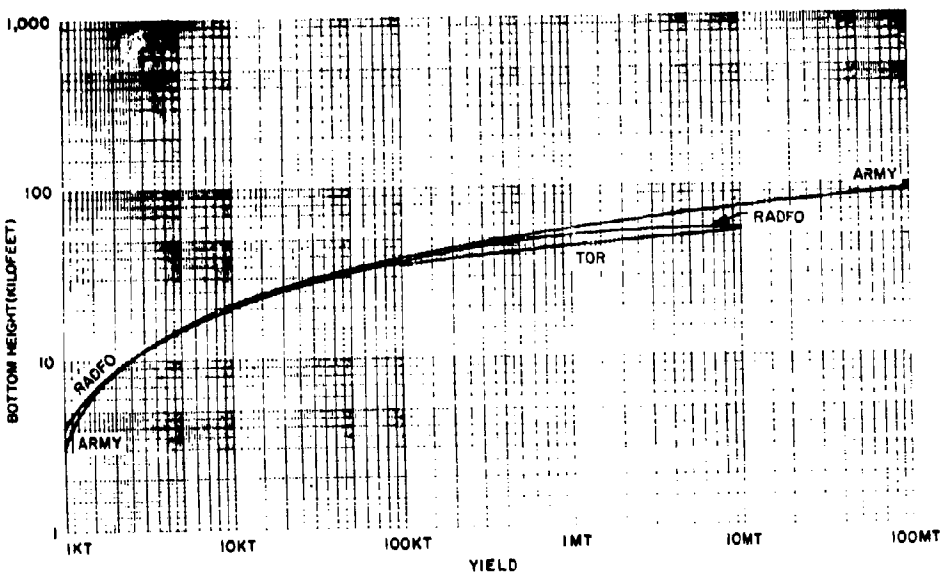

Fig. 7. Cap Bottom Heights
(2)

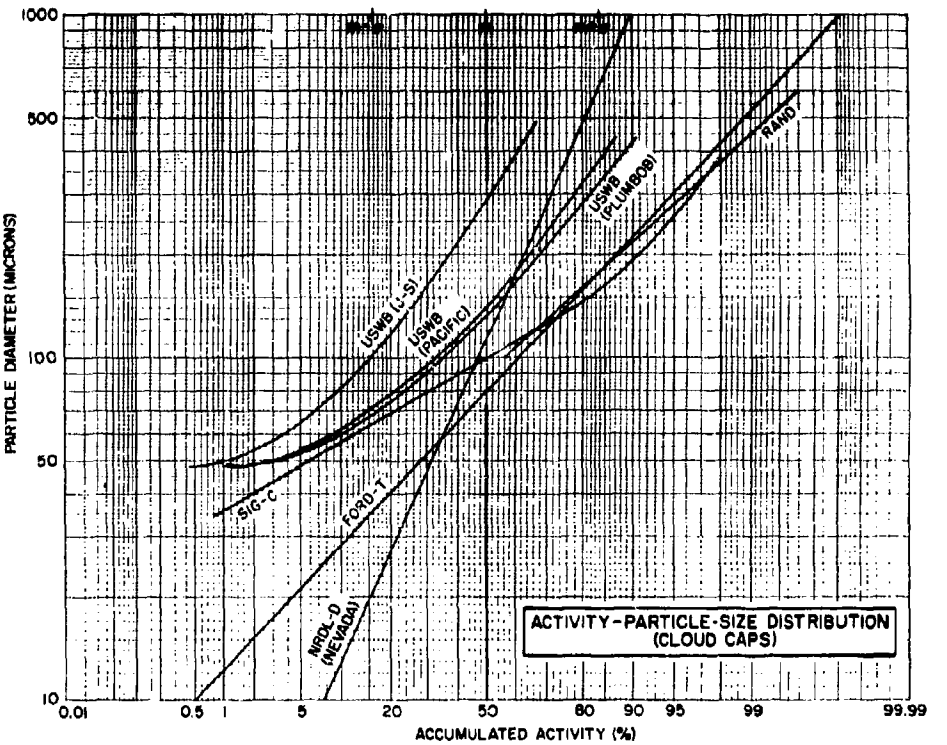

Fig. 8. Activity-Particle-Size Distribution (Cloud Caps)

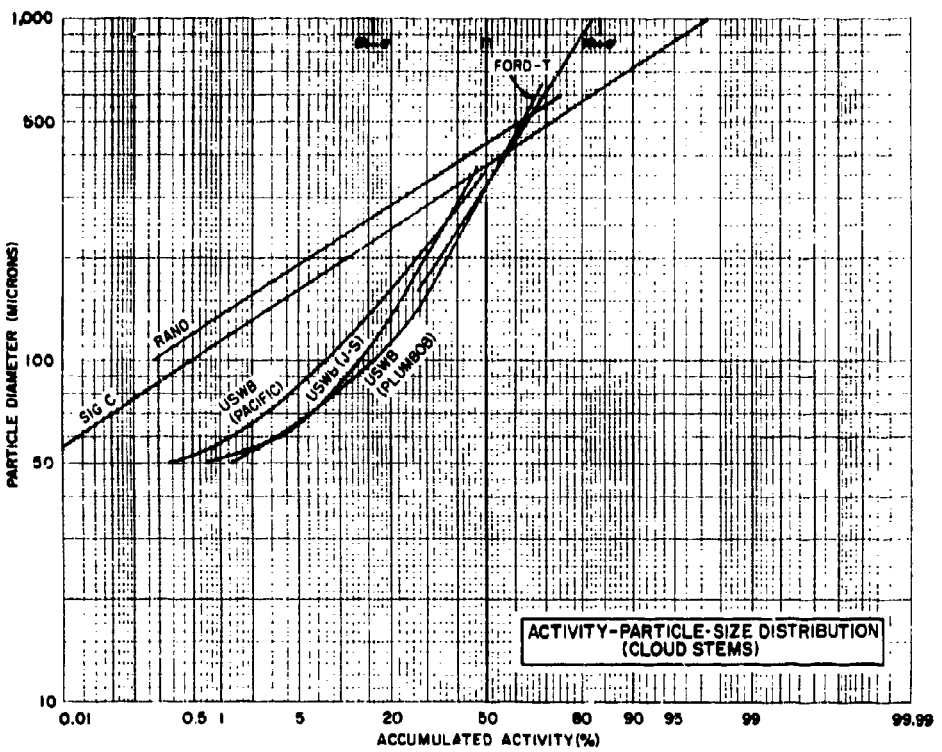

Fig. 9. Activity-Particle-Size Distribution (Cloud Stems)

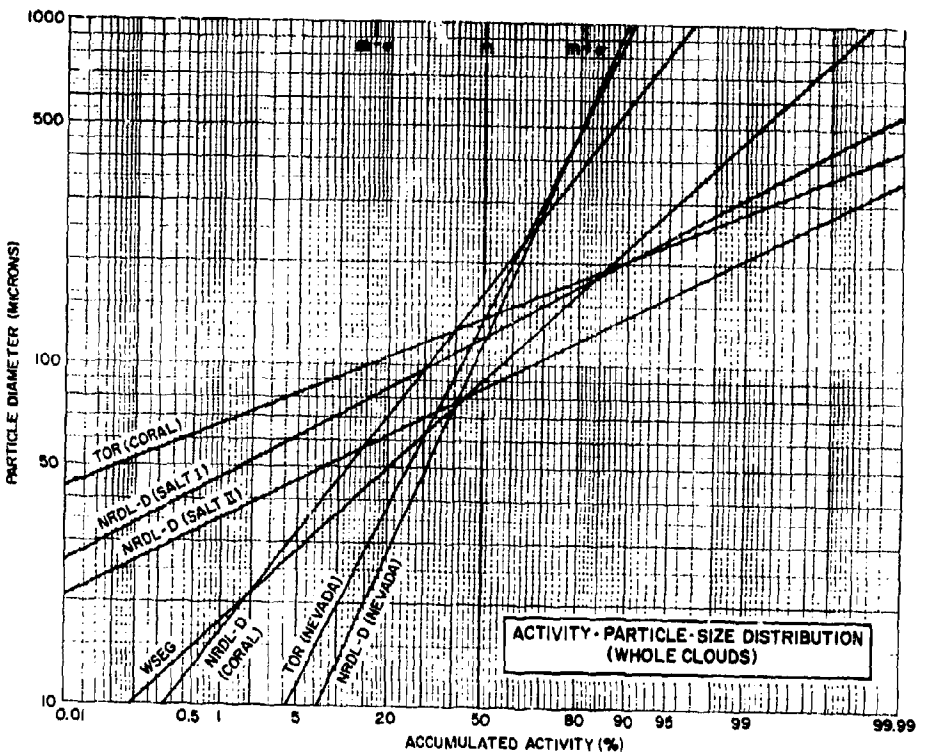

Fig. 10. Activity-Particle-Size Distribution (Whole Clouds)

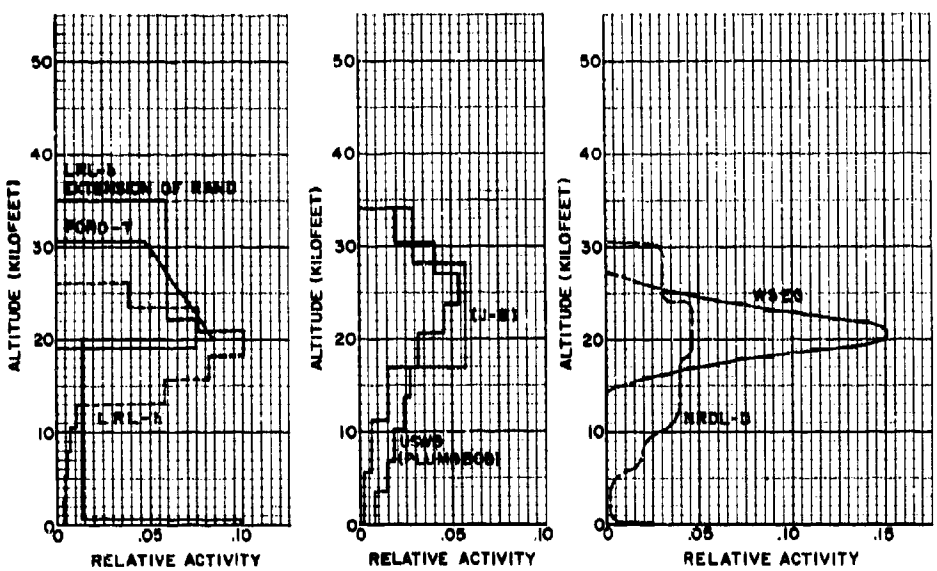

Fig. 11. Vertical Distribution of Activity for a Land-Surface Blast at MSL (20-KT Yield)

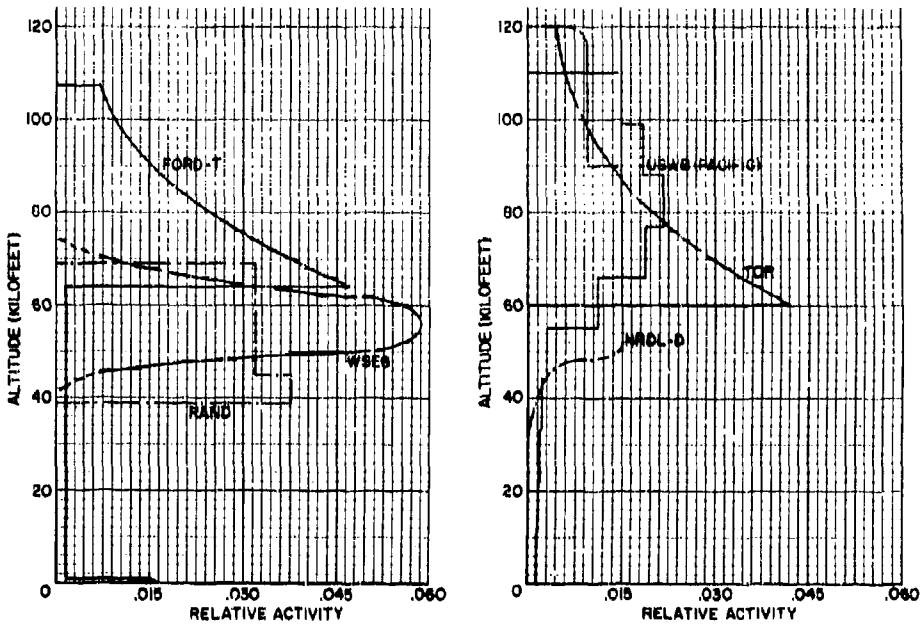

Fig. 12. Vertical Distribution of Activity for a Land-Surface Blast at MSL (20-MT Yield)

NORMALIZATION FACTORS

Model	NF (r /hr per KT/sq.st.mile)	
	Ideal Plane	Realistic Flat Terrain
RAND	1200-2660	----
WSEG	2400	----
NREC, CDRP	2500	----
TOR	1580	870
Ford-T	1200	900
NRDL-D	1682	1093
LRL-h,LRL-b	3380	2700
Signal Corps.	984	689
USWB	1500	1050
Dropsy	2585	----
DIA	1100	**

Fig. 13. Normalization Factors

EFFECTIVE FALLOUT WINDS

(Speed in knots/Conventional direction in degrees)

Model	Case I	Case III	Case V
RAND	7/343	---	25/294
WSEG	21/257	16/189	11/342
DIA	4.1/258	22/197	22/292
RADFO*	---	21.5/192	15/299
ARMY	19/273	15/185	17/325

Fig. 14. Effective Fallout Winds

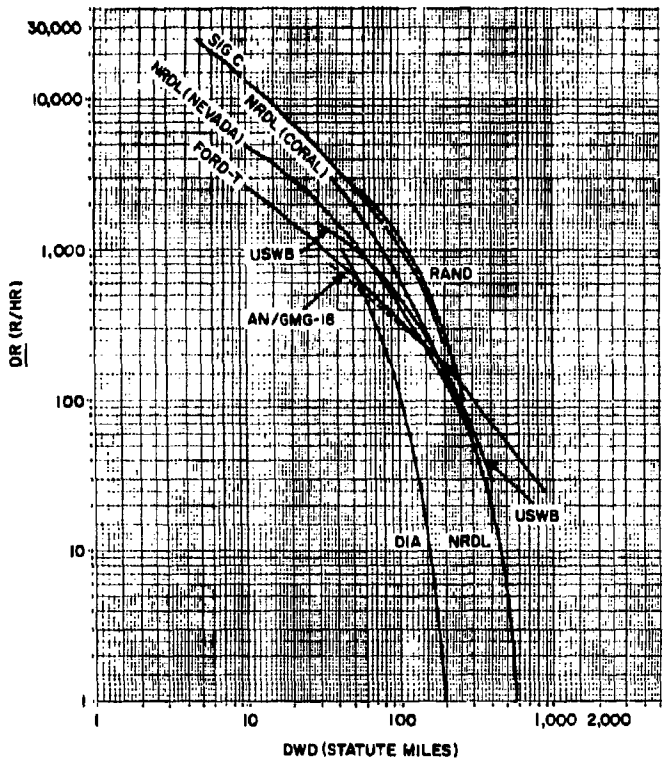

Fig. 15. DR as a Function of DWD (Cases I & II)

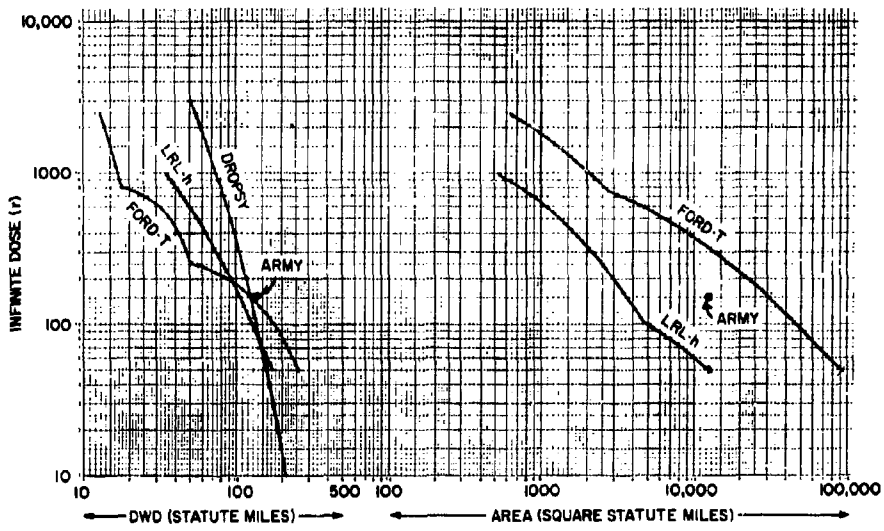

Fig. 16. Infinite Dose as a Function of DWD and of Area (Case V)

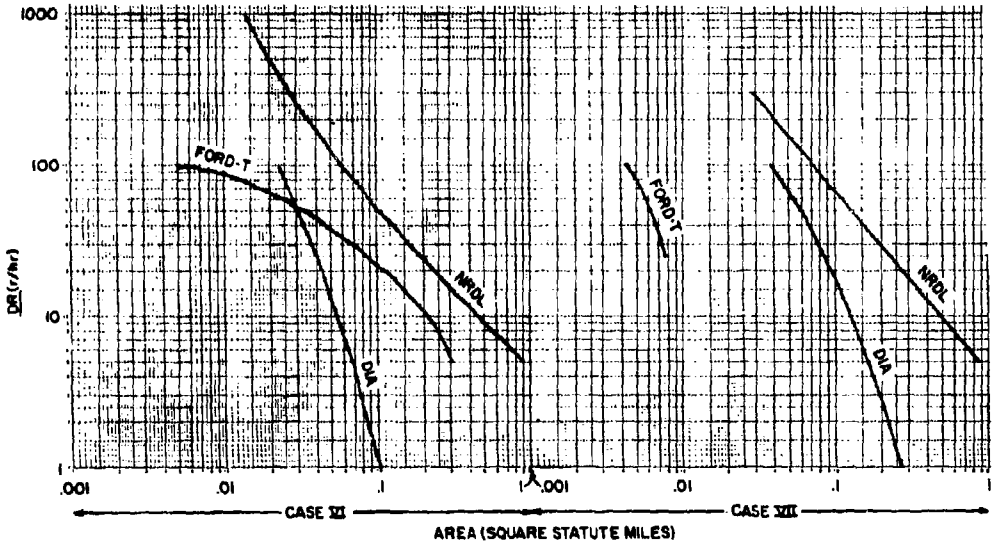

Fig. 17. DR as a Function of Area (Cases VI & VII)

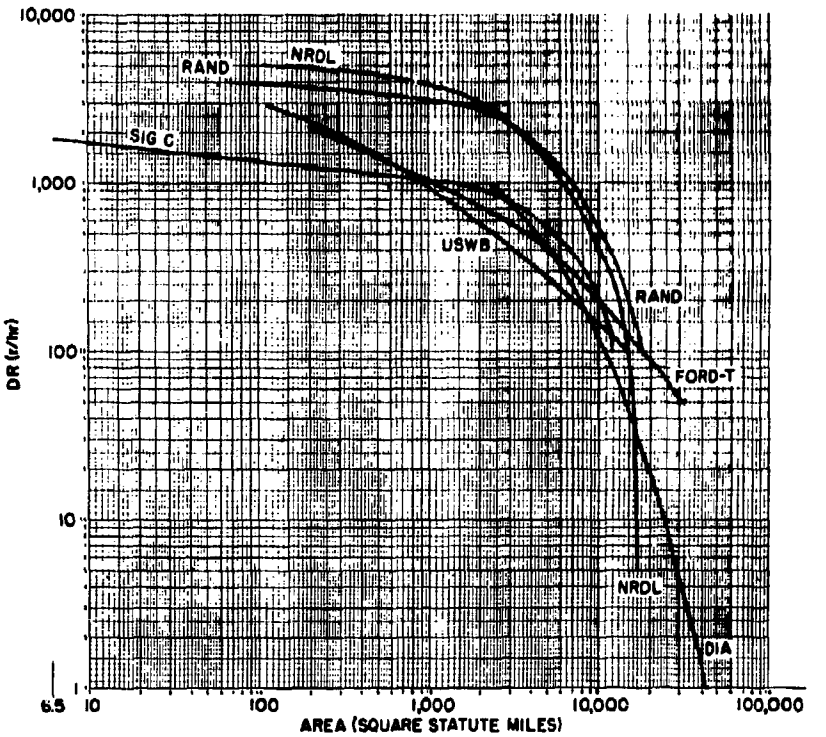

Fig. 18. DR as a Function of Area (Case X)

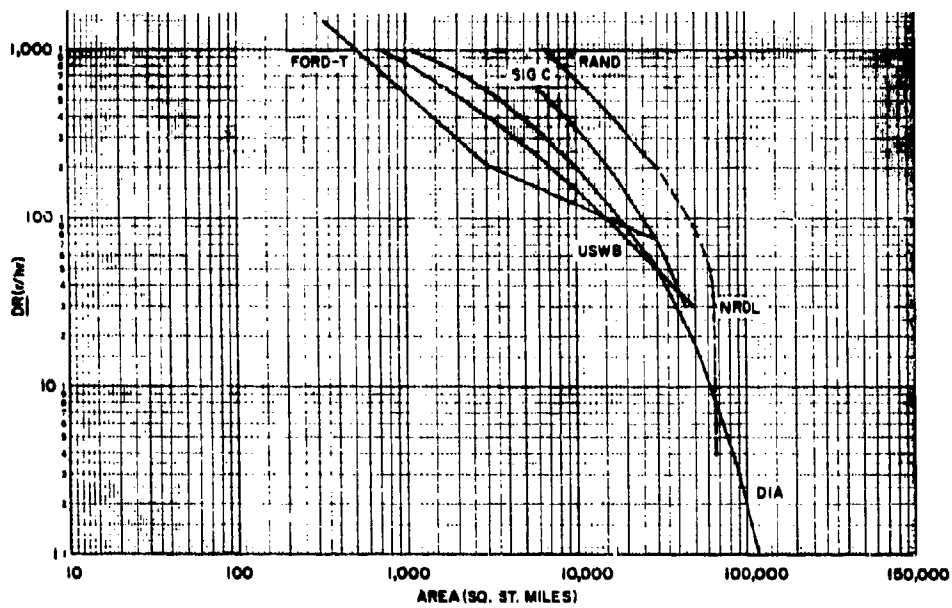

Fig. 19. DR as a Function of Area (Case XI)

TRANSPORT AND OUTPUT PROCESSOR MODULES FOR THE DOD FALLOUT PREDICTION SYSTEM

T. W. Schwenke
Technical Operations Research
Burlington, Massachusetts

ABSTRACT

1. The Transport Module

The specific purpose of the transport module is to accept a list of fallout particle properties and positions and mathematically transport these particles through a temporally and spatially varying wind velocity field until they land on the ground or until the researchers' interests are otherwise satisfied. The transport module has been divided for sake of flexibility and ease of construction into three major programs, each of which forms a separate chain link. These three links have the following general purposes:

Link 1. Initialization and control
Link 2. Wind field description
Link 3. Particle transport.

The wind field descriptions are accomplished as follows. A Cartesian coordinate system with origin at ground zero is established. With reference to this coordinate system, grid nets are specified in horizontal planes at arbitrarily spaced intervals in the vertical direction. The user provides a data set of wind vectors, arbitrary in number and independent of the grid system, that then is expanded and smoothed to yield interpolated or extrapolated wind vector components at each grid point. Three interpolation options are available for use in the data expansion calculations. In addition to this so-called macro-wind description system, provision is made for representation of certain special local circulation systems by analytical models. Specifically, models for mountain winds and sea breezes will be provided. The regions controlled by these models are bounded by planes perpendicular to the coordinate axes. Inside these regions, wind vectors are computed for specific circulation model parameters. Temporal variation of the wind field is achieved by periodically replacing the entire wind field description data set. The period of data replacement is specified by the user. Topographic variation of ground height is accomplished by specifying elevation heights of blocks in a grid system that

can be subdivided indefinitely to yield any resolution of detail desired. Topography of mountains covered by a mountain wind model cell is described by an analytical mountain shape function.

Particle trajectories through the atmosphere are computed in steps between boundaries defined by the grid-array planes. Lateral particle motion is taken as equal to that of the air currents. Vertical motion is taken as the sum of vertical air current motion and the terminal settling velocity computed for a sphere.

2. The Output Processor Module

The Output Processor of the DOD Fallout Prediction System is a very flexible, highly modular computer program for use in the interpretation of data representing grounded subdivisions of the radioactive cloud. It accepts descriptions of grounded cloud subdivisions, interprets them into a two-dimensional memory array or map image, and then prints the resulting array in a form suitable for viewing as a map. The interpretation processes required of the Output Processor are the computation of: (1) dose rate "normalized" to H + 1 hour, (2) dose rate at a specified time, (3) dose accumulated between two specified times, and (4) particle mass deposited per unit area.

INTRODUCTION

In this paper we consider the two final modules of the DOD Fallout Prediction System: the Transport Module and the Output Processor. Figure 1 represents the basic program modules of the prediction system and shows the sequence of their execution. At transport time, previously executed modules, specifically the Initial Conditions Module and the Cloud Rise and Circulation Module, have prepared inputs for the Transport Module.

The Initial Conditions, or "Fireball," Module begins with basic weapon and environmental parameters and ends with the beginning of entrainment-controlled rise. The Cloud Rise and Circulation Module then develops from these results a description of the distribution of fallout particles after cloud rise circulation is no longer important.

A Particle Activity Module may be called at this time to assign radioactivity to the particles on the basis of information supplied by the preceding modules.

Located just prior to the Transport Module is another module (not shown) that has become known as the Particle Set Expansion Module (PSE).

PARTICLE SET EXPANSION MODULE

The PSE Module stands as an interface between the Cloud Rise and Transport Modules. Because of computational limitations, Cloud Rise must deal with a small sample of the particles that eventually form the deposition pattern. The PSE Module uses the cloud-rise particle sample to define a larger set of particles to be transported. Thus, it can be said to expand the set of cloud-rise particles.

In Figure 2, which shows the operation of the PSE Module, the diagram on the left represents the distributed set of particles that results from cloud rise and circulation. The PSE Module operates by effectively loading and smoothing the original sample of particles into two three-dimensional arrays situated above ground zero. The center diagram of Figure 2 represents the relationship and subdivision of these two arrays. A particle-size mass distribution is determined for each cell in these arrays on the basis of the sample. Then each cell is subdivided spatially and in particle-size ranges to define the cloud subdivisions and central particles that will be actually transported. The resulting particle set represents an axially symmetric stabilized cloud and it is recorded on magnetic tape for future use.

To account for the effects of winds on particles while they are rising within the cloud and after they fall away from the circulating part of the cloud, adjustments are next made to the coordinates of all cloud subdivisions, and the results are recorded on a separate magnetic tape for use as an input to the Transport Module. The resulting distribution in space is represented by the right-hand diagram of Figure 2. Note that this distribution of particles (central particles of cloud subdivisions) is not axially symmetric and also that the time and spatial coordinates of each central particle represent it at the time when it left the circulating cloud and began its free descent through the flowing atmosphere.

Summarizing the inputs to the Transport Module, let us consider the elementary cloud subdivision and its characterization as shown in Figure 3.

The PSE Module produces cloud subdivisions that are rectangular boxes (square when viewed from above), and all have the same characteristic length, B, at the time of their definition. Each subdivision (central particle) is characterized by three spatial coordinates, a time coordinate, a (central) particle size, and the amount of mass that the cloud subdivision represents.

A large number of these elementary cloud subdivisions (central particles) are recorded at the time and position at which they depart from the rising cloud. At that time they represent (on magnetic tape) an asymmetric nuclear cloud defined in such a way that it is ready to be transported by the Transport Module. Such an asymmetric cloud is represented in Figure 4 within a box that indicates the limits of the volume of atmosphere for which a wind velocity field is to be defined.

TRANSPORT MODULE

The Transport Module accounts for the effect of atmospheric motion and results in a distribution of fallout debris on the ground. The transport of cloud subdivisions is represented pictorially in the left-hand diagram of Figure 5. Cloud subdivisions are transported independently of one another, and it should be noted that only central particles are actually handled by the Transport Module. Output processing, represented on the right-hand side of the figure, interprets the results of the Transport Module in the light of user requests for particular tabulations. The Output Processor in effect plots each grounded central particle on an output map, draws the subdivision's boundary onto the map, and then increments each grid point that lies within the boundary by an appropriately computed amount. We will return to discuss the Output Processor in greater detail later, but now let us consider how the atmospheric transport of particles is actually carried out.

The specific purpose of the Transport Module is to accept a list of fallout particle properties and positions and mathematically transport these particles through a temporally and spatially varying wind velocity field until they land on the ground, or until the researcher's interests are otherwise satisfied. The Transport Module has been

divided for the sake of flexibility and ease of construction into three major programs, each of which forms a separate chain link. These three links have the following general purposes:

(1) Initialization and control

(2) Wind field description

(3) Actual particle transport.

The wind field descriptions are accomplished as follows. A Cartesian coordinate system with arbitrary origin is established. With reference to this coordinate system, grid square arrays are specified on horizontal planes at arbitrarily spaced intervals in the vertical direction. Figure 6 illustrates how such a set of strata are used to fill the volume of atmosphere of interest. Each stratum is further subdivided into a number of wind cells in a regular manner as is shown in Figure 7.

To assign vectors to wind cells, the user may specify as input a data set of wind vectors and vector positions. This data set can be arbitrary in number and distributed in an arbitrary manner throughout the atmospheric volume of interest. The program then determines and associates a wind vector with each wind cell in the volume of interest. These wind cell vectors are based on the input data, and there are three interpolation-extrapolation computational options available for use in determining them. In the first option the program assigns to each wind cell the data vector nearest the cell's center. The second option uses the inverse-distance weighted-average of the N nearest data vectors, where the user is free to specify the number N. The third option uses a statistically derived three-dimensional linear model of the atmosphere based on the N nearest data vectors to perform the required interpolation or extrapolation for each cell.

MACRO FIELD AND LOCAL CELLS

Thus far in this paper we have been considering only what might be called the "macro" wind field of the prediction system. In addition to this so-called "macro-wind description system," provision is made for representation of certain special local circulation systems by analytical models. Specifically, models for mountain winds and sea breezes have been provided. The regions controlled by these models are bounded by planes perpendicular to the coordinate axes. Inside these regions, wind vectors are computed for specific circulation model parameters. Figure 8 represents three of these local circulation cells as they might be superimposed upon the macro stratum and wind cell structure. The relationship between flows within local cells and the nearby macro wind cells can be reasonably maintained if the local systems are represented by perturbation models. However, under certain conditions other representations may be appropriate as well.

ACTUAL TRANSPORT

Particle velocity for all particle transport is assumed to be given by the wind velocity (three dimensional) at the particle position minus the still-air particle-settling rate. Settling rates are computed as a function of particle size and altitude using a tabulated (standard) atmosphere. The Davies "definitive" equations for spheres along with a slip correction have been used. Within "macro" cells, particle trajectories are taken as straight lines and, thus, particles can be moved from one boundary to the next in one computational step. Such boundary-to-boundary transport is illustrated in two dimensions in Figure 9. Generalizing the boundary-to-boundary transport to other boundaries such as those of local circulation systems, we see in Figure 10 how a particle's trajectory is piecewise linear in the "macro" wind field but smoother within a local circulation system cell.

In addition to wind cell and stratum boundaries, time boundaries and topography boundaries are also used during transport. The following table is a list and explanation of the most important boundaries used by the transport program.

BOUNDARIES CONSIDERED BY THE
BOUNDARY-TO-BOUNDARY TRANSPORT

1. North-South Vertical Grid Planes
2. East-West Verticle Grid Planes
3. Horizontal Stratum Boundary Planes
4. Vertical Planes Which Bound Local Circulation Systems
5. The Horizontal Plane At The Maximum Topographic Height (not within a local cell)
6. Time Boundaries
   a. Time at which the wind field descriptions are to be updated.
   b. Time at which the user wishes the transport to be terminated.
7. Topography
   a. Planar or piecewise-planar topography in areas not covered by local circulation cells.
   b. Analytical topography within each local circulation system cell.

Temporal variation of the wind field is achieved by periodically replacing the entire wind field description data set. The period of data replacement is specified by the user.

With regard to topography, three different methods of specification are available. First the user can specify a planar deposition surface at any altitude for use in areas not covered by local circulation cells. Alternatively, a system has been provided to allow the user to specify the topography in a piecewise-planar manner, such as that illustrated in Figure 11. A grid system that can be subdivided indefinitely to yield any desired resolution of detail is used to achieve the desired resolution without the excessive redundancy of a strictly regular grid.

Within local circulation cells other topographic descriptions must be used. For instance, the topography of mountains covered by a mountain wind model cell is described by an analytical mountain shape function.

The final result of the Transport Module is a list (written on magnetic tape) of the impact points and times for all central particles that land during the time of user interest. Included in this list are all particle parameters used to characterize each elementary cloud subdivision, the tabulated particle-size mass distribution that was the basis for the original definition of particles, and, if a Particle Activity Module calculation has been done, a tabulation of activity vs. particle size.

OUTPUT PROCESSOR MODULE

The Output Processor of the DOD Fallout Prediction System is a very flexible, highly modular computer program for use in the interpretation of data representing grounded subdivisions of the radioactive cloud. It accepts descriptions of grounded cloud subdivisions, interprets them into a two-dimensional memory array or map image, and then prints the resulting array in a form suitable for viewing as a map. The interpretation processes required of the Output Processor are the computation of: (1) dose rate "normalized" to H + 1 hour, (2) dose rate at a specified time, (3) dose accumulated between two specified times, and (4) particle mass deposited per unit area.

Time of particle impact is appropriately accounted for by all interpretation options as required, but doses and dose rates resulting from cloud subdivisions that are in transit are not currently accounted for.

One of the features that distinguishes this Output Processor from prior work is its treatment of map areas and scale factors. Map limits in this program as well as scale factors, are decoupled from the

weapon and particle data and are under the direct control of the user. The user may specify the coordinate limits of any rectangular map oriented parallel to the coordinate axes. Virtually any scale factors may be specified for use and the resulting map will be printed automatically in as many strips as are required.

Although at this time the Output Processor can operate using the assumption of a single constant decay rate for all cloud subdivisions, plans have been made to achieve a physically more correct treatment of activity. The single constant decay rate will remain as an optional simple approximation, but modifications to the NRDL Particle Activity Module are now under way at NDL to facilitate its use within the Output Processor. When the work is successfully completed and appropriate modifications and additions are made to the Output Processor, it will be possible to estimate directly the effects of fractionation and perhaps even selected mass chains.

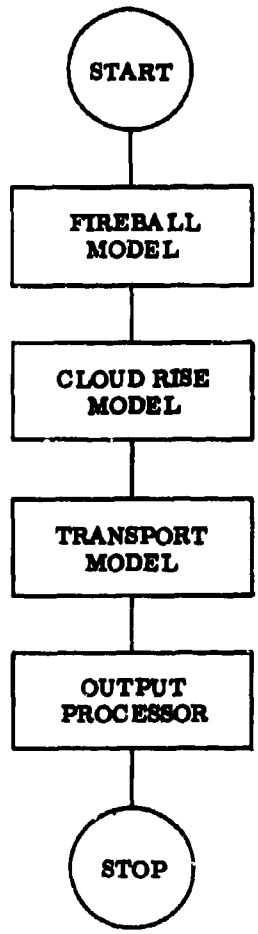

Fig. 1. The Basic Program Sequence in the DOD Fallout Model

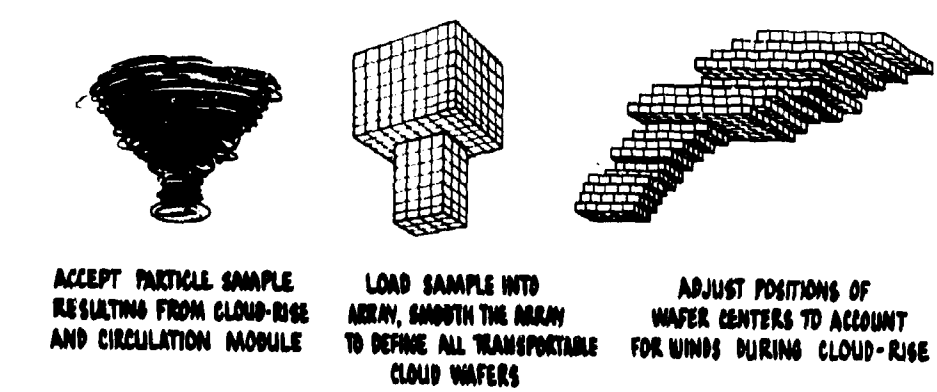

Fig. 2. Operations of the Particle Set Expansion (PSE) Module

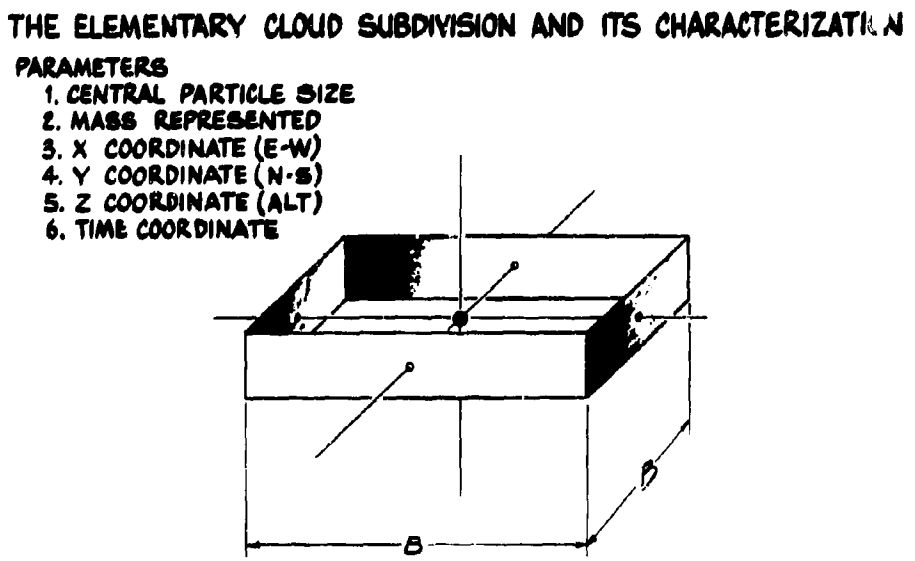

Fig. 3. The Elementary Cloud Subdivision and Its Characterization

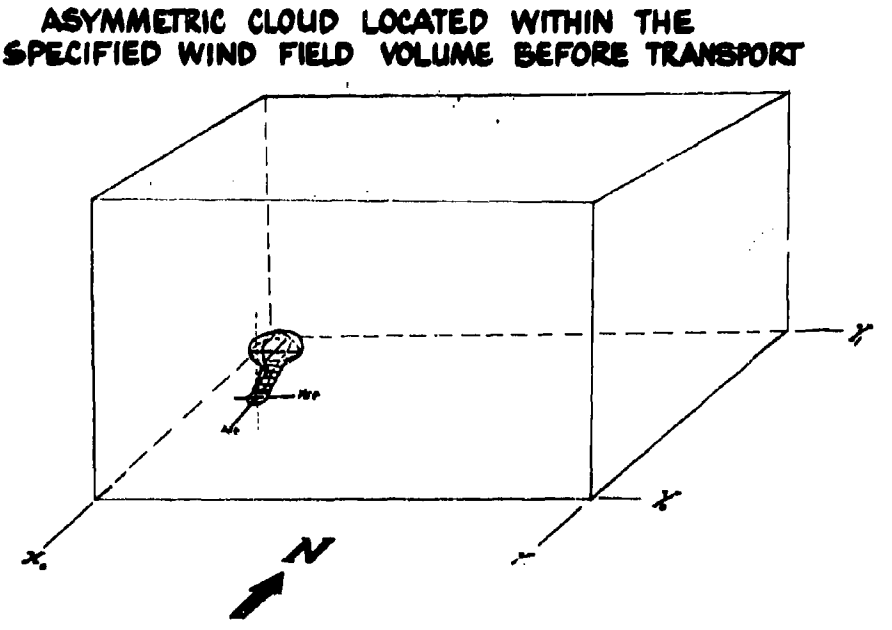

Fig. 4. Asymmetric Cloud Located Within the Specified Wind Field Volume Before Transport

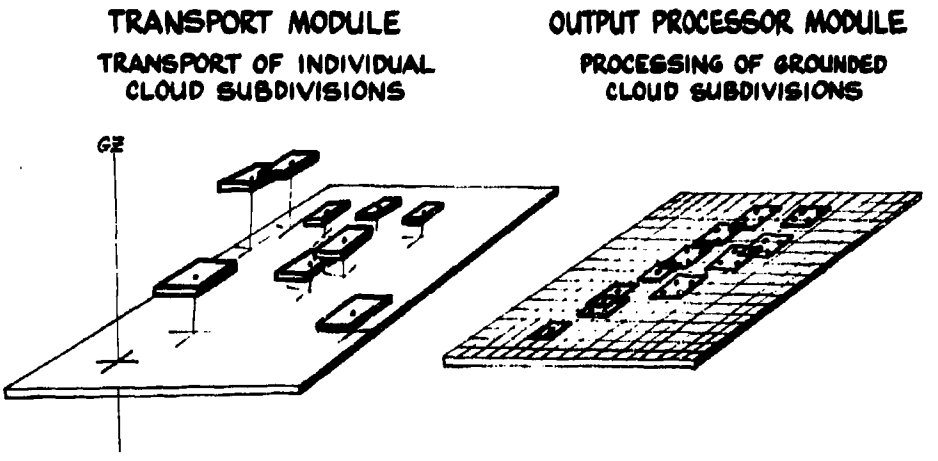

Fig. 5. Transport and Interpretation of Individual Cloud Subdivisions

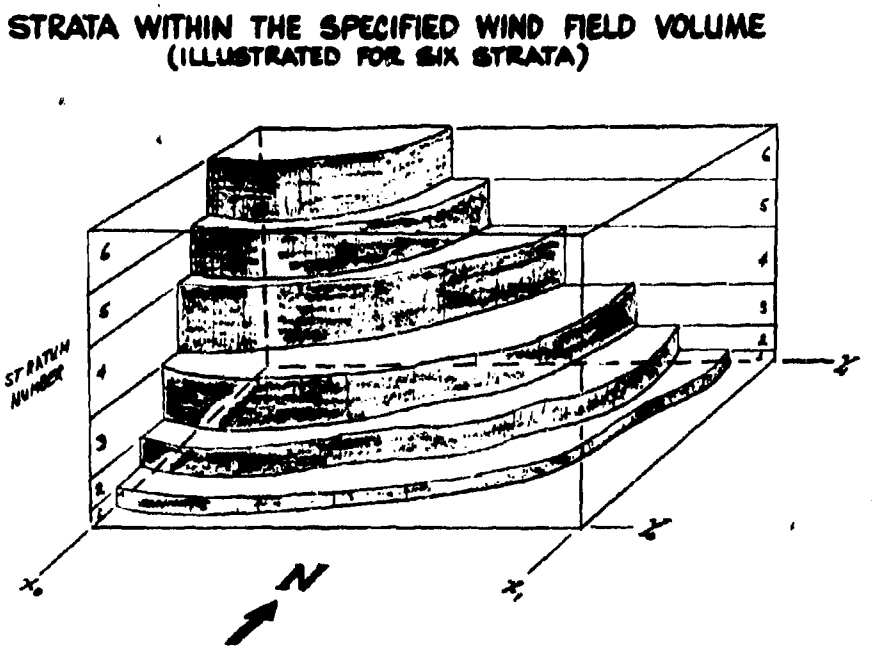

Fig. 6. Strata Within the Specified Wind Field Volume

WIND CELLS-SUBDIVISIONS OF A STRATUM
(ILLUSTRATED FOR THE J-TH STRATUM FROM THE BOTTOM)

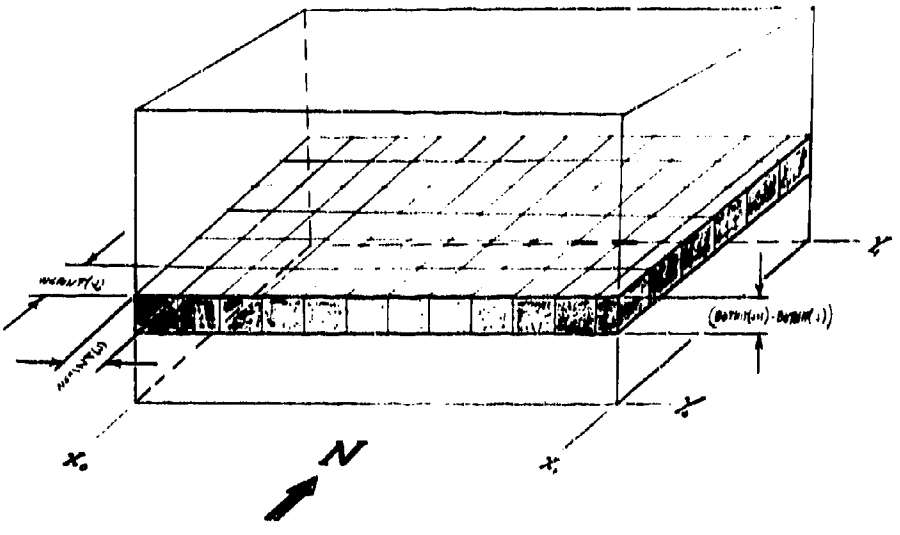

Fig. 7. Wind Cells-Subdivisions of a Stratum

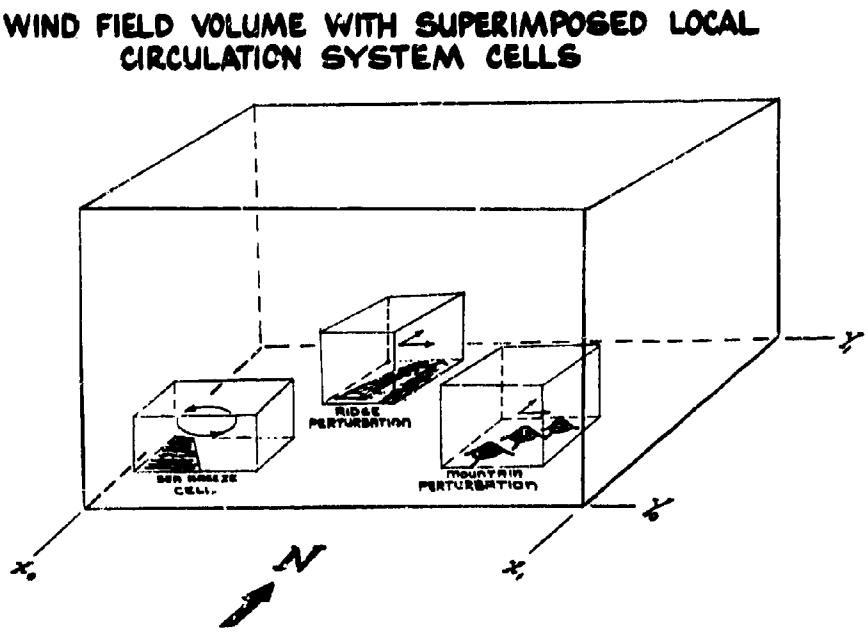

Fig. 8. Wind Field Volume with Superimposed Local Circulation System Cells

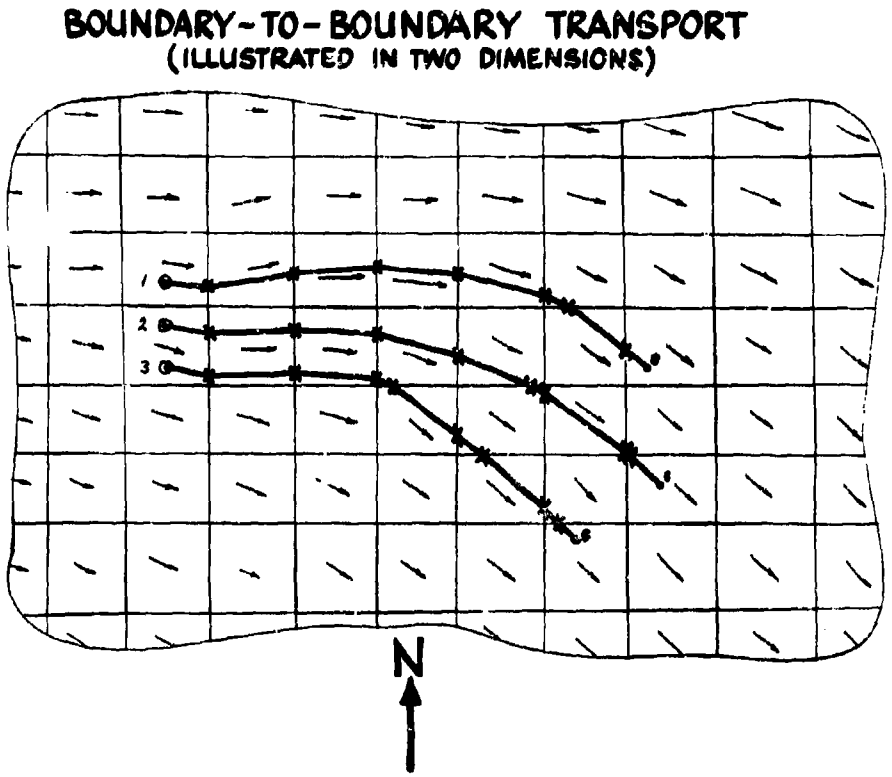

Fig. 9. Boundary-to-Boundary Transport

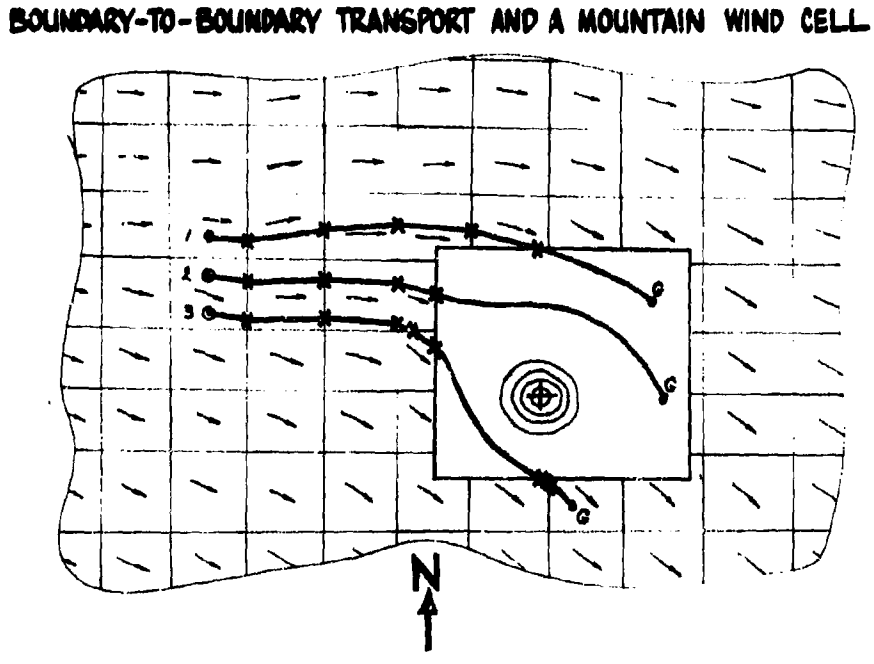

Fig. 10. Boundary-to-Boundary Transport and a Mountain Wind Cell

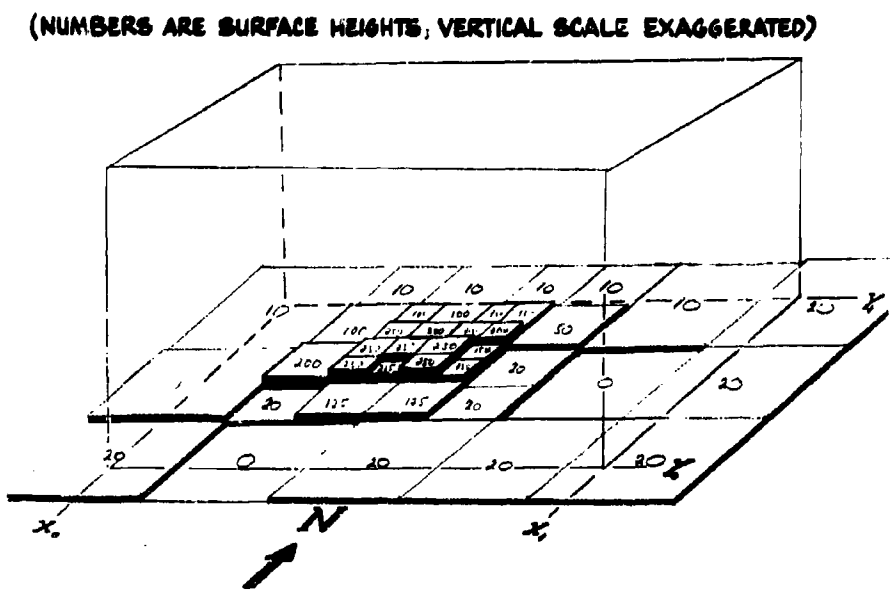

Fig. 11. Piece-Wise-Planar Topography Specification Below the "Macro" Wind Field Volume

DIFFERENCES IN TRANSPORT AND DEPOSITION OF CLOSE-IN AND INTERMEDIATE FALLOUT

E. C. Evans III and C. A. Young
U.S. Naval Radiological Defense Laboratory
San Francisco, California

ABSTRACT

"Close-in" and "intermediate" fallout are customarily distinguished by particle size. This paper assesses some of the differences in the phenomena of transport and deposition of these two classifications of fallout.

Particle falling speeds used by the USNRDL D-model are presented and used to establish regions of close-in and intermediate fallout. A special plotting system used to estimate particle sizes aloft or being deposited at any time and/or location is described. The effect of base surge and deposition on plant surfaces is evaluated to determine the extent to which such phenomena can alter close-in radiation fields. The probability of atmospheric modification of close-in and intermediate fallout intensity is discussed. Possibly important differences in deposition mechanisms characteristic of the close-in and intermediate fallout regions are enumerated in order to emphasize the problems of extending close-in fallout models to intermediate fallout and beyond.

INTRODUCTION

With the DOD-fallout model rapidly approaching completion, it is important to look again at the whole sequence of phenomena in an attempt to discover the most productive areas for subsequent sensitivity analyses or further model refinement. Since it is currently available, and, since its use does not significantly alter conclusions, the NRDL D-model is used for this construction. The overall event is intentionally inspected from a graphic point of view; therefore, emphasis is placed on curve shapes and general trends rather than on precise numerical values.

No model, present or future, can expect to duplicate the complete history of fallout particles in the real atmosphere; nor does such expectation appear practical. Certain aspects of particle transport and deposition, still omitted or approximated by all present fallout models, are again inspected to determine whether their effect on the final radiation field can be significant. These factors are divided into those affecting "close-in" fallout (particle diameters >50μ) and those affecting "intermediate" fallout (particle diameters between 50 and 10μ). Such division on the basis of particle size is admittedly arbitrary as well as being somewhat erroneous since the definition of close-in and intermediate fallout must, in part, depend on yield and height of burst.

PARTICLE FALLING SPEEDS

Particle falling speeds inevitably enter into any analysis of fallout behavior. Therefore, a brief summary of the terminal velocities used in the NRDL D-model is required, especially since Mr. C. F. Ksanda's investigation establishing such speeds has not been published. After critically examining the work of Burke and Plummer,[2] Dallavalle,[3] Davies,[4]

Krey,[5] Kunkel,[6] Martin,[7] Muttray,[8] Pettyjohn and Christiansen,[9] Prandtl and Tietjens,[10] Rapp and Sartor,[11] Schiller,[12] Wadell,[13] and others included in the British Compendium on "The Physics of Particle Size Analysis,[14] Mr. Ksanda constructed a plot of terminal velocities versus particle size for spheres, cylinders, disks, cubes, and polyhedrons (reproduced for spheres and cylinders in Figure 1). The dimensionless parameters:

$$\frac{[CN]^{1/3}}{\left[\frac{V}{dA}\right]^{1/3}} \text{ proportional to particle size, } \left[\frac{2(\rho-\rho_a)g\rho_o}{\mu^2}\right]^{1/3} d, \text{ and}$$

$$\left[\frac{N}{C}\right]^{1/3}\left[\frac{V}{dA}\right]^{1/3} \text{ proportional to particle velocity, } \left[\frac{\rho_o^2}{2(\rho-\rho_o)g\mu}\right]^{1/3} v,$$

are used; where

C = particle drag coefficient;

N = Reynold's number;

V = particle volume;

d = characteristic linear dimension of particle (for spheres and cylinders, diameter; for irregular particles, maximum projected dimension);

A = cross-sectional particulate area normal to direction of fall (particles were assumed to fall with their center of gravity as low as possible);

ρ = particle density;

ρ_o = fluid density;

g = acceleration of gravity;

μ = terminal particle velocity (Bernoulli effect, density flow, and slip correction not considered).

The 2:1 cylinder $\left[\frac{V}{dA}\right]^{1/3} = 0.925$ was selected as the best approximation to the falling speeds of irregular particles. Compared with a sphere of the same volume, this cylinder falls ~0.8 as fast for small N, ~0.7 as fast for intermediate N, and ~0.75 as fast for large N. Falling

rates so computed thus qualitatively agree with the results of Rapp and Sartor[11] for simulated angular particles at low Reynold's number. Compared with a sphere of the same diameter, the 2:1 cylinder falls nearly 1.4 times faster for small N, at about the same speed for intermediate N, and ~ 0.9 as fast for large N. Qualitatively, this observation agrees with the data of Krey,[5] Prockat,[15] and Rubey,[16] the latter two of which are based on diameters determined by sieving, which should best represent actual diameters. This result also compares favorably with the terminal velocity determinations of Broido, Corcos, and McMasters[17] using simulated irregular fallout particles in a small vertical wind tunnel. Mr. Ksanda therefore fitted the falling-rate for the 2:1 cylinder with the equation:

$$v = \frac{1.325b\mu}{\rho_o} \log_{10}^3 (bd + 1.163),$$

where

$$b = \left[\frac{2g\rho_o(\rho-\rho_o)}{\mu^2}\right]^{1/3}$$

and other notation has been previously indicated. This terminal velocity is further modified by Cunningham's slip correction factor:[18]

$$\left[1 + \left(\frac{L}{d}\right)\left\{2.514 + 0.8 \exp\left(-0.55\,\frac{d}{L}\right)\right\}\right] \text{, where L = mean free path}$$

of air "molecules" at a given altitude. Density and viscosity, both functions of altitude, are determined from any standard atmosphere table or from observations. In the USNRDL cloud rise module prepared for the DOD-model, these parameters also are determined for ambient conditions within the rising cloud.

The terminal velocity subroutine used in the NRDL D-model thus determines falling speeds for 2:1 cylinders for particles larger than

42 microns. Below that size, however, falling speeds are computed for spheres under the presumption that the majority of these smaller sizes have melted, and therefore have become spheroid. Some characteristic terminal velocities computed by the NRDL D-model subroutine using the ARDC 1961 standard atmosphere[19] and NTS soil (ρ = 2.6 g/cc) are presented in Figure 2.

SIZE CHANGES AND REGIONS OF FALL

On the basis of the falling speeds presented, it is possible to determine the approximate location and size of regions subjected to close-in and intermediate fallout. Idealized wind conditions are assumed, since variations due only to terminal velocity are desired. One fact, well recognized but not often specifically considered, should first be emphasized, viz: that the size-frequency distribution of particulate material remaining aloft as well as that being deposited during any given period is continuously changing with time. An approximate means of gauging these changes was suggested long ago by Anderson.[20]

Anderson's method, somewhat embellished, is presented in Figure 3. Here, the cumulative percent for each particle size class (PCS) is plotted against altitude at a specified time after burst. The plot is in effect a position display of all D-model disks aloft at a given time. The activity-size distribution in any altitude slice is determined by the PSC's falling through that slice at a given time. Since particles are assumed neither to be created nor destroyed, some notion of activity-size distribution can be obtained by inspecting the section of the input activity-size distribution as shown in the insert to Figure 3. While the distribution can no longer be log-normal, it can usually be approximated by such a distribution.

The cumulative percent of the total activity-size distribution for each PSC is also given across the top of the plot. The difference in total cumulative percent between the smallest and the largest completely

traversing PSC's multiplied by the proportion of these within the slice approximates the fraction of the total cloud activity contained. Since the cumulative percent lines are nearly parallel for a reasonably narrow altitude slice, all PSC's between the class just having traversed and the class just beginning to leave the altitude slice are represented by nearly the same proportion of their total populations as determined by difference. Although their contribution is small, classes partially traversing the altitude slice (either entering or leaving) may be added using their individual weighting factors again determined by difference (see examples in insert to Figure 3).

In a similar manner, the activity-size distribution and percent of total cloud activity next to be deposited can be estimated by taking an altitude slice of the appropriate thickness immediately above the ground. For this purpose, a scale indicating the time a given PSC will reach the ground has been added at the bottom of PSC lines approaching the ground.

Since the NRDL D-model can also print out mass associated with each disk,[21] similar plots can be constructed and used to estimate particulate mass aloft or deposited at any time. Such disk displays afford quick ways of estimating model sensitivity to various changes involving input particle size distributions.

Having noted the constantly changing size distribution both aloft or being deposited, consider now the regions of fall for particles >100μ diameter (2:1 cylinders), and for two PSC's whose midpoint diameters are 50μ (2:1 cylinders) and 30μ (spheres). These three regions certainly represent close-in fallout on the one hand and intermediate fallout on the other, with a grey region between. The farthest and closest point of deposition downwind have been determined by means of equations recently published by Ksanda,[22] thus:

$$D_c = U_2 \ (t_{H2}) - a$$

and

$$D_f = U_1 (t_{H1}) + a$$

where

D_c and D_f = the closest and farthest deposition distances from GZ,

U_1 and U_2 = the effective fallout wind speeds for the top and bottom of the atomic cloud.

t_{H1} and t_{H2} = the total time taken for a particle of stated size to fall from the highest and lowest altitude attained during cloud rise,

a = radius of the cloud.

The earliest and latest arrival times for a given particle, T_e and T_l, are respectively t_{H2} and t_{H1} plus the time required for rise. Using U_1 = 32 mph and U_2 = 21 mph representing maximal seasonal winds (spring, Southeast) and U_1 = 16 mph and U_2 = 12 mph representing minimal parameters (summer, North) from Callahan et al,[23] the various distances and times have been calculated for a range of yields and set forth in Table I. Tabulated values for the maximal seasonal winds are plotted in Figure 4 on the same scale for all yields assuming 10° and 30° eddy-diffusional spreads (for the latter case downwind depositional boundaries have been reduced by approximately one third).

Figure 4 is presented to emphasize two points: first, the vast difference in areas involved in close-in and intermediate fallout; and second, the separation of these two regions, especially for the larger yields. These large areas are not often seen since most local fallout models are terminated at 24 or 48 hours leaving a good fraction of particulate material still aloft; they are therefore included in Table I. The separation of the two regions also bears emphasis since depositional mechanisms, natural factors significantly influencing them, and subsequent particulate behaviour are probably different for each. Most military models, designed for close-in regions, are not properly applicable at the greater downwind distances.

Table I

Times of Arrival and Distances of Deposition*

Particle Size (μ, diam)	T_E (as ind)	T_l (as ind)	max. seasonal winds U_1 = 32 mph D_c (mi)	D_l (mi)	A_{10} (K sq mi)	U_2 = 21mph A_{30} (K sq mi)	min. seasonal winds U_1=16mph D_c (mi)	U_2 =12mph D_l (mi)
Y = 1 KT Z_T = 14,200 ft. Z_B = 6,400 ft. a = 0.45 mi.								
30	8.8h	19.h	180.	610.	26.	40.	100.	310.
50	2.2h	5.2h	43.	160.	1.7	2.7	24.	81.
10^2-10^3	2.2m	1.5h	0.13	45.		0.4	-0.12	22.
Y = 10 KT Z_T = 25,300 ft. Z_B = 11,500 ft. a = 1.13 mi.								
30	-	-	(320.)	(950.)	60.	100.	-	-
50	3.9h	8.0h	78.	250.	4.1	5.3	44.	130.
10^2-10^3	5.0m	2.2m	0.3	68.		1.0	-0.31	34.
Y = 100 KT Z_T = 45,000 ft. Z_B = 20,500 ft. a = 2.8 mi.								
30	1.1d	2.2d	540.	1650.	190.	340.	310.	830.
50	6.7h	13.h	140.	420.	11.	18.	76.	210.
10^2-10^3	12.m	3.7h	0.27	120.		2.6	-1.0	60.
Y = 1 MT Z_T = 70,100 ft. Z_B = 31,500 ft. a = 10 mi.								
30	1.6d	3.1d	800.	2400.	400.	840.	460.	1200.
50	10.h	18.h	190.	600.	25.	37.	110.	300.
10^2-10^3	20.m	5.0h	-4.8	170.		11.	-7.0	90.
Y = 10 MT Z_T = 106,000 ft. Z_B= 47,500 ft. a = 25 mi.								
30	2.3d	4.6d	1200.	3500.	800.	1600.	650.	1800.
50	14.h	1.0d	260.	810.	44.	79.	140.	420.
10^2-10^3	28.m	6.5h	-16.	230.		27.	-20.	130.

*NOTE: Y = yield; Z_T = cloud top; Z_B = cloud bottom; a = cloud radius; A_{10} = area for 10° eddy diffusion angle; A_{30} = area for 30° eddy diffusion angle; d = day; h = hour; m = minute; negative distances = upwind; all other symbols defined in text.

CLOSE-IN FALLOUT

The region of close-in fallout, extending to 200^{+} miles downwind and depending on yield, etc., seems adequately covered (with various individual biases) by the constantly growing family of military fallout models. Maximal and minimal hazards for specified military objectives in the close-in fallout region can be delineated. What significant factors yet remain to be evaluated and, if necessary, incorporated into these models? There appear to be four, viz: a) fractionation, b) base surge phenomena, c) retention on vegetation, and d) surface roughness factors.

The first and the last of these considerations are included in current fallout effort recently completed or approaching completion. Radionuclide fractionation has long been recognized as a potentially important factor. Accordingly, computer subroutines using Freiling's radial model[24-27] have been incorporated into the DOD model by NRDL as part of the Particle Activity Module (PAM).[28-30] The possible effect of decreasing average gamma photon energy with time after fission on surface roughness factors has also been investigated by Tomnovec, Ferguson, and Weldon.[31] Their findings indicate that as gamma energy declines, increased surface roughness attenuation is compensated by an increased build-up factor. It appears, therefore, that average energy changes can be neglected in surface roughness corrections. More important factors appear to be the correct selection of a suitable surface roughness factor and methods of including topographic factors for a given terrain. These and other matters are, however, discussed by Dr. Ferguson and Mr. Soule in the fourth section of this symposium.

Base surge has been extensively described and investigated for underwater nuclear bursts, but relatively little work has been done on land-surface bursts. No close-in fallout model contains a base surge subroutine, possibly because of the hopeful assumption that relatively little radioactivity is so transported. A number of samples

from Event Johnie Boy,[31-33] however, showed unexpectedly large amounts of neutron-induced activity, in some instances more than fission product activity (for example, see Fig. 5 of Ref. 31). The location of these samples bore no reasonable relationship to the fallout pattern recorded for the event. They were most frequently near and to the west of GZ, a region topographically lower than the remainder of the fallout field. Unfortunately, the number of samples analyzed for induced activity were few and sporadically selected so that a proper distribution pattern cannot now be constructed; however, it can be suggested that base surge, behaving as a density flow, deposited sufficient induced activity at these locations to equal or exceed fission product activity from fallout. That base surge exhibits density flow is generally accepted for water bursts,[34-36] but such acceptance has not been formally extended to underground bursts. Rohrer and Knox[37] do report density flow effects observed after a cratering H.E. shot in desert alluvium. From a helicopter at 2000 to 3000 ft., base surge was observed to accelerate down a trough 60-ft. wide and having a slope of 10 to 15%. This acceleration was relative to the remainder of the surge spreading radially over Frenchman's Flat. Apparently there is no other documentation of the phenomenon for underground bursts.

On a flat water surface, density flow has a convenient geometric symmetry; thus making it relatively easy to incorporate into fallout models. On land, topography can make base surge behavior considerably more complex. If significant amounts of induced activity are indeed transported, base surge flow could be important in the prediction of close-in, early-time radiation hazards. Base surge could, for instance, preferentially flow down canyons and into depressions. Furthermore, since forest stands would also represent an increased resistance to density flow, base surge might tend to flow along clearings or around denser stands. Whether, due to base surge flow behavior, forest stands could afford significant protection for troops remains an unanswered

question. The problem would appear, however, to warrant more detailed study.

The relative importance of fallout or base surge deposited on plant materials must also be evaluated from the standpoint of the close-in radiation field. Intermediate fallout deposition is discussed later; here the nature of close-in fallout is briefly evaluated in the light of Miller's preliminary findings on Operation Ceniza-Arena.[38-46] The deposition of "ceniza-arena" (ash-sand) originating from the Costa Rican volcano Irazu was studied by groups from SRI and NRDL. Geometric means for the deposited material ranged between 60 and 100μ (sieve diameter)[47,48] with a considerable percent of the total mass (10 to 20%) less than the 43μ sieve size. The density of the material was approximately 2.6 g/cc. The observed deposition mechanism is simply that of gravitational settling on plant surfaces. The size distribution retained on plant surfaces was generally the same as that on the ground, although there was some tendency toward more efficient retention of the smaller sizes. Hourly accumulation rates reported[39] usually range between 0.5 to 3.0 g/ft^2 with maximal rates of short duration as high as 14 g/ft^2. Such deposition rates are certainly within the range characteristic of close-in fallout, e.g., 10 g/ft^2 at the 1000 r/hr at 1 hr contour.[49]

Contamination factors, a_L, defined as

$$a_L = \frac{\frac{\text{g ceniza on plant}}{\text{g plant (dry wt.)}}}{\frac{\text{g ceniza on ground}}{\text{ft}^2}}$$

are reported for a number of truck garden crops. Values of a_L ranging between 0.001 and 0.1 are characteristic. Changes with growing season (especially for cereals) show interesting and perhaps significant trends associated with plant development (Appendix B). In general, contamination under humid conditions is roughly twice that under dry conditions, or:

$$a_L \text{ (humid)} \simeq 2\ a_L \text{ (dry)}.$$

Also noteworthy is the observation, applicable to larger plants (trees), that:

$$a_L \text{ (outermost leaves)} \simeq (2 \text{ or } 3)\ a_L \text{ (central leaves)}$$

A second factor, the foliar surface density, w_p, is defined as:

$$w_p = \frac{\text{g plant (dry wt.)}}{\text{ft}^2 \text{ of ground surface}}$$

Of special interest in the close-in fallout environment are the amounts of fallout temporarily retained on grasses, chaparral, or forest vegetation. The product $a_L w_p$ represents the fraction* of the total ceniza-arena deposit so retained. This product is more meaningful for crop plants where foliar surface density is relatively low; but for continuous cover by larger plants (chaparral, forest), w_p becomes so high that, with the range of factors observed, there is sufficient plant surface to retain more than the total fallout deposited per unit area.

Using Miller's values for a_L and w_p, mature grass stands are capable of temporarily retaining up to 80% of settling fallout with a lower retention factor of 10% more likely. For larger vegetation (chaparral, forest), the surface area available is sufficient to retain temporarily 100% of depositing fallout with lower factors of 30 to 50% more probable. Such retention is properly described as temporary since over a good range of wind speeds (3 to 16 mph) and plant surfaces (tomato to avocado), the half life for retention of dry ceniza-arena lies between 2 and 6 hours (axial retention or retention on plants shielded from the wind can be longer). Under humid and/or low wind conditions, such half lives can be increased by factors of 2 to 10. In view of the much longer retention half-lives reported by Russell[50] and by Martin,[51] ceniza-arena half lives must be described as temporary. Removal by rain (0.4

*usage is C.F. Miller's

inches) is nearly complete, except that plant parts near the ground can be recontaminated by spattering. Lastly, retention half-lives are not observed to be a function of plant loading, except in cases where loading is so great as to cause plant failure. Removal can therefore be assumed to be mainly dependent upon meteorological factors capable of disturbing the deposited material.

Temporary retention should not be important to browsing animals since, failing other removal, feeding disturbance alone would probably knock much of the contaminating material from the leaf surfaces. Temporary vegetative retention can, however, be important in modifying close-in exposure fields. Accordingly, a simple geometric approach[52-54] has been used to estimate changes in exposure rate due to contamination of plant surfaces. In the first case, grass is approximated by a slab 3 ft thick adjacent to a plane representing the ground (the grass is admittedly tall, however, shorter grass produces trivial effects). A certain fraction, f, of the total mixed fission product (MFP) deposit (1.25 Mev gamma to approximate early-time MFP spectrum[55]) is put on the plane, the remainder, (1-f), is uniformly distributed in the "grass" slab. Exposure rates at a detector 3 ft above the plane for various degrees of grass contamination are compared to the exposure rate with all activity on the plane (see Figure 5). The density of grass was estimated to be 0.005 g/cc, a value deduced from Miller's foliar surface densities for cereal crops. Since shielding due to grass reduces the bare plane exposure rate by a factor of 0.76, exposure rates are compared to those at a detector 3 ft over a grass-covered plane.

Similar calculations have been performed for trees, assuming a "tree" slab placed at some height above the plane, and having a density of 0.01 g/cc.* Two tree heights and canopy thicknesses (shown in Figures 6 and 7) have been assumed; also two types of distribution within the

*see Appendix B

canopy: one with uniformly distributed radioactivity as in the grass case, the second (and more likely) with the radioactivity retained in a thin layer at the top of the canopy. In all tree cases, some protection is afforded by the retention of activity on plant surfaces. For low trees, (Figurc 6), the exposure rate is reduced to 0.54 or to 0.40 of the original value depending upon the manner of distribution within the canopy. For taller trees (Figure 7) similar reductions are 0.36 and 0.21, again dependent upon distribution within the canopy.

These numbers cannot be considered anything more than approximations; nevertheless, they do indicate that vegetation can significantly reduce radiation fields. Two factors may contribute to this reduction, viz: the possibility of base surge deflection and the possibility of fallout retention in the forest canopy. Although the environmental half life for retention on plant surfaces can be relatively short (2 to 6 hours), even a short retention occurring at early time might constitute a decided advantage.

The effects of plant contamination on exposures to people within structures adjacent to the plant cover are so complex that almost any result can be obtained depending on the geometries and shielding factors assumed. Where direct penetration of the structure is important, exposures are particularly sensitive to the distance between the trees and the structure, to the height of the trees, and to the fraction of the deposit retained in the trees. For a light wooden structure (10 lb/ft^2 for floors, walls, and roof), standard calculations procedures[53,54] indicate that exposures in a basement can be increased by a factor of 10 due to direct penetration if all fallout is retained on trees (height 10 ft) which immediately surround the house (assuming no roof contamination). A similar increase would be expected in fox holes dug under trees. The exposure increases would be halved if a 10-foot clearing existed around the house or foxhole. If the roof is also assumed to be contaminated, exposure increases at a basement location due to tree

retention would be smaller, perhaps a factor of 4. For a second story location, in this same structure, the Engineering Manual[54] indicates a 40% increase in exposure for a 10 ft elevation of the source. Again roof contamination would make the relative increase smaller.

For a heavy concrete structure (5 inch floors, walls and roof), exposures at basement locations would be relatively insensitive to plant contamination due to the importance of in-and-down penetration and skyshine. Roof contamination would further reduce the effects of plant contamination, while the presence of windows would increase these effects, again due to direct penetration. A second story location would experience a 40% increase in exposure due to source elevation exactly as for the lighter structure. This increase would be greater if windows were considered and less if contamination remained on the roof.

INTERMEDIATE FALLOUT

Finally, a comparison of certain aspects of close-in fallout with the intermediate fallout indicates several differences which may be important. The vast difference in surface area affected by these two stages of fallout has already been emphasized, as has the difference in particle sizes being deposited. The smaller-sized particles composing the intermediate fallout are more influenced by meteorological conditions in the atmosphere (vertical currents and precipitation) and carry a greater proportion of fission products with volatile precursors. When deposited on plant surfaces, they behave in a way which may be different from that of ceniza-arena.

Feteris, Kessler, and Newburg[56] have determined the influence of vertical currents on the falling time of spherical particles as shown in Figure 8, taken from the referenced report. It is apparent that the effects are large when the terminal falling velocity for the particle and the vertical component of current velocity are equivalent. D-model

particle sizes falling at the indicated terminal velocity at sea level and at 30 thousand feet have been added to the figure; all sizes classify as close-in fallout. While the influence of horizontal wind velocities on fallout patterns is well known, the effect of vertical currents is less so. According to Feteris et al, "the time of arrival of particles is delayed by updrafts and expedited by downdrafts. ... The duration and total accumulation of fallout...is increased...beneath intensifying updrafts and decreased beneath weakening updrafts; beneath downdrafts, the converse holds." The depth of circulation and its intensity influence the magnitude of these effects, the greatest changes occurring for the slowest falling particles.

It is, therefore, of interest to ascertain the likelihood of vertical current modification of close-in and intermediate fallout. For this purpose, some general summary of the areas, velocities, ceilings, and durations of such vertical developments in the atmosphere is necessary. Since no table of such information could be located, data and estimates were gathered from many sources and assembled into Table II. The source material underlying this table is set forth in greater detail in Appendix A. Comparison of cross-sectional areas for vertically moving parcels of air with areas associated with the atomic cloud or regions of fallout is used to estimate relative importance of various vertical movements. These movements are somewhat arbitrarily assigned to three classes, viz:

Class I: large to very large area, relatively slow moving, relatively long duration.

Class II: intermediate to large area, intermediate to fast moving, relatively long duration (usually orographic).

Class III: small to intermediate area, relatively fast moving, relatively short duration (usually thermal).

From a comparison of areas (square miles versus thousands of square miles) only Class I would appear to have a large potential for affecting intermediate fallout. Certainly thunderstorms or mass fires (Class III)

Table II

BURST AND CLOUD PARAMETERS

(Areas in Square Miles)

Yield	Cloud Radius	Disk Area (as stated above)
1 KT	0.45	2/3
10 KT	1.13	4
100 KT	2.8	25
1 MT	10.	310
10 MT	25.	1900

FALLOUT REGIONS

(Areas in Thousands of Square Miles)

Yield	50a Fallout Region		30a Fallout Region	
	$A_{10°}$	$A_{30°}$	$A_{10°}$	$A_{30°}$
1/2	2	3	26	40
1	4	5	60	110
3	11	18	190	340
11	25	37	400	840
27	44	79	500	1600

		Cross-Sectional Area of Cell (as stated above)*	Upper Range of Vertical Velocities (ft/sec)*	Maximum Altitude of Development (K ft)	Probable Life Time of Parcel in Development (hrs)
Class I					
A:	Cyclones	1-10	1/4	50	10-20
B:	Frontal Upglide	1-10	1/4	25-30	10-20
C:	Sea Breeze	10-20	1	3	1-2
Class II					
A:	Lee Waves	50-100	20-50	15-50	1/2-1
B:	Slope Turbulence	10-50	10-25	10-15[2*]	1/4-1/2
C:	Mtn-Valley Winds	10-50	5-15	2-3[3*]	1/4-1/2
Class III					
A:	Thermals	1/50-1/25[4*]	6-20	3-8	1/10-1/5
B:	Strong Thermals	1/25-1/5	10-30	5-20[5*]	1/10-1/2
C:	Thunderstorms	1/4-1	50-120	30-60	1/10-1/5
D:	Mass Fire	1/25-1/5[6*]	10-30	25-30	1/4-3/4
	(Whirls)	0	500	2	1/20-1/10

* The areas reported are maximum cell cross sections; it must be noted that the upper range velocities also reported apply to the central core of the cell and therefore exist over much smaller areas.

2* height usually 2 x obstacle height; however, stationary wave of large amplitude reappears at 5 x obstacle height.

3* upslope currents are usually shallow; however, they can continue development as cumuli, thus attaining heights of 7 to 10,000 ft.

4* area given as that for a single cell, characteristically many such cells existing simultaneously can cover areas of tens to hundreds of square miles.

5* heights of 3 to 5,000 ft are maximal in coastal regions; in central U.S., heights of 18 to 25,000 ft are possible.

6* area given is for single convective column; many such columns would exist simultaneously over a large mass fire; such columns characteristically form over hot spots in the fire and shift from spot to spot.

would influence close-in fallout, especially for the smaller yields, if they occurred in the vicinity of GZ and shortly after burst. Such influences are borne out by Figures 9 and 10, where the altitudes above which particles fall faster than the stated velocity are plotted against particle size. Also indicated are the upper range velocities and vertical developments tabulated in Table II; cumulative percentage activity below stated size is given below the size scale. Thus, the altitudes and maximum particle sizes at which Class II and III vertical currents can cause large effects and their relative importance can be appreciated. Although sea-breeze circulation has been shown to alter fallout patterns,[57] cell depths are small as shown in Figure 10, and the effect is confined to a coastal strip 20 to 25 miles wide in temporate latitudes.

Only intermediate fallout with terminal velocities around 1 ft/sec or less (about 50 to 20% of the total activity) has a high probability of being affected by meteorological phenomena (vertical currents, precipitation, etc.). Duration of transport, the large cross-sectional area of cyclonic or frontal air movements, and the frequency of rainfall all operate to increase this probability. Air flow around or over mountains does affect fallout pattern shape as shown by Feteris et al,[56] but such changes do not alter fallout intensity except near the edges of the very large regions subjected to intermediate fallout. Vertical currents or rainfall do, on the other hand, cause variations in fallout intensity ("hot spots") but can influence only those particles still aloft, i.e., the slowly falling particles. In these size ranges, it is generally accepted that 90% of fallout activity is washed out by rain.[58] Thus a difference in deposition mechanism (rain scavenging as opposed to settling) can be postulated. Alexander's studies in Clallam Co.[59] suggest that "dry fallout" in the particle size ranges characteristic of intermediate-to-global fallout is a relatively unimportant deposition mechanism. Greenfield[60] has quantitatively analyzed the rain scavenging

process and found it to be highly efficient for particle sizes in the 10 to 50μ range. Finally, it is obvious that all close-in fallout models are not adequate for deposition mechanisms other than settling. A gray region of considerable extent exists between close-in models and models appropriate to intermediate fallout. This region should be more thoroughly investigated.

In the intermediate region, prediction of fallout hazards extends beyond the calculation of radiation fields to the consideration of fission product entry into the biosphere with plants acting as the principal interface for such incorporation. A complete description of intermediate fallout deposition and uptake into plants is beyond the scope of this paper; for such considerations the reader is referred to Fowler,[61] Eisenbud,[62] or Schultz and Klement.[63] The intent here is to discuss salient differences between intermediate fallout and close-in fallout as represented by ceniza-arena.

There appear to be at least three important differences. First, is the matter of particle sizes efficiently retained. Larson et al[64-66] have concluded from observations made at the Nevada Test Site (NTS) that sizes greater than about 44μ are not efficiently retained on plant surfaces. Their observations in that desert region are largely confined to such genera as Larrea, Artomisia, Atriplex, or Coleogyne, plants whose vestiture is variously described as scurfy, pubescent, canescent, glandular, or resinous. Such vestitures can certainly be expected to retain more large particles than the glabrous plant surfaces (avocado, camphor, etc.) observed on Operation Ceniza-Arena. Unfortunately, even though approximately 20% of the mass frequency distribution for ceniza-arena is reported to be below 44μ (sieve diameter),[47,48] the preponderance of larger sizes is such as to mask the retention of these smaller sizes. Furthermore, Russell[50,67] suggests that efficiently retained sizes are considerably smaller than 44μ. This hypothesis has recently been substantiated by the observations of Martin[51] who finds that most of the

fallout material retained on Artemisia tridentata and Atriplex confertifolia is less than 5μ in diameter (again plants with vestitures presumably more capable of retaining larger particles than glabrous tropical plants).

Secondly, the half life of intermediate fallout on plant surfaces is considerably longer than that characteristic of coniza-arena under dry conditions. Russell[68] has reported leaf retention half lives of 14 days. Martin[51] has shown by extensive statistical analysis that the environmental half life, T_E, ranges between 13 and 24 days for I^{131} and between 18 and 57 days for Sr^{89}. T_E is defined as loss due to factors other than decay and is therefore properly comparable to coniza-arena half lives (2 to 6 hours under similar conditions, i.e., dry, moderate winds). In this instance, the vestiture of the desert plants might partially explain the discrepancy; however, differences as high as two orders of magnitude seem too large for such an explanation.

The shorter half-life shown by I^{131} deserves special mention since this phenomenon is apparently an example of refractionation of volatile fission products after deposition. In his careful statistical analysis, Martin[51] is able to establish a validly shorter T_E for I^{131} of 14.5 days for close-in fallout at downwind distances of ~ 22 mi. He suggests that I^{131} in close-in fallout is in such a chemical or physical form that loss from plant surfaces by vaporization is possible. A similar hypothesis has been advanced by Cline.[69] Martin describes a sorting half life, T_{dsi}, defined as:

$$T_{dsi} = \frac{T_{Es} \times T_{Ei}}{T_{Es} - T_{Ei}}$$

where T_{Es} and T_{Ei} = the environmental half lives for Sr^{89} and I^{131} respectively. T_{dsi} can be considered the length of time necessary to sort half of a volatile fission product away from a non-volatile one. T_{dsi} is ~ 30 days for fallout at 22 miles, implying relatively rapid sorting in comparison to T_{dsi} of 189 days at more distant locations. The

physical and/or chemical causes for these changes in iodine behavior are not yet fully understood.

Thirdly and finally, the probability that close-in fallout arrives "dry" (at least in the absence of rainfall) is much greater than that for intermediate fallout, 90% of which is characteristically washedout by rain.[58] As far as subsequent uptake by the plant and relative importance to agriculture is concerned, the difference between dry settling and wet washout would appear important. Radioactive slurries or solutions are more deeply incorporated into the cuticular mosaic of leaf surfaces; indeed, Moorby and Squire[70] have suggested that Sr^{89} applied to cabbage, potato, and rye grass as a fine spray becomes airborne again after 2 to 3 weeks with the dehiscence of cuticle platelets. Within and under the leaf cuticle, moisture content is higher and more constant than on the leaf surface. This condition enhances foliar uptake, a process similar to root uptake,[61] both requiring liquid water and beginning with a cation exchange in the apoplast followed by a metabolically mediated absorption into the protoplasm.

The differences enumerated between intermediate fallout and ceniza-arena may be important. No argument is raised concerning the similarity of close-in fallout to ceniza-arena. In fact, preliminary ceniza-arena data are used in this paper to evaluate the importance of plant retention in the close-in region. When, however, intermediate fallout is considered, differences in sizes retained, in environmental half life, and in the deposition mechanism itself certainly reduce the confidence with which ceniza-arena data can be extended to assess agricultural hazards. More research is required to improve the prediction of agricultural hazards resulting from fallout. Also required is the clear recognition that present military fallout models are sufficient for the prediction of close-in fallout hazards, but become increasingly invalid with longer times after burst. Therefore, meaningful extension of present model systems to the intermediate fallout region must accompany the prescribed research.

APPENDIX A

VERTICAL CURRENTS

The following collection of notes were hastily gathered to obtain order of magnitude answers to such questions as:

(a) What vertical velocities are to be found in the troposphere?

(b) How big are they (cross-sectional area, height of vertical movement, or any other appropriate measure)?

(c) What is the probability of encountering such vertical air currents in a given region (especially of the U.S.), time of day, or season?

(d) How long is a given parcel of air influenced by such vertical movement?

These questions are not easily answered.* Many of the answers given here are subject to argument. Therefore, the source data and modifying comments from which the numerical values in Table II were estimated are assembled into this appendix. In general, it should be noted that the areas given are maximum cross-sectional areas for the particular phenomenon, while the upper range velocities given apply only to the center or core of the development whose cross-sectional area could be 1/10 to 1/100 of the maximum. Altitudes reported are the upper range normally observed for the phenomenon. Durations of influence on a given parcel (reported in Table II) are estimated on the basis of average vertical velocity and height of column. These last especially, must be considered no better than order of magnitude estimates.

*Machta[72] mentions among weathermen's failings: "failure to measure vertical currents or atmospheric turbulence."

Class I: Large area, relatively slow moving, relatively long duration, usually large air mass developments.

A: CYCLONES[56,71,72] —— large vertically moving parcels of air resulting from convergence or divergence.

Area: thousands to tens of thousands sq mi (core: tens to thousands sq mi)

Velocities: 0.03 to 1.0 ft/sec (see Notes)

Altitude: to 50K

Notes: Velocities of 1 ft/sec are extreme values reported by Rex; according to Machta[73] normal maximum velocities should be a quarter of this extreme value. Although Rex calculates that velocities can increase on ascending, the reverse would more usually be observed since such behavior is consistent with expansion on ascending. Particles converge at base of updraft columns and diverge at base of downdraft columns; also there is advection of particles from downdraft to updraft regions. Vertical motions organized into upward and downward parcels having dimensions of many hundreds of square miles.

B: FRONTS[74] —— upglide of warm air at frontal surfaces.

Area: thousands to tens of thousands sq mi

Velocities: 0.03 to 1.0 ft/sec (see Notes)

Altitude: to 25K ft

Notes: These movements are similar to cyclones described above. Again vertical velocities of 1 ft/sec must be regarded as extreme, see discussion under cyclones.

C: SEA-BREEZE[57,75] —— a landward current adjacent to earth's surface with a much weaker, but deeper, return flow at low altitude - dependent upon land-sea temperature differences.

Area: tens to twenties of sq mi for individual cells - along coasts penetrating inland 20 - 25 mi. (temperate region).

Velocities: to 1 ft/sec

Altitude: 150 ft to 3K

Notes: Cells first develop at sea then move inland during day until at ~ 1500 (time of maximum development), horizontal velocities to 35 ft/sec with accompanying vertical velocities of 1/100 to 1/50 this value are developed. The circulation dissipates after 1500 and is usually gone by 2000. Reverse flow during night is also observed. In tropics, development can extend several hundred miles inland with vertical developments to 10K or 12K ft.

Class II: Intermediate to large area, intermediate to fast moving, long duration but dependent on wind speed - usually orographic developments.

A: LEE WAVES[75,78,79]—— a laminar flow phenomenon forming in lee of mountains, hills, and ridges.

Area: fifties to hundreds sq mi - function of topography: can be as long as the obstacle on the ground and extend downwind to distances of 10 to 100 mi.

Velocity: low: 1/2 to 1 ft/sec
avg: 10 to 20 ft/sec
hi: to 50 or 100 ft/sec

Altitude: 1K to 20K ft with high stability and moderate winds
15K to 50K ft with lower stability and strong winds
usually 3x to 5x height of obstacle

Notes: Foremost lee wave is strongest; wave crests are stationary. Wavelength is primarily a function of wind speed and atmospheric stability (wavelengths of 1 to 10 mi. characteristic). Wave amplitude is primarily function of obstacle shape. Waves can exist for long periods of time (as long as wind and stability last), but mid-day turbulence tends to weaken or break them up. Can reform in late afternoon or night if wind and stable conditions continue. Parcel of air moves through lee waves at wind speed (usually 20 to 80 ft/sec). Rotors are occasionally formed under lee waves of large amplitude; Sierra lee waves have developed rotors rising to 16K ft. Clear air turbulence is thought to occur upon transition from strong winds to weaker ones.

B: SLOPE TURBULENCE[75,78,79]—— turbulence developed in unstable air blowing against hills or mountain ridges

Area: tens to fifties sq mi, function of topography

Velocity: function of windspeed - usually 10 to 25 ft/sec

Altitude: 10 to 15K - usually not greater than 2 x height of obstacle (but frontal waves reappear at 4 to 5 x height of obstacle).

Notes: Really little data other than comments of sail-plane pilots. If flow laminar, air tends to flow around obstacle, and there is little lift according to sail-plane pilots.

C: MOUNTAIN-VALLEY WINDS[75,78]—— diurnally varying winds due to differential heating between valley floor and ridges.

Area: tens to fifties sq mi, function of valley dimensions.

Velocity: downslope (night) to 8 ft/sec; upslope (midday) to 13 ft/sec; along valley approximately same magnitude as reported for slope winds.

Altitude: 1000 ft above ridges; upslope at midday can continue into cumulus development (7K to 10K ft).

Notes: These winds flow down-valley during late night; in morning upslope winds start providing return flow for down-valley winds. Flow reverses to up-valley winds (first with upslope, then pure up-valley) during late afternoon. In early evening downslope winds begin, eventually reversing flow during late night to down-valley winds described initially. Maximum slope velocities encountered at 100 to 150 ft above slope surface; flow is steady on gentle slopes, tends toward gustiness on steeper slopes. It is not uncommon for valley wind systems to run at right angles to winds at altitudes greater than ridge height.

Class III: Small to intermediate area, relatively fast moving, short duration —— usually thermal developments.

A: THERMALS[74,77,79]—— thermal bubbles or columns rising from a heat source on the ground to cloud base height where they dissipate.

Area: 0.02 - 0.04 sq mi or 600K to 1000K ft^2 (dia. 500-1000 ft for single cell near ground expanding upon ascent——see clusters, under notes).

Velocity: 6 to 20 ft/sec (near base)

Altitude: 2 to 5K ft depending on local conditions

Notes: Thermals are arbitrarily divided into mild or central valley thermals and large or "desert" thermals which do not develop near coast. Velocities are characteristically greatest at the base. Atmospheric turbulence tends to break up thermals. A cluster or family of thermals can cover half the surface area of a sq mi——they form a complex of downdrafts and stronger updrafts periodically breaking from the heat source and moving with the surface wind. Fair-weather cumuli (U.S.) have typical updrafts of 1 to 5 ft/sec preceding cloud which is followed by somewhat weaker downdrafts. A vigorous cell lasts a few tens of minutes; development 2K to 8K ft near coast, 5K to 17K ft in central U.S., and 10K to 25K ft over New Mexico.

B: STRONG THERMALS[74,79]—— inland thermals developing over playas or desert flats (more intense heat sources than found near coasts).

Area: 0.04 to 0.15 sq mi or 800 to 3000K ft^2 (dia. 50 to 2000 ft near ground expanding to 1 or 2 mi on ascending).

Velocity: 20 to 30 ft/sec near ground decreasing with ascent.
Velocities in thermal core:
10-20 ft/sec = normal strong
20-30 ft/sec = very strong
20-60 ft/sec = maximum (really cumulonimbus development, see Thunderstorm).

Altitude: to 18 or 25K ft in central U.S.
(higher development possible in thunderstorms)

Notes: Dust devils spin on ground for 2 to 5 minutes, then thermal bubble "breaks off" and rises to 5K or 10K ft usually, but to 18K ft over Mohave or near Reno. Velocity greatest at lower altitude; bubble expands as it ascends and vertical velocities decrease. Dust is visable to sail-plane pilots riding these thermal bubbles; therefore, bubble acts like parcel capable of carrying dust. Further evidence of parcel behavior; pilots say they can smell thermals, especially if they originate over a barnyard. Atmospheric turbulence tends to break up thermals, making them less powerful sources of lift.

C. THUNDERSTORMS[77,80]—— consist of several violent thermal cells, each of which has three life stages. (see Notes.)

Area: 1/4 to 1 sq mi (developing); 3 to 3 sq mi (mature and dissipating - but see notes on storm complexes).

Velocity: 50-70 ft/sec (developing)
100-120 ft/sec (mature, updraft)
50-70 ft/sec (mature, downdraft)
decreasing velocities during dissipation
(a 350 ft/sec downdraft has been reported)

Altitude: 10-15K (developing)
20-25K (mature)
37-50K (dissipating)

Notes: Thunderstorms are a complex system of violent thermal cells. Life stages of cells are: (1) developing cell——sometimes can develop from cumulus to cumulonimbus in 10 minutes (from 3500 ft to 3 mi in diameter) forming tall cylindrical column (height: 15K ft) of warm air with speeds in upper part of 50 ft/sec; 2) mature cell——column rises to heights of 20 to 25K ft, lasting 15 to 30 minutes; updraft speeds of 100 to 120 ft/sec; falling rain starts downdrafts; downdraft speeds of 50 to 70 ft/sec; 3) dissipating cell——development can reach heights of 37 to 50K ft; vertical velocities decreasing; dissipating stages more prolonged (can last hours). A complex of thunderstorm cells (~ 3 mi dia.) can exist over an area of 200 sq mi with non-turbulent air between cells. Highest velocities near cloud tops (cf. other vertical currents); duration from 10 to 40 minutes.

D: **MASS FIRES**[81-83]—— consist of a complex system of convective columns (large and small) and associated larger downdrafts over burning fuel; phenomenon further complicated by fire whirl formation.

(a) Convection Columns

Area: thousands to tens of thousands sq ft extending over area of burn; function of size of hot spots and topography.

Velocity: to 50 ft/sec immediately over burn; at 1000 ft velocity corresponding to strong thermals (10 - 30 ft/sec) decreasing with altitude

Altitude: to 10 - 30K ft depending on size of burn and wind shear

(b) Fire Whirls

Area: very small - tens to hundreds of sq ft

Velocity: reaching tornado speeds (500 - 1000 ft/sec vertical development has been observed.

Altitude: 600 to 2000 ft (maximum)

Notes: Whirls usually form on lee of burning ridges; however, little is presently known about them.

APPENDIX B

OPERATION CENIZA-ARENA

The following notes were taken from the preliminary reports of Carl F. Miller et al[38-46] of Stanford Research Institute (SRI) and two final USNRDL reports.[47,48] The numbers given are simply representative of the raw data reported. Since unpublished material, not known to the authors, may alter matters considerably, values given in this appendix must be regarded as only approximate until confirmed by Miller's final report. Little attempt has been made to correlate the raw data from one preliminary report with that from others; therefore, the data is largely organized by basic reference.

1. ESTIMATION OF w_p AND ρ_t FOR TREES AND GRASSES.

Foliar surface density, w_p, is defined:

$$w_p = \frac{\text{g plant (dry wt)}}{\text{ft}^2 \text{ of surface}} \text{ assuming normal stand density.}$$

In a forest, crown interception tends to a minimum, therefore, the canopy diameter is used to determine surface area covered by a forest tree. In the estimation of tree density, ρ_t, certain simple geometric shapes are assumed to be characteristic of tree habit. Conversion from tree dimensions to dry weight is done by means of Woodwell's formulas.[84]

dry weight of leaves = $0.002hd^2$

total dry weight above ground = $0.029hd^2$

total dry weight excluding leaves = $0.027hd^2$

where

h = tree height in meters, and

d = trunk diameter at breast height in centimeters, for dry weight in kilograms.

This formula is particularly sensitive to tree diameter, a parameter not yet measured by Miller et al. Estimates of such diameters were obtained from members of the Operation Coniza-Arena team. Values of w_p are given for the whole tree (above ground) and for leaf weight only. The latter is probably the best value to be used in the estimation of total retentive plant surface (although trunk, twigs, etc., do increase that surface). Accordingly, leaf weight is used in the calculation of the percentage of total deposition per unit area retained by the plant.

In the calculation of tree density, ρ_t, Woodwell's dry weight must be converted to live weight. For this conversion, the live weight of woody material is assumed to be twice dry weight and live weight of leaves ten times dry weight. For radiation field calculations, the density of the "tree slab" (that of the canopy only) is desired. It is therefore assumed that 1/4 of the woody material is contained in the trunk below the canopy. Thus, the live weight of interest becomes:

$LW_{trees} = [2 \times 0.027 \times 3/4 + 10 \times 0.002]\ hd^2 = 0.06hd^2$ and the

dry weight formulas are, as given before:

$DW_{leaves} = 0.002hd^2$

$DW_{total} = 0.029hd^2$

Actually the density of the "tree slab" must include air as well as plant material. Since the amount of air displaced by the tree is negligible when compared to the total volume of the canopy, air density (0.001 g/cc) is simply added to the calculated tree density and the sum reported as ρ_{ta}.

A. LAUREL TREE (Kalmia? Umbellularia? Described as small broad-leaf trees (mountain-laurel like), approx. 1 mi. from Rancho Redondo, Station 15, Ref. 45).

height: 15 ft, 4-1/2 m (heights 10 to 20 ft densely packed stand)

trunk (est): 6" (DBH*), 15 cm

$\therefore hd^2 = 1000$

canopy: 8 ft (diam)

$\therefore A = 50\ ft^2$

assumed canopy shape: sphere with 8 ft diameter

$\therefore V = 4/3\ \pi\ (4)^3 = 268\ ft^3 = 7.6\ m^3$

$LW_{trees} = 60.\ kg$ $\rho_t = .0079\ g/cc$ $\rho_{ta} = .0089\ g/cc$

$DW_{leaves} = 2.0\ kg$ $w_p(lvs) = 40\ g/ft^2$

$DW_{total} = 29.\ kg$ $w_p(tot) = 580\ g/ft^2$

$a_L(ave) = 0.04$ range: 0.001 to 0.1

$W_p(lvs)\ a_L = 1.6$ 0.04 to 4.0

percent retained = 100% 4% to 100%

B. PINE TREE (Pinus? Described as pine-type trees on ridge near Rancho Redondo, Station 16, Ref. 46).

height: 25 ft, 7-1/2 m

trunk (est): 5" (DBH), 13 cm

$\therefore hd^2 = 1300$

canopy: 8 ft (diam)

$\therefore A = 50\ ft^2$

*Note: DBH = diameter breast height

assumed canopy shape: cone with 8 ft base diameter and 20 ft height

$\therefore V = 1/3\ \pi\ 4^2 \times 20 = 335\ ft^3 = 9.5m^3$

LW_{trees} = 78. kg ρ_t = 0.0082 g/cc ρ_{ta} = 0.0092 g/cc

DW_{leaves} = 2.6 kg $w_p(lvs)$ = 52 g/ft^2

DW_{total} = 38. kg $w_p(tot)$ = 760 g/ft^2

$a_L(ave)$ = 0.0068 range: 0.0001 to 0.02

$w_p(lvs)\ a_L$ = 0.035 0.0052 to 1.04

percent retained = 3-1/2% 1/2% to 100%

C. AVOCADO (Persea americana? Tree located near Plot #1, Ref. 43)

height: 15 ft, 4-1/2 m

trunk (est): 8" [DBH], 20 cm

$\therefore hd^2 = 1800$

canopy: 8 ft (diam)

$\therefore A = 50\ ft^2$

assumed canopy shape: truncated cone with 8 ft base diameter, 3 ft top diameter, and 10 ft height.

$\therefore V = 1/3\ \pi\ (1^2 \times 16 - (1.5)^2 \times 6) = 254\ ft^3 = 7.2m^3$

LW_{trees} = 108. kg ρ_t = 0.015 g/cc ρ_{ta} = 0.016

DW_{leaves} = 3.6 kg $w_p(lvs)$ = 72 g/ft^2

DW_{total} = 54. kg $w_p(tot)$ = 1080 g/ft^2

a_L(ave) = 0.01 range: 0.004 to 0.02

w_p(lvs) a_L = 0.72 0.29 to 1.4

percent retained = 72% 29% to 100%

D. CAMPHOR TREE (Cinnamomium camphora? Aborescent tree near Plot #2, Ref. 43)

height: ~ 12 ft., 3-1/2 m.

trunk: 3 trunks, 2-1/2" diam; equiv. circle 4.3", 11 cm.
$\therefore hd^2 = 420$

canopy: 6 ft
$\therefore A = 28\ ft^2$

assumed canopy shape: cylinder with 6 ft diameter and height of 6 ft
$\therefore V = \pi 3^2 \times 6 = 169\ ft^3 = 4.8 m^3$

LW_{trees} = 25. kg ρ_t = 0.0053 g/cc ρ_{ta} = 0.0063 g/cc

DW_{leaves} = .84 kg w_p(lvs) = 30 g/ft^2

DW_{total} = 12. kg w_p(tot) = 430 g/ft^2

a_L(ave) = 0.016 range: 0.005 to 0.03

w_p(lvs) a_L = 0.48 0.15 to 0.90

percent retained = 48% 15% to 90%

E. "Tree" slab desities are affected by the assumed canopy shapes which are debatable; therefore, desities for the four types described are averaged to obtain a value for the radiation field calculations.

$$\overline{\rho_{ta}} = 0.01 \text{ g/cc}$$

F. GRASSES

Some of Miller's reported w_p for cereals and other plants are presented below; either the high value or the range of values are tabulated:

	barley (g/ft^2)	oats (g/ft^2)	wheat (g/ft^2)	corn (g/ft^2)	beans (g/ft^2)
1 mo	8.1	13.	9.2		3.1
2 mo	46.	37.	38.	0.2 - 2.	8.9
3 mo	32. - 60.	31. - 78.	19. - 27.	8. - 22.	5. - 13.
4 mo	35. - 59.	41. - 70.	20. - 34.	6. - 40.	
5 mo	33. - 91.	37. - 81.	21. - 36.	19. - 42.	

Assume w_p for wild grasses ranges between 20 and 80 g/ft^2.

a_L .001 at 3 mo
.01 at 4 mo
.05 at 1 mo (lawns and young wild grasses), or at
5 mo (mature grain-bearing grasses).

thus: lawns or grain-bearing grass — 100%; Young wild grass — 2 to 8%; mature wild grass — 20 to 80%

Grasses may be compared with other types of vegetative cover. Thus:

GRASSES	CHAPARRAL	FOREST		
			leaves	total
20 - 80 g/ft^2	? (probably more like forest)	laurel	40 g/ft^2	580 g/ft^2
		pine	52	760
		avocado	72	1080
		camphor	30	430

Note that foliar surface density from grass to forest remains about the same. This constancy implies a maximum leaf density beyond which photosynthetic efficiency begins to drop. Foliar surface density, w_p, should

exhibit a sigmoid growth curve, which it probably does although observation intervals are too long for good growth data.

Miller's reported a_L for cereals and other plants (range and ave. values) are as follows:

	barley	oats	wheat	corn	beans
1 mo	.006-.11 .05	.005-.05 .03	.006-.11 .06		.01-1.3 .2
2 mo	.001-.04 .05	.0005-.04 .01	.001-.03 .001		.003-.05 .03
3 mo	~0-.03 .0008	.001-.02 .0006	.001-.02 .0008	.01-.07 .03	.007-.04 .02
4 mo	.006-.01 .007	~0-.009 .008	.0002-.01 .004	.02-.08 .02	
5 mo	~0-.1 .05	~0	.007	.002-.2 .06	
6 mo				.04-.3 .1	

Trend of a_L (ave) for cereals is interesting and could be characteristic of growth and habit (other explanations entirely unassociated with growth are also possible). The decrease by two orders of magnitude between one-month-old and three-month-old crops suggests that as grasses increase in height their bending in response to winds significantly decreases their ability to retain foliar contamination. The fact that a_L (ave) subsequently increases by an order of magnitude from a low at 3 month is probably indicative of the increased retentive capacity of the developing heads of grain.

2. MISCELLANEOUS NOTES

A. DEPOSITION RATES

Rates of dry ceniza deposition reported range between 0.05 g/ft^2 per hour to 2.8 g/ft^2 per hour (ref. 39). One dew balance rate is ~14 g/ft^2 per hour, all in 1 hr with a zero rate for 2 hours to either

side (suspect a stuck balance). Total loadings of 444 g/ft^2 are reported.

B. WIND WEATHERING

Situation #1 (ref. 39): 2-mo-old wheat (wheat 1 located on windward side of plot, wheat 2 located near center of plot); loading ~7 $\frac{\text{g ceniza}}{\text{g plt (dry wt.)}}$; reference time 0600 7/18; initial a_L = 0.058 and 0.042 (wheat 1 and wheat 2, respectively).

fraction remaining on plt		Δt (hrs)	ave wind spd (mph)
wheat 1	wheat 2		
.205	.113	2.50	3.2
.155	.102	2.88	4.0
.061	.180	3.33	4.5
.043	.170	3.83	4.9
.029	.100	5.75	5.2
.018	.127(spatter)	9.75	5.4+ 0.01" rain

Situation #2 (ref. 40): (damp condt.; wind = 7-1/2 mph; duration = 2-1/2 hr) fraction remaining on heads: barley = 0.90; oat = 0.71; wheat = 0.68.

Situation #3 (ref. 40): (dry condt?; wind = 2.9 mph; duration = 6 hrs) fraction remaining on plant or plant-part indicated:

beets	0.12	squash lvs	0.40	oat heads	0
cabbage	0.38	barley stalks	0.21	rye heads	0.23
carrots	0.30	barley heads	0.58	wheat stalks	0.25
corn	0.36	oat stalks	0.14	wheat heads	0.24

Smooth, vertical foliage plants lose 80-90% of particles in 6 hours; other plants 66-75%; barley heads 50%.

Situation #4 (ref. 41): (dry condt?)

fraction remaining on plt		Δt (hrs)	ave wind spd (mph)
wheat heads	.71	0.53	8.8
	.63	1.20	9.0
	.41	1.53	9.0
squash	.42	0.58	8.8
	.50	1.13	9.0

Situation #5 (ref. 43):

	fraction remaining on plt	Δt (hrs)	ave wind spd (mph)
avocado	.21	6	5.3(gusts to 14.)
beet	.31	6	5.3(gusts to 14.)
corn	.16	6	5.3(gusts to 14.)
squash	.29	6	5.3(gusts to 14.)
oat heads	.71	6	5.3(gusts to 14.)
rye heads	.67	6	5.3(gusts to 14.)
camphor tree	.25	24	3. (gusts to 14.)
rye heads	.25	24	3. (gusts to 14.)

Environmental half life is usually less than 6 hrs (except cereal heads); half lives of 1 to 1-1/2 hour are often observed.

C. RAIN WEATHERING

Rain (0.4 inches) cleans cereal heads effectively but spatter can recontaminate (ref. 40). Spatter can only be important for low vegetable crops. For rains between 0.4" and 0.8", the fraction remaining on plants ranges between 0 to .3 (excepting one value of 0.6 for wheat heads). Little trend is apparent for increased amounts of rain.

	fraction remaining on plant after		
	0.43" rain	0.77" rain	0.84" rain
barley heads	0.14	0.13	0.076
barley stalks	--	0.031	0.28
oat heads	0.016	~0.0	~0.0
oat stalks	--	0.15	0.096
wheat heads	0.047	0.61	~0.0
wheat stalks	--	0.32	0.053
squash leaves	--	0.076	--

D. WET VS DRY DEPOSITION

Usually the contamination factor under wet or humid conditions is about twice that under dry conditions (ref. 42). Thus:

$$a_L \text{ (wet)} = 2 \times a_L \text{ (dry)}$$

Considerable variation is, however, reported in this ratio (ref. 42):

	a_L(wet)/a_L(dry); (wind = 7 mph)
bean	4.9
beet	7.2
lettuce	2.7
onion	1.4
tomato	1.1
squash (leaves)	1.2 to 1.6

Particles remain on leaves of trees when leaves are damp and tend to continue as leaves dry; but dry particles are easily brushed off (ref. 45).

E. LARGE PLANT CONTAMINATION

Differences in the contamination factor, a_L, are observed for various locations within the canopy of a tree (ref. 44). Thus:

a_L (outermost leaves; windward side) = (2 to 3) x a_L (central leaves)

Differences are also reported with height (ref. 45). Thus:

$$a_L = 0.001 \text{ bottom of canopy}$$

$$a_L = 0.07 \text{ top of canopy}$$

F. PARTICLE SIZE

Mass median diameter (sieve diam.) of ceniza ranges between 60 and 100μ (ref. 47).

sieve size	% mass remaining on sieve
495	.005
295	.034
246	.082
175	1.28
147	3.44
104	24.6
88	15.6
61	27.9
43	7.72
<43	19.2

Thus, approximately 20% to toal ceniza mass is less than 43μ sieve diameter.

REFERENCES

1. Cassidy, S. H., The Fortran Computer Program for the USNRDL Dynamic Fallout (D) Model, USNRDL TR-837, 22 March 1965.

2. Burke, S. P., and Plummer, W. B., "Suspension of Macroscopic Particle in a Turbulent Gas Stream", Ind. and Eng. Chem. 20:2, 1200, (1928).

3. Dallavalle, J. M., Micromeritics, 2nd Ed., Pitman, New York (1948).

4. Davies, C. N., "Definitive Equations for the Fluid Resistance of Spheres", Proc. Roy Phys. Soc. (London) 57, 259 (1945).

5. Krey, H., data given in Schiller, L., Handbuch der Exper. Physik, Wien and Harms (ed.), Vol. IV:2, pp. 379-380.

6. Kunkel, W. B., "Magnitude and Character of Errors Produced by Shape Factors in Stoke's Law Estimates of Particle Radius", J. Appl. Phys. 19, 1056 (1948).

7. Martin, G., "Researches on the Theory of Fine Grinding, Part IV", Trans. Cer. Soc. (England) 26, 21 (1927).

8. Muttray, H., "Die Experimentellen Tatsachen des Widerstandes ohne Auftrieb", Handbuch der Exper. Physik, Wien and Harms (ed.), Vol IV:2, 233 (1932), esp. pp. 313 and 315.

9. Pettyjohn, E. S., and Christiansen, E. B., "Effect of Particle Shape on Free-settling Rates of Isometric Particles", Chem. Eng. Progr., 44, 157 (1948).

10. Prandtl, L., and Tietjens, O. G., Applied Hydro- and Aeromechanics, McGraw-Hill (1934).

11. Rapp, R. R., and Sartor, J. D., "Rate of Fall Through the Atmosphere of Irregularly Shaped Particles", Rand Research Memorandum RM-2006, 1 Nov 1957.

12. Schiller, L., "Fallversuche mit Kugeln und Scheiben", Handbuch der Exper. Physik, Wien and Harms, (ed.), Vol IV:2, 337 (1932), esp. pp. 367, 369 and 376.

13. Wadell, H., "The Coefficient of Resistance as a Function of Reynolds Number for Solids of Various Shapes", J. Frank. Inst. 217, 459 (1934).

14. "The Physics of Particle Size Analysis", Brit. J. of Appl. Phys. (London) Suppl. 3 (195).

15. Prockat, F., data given in Schiller, L., Handbuch der Exper. Physik, Wien and Harms, (ed.), Vol IV:2, pp 379, 380.

16. Rubey, W. W., "Settling Velocities of Gravel, Sand, and Silt Particles", Amer. J. Sci. 25, 325 (1933).

17. Broido, A., Corcos, G. M., and McMasters, A., A Simple Method of Determining Fall Velocity of Fallout Particles, Civ. Def. Res. Proj., series 2, issue 38 (14 July 1961).

18. Cunningham, E., "On the Velocity of Steady Fall of Spherical Particles Through Fluid Medium", Proc. Roy. Soc. (London) 83 (Ser. A), 357 (1910).

19. U.S. Standard Atmosphere from Handbook of Geophysics (Rev. ed.) MacMillan (1961).

20. Greenfield, S. M., and Rapp, R. R., RAND Fallout Symposium (U), AFSWP-1050, 1 April 1957; presentation of A. D. Anderson, Appendix C, p. 54, Figure 2.

21. Cassidy, S. H., The Fortran Computer Program for a Dynamic Fallout Mass Model, USNRDL LR-168, 25 Feb 1966.

22. Ksanda, C. F., Some Relations Between the Times of Arrival and Cessation of Fallout, USNRDL TR-833, 17 March 1965.

23. Callahan et al, The Probable Fallout Threat Over the Continental United States, Report No. TO-B 60-13, Technical Operations, Inc., 1 Dec 1960.

24. Freiling, E. C., Fractionation I, High-Yield Surfaces Burst Correlation, USNRDL TR-385, 13 Jan 1960.

25. Freiling, E. C., and Rainey, S. C., Fractionation II, On Defining the Surface Density of Contamination, USNRDL TR-631, 13 Mar 1963.

26. Freiling, E. C., Fractionation III, Estimation of Degree of Fractionation and Radionuclide Partition for Nuclear Debris, USNRDL TR-680, 12 Sept 1963.

27. Freiling, E. C., Kay, M. A., and Sanderson, J. V., Fractionation IV, Illustrative Calculations of the Effect of Radionuclide Fractionation of Exposure-Dose Rate from Local Fallout, USNRDL TR-715, 6 Jan 1964.

28. Cassidy, S. H., Generalized Land Fallout Model Computer Program (GLFMCP), USNRDL 15 Dec '65 Prototype, USNRDL LR-149, 17 Dec 1965.

29. Cassidy, S. H., Fortran Statement of the Generalized Land Fallout Model Computer Program (GLFMCP), USNRDL 15 Mar '66 Prototype, USNRDL LR-176, 16 Mar 1966.

30. Cassidy, S. H., The Computer Program (TSABND) Which Produces Tables of Mass-Chain Refractory and Fission-Product Radioactivity Content for the Particle-Activity Module of the DOD Fallout Model, USNRDL LR-173, 8 March 1966.

31. Tomnovec, F. M., Ferguson, J. M., and Weldon, D. M., The Effect of a Changing Gamma-Ray Fallout Spectrum on the Ground Roughness Factor, USNRDL TR-915, 22 Sept 1965.

32. Private communication with J. M. Ferguson.

33. Clark, D., Kawahara, F. K., and Cobbin, W. C., Fallout Sampling and Analysis: Radiation Dose Rate and Dose History at 16 Locations (U), POR 2289, 24 Oct 1963.

34. Evans III, E. C., and Shirasawa, T. H., Characteristics of the Radioactive Cloud from Underwater Bursts (U), WT-1621, 15 Jan 1962.

35. Young, G. A., The Physics of the Base Surge, NOL TR-103, 17 June 1965.

36. Penney, W. G., and Thornhill, C. K., "The Dispersion Under Gravity of a Column of Fluid Supported on a Rigid Horizontal Plane," Phil. Trans. Roy. Soc. A 244, 285 (1952).

37. Rohrer, R., and Knox, J. B., Base Surge Analysis, Project Pre-Buggy, PNE-304, Sept 1963.

38. Miller, C. F., and Lane, W. B., Operation Ceniza-Arena: 1. The Contamination of One-Month-Old Crop Plants by Particles Ejected by Volcan Irazu (Preliminary) SRI Project No. IMU-4890, preliminary report dtd June 1964.

39. Miller, C. F., and Lane, W. B., Operation Ceniza-Arena: 2. The Contamination of Two-Month-Old Crop Plants by Particles Ejected by Volcan Irazu (Preliminary) SRI Project No. IMU-4890, preliminary report dtd June 1964.

40. Miller, C. F., and Lane, W. B., Operation Ceniza-Arena: 3. The Contamination of Three-Month-Old Crop Plants by Particles Ejected by Volcan Irazu (Preliminary) SRI Project No. IMU-4890, preliminary report dtd Aug 1964.

41. Miller, C. F., and Lane, W. B., Operation Ceniza-Arena: 4. The Contamination of Four-Month-Old Crop Plants by Particles Ejected by Volcan Irazu (Preliminary), SRI Project No. IMU-4890, preliminary report dtd Sept 1964.

42. Miller, C. F., Lane, W. B., and Sartor, J. D., Operation Ceniza-Arena: 5. The Contamination of Five-Month-Old Crop Plants by Particles Ejected by Volcan Irazu (Preliminary) SRI Project No. IMU-4890, preliminary report dtd Oct 1964.

43. Lane, W. B., Sartor, J. D., and Miller, C. F., Operation Ceniza-Arena: 6. The Contamination of Six-Month-Old Crop Plants by Particles Ejected by Volcan Irazu (Preliminary) SRI Project No. IMU-4890, preliminary report dtd Nov 1964.

44. Miller, C. F., and Lane, W. B., Operation Ceniza-Arena: 7. The Contamination of Seven-Month-Old Crop Plants by Particles Ejected by Volcan Irazu (Preliminary) SRI Project No. IMU-4890, preliminary report dtd Dec 1964.

45. Miller, C. F., and Lane, W. B., Operation Ceniza-Arena: 8. The Contamination of Crop Plants and Tree Foliage by Particles Ejected by Volcan Irazu (Preliminary) SRI Project No. IMU-4890, preliminary report dtd Jan 1965.

46. Miller, C. F., Lane, W. B., and Joyce, J. L., Operation Ceniza-Arena: 9. The Contamination of Crop Plants and Tree Foliage by Particles Ejected by Volcan Irazu (Preliminary) SRI Project No. IMU-4890, preliminary report dtd Feb 1965.

47. Soule, R. R., Studies of Volcanic Fallout Related to OCD Problems, Phase I, USNRDL LR-53, 1 May 1964.

48. Crew, R. J., and Kawahara, F. K., Studies of Volcanic Fallout Related to OCD Problems, Phase II, USNRDL LR-60, 19 June 1964.

49. Miller, C. F., Fallout and Radiological Countermeasures, Vol I and II, SRI Project No. IM-4021, Jan 1963.

50. Russell, R. Scott, "An Introductory Review - Interception and Retention of Airborne Material on Plants," Health Physics 11, 1305 (1965).

51. Martin, W. E., "Interception and Retention of Fallout by Desert Shrubs," Health Phys. 11, 1341 (1965).

52. Ksanda, C. F., "Ship Shielding Calculations," Proc. Tripartite Symp. on Technical Status of Radiological Defense in the Fleets USNRDL R&L No. 103, May 1960.

53. Ksanda, C. F., et al, Gamma Radiations from Contaminated Planes and Slabs, USNRDL TM-27, 19 Jan 1955.

54. Design and Review of Structures for Protection from Fallout Gamma Radiation, OCD Professional Manual, PM 100-1.

55. LaRiviere, P. D., Early-Time Gamma Ray Properties of U^{235} Gross Fission Products, USNRDL TM-89, 9 July 1958.

56. Feteris, P. J., Kessler III, E., Newburg, E. A., The Influence of Local Winds on Fallout, Travelers Research Center, Prog. Rept. #1 Contract DA 36-039, AMC-03283 (E) dtd July - Dec 1963.

57. Kangos, J. D., The Influence of Local Winds on Fallout, Travelers Research Center Technical Report ECOM-00392-F dtd March 1966.

58. Kulp, J. L., and Schulert, A. R., Strontium-90 in Man and His Environment, Vol I: Summary, Atomic Energy Commission, Div of Biol. and Med. Report NYO-9934, May 1962.

59. Alexander, L. T., and Hardy, E. J., "Rainfall and Deposition of Sr^{90} in Clallam County, Washington," Science 136, 881 (1962).

60. Greenfield, S. M., Rain Scavenging of Radioactive Particulate Matter from the Atmosphere, J. Meteor. 4, 115 (1957).

61. Fowler, E. B. (ed), Radioactive Fallout, Soils, Plants, Foods, Man, Elsevier (1965).

62. Eisenbud, M., Environmental Radioactivity, McGraw-Hill (1963).

63. Schultz, V., and Klement, A. W., Radioecology, Reinhold Publ. Co. (1963).

64. Larson, K. H., Neel, J. W., et al. Summary Statement of Findings Related to the Distribution Characteristics, and Biological Availability of Fallout Debris Originating from Testing, UCLA-438, 1960.

65. Lindberg, R. G., et al. Factors Influencing the Biological Fate and Persistence of Radioactive Fallout, Operation Teapot, WT-1177, 1959.

66. Romney, E. M., Lindberg, N. G., Hawthorne, H. A., Bystrom, B. G., and Larson, K. H., "Contamination of Plant Foliage with Radioactive Fallout," Ecology 44, 343 (1963).

67. Russell, R. S., and Possingham, J. V., "Physical Characteristics of Fallout and its Retention on Herbage," Progr. Nucl. Energy, Series VI, Vol 3, Sect. 2, Pergamon (1961).

68. Russell, R. S., "The Extent and Consequences of the Uptake by Plants of Radioactive Nuclides," Ann. Rev. Plant Phys. 14, 271 (1963).

69. Private communication, J. F. Cline.

70. Moorby, J., and Squire, H. M., "The Loss of Radioactive Isotopes from the Leaves of Plants in Dry Conditions," Radiation Botany 3, 163 (1963).

71. Dean, G. A., and Ohmstead, W. D., Oahu Research Center Special Report No. 1, AF 19 (604) - 546.

72. AFSWP Fallout Symposium AFSWP-895 (1955), presentation of D. Rex pp 461-472; comment of L. Machta, p. 205.

73. Personal communication with L. Machta.

74. Fletcher, The Physics of Rainclouds, Cambridge Univ. Press (1962).

75. Defant, F., "Local Winds" Compendium of Meteorology, T. F. Malone (ed.), pp 655-671, American Meteorological Society, Boston (1951).

76. Booker, D. R., "Modification of Convective Storms by Lee Waves," Meteor. Monogr. 5:27, 129 (1963).

77. Scorer, R. S., Natural Aerodynamics, Pergamon Press (1958).

78. Geiger, R., The Climate Near the Ground, Harvard Univ. Press (1965).

79. Private communication with L. Arnold.

80. Ludlam, F. H., "Severe Local Storms: a Review," Meteor. Monogr. 5:27, 1 (1963).

81. Broido, A., and McMasters, A. W., The Influence of a Fire-Induced Convective Column on Radiological Fallout Patterns, Calif. Forest and Range Experimental Station, Technical Paper #32, dtd March 1959.

82. Countryman, C. M., Mass Fires and Fire Behavior, U.S. Forest Service Research Paper, PSW-19 (1964).

83. Evans III, E. C., and Tracey, E. T., Observations of Mass Fire 460-14 at Mono Lake," USNRDL LR-158, 24 Jan 1966.

84. Woodwell, G. M., "Radiation and the Patterns of Nature," Brookhaven Lecture Series No. 45, 24 March 1965.

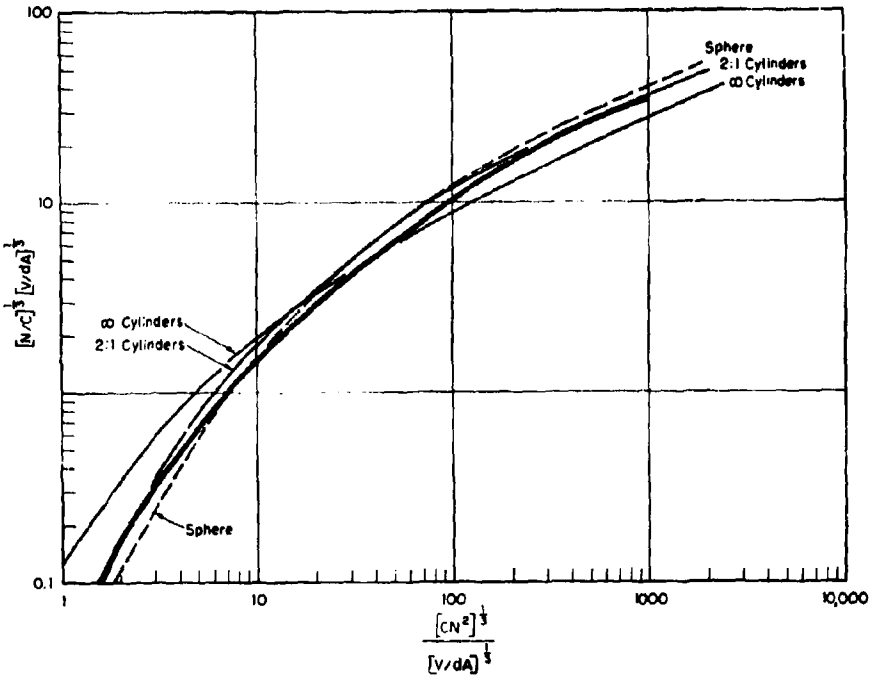

Fig. 1. A Comparison of Terminal Falling Speeds for Spheres and Cylinders as a Function of Diameter. (See text for explanation of dimensionless parameters employed.)

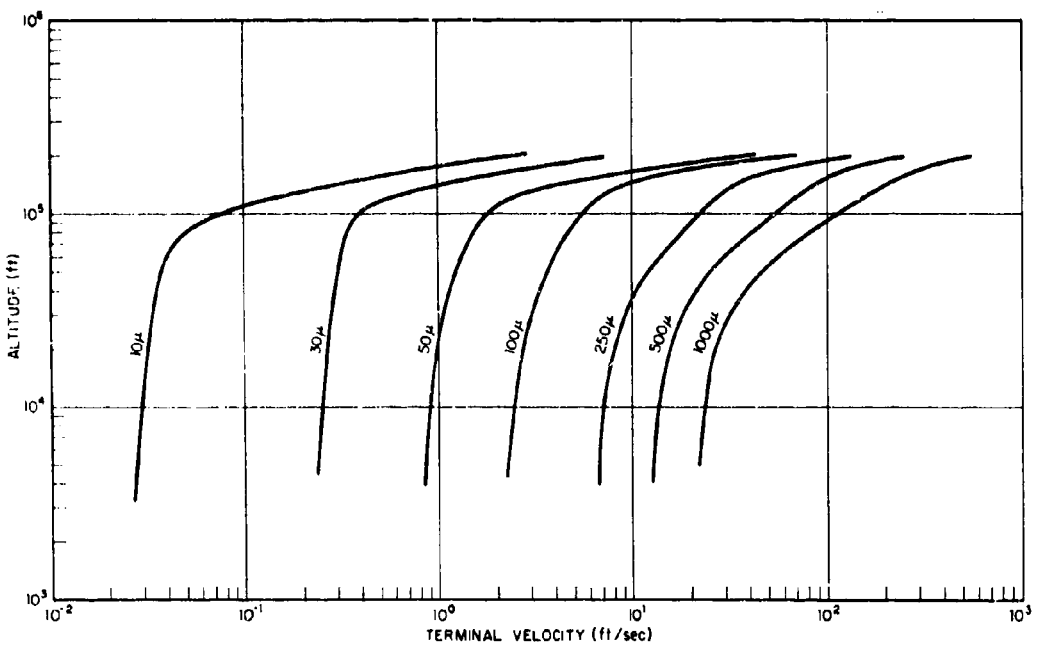

Fig. 2. Terminal Velocities as a Function of Altitude for D-Model Fallout Particles of Various Sizes

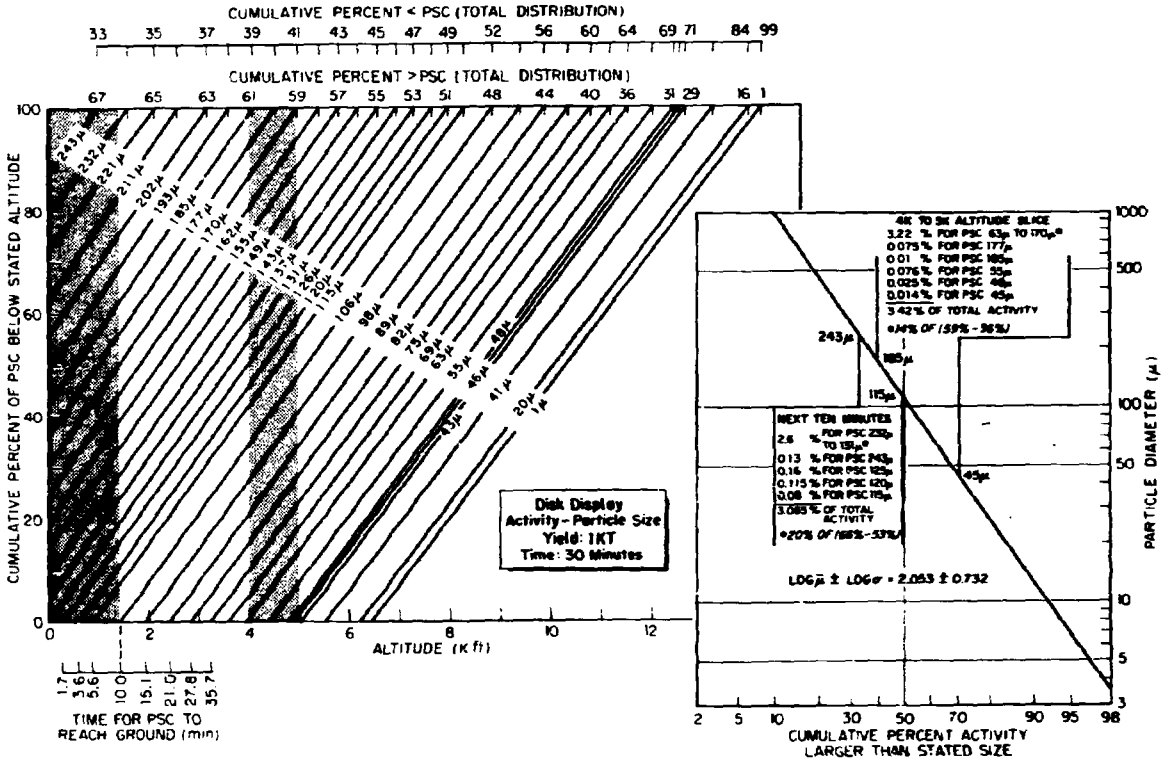

Fig. 3. USNRDL D-Model Disk Display at 30 Minutes after a 1 KT Burst. (Activity-Particle size distribution for NTS soil; ARDC 1961 atmosphere.)

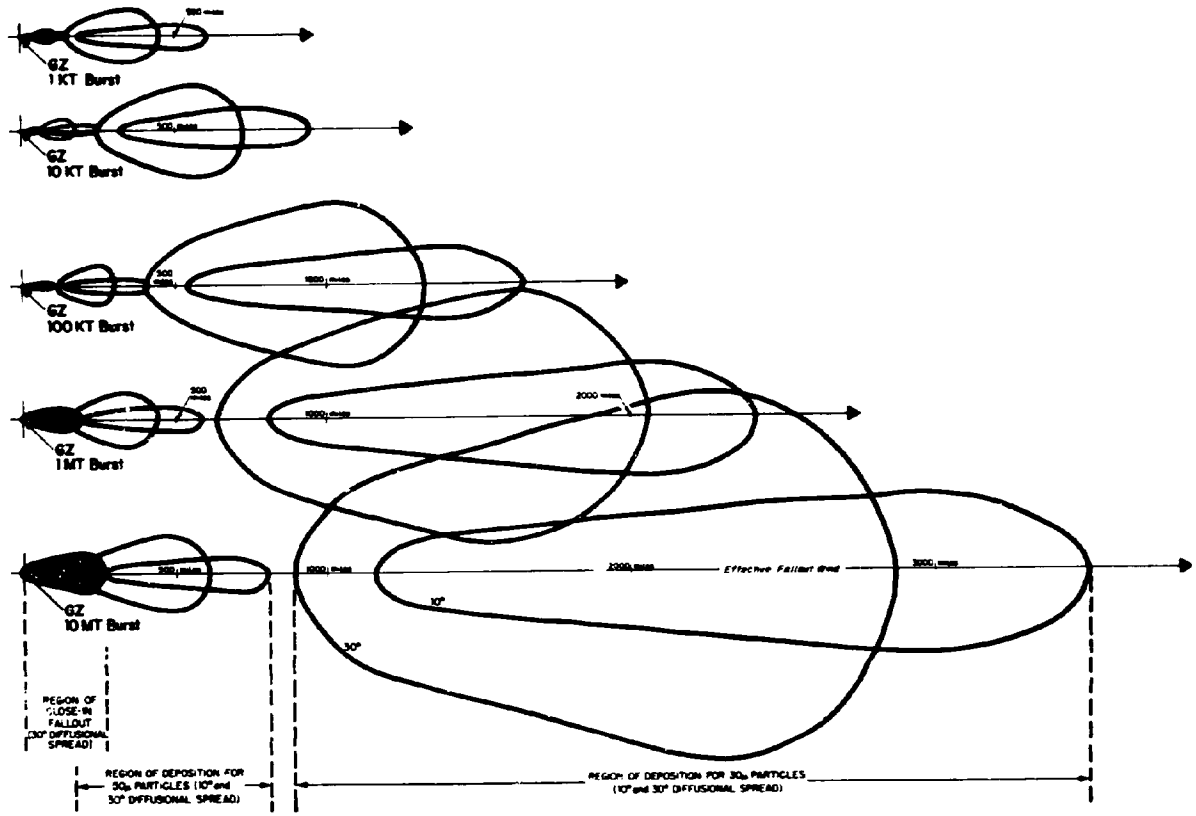

Fig. 4. Close-in and Intermediate Fallout Regions for 1 KT, 10 KT, 100 KT, 1 MT and 10 MT Bursts

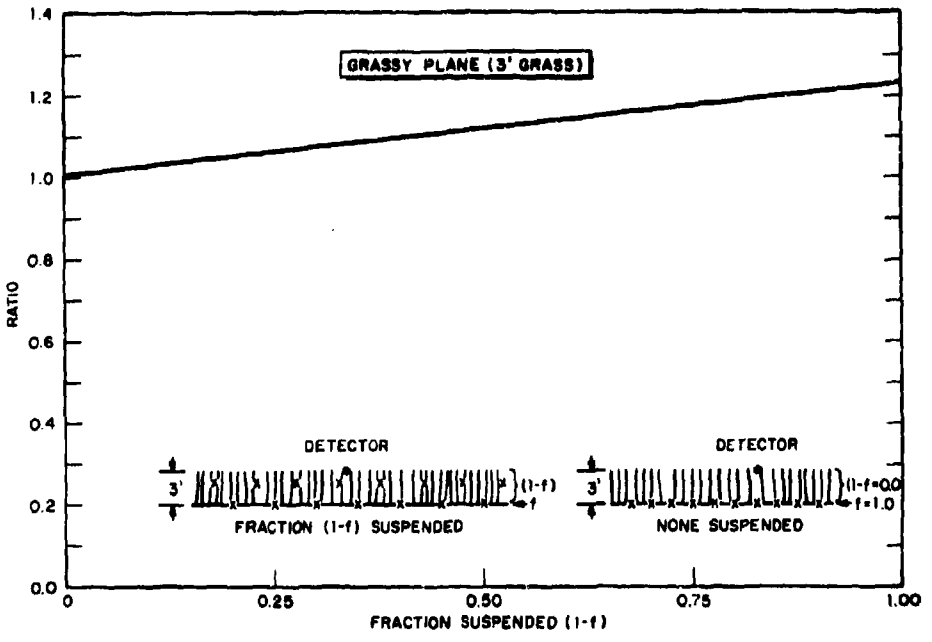

Fig. 5. Changes in Radiation Field Due to Retention of Fallout on Grass (1.25 Mev gamma)

$$\text{Ratio} = \frac{\text{3' Exposure over Grassy Plane with Fraction Suspended}}{\text{3' Exposure over Grassy Plane with None Supsended}}$$

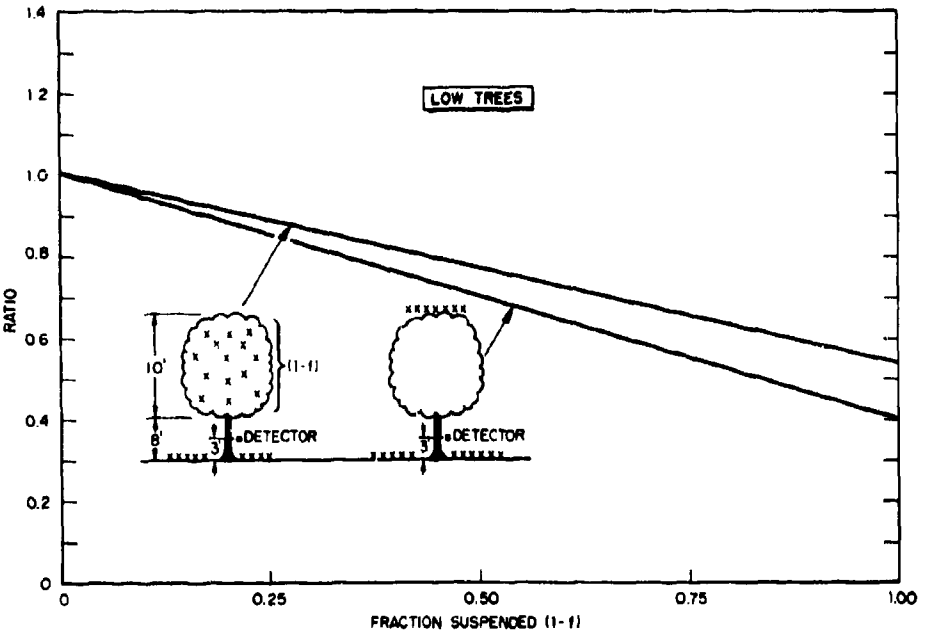

Fig. 6. Changes in Radiation Field Due to Retention in Canopy of Low Trees (1.25 Mev gamma)

$$\text{Ratio} = \frac{\text{3' Exposure Over Plane w/Fraction Suspended in Canopy}}{\text{3' Exposure Over Plane w/None Suspended in Canopy}}$$

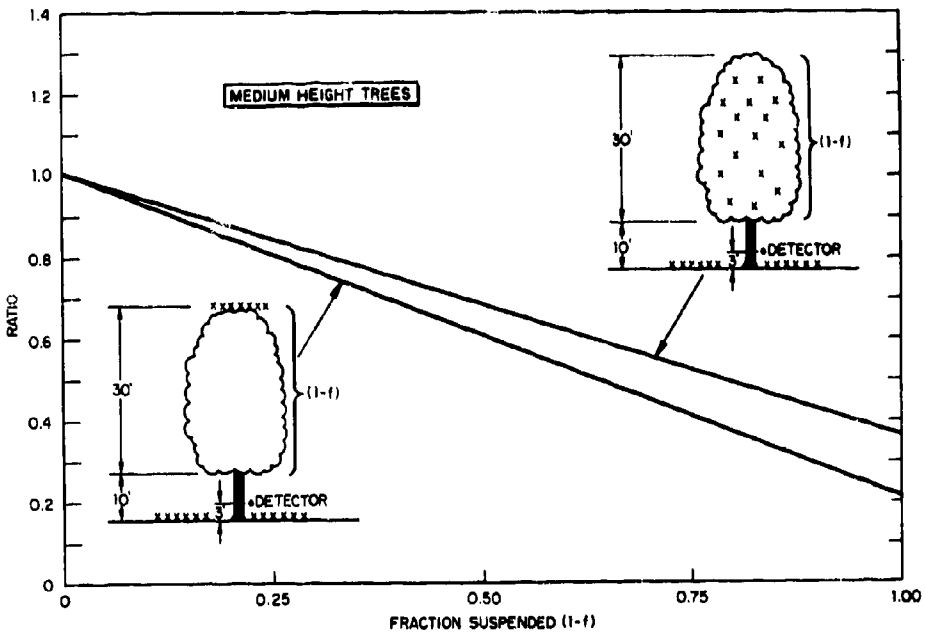

Fig. 7. Changes in Radiation Field Due to Retention in Canopy of Medium Height Trees

$$\text{Ratio} = \frac{\text{3' Exposure Over Plane w/Fraction Suspended in Canopy}}{\text{3' Exposure Over Plane w/None Suspened in Canopy}}$$

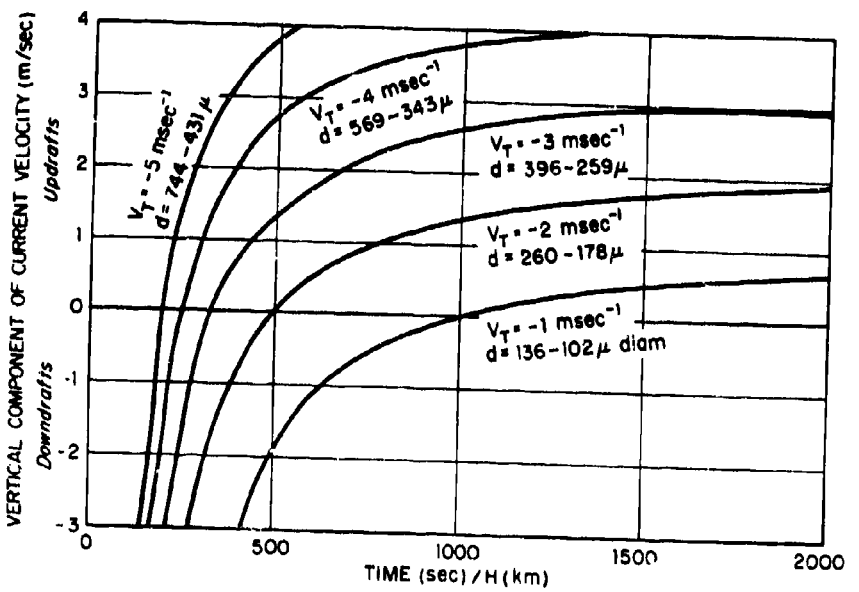

Fig. 8. Arrival Times of Fallout with Different Terminal Falling Velocities Descending through Updraft and Downdraft Columns (from ref. 56). H = height of column; V_T = terminal falling velocity (m/sec); d = particle sizes falling at stated terminal velocity at sea level and at 30K ft, respectively.

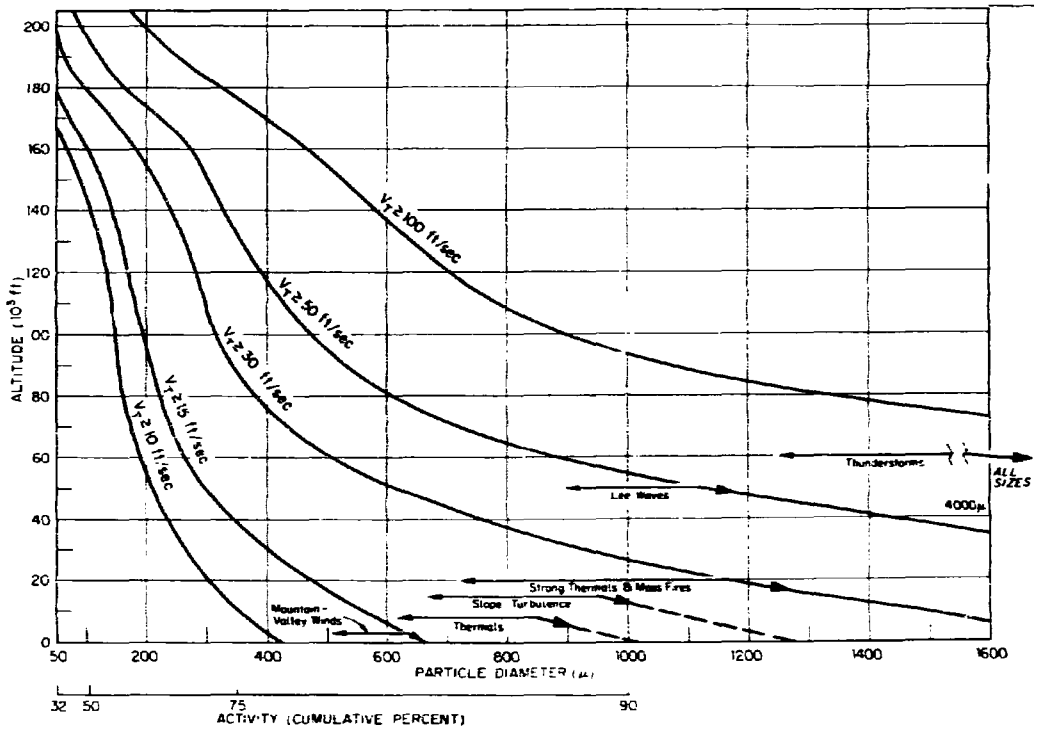

Fig. 9. Altitudes Above Which Particles Fall at Greater than Stated Terminal Velocities ($V_T \geq 10$ ft/sec to $V_T \geq 100$ ft/sec)

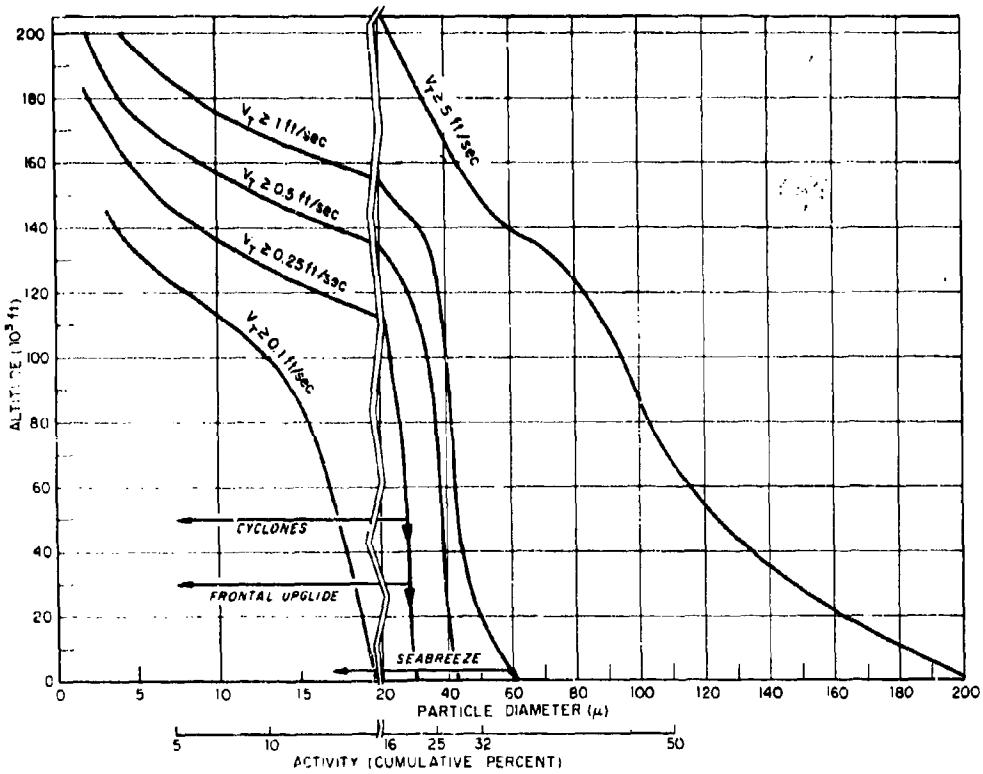

Fig. 10. Altitudes Above Which Particles Fall at Greater than Stated Terminal Velocities ($V_T \geq 0.1$ ft/sec to $V_T \geq 5$ ft/sec)

THE DOD LAND FALLOUT PREDICTION SYSTEM

R. C. Tompkins
US Army Nuclear Defense Laboratory

ABSTRACT

The DOD Land-Fallout Prediction System is a computer program based on a comprehensive description of the physics of radioactive fallout from burst until after deposition. It is designed to satisfy the following DOD requirements:

(1) The prediction of fallout for long-range planning purposes to include the estimation of the effects of potential enemy attacks and the analysis of enemy post-strike capabilities.

(2) A standard prediction system useful for determining and evaluating the intent to which given input parameters affect prediction accuracy.

(3) A comprehensive prediction model that can serve as the basis for the development of field operational prediction systems through selective simplification.

The DOD model is primarily a research tool, not an operational predictor. It is not designed to provide real-time predictions. Emphasis has been placed upon comprehensiveness, flexibility, and fidelity to the physical processes. Flexibility is achieved by a modular design that permits piecewise modifications and a variety of user options.

This model is being developed under the sponsorship of the Defense Atomic Support Agency with management by the U.S. Army Nuclear Defense Laboratory and participation by the U.S. Naval Radiological Defense Laboratory and the U.S. Army Electronics Command. A large portion of the work is under contract to Technical Operations, Incorporated.

The initial version of the computer program is scheduled to be available to users on 30 June 1966.

The DOD Fallout Model was motivated by the realization that we were faced with a proliferation of fallout prediction systems of various degrees of complexity and generally questionable reliability. This multitude of models resulted from largely uncoordinated efforts by many organizations. These old models differ in basic assumptions, technique, and nature of output. Unfortunately, they also differ in their predictions. They certainly cannot all be right, and there is a strong suspicion that none of them are. One disturbing characteristic of most past models is their calibration against some particular test detonation. Later comparisons of predictions with other tests have usually proved embarrassing.

The DOD Model is designed to avoid these difficulties insofar as possible. The effort is highly coordinated under the sponsorship of the Defense Atomic Support Agency and the management of the Nuclear Defense Laboratory. Participating in various phases of the development are two other government laboratories, the Naval Radiological Defense Laboratory and the Army Atmospheric Sciences Laboratory, and one contractor, Technical Operations Research.

The DOD Model is conceived primarily as a research tool. We expect it to serve as a standard of comparison and as a basis for assessing the requirements for input accuracy. Practical systems for specialized purposes and real-time prediction will be derived from the DOD Model by selective simplification.

The guiding philosophy has been to approach as nearly as possible the physical realities of the fallout process on a theoretical basis. Under the severe time limitations of this project, we have been forced into the unfortunate necessity of introducing a certain amount of empiricism. However, we are not calibrating against some handy test shot. Rather, we have interpolated and extrapolated data from a number of tests to arrive at some of the parametric constants.

The DOD Model will take the form of a very large computer program coded in FORTRAN IV. The program will be fully documented so that there will be no question as to the relation between the computer code and the underlying physics and mathematics of the model. In other words, this model will not be a mystery known only to some computer.

The documentation will consist of a general description of the system, a description of each module, and an operator's manual. The format for the module descriptions is shown in Fig. 1. The operator's manual will contain Sections H, I and J for each module.

We have placed great emphasis on flexibility in order both to facilitate incorporation of the results of future research and to serve the divers needs of prospective users. Mr. Schwenke has already described the flexibility in output. Beyond this we are constructing the model in a modular fashion. Hence, individual modules can be replaced as required with improved versions or supplanted by numerical information from another source.

There are five principal modules in the program. These are: Initial Conditions, Cloud Rise, Transport, Particle-Activity, and Output Processor. Each of these modules in turn has sub-modules.

The Initial Conditions Module was developed by Technical Operations under contract to Nuclear Defense Laboratory. The inputs are weapon yield, height or depth of burst, soil category, and the particle-size distribution of the preshot soil. The outputs are temperature, mass of soil, particle-size distribution, and phase distribution in the fireball at a specified time. This time is taken as the end of the hover period.

The initial time was related to yield and height of burst by an empirical fit to data from 14 test detonations. The corresponding temperature is obtained by extrapolating the data of Hillendahl.[1]

Data from 9 test detonations were used to derive the soil burden of the fireball. Two methods were used to calculate mass of soil. One was the integration of mass collections over the fallout pattern. The other was based on the specific activity of either Ce^{144} or Mo^{99} in the collected fallout. Where both methods could be applied, the results were in good agreement. Scaling functions for yield and height or depth of burst were set up to be consistent with Nordyke's crater scaling.(2)

The initial time is sufficiently late that we can assume that residence of particles in the hot regions of the cloud have been long enough to cause complete vaporization. On the other hand, the initial time is sufficiently early that little particle growth could have occurred. Therefore, we conclude that soil particles present in the cooler regions of the cloud have the preshot soil size-freqneucy distribution.

A satisfactory answer to the question of phase distribution has not been found. At present we are using a tentative assumption that 20 percent of the soil mass is in the vapor state at the initial time.

The Initial Conditions Module is by far the most empirical part of the DOD Model. We had hoped at the outset to put it on a much more theoretical basis, but it is now evident that such a development will require a large project of its own.

The Initial Conditions Module sets the stage for the Cloud Rise Module which has been described for you by Dr. Norment. As early as our original proposal to DASA for this work, we desired to include internal circulation of the cloud in the model. In the early planning stages, however, some doubts arose as to whether this approach could be carried to a successful conclusion at the present state-of-the-art. Therefore, NRDL was assigned a parallel task of modifying Mr. Huebsch's Water Surface Cloud Rise model to apply to a land surface burst.(3)

In this way we provided ourselves with a sort of insurance. As a result we now have two cloud rise modules.

The Transport Module and the Output Processor have already been described by Mr. Schwenke.

The Particle Activity Module is an assembly of bits and pieces from a number of different programs developed at NRDL. These include Mr. Cassidy's programs[4,5] for the Freiling Radial Distribution Model,[6] and the Decay Analysis Routine and Buildup and Decay Routine of Hogan, Crawford, and Goddard.[7] The structure of the Particle Activity Module is shown in Fig. 2 which lists the FORTRAN subroutines.

Subroutine DARO reads in the nuclear transitions of the fission products and sorts and edits them into the form required later in the program. This subroutine is essentially the same as the Decay Analysis Routine of Hogan, Crawford, and Goddard with the neutron capture reactions removed. Subroutine YIELD simply reads in the fission-yield data for the type of fission occurring in the detonation of interest. FRACTD carries out further editing on the decay subchains. ROBIN which stands for reorder by indices NPARNT, is a subroutine for sorting the table of fission products into meaningful order. The computations up to this point are required only once for any particular burst.

Subroutine INGEN computes the complex, sequential decay of the fission product by means of the Bateman equation. The Bateman coefficients are computed by BATMAN and then either the abundance of each fission product or the accumulated dose from each fission product is computed according to the user's request.

Subroutine FRATIO takes the fission-product abundances computed by INGEN for the time at which the cloud reaches the condensation temperature of the soil, and computes the Freiling F_R factor on the basis of the fission-product boiling point. This subroutine is exercised only once for each burst.

Subroutine GXPSR first reads in Sam Rainey's exposure-rate multipliers,[8] which convert the activity per unit area of each fission product into R/hr. These multipliers are then used with the fission-product activity computed at the time of interest to compute mass chain normalization factors. The mass chains are then distributed over the various particle sizes on the basis of Freiling's radial distribution model.

The Induced Activity Module was developed by Mr. Tom Jones of NRDL.[9] The basic assumption in this subroutine is that the soil which appears as fallout will absorb all of the neutrons seen by the apparent crater. The induced nuclides are distributed with particle size on the assumption that they are refractory in the sense of Freiling.

Subroutine MCHDEP (for mass chain deposit) provides the user the option of requesting the fallout of any one of 90 mass chains in curies per cm^2. The procedure is similar to that in GXPSR except, of course, that there are no exposure-rate multipliers here. It should be noted that it is impracticable to have an output of individual fission-product nuclides because the Freiling model works in terms of mass chains. However, in most of the mass chains of concern to users such as Civil Defense, only one member of the chain is of significance at the times of interest.

The model will be tested against a number of test detonations. We cannot, however, expect perfect agreement for two reasons. In the first place there are many uncertainties in the observed fallout patterns. Secondly, the DOD Model requires more comprehensive environmental inputs, especially meteorological conditions, than are available for test shots. However, we do require consistency.

The initial version of the DOD Model is scheduled for delivery to DASA on 30 June 1966. Some additional polishing of rough edges will be carried out during the summer. DASA expects that this model will be adopted as the standard for all DOD Agencies.

REFERENCES

1. Hillendahl, R. W. Characteristics of the Thermal Radiation from Nuclear Detonations, Vol III, USNRDL-TR-383 (1959) (Secret RD)

2. Nordyke, M. D. On Cratering: A Brief History, Analysis, and Theory of Cratering, UCRL-6578 (1961)

3. Huebsch, I. O. Development of a Land Surface Burst Cloud Rise Model, USNRDL-LR-145 (1965)

4. Cassidy, S. H. FORTRAN Statement of the Generalized Land Fallout Model Computer Program (GLFMCP), USNRDL-LR-176 (1966)

5. Cassidy, S. H. The Computer Program (TSABND) which Produces the Tables of Mass Chain Refractory and Fission Product Radioactivity Content for the Particle Activity Module of the DOD Fallout Model, USNRDL-LR-173 (1966)

6. Freiling, E. C. Fractionation III. Estimation of Degree of Fractionation and Radionuclide Partition for Nuclear Debris, USNRDL-TR-680 (1963)

7. Hogan, M. A., Crawford, J. K., Goddard, V. A Computer Program for Calculating Fission Product Abundances, USNRDL-TR-921 (1965)

8. Crocker, G. R., Connors, M. A. Gamma Emission Data for the Calculation of Exposure Rates from Nuclear Debris. Volume I. Fission Products, USNRDL-TR-876 (1965)

9. Jones, T. H. A Prediction System for the Neutron-Induced Activity Contribution to Fallout Exposure Rates, USNRDL-LR-161 (1966)

Section	Title and Commentary
A	Table of Contents
B	Table of Figures
C	Table of Flow Diagrams
D	Introduction
E	Physical and Mathematical Models
F	Program Outline - programming strategy and overall program organization diagrams
G.	Program Description - detailed flow charts, computational options, and error stops
H	FORTRAN Listings
I	Operating Instructions - input card formats, auxiliary tape requirements, etc.

Fig. 1. Outline of Documentation

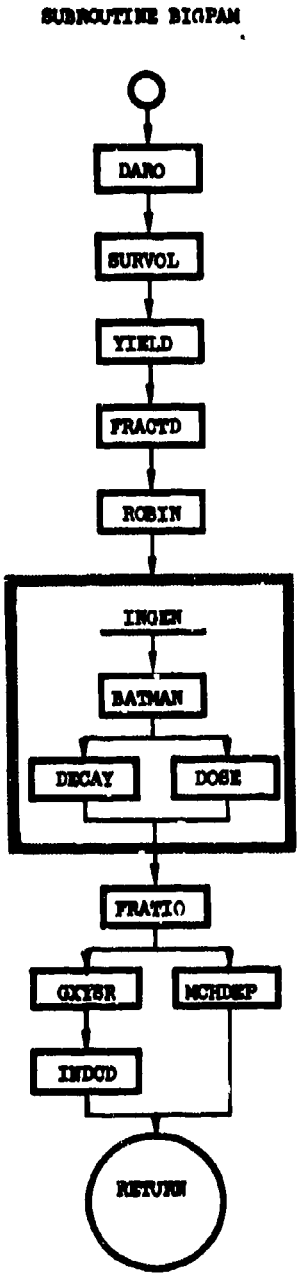

Fig. 2. Particle Activity Module

SESSION FOUR

RADIATION FIELDS

PREDICTIONS OF SOME RADIATION PROPERTIES OF UNFRACTIONATED AND FRACTIONATED FALLOUT FIELDS

G. R. Crocker
U.S. Naval Radiological Defense Laboratory
San Francisco, California

ABSTRACT

Calculations have been made of the activities, gamma-spectra, and exposure rates at 3 feet above an infinite plane for unfractionated fission products resulting from 12 different fission cases. The predictions were made for 29 time points, ranging from 1 hr to 70 yr after fission. The same calculations were made for fractionated fission products, using an empirical method to estimate fractionation parameters for both high-yield and low-yield bursts and for typical cases of both local and long-range fallout. The results of the calculations were compared with those from previous calculations and differences between the results for the various fission cases and between the fractionated and unfractionated cases were analyzed. For each of the 12 fission cases (at each time point), the principal contributors to the activity and to the exposure rate were selected from the computer output. In the unfractionated case, most of the activity and exposure-rate at any time can be attributed to a relatively small number of nuclides--fewer than 10. At almost all times after fission, these principal contributors are dominated by nuclides that are subject to fractionation, such as the iodine isotopes, Ba^{140}-La^{140}, and Cs^{137}-Ba^{137m}. The iodines are of particular importance for the first several days after fission. In fractionated fallout which is depleted in these nuclides, such as the close-in fallout from surface bursts, the exposure rates are much reduced. Conversely, the exposure rates of fallout enriched in these nuclides, i.e., world-wide fallout from surface bursts, are increased.

INTRODUCTION

Computer calculations were made of the activities, the exposure rates at three feet above an infinite, uniformly-contaiminated plane, and the gamma-emission spectra resulting from unfractionated fission-product mixtures. The input data were considerably improved over that used in earlier calculations[1,2,3,4] for the thermal-neutron fission of U^{235}. The fission-product decay chains used in the present calculation, including half-lives and branching fractions, have been presented in Reference 5. Chain and independent yields were taken from Reference 6, and gamma-photon energies and abundances from Reference 7. A detailed description of the computer program for calculating the build-up and decay of the fission-product radio-nuclides is given in Reference 8.

CALCULATIONS FOR UNFRACTIONATED CASES

The present calculations have been extended to cover several fission cases other than the thermal-neutron fission of U^{235}, viz:

(1) U^{235}, fission-spectrum neutrons
(2) U^{235}, 14-Mev neutrons
(3) U^{233}, fission-spectrum neutrons
(4) Pu^{239}, fission-spectrum neutrons
(5) U^{238}, fission-sepctrum neutrons
(6) U^{238}, thermonuclear neutron fission

The calculations were carried out for 29 time points, ranging from 1 hr to 70 yr after fission. For each time point, the computer listed the activity and exposure rate contribution for each fission-product nuclide contributing 1% or more of the total. The gamma-spectra calculation gave the number of photons per second emitted by the products

of 10^4 fissions in each of forty 0.1 Mev energy increments ranging from zero to 4.0 Mev. Unfractionated fission-product normalization factors at 1, 10, and 100 hours were also calculated.

This paper will present only a general discussion of the results of the calculations, since details of the prediction for the individual cases are being published in an NRDL report.

CALCULATIONS FOR FRACTIONATED CASES

Predictions of the radiation properties of fallout fields must refer to a fission-product mixture of specified composition. In the unfractionated cases, the composition is implied by the mass-chain yield curve for the type of fission under consideration. For the fractionated cases, the composition can be simply expressed by choosing one mass chain as a reference. Concentrations of other mass chains can then be specified as ratios of their concentrations to the concentration of the reference chain. Convenient units are equivalent fissions; i.e., the number of fissions required to produce the amount of the nuclide present. In the present calculations, the compositions are referred to equivalent fissions of the mass-95 chain, f_{95}. The amount of any other mass-chain $\underline{i}$ is given by the ratio:

$$r_{i,95} = \frac{f_i}{f_{95}}$$

An empirical method was used to assign values of $r_{i,95}$ for the fission-product mass chains for various kinds of fractionated fallout. Predictions were then made of the radiation properties of the fission products present in a sample containing 10^4 equivalent fissions of Zr^{95}.

The method of assigning the $r_{i,95}$ values was suggested by Freiling.[9] The values of $r_{89,95}$ was first assigned arbitrarily, choosing a value known to be representative of those actually observed in fallout.

The $r_{i,95}$ were then computed from the equations:

$$r_{i,95} = (r_{89,95})^{1-b}$$

where $$b = (F_R)^{1/2}$$

The value of F_R, the fraction of refractory atoms in a mass-chain at the time of soil condensation, was computed by the build-up and decay program. The time of condensation depended on the explosive yield of the burst and was calculated from Miller's[10] scaling equation. The condensing soil was assumed to be a silicate melting at 1400°C. Estimations were made for both a large burst and a small burst for fission-spectrum neutron fission of both U^{235} and Pu^{239}. For thermonuclear fission of U^{238}, the predictions were made for a large burst. For all these conditions, a prediction was made for local (depleted) fallout having $r_{89,95}$ equal to 0.1 and for long-range (enriched) fallout with $r_{89,95}$ equal to 2.0.

RESULTS AND DISCUSSION

PREDICTIONS FOR UNFRACTIONATED CASES

The results of the calculations for the thermal-neutron fission of U^{235} were compared with earlier predictions. The gross activity decay curve from the present calculation shows only slight differences from that of Bolles and Ballou.[1] The exposure rates at 3 ft above an infinite, uniformly contaiminated plane are generally about 10% lower than those calculated by Miller,[2] but this appears to be due to a difference in the curve used for converting photon energies in Mev to exposure rates at 3 ft above an infinite plane. The gamma spectra for thermal neutron fission of U^{235} are in reasonably good agreement with the prediction of Björnerstedt,[3] but show more significant differences from the spectra of Nelms and Cooper.[4] It appears that the many changes in the input data which entered into the new calculation did not have important effects on the gross predictions. Presumably, the effects of

the individual changes were random in direction and magnitude and tended to cancel out.

As was known from the earlier predictions and from experimental measurements, the gross decay of fission products can be roughly expressed as:

$$\log A = \log A_o - n \log t$$

where A is either activity or exposure rate at time t, A_o is the same quantity at unit time and n is a constant close to 1.2. Figures 1 and 2 show the calculated activity and exposure-rate decay curves from unfractionated fission products of the thermonuclear fission of U^{238}. The slope of the log-log decay plots does not have a constant value of -1.2, of course, but varies continuously in the neighborhood of this value, at least for times up to about 1 yr after fission. During this time interval, a slope calculated on the basis of two points from the curve chosen at random will generally have a value between -1.0 and -1.4. The n = -1.2 approximation should be used with discretion in calculations which are sensitive to fluctuations of this magnitude and should probably not be used at all for times longer than about 1 year. The decay curves for the seven different fission cases all appeared to obey the n = -1.2 rule equally well.

The variation in calculated exposure rates for the different fission cases is indicated in Table 1, which lists values of the unfractionated fission-product normalization factors based on the calculations for 1, 10 and 100 hours after fission.

In general, the rates were highest for thermal-neutron fission of U^{235} and lowest for the fission-spectrum neutron fission of Pu^{239} for the first several hours after fission, but crossovers occurred at later times.

Table 1

Values of the Theoretical Unfractionated Normalization Factor at Three Times after Fission

Fission Case	R/hr per kt/mi^2		
	1 hr	10 hr	100 hr
U^{235}, thermal neutrons	3270	168	8.7
U^{235}, fission-spectrum neutrons	3110	168	8.7
U^{235}, 14-Mev neutrons	2720	151	8.3
U^{233}, fission-spectrum neutrons	2760	146	8.1
U^{238}, fission-spectrum neutrons	3130	163	8.3
U^{238}, thermonuclear fission	2920	160	8.1
Pu^{239}, fission-spectrum neutrons	2730	149	8.7

Figures 3 and 4 show the most important contributions from individual radionuclides to the total activity and exposure rate from unfractionated fission products of the thermonuclear fission of U^{238}. Examination of similar plots for the other fission cases revealed numerous differences in the relative importance of the individual radioactivities. These differences result, of course, from differences in chain and independent yields. Nonetheless, the two or three leading contributors are usually the same for all fission cases. The exposure rate, in particular, is strongly dominated by a very few nuclides. The dominance shifts from one nuclide to another as the fission products decay. Except for brief intervals at early times, one nuclide alone always accounts for 20% or more of the exposure rate. For the first several days after fission, the iodine isotopes--I^{131} through I^{135}--are extremely important in determining the exposure rates from unfractionated fission products. Other nuclides which are invariably leading contributors (at later times) are La^{140}, Zr^{95}-Nb^{95}, and Ba^{137m}. The iodine isotopes, La^{140} and Ba^{137m} all fractionate from Zr^{95}-Nb^{95} in nuclear debris. At late times there is considerable variation in the contributions of Ru^{106}-Rh^{106} and Sb^{125} to the activity and exposure rates for the different fission cases. This is

due to the fact that the yields for these mass chains are quite sensitive to kind of fissionable material and to the energies of the neutrons.

The gamma spectra for the different fission cases also showed differences, but these were mainly differences in intensity rather than in sepctral shape. It would be possible, of course, to predict spectra showing more striking differences by increasing the resolution (decreasing the width of the energy increments in the calculations). However, the 0.1 Mev resolution chosen is convenient and adequate for many calculational applications. The spectra for all the fission cases show a rather pronounced decrease with time in the number of high-energy photons, relative to the number of low-energy photons.

PREDICTIONS FOR FRACTIONATED CASES

As might be expected, the predictions for the fractionated cases are sensitive to the choice of fractionation parameters for the iodine mass chains (131 through 135), since these iodine isotopes dominate the gamma-radiation properties of unfractionated fission products for several days after fission. In the prediction for long-range fallout ($r_{89,95} = 2.0$), which is enriched in fractionating mass chains, the influence of these nuclides is even more pronounced. Rather surprisingly, they lose little of their prominence in the local fallout ($r_{89,95} = 0.1$), which is depleted (in surface bursts) in the fractionating mass chains.

The activity and exposure-rate decay curves for fractionated fallout (as predicted by this method) are not strikingly different in shape from those predicted for unfractionated fallout, at least for times up to 100 to 200 days after fission. Figure 5 shows the comparison for thermonuclear fission of U^{238}. The curves for the enriched fallout, in fact, are almost parallel to those for the unfractionated fallout. Those for depleted fallout show somewhat more fluctuation around a nominal overall slope of -1.2. The intensity of the radiation is, of course, rather strongly affected by fractionation. For example, in the case of fission-spectrum

neutron fission of U^{235} (1.7 kt burst), the exposure rate for enriched fallout is rather uniformly about 140% that for unfractionated fallout for the first 20 days after fission; while that for depleted fallout is about 40% of the exposure rate for unfractionated fallout. These figures can be compared with field observations of the exposure rates of enriched fallout from the Danny Boy event and depleted fallout from the Smallboy event. If an allowance of 50% is made for reduction of exposure rates measured in the field by ground roughness and instrument self-shielding, the Danny Boy exposure rates were about 170% of the unfractionated value and those at Smallboy were about 35% of the unfractionated value.[11]

The gamma-emission spectra for the fractionated cases, like the decay-rate curves, show strong differences in intensity from those for the unfractionated cases but not much characteristic difference in shape, at least for the first 100 to 200 days.

During the period between approximately 150 and 250 days after fission the differences between fractionated and unfractionated fallout are least conspicuous, since at this time the radiation properties of fission-product mixtures are dominated by the reference pair Zr^{95} -Nb^{95}. If attention is restricted to the radiation properties of this pair, there will be no apparent difference between an unfractionated fallout sample containing 10^4 fissions and a fractionated fallout sample containing 10^4 equivalent fissions of Zr^{95}. From one year after fission onward, the radiation characteristics of the highly fractionated pair Cs^{137} -Ba^{137m} become increasingly important, and the radiation properties of unfractionated fallout and the depleted case of fractionated fallout diverge rapidly.

In connection with the gamma-exposure decay curves some explanation is in order, since calculations based on the spectral predictions of Nelms and Cooper[4] indicated an appreciably faster decay rate for fractionated fallout, relative to the unfractionated case. The reason for this seems

to be that the Nelms and Cooper scheme dropped the iodine isotopes completely, along with bromine and the rare gases. The present NRDL prediction regards these nuclides as being fractionated to an intermediate extent; i.e., the mixture is depleted (in the local fallout case) in these nuclides relative to Zr^{95}, but they are not completely absent; in fact, they are not so extensively depleted as Sr and Cs. This viewpoint seems more in line with field evidence, so far as iodine isotopes are concerned, although the exact degree of depletion remains uncertain. On the other hand, the NRDL fractionation scheme retains some rare gases and bromine daughter isotopes in the fractionated mixture. It would probably be more realistic to drop these entirely, as did the Nelms and Cooper scheme, and the computer program is being modified to do this. However, the effect on the predictions of gamma radiation properties will be minor, since the bromine and rare gas isotopes contribute far less strongly than the iodine isotopes.

REFERENCES

1. R. C. Bolles and N. E. Ballou, "Calculated Activities and Abundances of U^{235} Fission Products", U.S. Naval Radiological Defense Laboratory Research and Development Report USNRDL-456, 30 August 1956.

2. C. F. Miller, "Ionization Rate and Photon Pulse Decay of Fission Products from the Slow-Neutron Fission of U^{235}", U. S. Naval Radiological Defense Laboratory Technical Report USNRDL-TR-247, 4 August 1958.

3. R. Björnerstedt, "Health Hazards from Fission Products and Fallout. II. Gamma Radiation from Nuclear Weapons Fallout", Ark. för Fysik 16:293, 1959.

4. Ann T. Nelms and J. W. Cooper, "U^{235} Fission Product Decay Spectra at Various Times after Fission", Health Physics 1:427, 1959.

5. D. D. Kochendorfer, "Calculated Activities of U^{235} Fission Products for Very Short Nuclear Reactor Operation. Vol. I. Discussion, Diagrams, and Figures", U.S. Naval Radiological Defense Laboratory Technical Report USNRDL-TR-757, 18 June 1964.

6. L. E. Weaver, P. O. Strom and P. A. Killeen, "Estimated Total Chain and Independent Fission Yields for Several Neutron-Induced Fission Processes", U. S. Naval Radiological Defense Laboratory Technical Report USNRDL-TR-633, 5 March 1963.

7. G. R. Crocker and M. A. Connors, "Gamma-Emission Data for the Calculation of Exposure Rates from Nuclear Debris", U. S. Naval Radiological Defense Laboratory Technical Report USNRDL-TR-921, 15 October 1965.

8. M. A. Hogan, J. K. Crawford and V. Goddard, "A Computer Program for Calculating Fission Product Abundances", U. S. Naval Radiological Defense Laboratory Technical Report USNRDL-TR-921, 15 October 1965.

9. E. C. Freiling, "Fractionation III. Estimation of Degree of Fractionation and Radionuclide Partition for Fractionated Nuclear Debris", U. S. Naval Radiological Defense Laboratory Technical Report USNRDL-TR-680, 12 September 1963.

10. C. F. Miller, Fallout and Radiological Countermeasures, Stanford Research Institute, Menlo Park, California (1963).

11. G. R. Crocker, "The Effect of Radionuclide Fractionation on the Normalization Factor for Fallout Fields", U. S. Naval Radiological Defense Laboratory Technical Report USNRDL-TR-892, 4 August 1965.

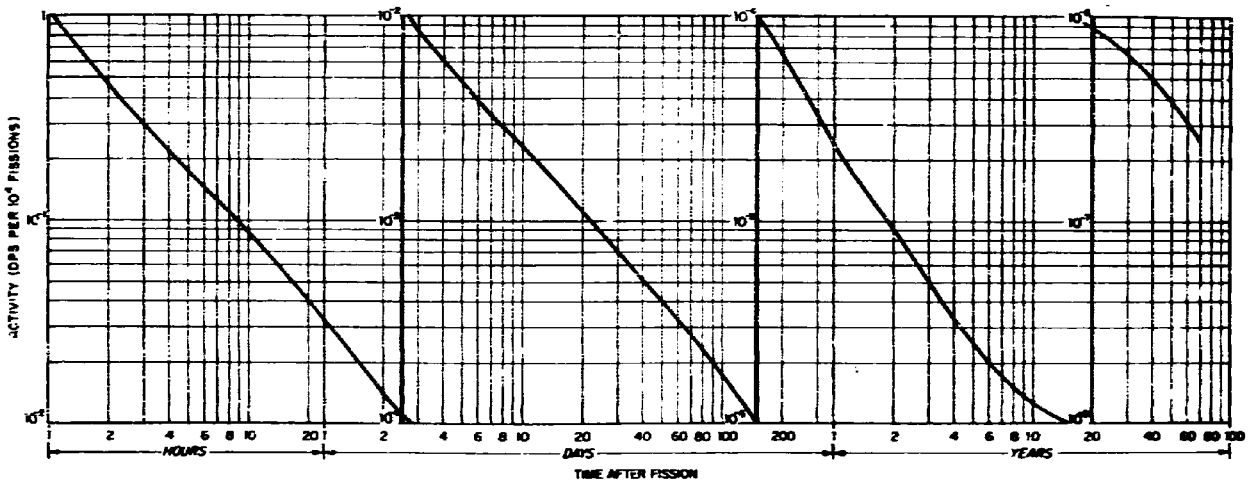

Fig. 1. Decay of Activity of Fission Products of the Fission of U^{238} by Thermonuclear Neutrons

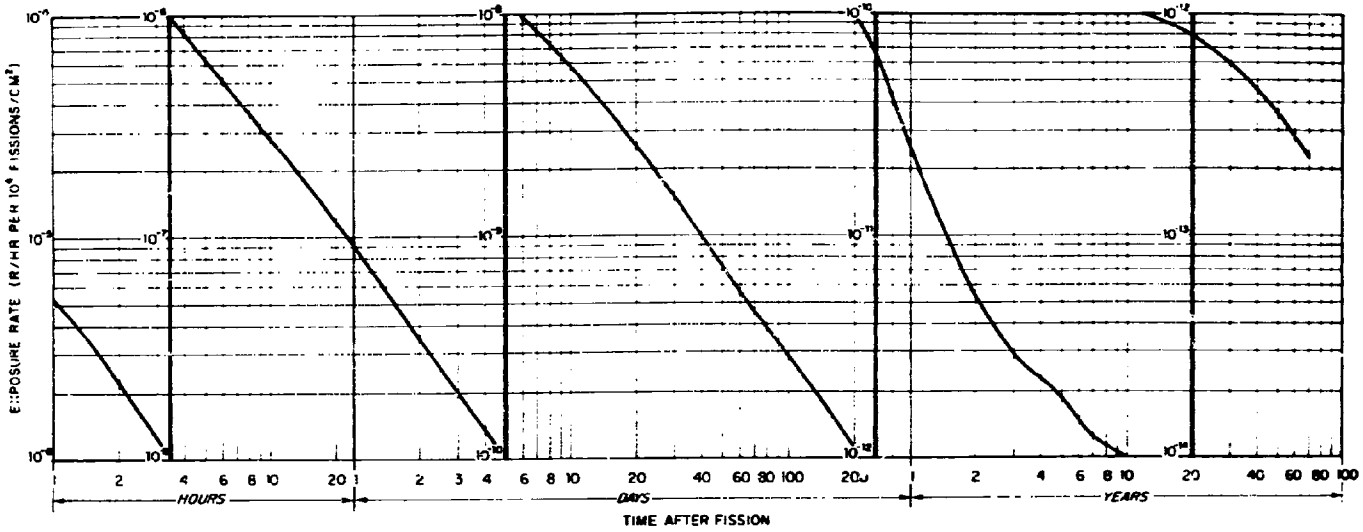

Fig. 2. Decay of Exposure Rate from Fission Products of the Fission of U^{238} by Thermonuclear Neutrons

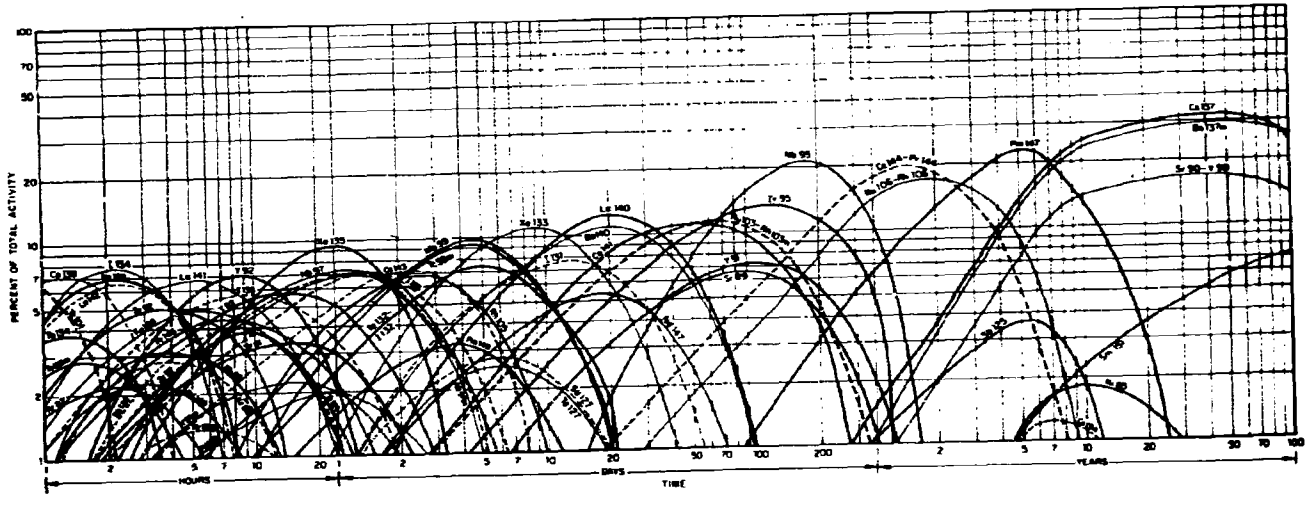

Fig. 3. Principal Contributions to the Total Activity of Fission Products of the Fission of U^{238} by Thermonuclear Neutrons

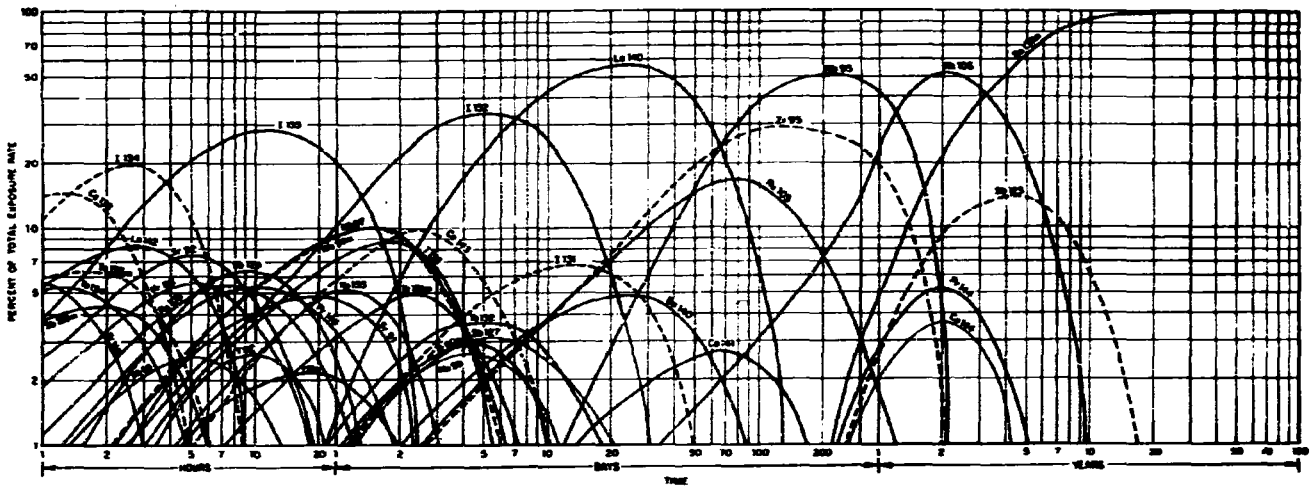

Fig. 4. Principal Contributions to the Total Exposure Rate from Fission Products of the Fission of U^{238} by Thermonuclear Neutrons

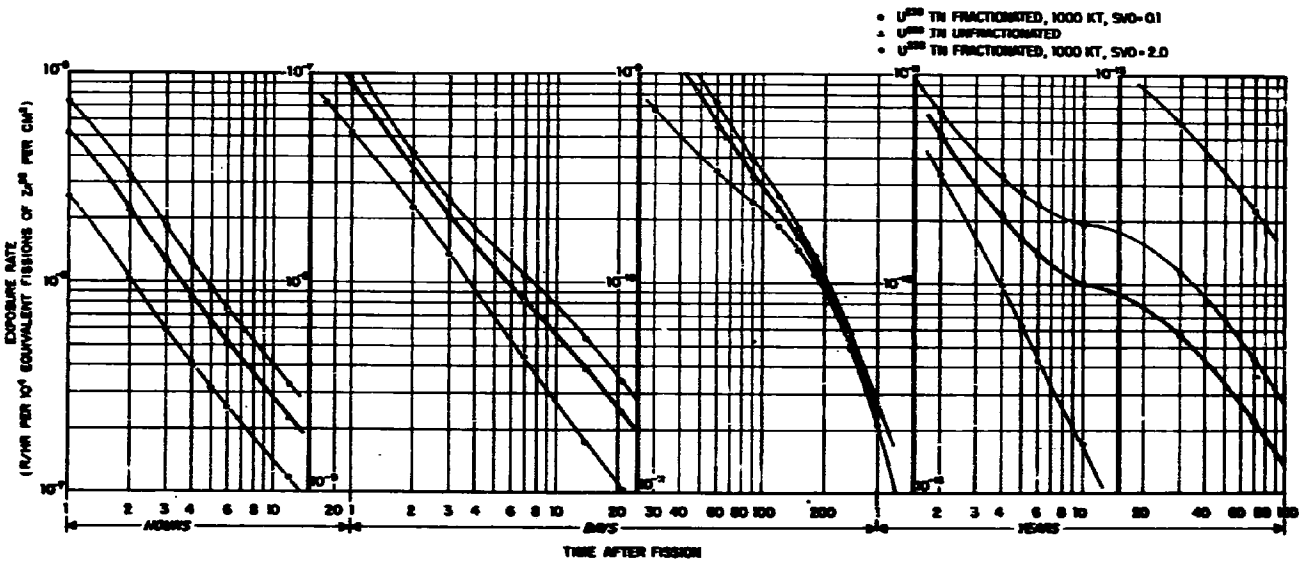

Fig. 5. Comparison of the Exposure Rate Decay for Unfractionated Fission Products of the Thermal Neutron Fission of U^{235} with Two Fractionated Cases

GAMMA RAY FIELDS ABOVE ROUGH CONTAMINATED SURFACES

R. R. Soule
U.S. NAVAL RADIOLOGICAL DEFENSE LABORATORY
San Francisco, California

ABSTRACT

The object of this experiment is to determine the gamma radiation fields above uniformly contaminated surfaces of infinite extent and varying roughness.

Radioactive contaminant (Au^{198} suspended in glass microbeads) was distributed evenly over a circular area 10 ft in diameter in the center of various test surfaces. Ionization chambers were employed to measure the radiation field at various distances out to 128 meters horizontally and 16 meters vertically from the center of the area. These data were then operated upon to obtain the radiation fields to be expected from surfaces of infinite extent. Comparisons of the results from a given surface with those obtained from an ideally smooth (glass) plane provide a measure of surface roughness. Surfaces tested included sand, gravel and grass.

The theory and assumptions used in integrating the data from the finite discs to determine the fields for infinite planes are presented. Preliminary examination of the data from the experimental work indicates the following results:

Surface Roughness Factors for Test Surfaces
at a Height of 1 Meter Above the Surfaces

Surface	Infinite Plane Dose Rate (r/hr)/(c Au^{198}/ft^2)	Surface Roughness Factor
Plate Glass	77.0	1.00
Grass (wet)	61.0	0.79
Coarse Sand	50.3	0.65
Fine Gravel	47.7	0.62
Pea Gravel	42.9	0.56
Medium Gravel	44.5	0.58

Measurements were also made with a point source of Au^{198}. Buildup factors derived from these measurements are presented.

Recent experimentation has been performed at the Camp Parks Facility of the Naval Radiological Defense Laboratory to determine the effect of surface roughness upon gamma ray fields. The objective of this experimentation is to determine the gamma radiation fields above uniformly contaminated surfaces of infinite extent and varying roughness.

In this experimentation[1] radioactive contaminant is spread over a circular area 10 feet in diameter in the center of various test surfaces. Measurements of the radiation field are taken at predetermined distances horizontally and vertically from the center of the area. These data are then operated upon to obtain the radiation fields to be expected from surfaces of infinite extent. Comparison of the results from a given surface with those obtained from an ideally smooth (glass) plane provide a measure of surface roughness.

In order to fully expose the assumptions and limitations inherent in the extrapolation from a finite disc to an infinite field, the scheme used is developed below.

A disc of finite size may be used to approximate a uniformly contaminated plane. The disc is large (dia. 10 ft) in relation to the irregularities which characterize the roughest surfaces used, but is small enough to facilitate the handling and control of the radioactive contaminant. The radiation field (R_0) measured above the center of the contaminated disc is the first term in a series approximation to the field (R) above an infinite plane. The second term in the series is obtained by taking the radiation contribution (R_1) from an annulus (1 disc diameter in width) adjoining the disc. Successive terms are composed of the radiation contributions (R_2, R_3, ...R_n) from additional adjoining annuli. The approximation of the radiation field due to a contaminated infinite plane becomes better as the number of annuli increase.

$$R \approx R_0 + R_1 + R_2 + \ldots R_n \qquad (1)$$

If the radiation contribution (r_n) from a sector of an annulus is known, the contribution (R_n) from the entire annulus can be found by multiplying the sector contribution by b_n, where b_n is defined as the ratio of the area of the annulus to the area of the sector.

$$R_n = b_n r_n, \quad b_n \equiv \frac{\text{area of annulus } n}{\text{area of sector}} \quad \text{for } n \geq 1$$

If the sector of an annulus 1 disc diameter wide is chosen to have the same area as a disc of the chosen diameter, the coefficients b_n are simply multiples of 8, and the approximation can be expressed as

$$R \approx R_0 + 8r_1 + 16r_2 + 24r_3 + \cdots + 8nr_n \qquad (2)$$

The radiation contribution (c_n) from a disc of the chosen diameter, contained within the annulus, can be used to approximate the radiation contribution (r_n) from the sector of the annulus. Differences in the actual contributions of the disc and the sector can be adjusted by the use of a correction factor k_n, where k_n is defined to be the ratio of the radiation contribution of a sector to the radiation contribution of a disc.

$$r_n = k_n c_n, \quad k_n \equiv \frac{\text{radiation contribution from sector}}{\text{radiation contribution from disc}} \quad \text{for } n \geq 1$$

and then $$R_n = 8nr_n = 8nk_n c_n \qquad (n \geq 1) \qquad (3)$$

The values of the correction factors k_n were determined by calculating the radiation contributions from elemental areas of both the disc and the sector, summing for each, and finding the ratio of the sums for a smooth plane. The circle was divided into areas a_1, a_2, a_3, $\cdots$ a_m, and the sector into areas s_1, s_2, s_3, $\cdots$ s_m, at mean horizontal distances d_1, d_2, d_3, $\cdots$ d_m from the detector (See Fig. 1). If the response of a detector at a height h is 1 unit/unit area at unit distance, the response due to the circle will be

$$c_n = \frac{a_1}{h^2+d_1^2} B_1 e^{-\mu d_1'} + \frac{a_2}{h^2+d_2^2} B_2 e^{-\mu d_2'} + \cdots \frac{a_m}{h^2+d_m^2} B_m e^{-\mu d_m'} \qquad (4)$$

where B is the buildup factor, $e^{-\mu d'}$ is due to air attenuation, and $\frac{1}{h^2+d^2}$ is the geometrical factor. The slant range $d' = (h^2+d^2)^{1/2}$. The response due to the sector will be

$$r_n = \frac{s_1}{h^2+d_1^2} B_1 e^{-\mu d_1'} + \frac{s_2}{h^2+d_2^2} B_2 e^{-\mu d_2'} + \cdots + \frac{s_m}{h^2+d_m^2} B_m e^{-\mu d_m'} \qquad (5)$$

The correction factor for the disc approximation of the sector contribution to the radiation field will be

$$k_n = \frac{\sum_{i=1}^{m} \frac{s_i}{h^2+d_i^2} B_i e^{-\mu d_i'}}{\sum_{i=1}^{m} \frac{a_i}{h^2+d_i^2} B_i e^{-\mu d_i'}} \qquad (6)$$

The dimensions of the disc and the sector are such that changes in the air attenuation and buildup factors are small for changes of less than 1 disc diameter in the horizontal distance to the detector. Thus, buildup and air attenuation can be assumed constant for each k_n determination, and k_n becomes

$$k_n = \frac{\sum_{i=1}^{m} \frac{s_i}{h^2+d_i^2}}{\sum_{i=1}^{m} \frac{a_i}{h^2+d_i^2}} \qquad (7)$$

The expression $\sum_{i=1}^{m} \frac{a_i}{h^2+d_i^2}$ cannot be easily evaluated analytically so it was evaluated numerically. However the expression $\sum_{i=1}^{m} \frac{s_i}{h^2+d_i^2}$

approaches $\int_{r_1}^{r_m} \int_{0}^{\pi/4n} \frac{r\, d\theta\, dr}{h^2 + r^2}$ as the width of the elemental areas approaches zero. Analytical evaluation of the latter expression gave results which agreed to within 0.01% with the numerical evaluation of $\sum_{i=1}^{m} \frac{s_i}{h^2+d_i^2}$

The values of k_n were determined for the case of a detector located at a height of 1 meter and for disc diameter and annuli widths of 10 ft (See Figure 1). The value of k_1, for the first annulus, was found to be 0.949, k_2 was found to be 0.989, and the values of k_n for $n>2$ were taken to be unity.

The final form of the approximation of the infinite plane radiation field then becomes

$$R = R_0 + 8(0.949)c_1 + 16(0.989)c_2 + 24c_3 + 32c_4 + \ldots + 8nc_n \qquad (8)$$

where R_0 is the measured radiation contribution above the center of a 10 ft diameter contaminated disc, and c_n is the radiation contribution measured at a horizontal distance of 10n ft from the center of the disc (all measurements made at a height of 1 meter).

The basic experiment consists of measuring the total gamma radiation field at selected heights and distances from contaminated discs of materials of varying degrees of roughness. Gamma measurements are made using ionization chambers. Data from these measurements are extrapolated (integrated) to predict the dose rate for infinite plane sources.

The test surfaces used during this series of experiments were:

1. Plate glass - a smooth surface.
2. Coarse sand (1190 - 2000 μ particle size) (3/64 - 1/64 inches)
3. Fine gravel (2362 - 5613 μ particle size) (3/32 - 7/32 inches)

4. Pea gravel (6680 - 9423 μ particle size) (1/4 - 3/8 inches)
5. Medium size gravel (13,330 - 15,585 μ particle size) (1/2 - 5/8 inches)
6. Grass (lawn type)

The isotope used for this series was Au^{198}, a gamma emitter with an energy of 0.411 Mev. The isotope, enclosed in a microbead carrier, was uniformly dispersed at a mass loading of approximately 12 grams/sq. ft over a 10 ft diameter disc in the center of the test surfaces.

The basic gamma measurements were taken with ionization chambers at combinations of horizontal distances from 0 to 128 meters and vertical distances from 1 to 16 meters from the center of the test surface.

The data from the tests where the isotope was dispersed uniformly over the "ideally smooth surface" (plate glass) was taken as the basis for comparison with the other surfaces of varying roughness. Thus the surface roughness factor depends on the determination of a smooth surface infinite plane exposure as well as on a rough surface infinite plane exposure.

If certain factors, such as the build-up factors, are known, the smooth surface exposure can be calculated to provide a check on the experimentally obtained smooth surface exposure values. Since the experiment was concerned with the region close to the ground-air interface, it was not reasonable to use the infinite medium build-up factors available. For this reason, a supplemental test was conducted in which a series of measurements were made using a gold wire as a point source for the purpose of determining the build-up factor for Au^{198} under the conditions of the experiment.

The gold wire was 5 cm long by 0.095 cm in diameter. All radiation measurements were made in a direction normal to the axis of the wire. The diameter and cross section of the wire were chosen to minimize self-absorption and eliminate angular dependence of gamma rays emitted

perpendicular to the axis of the wire. The length of the wire was selected so that it was long enough to provide the required source strength and yet short enough so that no appreciable error was introduced in considering the wire as a point source at the minimum measurement distance of one meter.

The wire was irradiated to produce an initial activity of about 100 curies. The wire was then placed upon the glass plate in the center of the test pad and radiation field measurements were made at distances from 1 meter to 128 meters from the source at heights of 1, 4, 8, and 16 meters above the plane of the glass plate.

The build-up factors as a function of position of the detector were determined from the expression $I = I_o \frac{e^{-\mu_o r}}{r^2} B$ where I is the intensity in r/hr at the detector position, I_o is the intensity at unit distance from the source in an infinite medium of air, μ_o is the total attenuation coefficient and B is the build-up factor.

Experimentation was conducted on a test surface located at the intersection of two streets which are paved with asphaltic concrete. There are no buildings in the area. A level concrete pad, 30 ft square, was constructed at the intersection of the streets. The central 15 ft square section was further leveled by grinding the surface flat to within ± 1/8 inch, and the test surfaces were centered in this area. For the smooth surface, six sections of 1/4 inch thick plate glass were arranged horizontally on a 1/4 inch thick sponge rubber pad and leveled to provide a smooth level test surface 11 ft square.

For the rough surfaces, a sheet of 5 mil thick plastic was placed on the plate glass surface and the loose material was spread on it. (Figure 2.) A single layer technique was used in spreading the sand and gravel test surfaces. No binder was used, and the intent was to spread a single layer of the sand or gravel and then add additional material

until no visible holes remained in the layer. This resulted in a layer of the material only slightly thicker than the maximum size of the material.

Because the test area is in the open, a plastic dome was constructed to cover the test surface and prevent the wind from moving the contaminant. The dome is approximately 14 ft square by 3 ft high, and the 3 mil thick Mylar sheeting is supported by an aluminum framework that provides a clear span across the entire width. Since the dome is kept in place over the test surface at all times, one end of the dome is hinged to allow for the entrance and removal of the contaminant and the contaminant dispersal equipment.

The source of radiation for all the tests was the isotope Au^{198}. The radioactive isotope was enclosed in a microbead carrier for the tests in which it was dispersed uniformly over the various test surfaces, and was a single piece of metallic gold for the point source tests. The beads were taken to the test area in a shielded container from which they were delivered into a disperser (Figure 3).

The disperser that distributes the microbeads onto the test surface is a hopper mounted on a small portable motorized bridge crane. As the hopper moved from one side of the area to the other, an auger bit in the bottom of the hopper provided a continuous flow of the microbeads at a constant dispersal rate through four outlets. Four baffles below the outlets spread the microbeads to give an even distribution on the test surface.

The size of the contaminated area was controlled by a mask that rested on the framework of the disperser assembly below the level of the hopper and baffles. Eight aluminum pans were fitted together to form the mask to control the size and shape of the contaminated area (Figure 4). The mask had outside dimensions of an 11 ft 10 inch square and had a 10 ft diameter circular cut-out in the center. As the hopper moved from one side of the disperser to the other, the

contaminant fell on the test surface inside the circle while the mask caught the excess. Complete coverage inside the circle was obtained by first dispersing along one side of the mask and indexing the hopper over one hopper width after each pass. After the dispersal of the contaminant, the disperser, including the hopper and mask containing the excess contaminant, was removed from under the plastic dome, and the hinged end of the dome was closed for the duration of the test. The excess contaminant was removed from the test area and measurements were started using Victoreen ionization chambers mounted on a light portable mast (Figure 5).

Preliminary results are available from the experimental work. Figure 6 shows the build up factors derived from data measured with the point source of Au^{198}. It is interesting to note that the 16 meter height factors are below those for heights of 4 and 8 meters.

Figures 7 and 8 present data for the pea gravel surface and grass surface typical of those obtained during the experiments. This type of data was used in conjunction with equation 8 to obtain the infinite plane exposure rates at 1 meter above the surface. Comparison of the various surfaces with the glass surface gave measures of surface roughnesses. The infinite plane exposure rates and the roughness factors are given in Table 1.

A small amount of additional experimental work will be done to obtain an indication of the effect of gamma ray energy upon surface roughness factors. Lutetium-177 with a gamma energy of about .200 mev will be employed on two or three surfaces for this purpose. Point source measurements will also be made with the Lu^{177}.

REFERENCES

1. R. C. Bolles and N. E. Ballou, "Calculated Activities and Abundances of U^{235} Fission Products", U.S. Naval Radiological Defense Laboratory Research and Development Report USNRDL-456, 30 August 1956.

2. C. F. Miller, "Ionization Rate and Photon Pulse Decay of Fission Products from the Slow-Neutron Fission of U^{235}", U. S. Naval Radiological Defense Laboratory Technical Report USNRDL-TR-247, 4 August 1958.

3. R. Björnerstedt, "Health Hazards from Fission Products and Fallout. II. Gamma Radiation from Nuclear Weapons Fallout", Ark. för Fysik 16:293, 1959.

4. Ann T. Nelms and J. W. Cooper, "U^{235} Fission Product Decay Spectra at Various Times after Fission", Health Physics 1:427, 1959.

5. D. D. Kochendorfer, "Calculated Activities of U^{235} Fission Products for Very Short Nuclear Reactor Operation. Vol. I. Discussion, Diagrams, and Figures", U.S. Naval Radiological Defense Laboratory Technical Report USNRDL-TR-757, 18 June 1964.

6. L. E. Weaver, P. O. Strom and P. A. Killeen, "Estimated Total Chain and Independent Fission Yields for Several Neutron-Induced Fission Processes", U. S. Naval Radiological Defense Laboratory Technical Report USNRDL-TR-633, 5 March 1963.

7. G. R. Crocker and M. A. Connors, "Gamma-Emission Data for the Calculation of Exposure Rates from Nuclear Debris", U. S. Naval Radiological Defense Laboratory Technical Report USNRDL-TR-921, 15 October 1965.

8. M. A. Hogan, J. K. Crawford and V. Goddard, "A Computer Program for Calculating Fission Product Abundances", U. S. Naval Radiological Defense Laboratory Technical Report USNRDL-TR-921, 15 October 1965.

9. E. C. Freiling, "Fractionation III. Estimation of Degree of Fractionation and Radionuclide Partition for Fractionated Nuclear Debris", U. S. Naval Radiological Defense Laboratory Technical Report USNRDL-TR-680, 12 September 1963.

10. C. F. Miller, Fallout and Radiological Countermeasures, Stanford Research Institute, Menlo Park, California (1963).

11. G. R. Crocker, "The Effect of Radionuclide Fractionation on the Normalization Factor for Fallout Fields", U. S. Naval Radiological Defense Laboratory Technical Report USNRDL-TR-892, 4 August 1965.

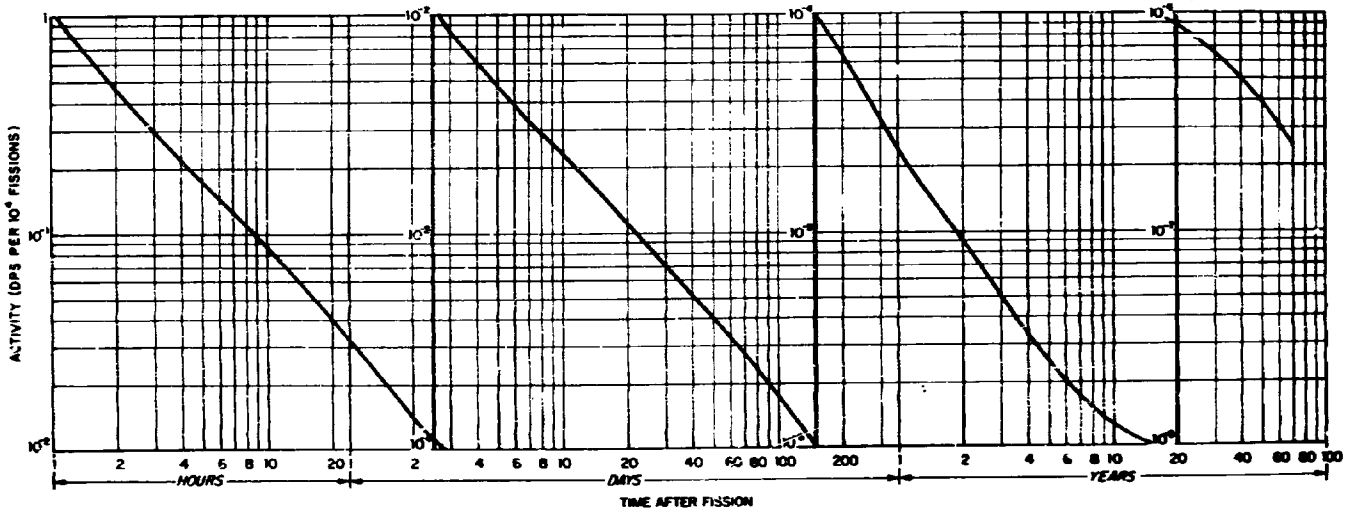

Fig. 1. Decay of Activity of Fission Products of the Fission of U^{238} by Thermonuclear Neutrons

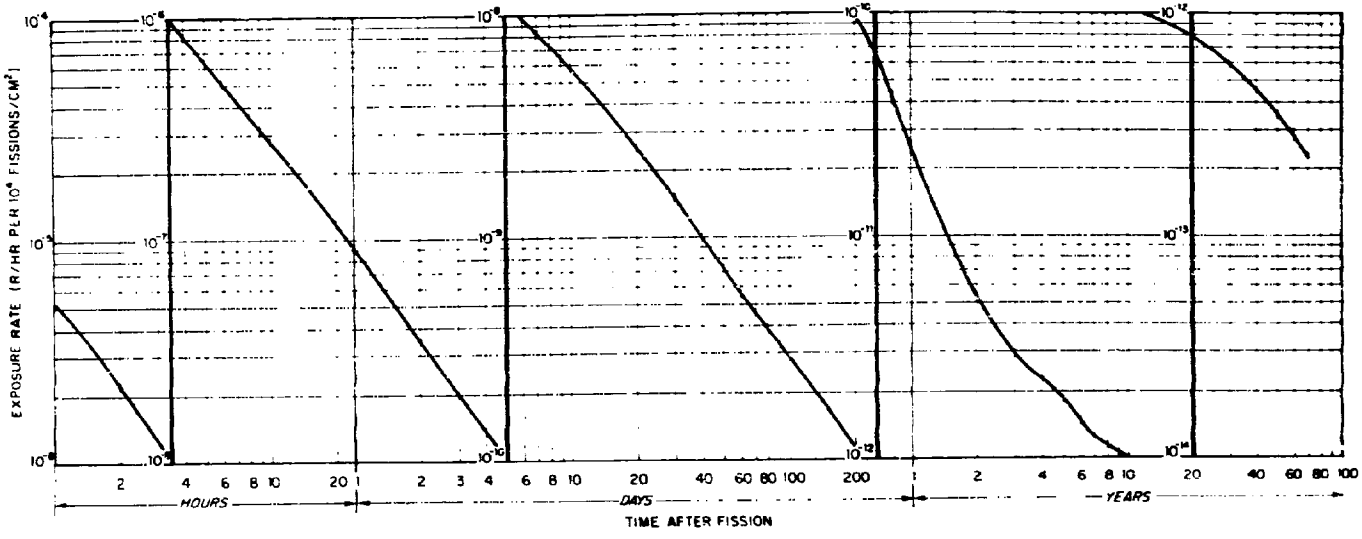

Fig. 2. Decay of Exposure Rate from Fission Products of the Fission of U^{238} by Thermonuclear Neutrons

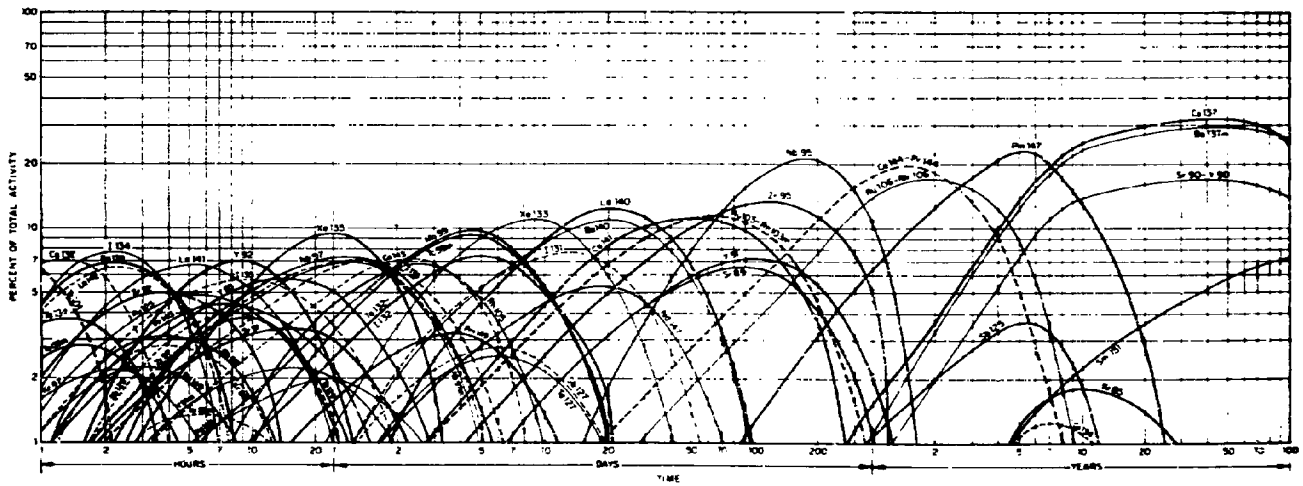

Fig. 3. Principal Contributions to the Total Activity of Fission Products of the Fission of U^{238} by Thermonuclear Neutrons

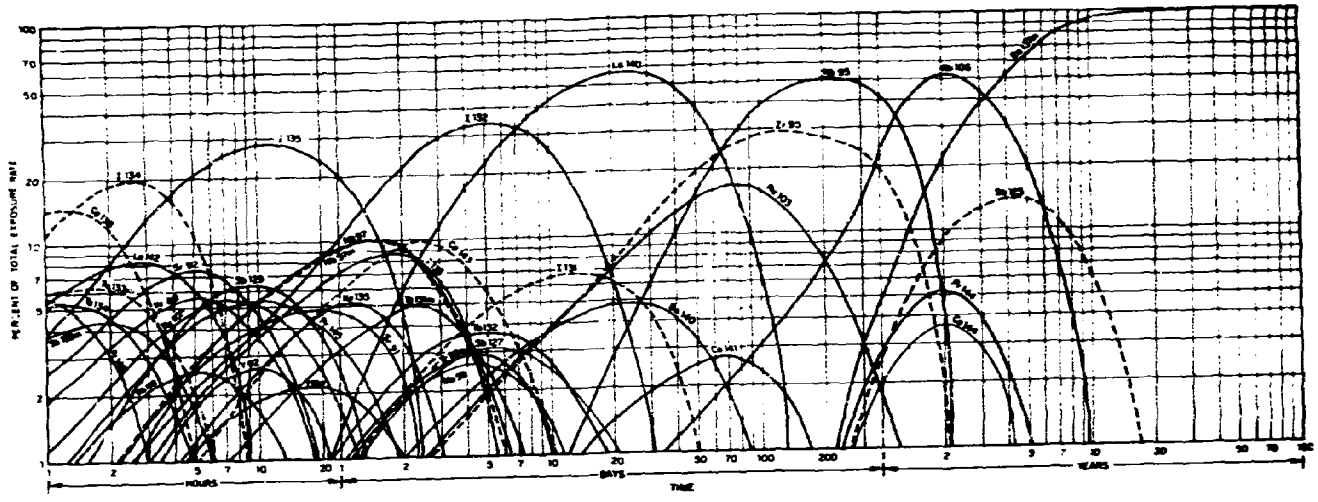

Fig. 4. Principal Contributions to the Total Exposure Rate from Fission Products of the Fission of U^{238} by Thermonuclear Neutrons

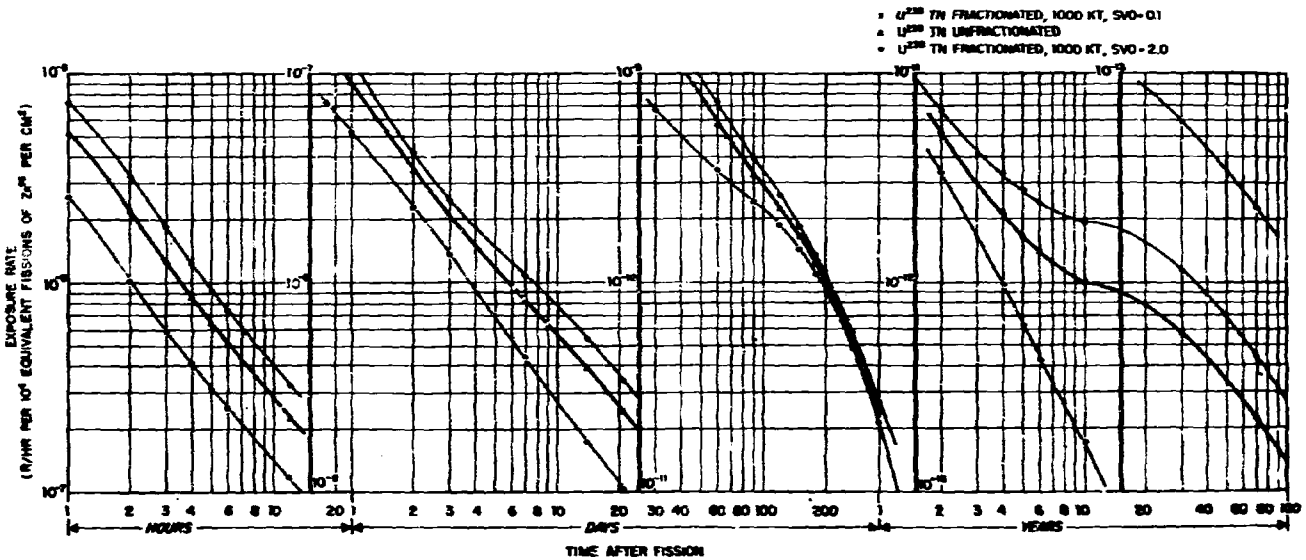

Fig. 5. Comparison of the Exposure Rate Decay for Unfractionated Fission Products of the Thermal Neutron Fission of U^{235} with Two Fractionated Cases

GAMMA RAY FIELDS ABOVE ROUGH CONTAMINATED SURFACES

R. R. Soule
U.S. NAVAL RADIOLOGICAL DEFENSE LABORATORY
San Francisco, California

ABSTRACT

The object of this experiment is to determine the gamma radiation fields above uniformly contaminated surfaces of infinite extent and varying roughness.

Radioactive contaminant (Au^{198} suspended in glass microbeads) was distributed evenly over a circular area 10 ft in diameter in the center of various test surfaces. Ionization chambers were employed to measure the radiation field at various distances out to 128 meters horizontally and 16 meters vertically from the center of the area. These data were then operated upon to obtain the radiation fields to be expected from surfaces of infinite extent. Comparisons of the results from a given surface with those obtained from an ideally smooth (glass) plane provide a measure of surface roughness. Surfaces tested included sand, gravel and grass.

The theory and assumptions used in integrating the data from the finite discs to determine the fields for infinite planes are presented. Preliminary examination of the data from the experimental work indicates the following results:

Surface Roughness Factors for Test Surfaces
at a Height of 1 Meter Above the Surfaces

Surface	Infinite Plane Dose Rate (r/hr)/(c Au^{198}/ft^2)	Surface Roughness Factor
Plate Glass	77.0	1.00
Grass (wet)	61.0	0.79
Coarse Sand	50.3	0.65
Fine Gravel	47.7	0.62
Pea Gravel	42.9	0.56
Medium Gravel	44.5	0.58

Measurements were also made with a point source of Au^{198}. Buildup factors derived from these measurements are presented.

Recent experimentation has been performed at the Camp Parks Facility of the Naval Radiological Defense Laboratory to determine the effect of surface roughness upon gamma ray fields. The objective of this experimentation is to determine the gamma radiation fields above uniformly contaminated surfaces of infinite extent and varying roughness.

In this experimentation[1] radioactive contaminant is spread over a circular area 10 feet in diameter in the center of various test surfaces. Measurements of the radiation field are taken at predetermined distances horizontally and vertically from the center of the area. These data are then operated upon to obtain the radiation fields to be expected from surfaces of infinite extent. Comparison of the results from a given surface with those obtained from an ideally smooth (glass) plane provide a measure of surface roughness.

In order to fully expose the assumptions and limitations inherent in the extrapolation from a finite disc to an infinite field, the scheme used is developed below.

A disc of finite size may be used to approximate a uniformly contaminated plane. The disc is large (dia. 10 ft) in relation to the irregularities which characterize the roughest surfaces used, but is small enough to facilitate the handling and control of the radioactive contaminant. The radiation field (R_0) measured above the center of the contaminated disc is the first term in a series approximation to the field (R) above an infinite plane. The second term in the series is obtained by taking the radiation contribution (R_1) from an annulus (1 disc diameter in width) adjoining the disc. Successive terms are composed of the radiation contributions (R_2, R_3, $\ldots R_n$) from additional adjoining annuli. The approximation of the radiation field due to a contaminated infinite plane becomes better as the number of annuli increase.

$$R \approx R_0 + R_1 + R_2 + \ldots R_n \qquad (1)$$

If the radiation contribution (c_n) from a sector of an annulus is known, the contribution (R_n) from the entire annulus can be found by multiplying the sector contribution by b_n, where b_n is defined as the ratio of the area of the annulus to the area of the sector.

$$R_n = b_n r_n, \quad b_n \equiv \frac{\text{area of annulus } n}{\text{area of sector}} \text{ for } n \geq 1$$

If the sector of an annulus 1 disc diameter wide is chosen to have the same area as a disc of the chosen diameter, the coefficients b_n are simply multiples of 8, and the approximation can be expressed as

$$R \approx R_0 + 8r_1 + 16r_2 + 24r_3 + \ldots + 8nr_n \qquad (2)$$

The radiation contribution (c_n) from a disc of the chosen diameter, contained within the annulus, can be used to approximate the radiation contribution (r_n) from the sector of the annulus. Differences in the actual contributions of the disc and the sector can be adjusted by the use of a correction factor k_n, where k_n is defined to be the ratio of the radiation contribution of a sector to the radiation contribution of a disc.

$$r_n = k_n c_n, \quad k_n \equiv \frac{\text{radiation contribution from sector}}{\text{radiation contribution from disc}} \text{ for } n \geq 1$$

and then

$$R_n = 8nr_n \approx 8nk_n c_n \qquad (n \geq 1) \qquad (3)$$

The values of the correction factors k_n were determined by calculating the radiation contributions from elemental areas of both the disc and the sector, summing for each, and finding the ratio of the sums for a smooth plane. The circle was divided into areas a_1, a_2, a_3, $\ldots$ a_m, and the sector into areas s_1, s_2, s_3, $\ldots$ s_m, at mean horizontal distances d_1, d_2, d_3, $\ldots$ d_m from the detector (See Fig. 1). If the response of a detector at a height h is 1 unit/unit area at unit distance, the response due to the circle will be

$$c_n = \frac{a_1}{h^2+d_1^2} B_1 e^{-\mu d_1'} + \frac{a_2}{h^2+d_2^2} B_2 e^{-\mu d_2'} + \ldots \frac{a_m}{h^2+d_m^2} B_m e^{-\mu d_m'} \qquad (4)$$

where B is the buildup factor, $e^{-\mu d'}$ is due to air attenuation, and $\frac{1}{h^2+d^2}$ is the geometrical factor. The slant range $d' = (h^2+d^2)^{1/2}$. The response due to the sector will be

$$r_n = \frac{s_1}{h^2+d_1^2} B_1 e^{-\mu d_1'} + \frac{s_2}{h^2+d_2^2} B_2 e^{-\mu d_2'} + \cdots + \frac{s_m}{h^2+d_m^2} B_m e^{-\mu d_m'} \qquad (5)$$

The correction factor for the disc approximation of the sector contribution to the radiation field will be

$$k_n \equiv \frac{\sum_{i=1}^{m} \frac{s_i}{h^2+d_i^2} B_i e^{-\mu d_i'}}{\sum_{i=1}^{m} \frac{a_i}{h^2+d_i^2} B_i e^{-\mu d_i'}} \qquad (6)$$

The dimensions of the disc and the sector are such that changes in the air attenuation and buildup factors are small for changes of less than 1 disc diameter in the horizontal distance to the detector. Thus, buildup and air attenuation can be assumed constant for each k_n determination, and k_n becomes

$$k_n = \frac{\sum_{i=1}^{m} \frac{s_i}{h^2+d_i^2}}{\sum_{i=1}^{m} \frac{a_i}{h^2+d_i^2}} \qquad (7)$$

The expression $\sum_{i=1}^{m} \frac{a_i}{h^2+d_i^2}$ cannot be easily evaluated analytically so it was evaluated numerically. However the expression $\sum_{i=1}^{m} \frac{s_i}{h^2+d_i^2}$

approaches $\int_{r_1}^{r_m} \int_{0}^{\pi/4n} \frac{r\, d\theta\, dr}{h^2 + r^2}$ as the width of the elemental areas approaches zero. Analytical evaluation of the latter expression gave results which agreed to within 0.01% with the numerical evaluation of $\sum_{i=1}^{m} \frac{s_i}{h^2+d_i^2}$

The values of k_n were determined for the case of a detector located at a height of 1 meter and for disc diameter and annuli widths of 10 ft (See Figure 1). The value of k_1, for the first annulus, was found to be 0.949, k_2 was found to be 0.989, and the values of k_n for $n>2$ were taken to be unity.

The final form of the approximation of the infinite plane radiation field then becomes

$$R = R_0 + 8(0.949)c_1 + 16(0.989)c_2 + 24c_3 + 32c_4 + \ldots + 8nc_n \qquad (8)$$

where R_0 is the measured radiation contribution above the center of a 10 ft diameter contaminated disc, and c_n is the radiation contribution measured at a horizontal distance of 10n ft from the center of the disc (all measurements made at a height of 1 meter).

The basic experiment consists of measuring the total gamma radiation field at selected heights and distances from contaminated discs of materials of varying degrees of roughness. Gamma measurements are made using ionization chambers. Data from these measurements are extrapolated (integrated) to predict the dose rate for infinite plane sources.

The test surfaces used during this series of experiments were:

1. Plate glass - a smooth surface.
2. Coarse sand (1190 - 2000 μ particle size) (3/64 - 5/64 inches)
3. Fine gravel (2362 - 5613 μ particle size) (3/32 - 7/32 inches)

4. Pea gravel (6680 - 9422 μ particle size) (1/4 - 3/8 inches)
5. Medium size gravel (13,330 - 15,585 μ particle size) (1/2 - 5/8 inches)
6. Grass (lawn type)

The isotope used for this series was Au^{198}, a gamma emitter with an energy of 0.411 Mev. The isotope, enclosed in a microbead carrier, was uniformly dispersed at a mass loading of approximately 12 grams/sq. ft over a 10 ft diameter disc in the center of the test surfaces.

The basic gamma measurements were taken with ionization chambers at combinations of horizontal distances from 0 to 128 meters and vertical distances from 1 to 16 meters from the center of the test surface.

The data from the tests where the isotope was dispersed uniformly over the "ideally smooth surface" (plate glass) was taken as the basis for comparison with the other surfaces of varying roughness. Thus the surface roughness factor depends on the determination of a smooth surface infinite plane exposure as well as on a rough surface infinite plane exposure.

If certain factors, such as the build-up factors, are known, the smooth surface exposure can be calculated to provide a check on the experimentally obtained smooth surface exposure values. Since the experiment was concerned with the region close to the ground-air interface, it was not reasonable to use the infinite medium build-up factors available. For this reason, a supplemental test was conducted in which a series of measurements were made using a gold wire as a point source for the purpose of determining the build-up factor for Au^{198} under the conditions of the experiment.

The gold wire was 5 cm long by 0.095 cm in diameter. All radiation measurements were made in a direction normal to the axis of the wire. The diameter and cross section of the wire were chosen to minimize self-absorption and eliminate angular dependence of gamma rays emitted

perpendicular to the axis of the wire. The length of the wire was selected so that it was long enough to provide the required source strength and yet short enough so that no appreciable error was introduced in considering the wire as a point source at the minimum measurement distance of one meter.

The wire was irradiated to produce an initial activity of about 100 curies. The wire was then placed upon the glass plate in the center of the test pad and radiation field measurements were made at distances from 1 meter to 128 meters from the source at heights of 1, 4, 8, and 16 meters above the plane of the glass plate.

The build-up factors as a function of position of the detector were determined from the expression $I = I_o \frac{e^{-\mu_o r}}{r^2} B$ where I is the intensity in r/hr at the detector position, I_o is the intensity at unit distance from the source in an infinite medium of air, μ_o is the total attenuation coefficient and B is the build-up factor.

Experimentation was conducted on a test surface located at the intersection of two streets which are paved with asphaltic concrete. There are no buildings in the area. A level concrete pad, 30 ft square, was constructed at the intersection of the streets. The central 15 ft square section was further leveled by grinding the surface flat to within ± 1/8 inch, and the test surfaces were centered in this area. For the smooth surface, six sections of 1/4 inch thick plate glass were arranged horizontally on a 1/4 inch thick sponge rubber pad and leveled to provide a smooth level test surface 11 ft square.

For the rough surfaces, a sheet of 5 mil thick plastic was placed on the plate glass surface and the loose material was spread on it. (Figure 2.) A single layer technique was used in spreading the sand and gravel test surfaces. No binder was used, and the intent was to spread a single layer of the sand or gravel and then add additional material

until no visible holes remained in the layer. This resulted in a layer of the material only slightly thicker than the maximum size of the material.

Because the test area is in the open, a plastic dome was onstructed to cover the test surface and prevent the wind from moving the contaminant. The dome is approximately 14 ft square by 3 ft high, and the 3 mil thick Mylar sheeting is supported by an aluminum framework that provides a clear span across the entire width. Since the dome is kept in place over the test surface at all times, one end of the dome is hinged to allow for the entrance and removal of the contaminant and the contaminant dispersal equipment.

The source of radiation for all the tests was the isotope Au^{198}. The radioactive isotope was enclosed in a microbead carrier for the tests in which it was dispersed uniformly over the various test surfaces, and was a single piece of metallic gold for the point source tests. The beads were taken to the test area in a shielded container from which they were delivered into a disperser (Figure 3).

The disperser that distributes the microbeads onto the test surface is a hopper mounted on a small portable motorized bridge crane. As the hopper moved from one side of the area to the other, an auger bit in the bottom of the hopper provided a continuous flow of the microbeads at a constant dispersal rate through four outlets. Four baffles below the outlets spread the microbeads to give an even distribution on the test surface.

The size of the contaminated area was controlled by a mask that rested on the framework of the disperser assembly below the level of the hopper and baffles. Light aluminum pans were fitted together to form the mask to control the size and shape of the contaminated area (Figure 4). The mask had outside dimensions of an 11 ft 10 inch square and had a 10 ft diameter circular cut-out in the center. As the hopper moved from one side of the disperser to the other, the

contaminant fell on the test surface inside the circle while the mask caught the excess. Complete coverage inside the circle was obtained by first dispersing along one side of the mask and indexing the hopper over one hopper width after each pass. After the dispersal of the contaminant, the disperser, including the hopper and mask containing the excess contaminant, was removed from under the plastic dome, and the hinged end of the dome was closed for the duration of the test. The excess contaminant was removed from the test area and measurements were started using Victoreen ionization chambers mounted on a light portable mast (Figure 5).

Preliminary results are available from the experimental work. Figure 6 shows the build up factors derived from data measured with the point source of Au^{198}. It is interesting to note that the 16 meter height factors are below those for heights of 4 and 8 meters.

Figures 7 and 8 present data for the pea gravel surface and grass surface typical of those obtained during the experiments. This type of data was used in conjunction with equation 8 to obtain the infinite plane exposure rates at 1 meter above the surface. Comparison of the various surfaces with the glass surface gave measures of surface roughnesses. The infinite plane exposure rates and the roughness factors are given in Table 1.

A small amount of additional experimental work will be done to obtain an indication of the effect of gamma ray energy upon surface roughness factors. Lutetium-177 with a gamma energy of about .200 mev will be employed on two or three surfaces for this purpose. Point source measurements will also be made with the Lu^{177}.

Table 1

Surface Roughness Factors for Test Surfaces at a Height of 1 Meter Above the Surfaces

Surface	Infinite Plane Exposure Rate (r/hr)/c Au^{198}/ft^2	Surface Roughness Factor
Plate Glass	77.0	1.00
Grass	61.0	0.79
Coarse Sand	50.3	0.65
Fine Gravel	47.7	0.62
Pea Gravel	42.9	0.56
Medium Gravel	44.5	0.58

REFERENCES

1. Kehrer, W. S., et al., Gamma Ray Fields Above Rough Contaminated Surfaces. Progress to 31 January 1966. USNRDL-Letter Report in preparation.

GENERAL REFERENCES

1. Ksanda, C. F., A. Moskin, E. S. Shapiro, Gamma Radiation From a Rough Infinite Plane, USNRDL-TR-108, 18 January 1956.
2. Spencer, L. V., Structure Shielding Against Fallout Radiation From Nuclear Weapons, U.S. Department of Commerce, National Bureau of Standards, Monograph 42, 1 June 1962.
3. Ferguson, J. M., Ground Roughness Effects for Fallout-Contaminated Terrain: Comparison of Measurements and Calculations, USNRDL-TR-645, 7 May 1963.
4. Triffet, T., P. D. LaRiviere, Characterization of Fallout, Operation REDWING (U), WT-1317, 1961 (Secret-RD).
5. Clifford, C. D., Effects of the Ground on the γ Dose From Distributed ^{137}Cs Sources, Canadian Journal of Physics, Vol. 42, pp. 2373-2383, 1964.
6. Huddleston, C. M., et al, Ground Roughness Effects on the Energy and Angular Distribution of Gamma Radiation From Fallout, U.S. Atomic Energy Commission, CEX 62.81, July 1964.
7. Schlemn, C. L., et al, Scattered Gamma Radiation Measurements From a Co^{60} Contaminated Field, AFSWC-TN-59-6, 1959.
8. Mahoney, J. J., R. B. Price, Experimental Tests of Shielding and Attenuation of Gamma Radiation From Radioactive Tantalum Versus Infinite Plane Theory, CRLIR 94, 1952.
9. Strope, W. E., Evaluation of Countermeasure System Components and Operation Procedures, WT-1464, 1958.
10. Starbird, A. W., J. F. Batter, Angular Distribution of Skyshine Radiation at the Surface of a Place of Fallout Contamination, Technical Operations Research, TO-B 63-40, March 1964.
11. Mather, R. L., et al, Gamma Radiation Field Above Fallout Contaminated Ground, WT-1225, 1959.

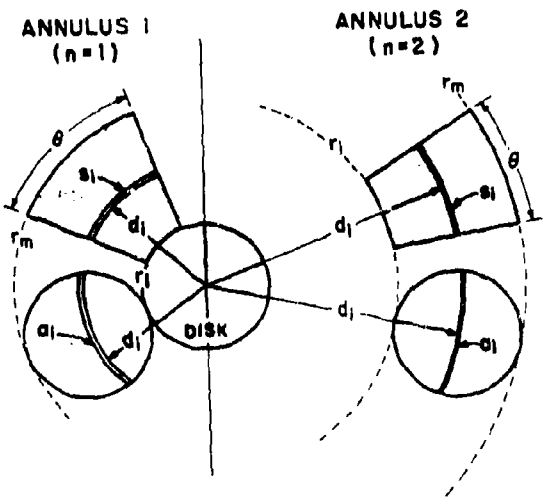

Fig. 1. Disc and Sector Used in Determining the Radiation Contribution From a Sector of a Contaminated Annulus

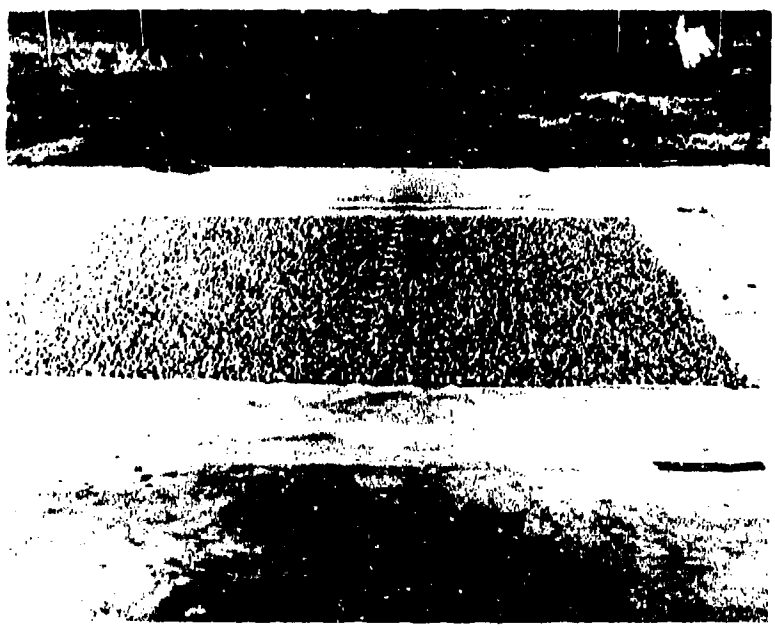

Fig. 2. Medium Gravel Test Surface

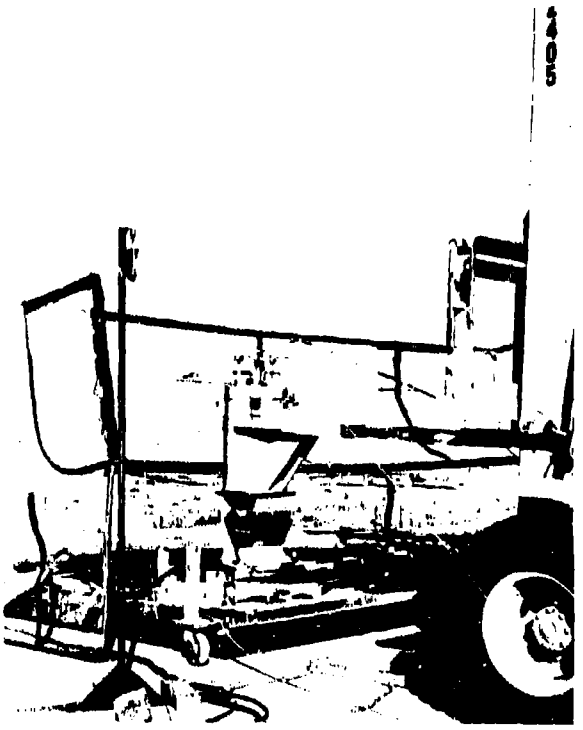

Fig. 3. Shielded Container and Contaminant Disperser

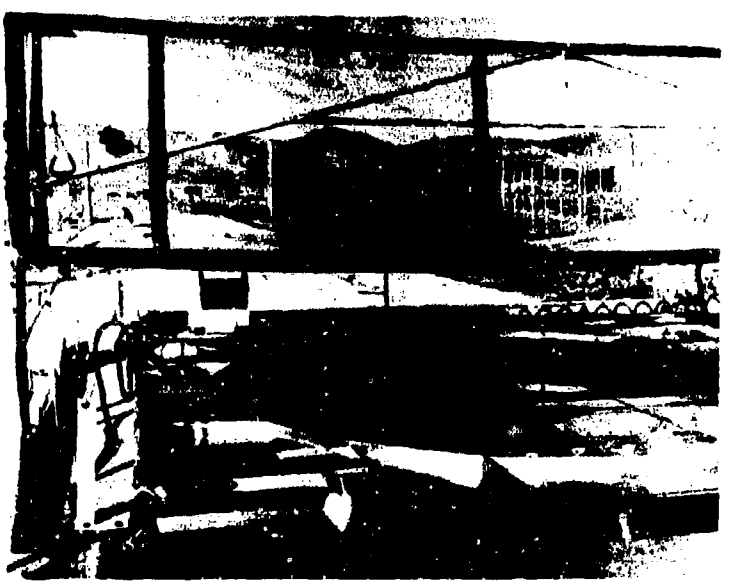

Fig. 4. Disperser and Circular Mask

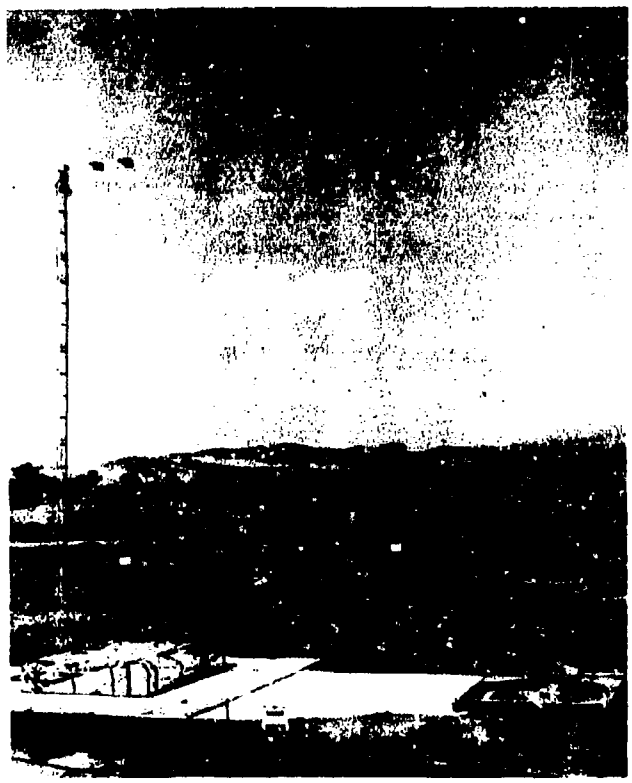

Fig. 5. Test Surface and Instrument Mast

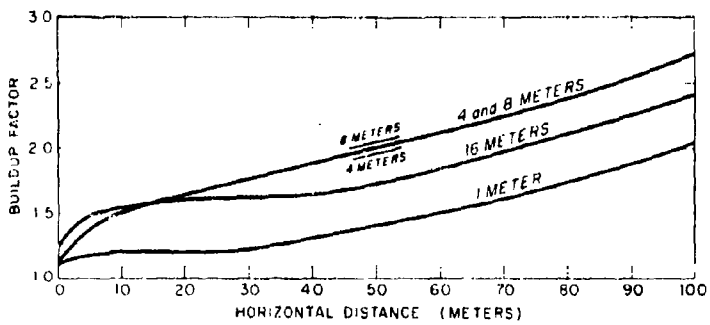

Fig. 6. Buildup Factors vs Horizontal Distances at Vertical Distances of 1,4,8 and 16 Meters Point Source at Au^{198} of Plate Glass Surface

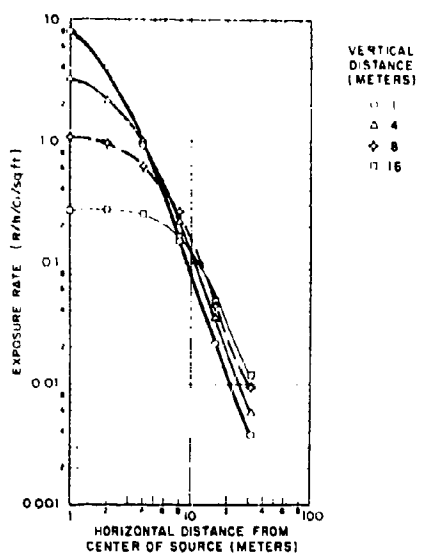

Fig. 7. Exposure Rate from 10 ft Diameter Disc of Au^{198} Contaminant on a Pea Gravel Surface

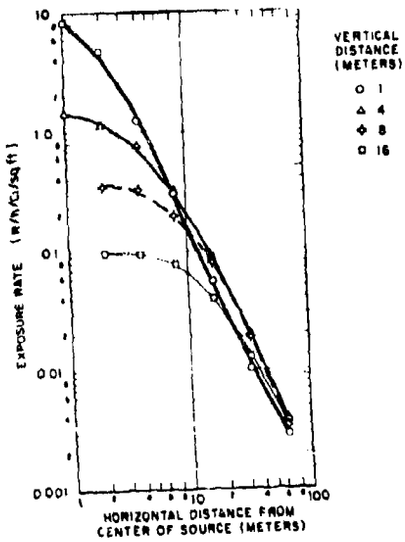

Fig. 8. Exposure Rate from 10 ft Diameter Disc of Au^{198} Contaminant on a Grass (Lawn Type) Surface

DISINTEGRATION RATE MULTIPLIERS IN BETA EMITTER DOSE CALCULATIONS*

S. L. Brown
Stanford Research Institute
Menlo Park, California

ABSTRACT

The possible biological doses from external beta emitters will be discussed and compared with those from external gamma emitters. A detailed analysis has been made of the dose distribution in tissue to be expected from individual beta-emitting radionuclides in contact dose or beta bath plane geometries. In the former case, a thin plane source is sandwiched between two semi-infinite media, the absorber and the back-scatterer. For the latter case, a third medium, an attenuator of finite thickness, is introduced between the backscatterer and absorber, with the source between the backscatterer and attenuator. Point isotropic dissipation functions due to Spencer were integrated over the plane and corrected for backscatter using his plane perpendicular functions.(6) These functions are given for monoenergetic electrons; hence another integration was performed over the beta energy spectrum for each radionuclide. Spectra for nearly 400 beta-emitting radionuclides have been taken from calculations of Hogan, Zigman, and Mackin.(7) Disintegration rate multipliers, which convert contamination levels in dis/sec/cm^2 to dose rates in rad/sec, have been calculated for these radioisotopes for several depths in tissue and widths of air gap. Simplified models based on the beta end-point energy will also be discussed and comparisons will be made with the simplified results and with a simplified gamma model. The conclusion to be offered is that beta radiation can be a serious hazard in comparison with gamma radiation if there are unprotected radiosensitive tissues at shallow depths in the exposed organism.

*Research supported by the Office of Civil Defense.

INTRODUCTION

The ultimate danger from the radioactivity of fission products and other radionuclides, whether the source is fallout from nuclear weapons or is produced by some other method, is the release of ionizing energy in living tissue. This damage to cellular matter can range from the death of a few cells, as occurs every day as a result of natural radiation, to the massive disruption of tissue throughout the entire organism leading to immediate death, as occurs under exposure to enormous fluxes of gamma radiation.

From experience with X-rays used in medical diagnosis and treatment and from direct experiment with laboratory animals and plants, the effects of externally applied X and gamma radiation are relatively well-known. This aspect of nuclear hazards has also received a good deal of study both theoretically and experimentally as a result of the threat of nuclear war.

A second danger from radionuclides is introduced by internal sources, deposited through ingestion, inhalation, injection, or absorption. This danger has been recognized, but presents certain difficulties of evaluation mainly because of the lack of adequate experimental information. However, considerable progress has been made in this area by theoretical extrapolations from available data. The internal dose models usually treat all ionizing radiation and in particular include both beta and gamma radiation.[2,3]

The final category of possibly hazardous radiation is external beta radiation. This has had the least systematic investigation. Besides the difficulty in interpreting the rather scanty experimental data, there has been a tendency to consider this source of radiation exposure as being negligible in comparison with the other sources. The latter

observation is, in fact, justified for a number of ordinary conditions for the following reasons. Beta rays are much less penetrating than gamma rays. For instance, the flux of beta particles (energetic electrons, most often of negative charge but sometimes positive) will be reduced to 1/10 of its surface value after a penetration of perhaps one centimeter of tissue even for the most energetic particles. On the other hand, gamma rays of ordinary energies are hardly attenuated by a foot of tissue, so that the interior of a man's body receives practically the same dose as does his skin. For beta rays, the latter statement would only be approximately true for the smallest organisms. Since in a gross sense, most radionuclides release in total about as much gamma as beta energy, it is clear that beta doses (absorbed energy per unit mass) are always negligible in comparison to gamma doses in the interior of a large animal or plant, because relatively few beta particles will penetrate to lose their energy there.

Similarly, it is found that a few meters of air will considerably reduce the beta flux, and of course denser shielding such as afforded by buildings or even by a few millimeters of clothing would almost assure protection against the beta hazard in comparison with that from gammas. Because of the air attenuation and the thickness of hair, skin, bark, or the like, most large animals and plants such as trees would probably also satisfy the above conditions.

On the other hand, it is not impossible to describe situations in which the injury from external beta radiation can be serious or even limiting. For instance, in the case of the Marshallese,[1,4] the occurrence of beta burns seemed to be much more prevalent than the appearance of a whole body radiation syndrome. This can be explained by the following paragraph when coupled with the facts that the Marshallese were essentially naked and did not attempt to wash away the fallout.

Since, as was implied earlier, a typical fission product mixture releases roughly the same total energy in the form of beta particles as

in gamma photons, and since less energy penetrates to great depths in tissue for betas, it follows that much more energy is absorbed by the tissues at relatively shallow depths. Hence, relatively high beta doses can be delivered to a thin layer of tissue in close proximity to the source. And thus the observation that directly contaminated skin can experience beta burns. From the same argument it is possible to describe several other situations in which comparatively high beta doses might obtain. Naturally, any other cases in which sensitive tissue was directly contaminated would be included. Any animal with an unprotected skin would fall in this category, as would plants with thin horizontal leaves that could retain substantial amounts of fallout, where cells below the leaf surface are the radiosensitive tissue. If the area surrounding a junction of leaf and stem were sensitive, as it might be in younger plants, it might be at risk from fallout caught in the cusps. If the hazard was from contamination on the ground surface, unprotected small animals and plants might be severely burned. In the case of very small organisms, such as certain of the insects and other lower orders, even a whole body beta dose might be a problem, in that at very small depths the beta dose can be perhaps forty times the gamma doses.[5]

The purpose of the research reported here is to provide a computational basis for estimating the prevalence of such beta dose effects. Although it is not the intention to assess the biological effects of a given absorbed dose, it is hoped that the calculations will make it possible to compute the absorbed dose for a variety of exposure geometries corresponding to the possible configurations of sensitive tissue.*

*Although it was beyond the scope of this research to investigate the radiosensitivity of tissues, in general the tissues which produce new growth are the radiosensitive ones in the sense that their loss is most significant to the organism. In plants, these are known as meristematic tissues.

ANALYSIS

It will be assumed in this section that the basic theory of the emission and absorption of beta particles is known. One calculation of fast electron energy dissipation has been performed by L. V. Spencer using a moments method in the continuous slowing-down approximation.[6] The results of that computation are the basis of the analysis presented in this section. The analysis is valid for forbidden as well as allowed spectral shapes, and automatically adds the contributions for a single nuclide that emits betas with several different end-point energies. The detailed analysis can be compared to two simplified empirical analyses which result in dose distributions that vary as an exponential or exponential integral of the depth in the medium.

The basic radiation source geometry assumed for all computations is that of a thin plane source of uniform contamination. In calculating the contact dose, the source is sandwiched between two semi-infinite media, in which medium one is considered an absorber in which the dose is to be calculated, and medium two serves as a backscatterer (Figure 1a). In calculating beta bath dose, a third medium, an attenuator, is inserted as a thick plane slab between the source plane and the absorber. In this case, the attenuator is designated medium two and the backscatterer becomes medium three (Figure 1b).

Spencer[6] has calculated energy dissipation functions in infinite media for two source geometries, the point isotropic source and the plane perpendicular source. These functions, which are here designated as J_I and J_P, respectively, give the energy dissipated by the electrons in spherical shells or plane layers, each of unit thickness, and normalized by the stopping power or initial energy loss rate. They are given in terms of the absorbing medium, primarily represented by its density ρ, the energy E of the monoenergetic beta group, and the distance of penetration into the medium, normalized by the range of the

beta group in that medium. The latter parameter is designated by x. He also gives values for the ranges in g/cm^2, and the stopping powers, in $Mev \cdot cm^2/g$. Because the values chosen for the beta energy groups were somewhat coarse for the present purpose, Spencer's tabulations were interpolated and smoothed graphically before using as inputs.

For this study, the important absorbing medium in which the dose is to be calculated is living biological animal or vegetable tissue. Since polystyrene approximates tissue both in chemical makeup and especially in density, it was chosen from Spencer[6] as medium 1. Spencer does perform calculations specifically for air, so that those results are directly applicable for medium 2, which in the contact dose is the backscatterer but in the beta bath is the attenuator. In the latter geometry, the backscatterer (medium 3) should be specified as soil. The closest Spencer comes to this is aluminum, which approximates compacted soil fairly well in mass density and to a lesser extent in electronic density, as measured roughly by the atomic number. Aluminum is also a prominent component of certain soils, and hence was chosen as medium 3.

Since the source postulated in an ensemble of point isotropic sources uniformly distributed over an infinite plane with density B_o disintegrations per second per square centimeter of nuclide i, the resulting energy dissipation functions are integrals over Spencer's point isotropic functions. The source strength of an element of area $2\pi RdR$ on the plane is $S = B_o(2\pi RdR)$ and is at a distance

$$r = \sqrt{(R^2 + z^2)} \tag{1}$$

from the point at which the dose rate is to be calculated, in a plane a distance z from the source plane. The rate of energy dissipation from this source, in $Mev/cm^3 \cdot sec$, when Spencer's normalization is taken into account and the spherical geometry is recognized, is

$$\frac{S}{4\pi r^2} \frac{\rho}{dr} \frac{dE}{dr} J_I (E, x, \rho). \tag{2}$$

Therefore the total energy dissipation from the plane is

$$I(z,E,\rho) = B_o \frac{\rho}{2} \frac{dE}{dr} \int_o^\infty J_I(E,x,\rho) \frac{RdR}{r^2} \qquad (3)$$

which by making use of (1) can be rewritten as

$$I(z,E,\rho) = B_o \frac{\rho}{2} \frac{dE}{dr} \int_z^\infty J_I(E,x,\rho) \frac{dr}{r} \ . \qquad (4)$$

Equation (4), however, applies only to a uniform absorbing medium. Therefore, the first correction that must be made is for the backscattering medium on the opposite side of the source plane as in the contact dose. The assumption to be made here is that the contribution of the backscatterer to the dose rate is independent of the absorbing material. Thus the overall dose rate in the absorbing medium must be corrected by subtracting out the backscatter contribution that would occur if the backscattering medium were the same as the absorbing medium 1, and then adding instead the backscatter contribution from the actual backscattering medium 2. A reasonable estimate of this backscattering contribution at various depths is the value of the plane perpendicular dissipation function for negative arguments. The contribution from the absorbing medium itself would then of course be proportional to the plane perpendicular function for positive arguments, so that the rate of energy dissipation for the contact dose is approximated by

$$I_C(z,E,\rho_1) = I(z,E,\rho_1) \left[1 + \frac{J_p(E,-x,\rho_2) - J_p(E,-x,\rho_1)}{J_p(E,x,\rho_1)} \right] \qquad (5)$$

In this expression the value to be taken for x is

$$x = \rho_1 z / r_o(\rho_1, E) \quad , \qquad (6)$$

which is also the lower limit of integral (4) when dr/r is replaced by dx/x. The range, r_o, is a function of beta energy and the absorbing medium, as is the stopping power dE/dr in Equations (2), (3), and (4).

Expression (5) gives the energy dissipation for a particular energy E of a monoenergetic beta group. Actual radionuclides emit a spectrum

of energies with one or more end point energies, the highest of which is here designated E_m. Hogan, Zigman, and Mackin[7] have computed beta spectra using the Fermi theory for all beta emitters for which sufficient input data were available. If the fraction of disintegrations that result in a beta of energy E in energy interval dE is (dN/dE)dE, then with appropriate constants the beta dose rate can be written

$$D_C = \frac{c}{\rho_1} \int_o^{E_m} I_C(z, E, \rho_1) \frac{dN}{dE} dE \quad , \tag{7}$$

where $c = 1.6 \times 10^{-8}$ Rad/(Mev/g). The disintegration rate multiplier is defined as the dose rate per unit disintegration rate, or alternatively as the dose per disintegration and is thus

$$F_i(z) = D_C/B_o \quad , \tag{8}$$

where for convenience the subscript C has been dropped on the left and is understood to be part of the geometrical description as symbolically represented by the parameter z. The subscript i, on the other hand, has been added to indicate that a disintegration rate multiplier can be calculated for any beta emitter, in particular the i^{th} one.

With one additional assumption the same methods can be used to estimate the disintegration rate multipliers for the beta bath geometry. This assumption is that the effect of the interface between the attenuating medium and the absorbing one can be essentially ignored by reducing each medium to equivalence by adjusting the path length in each according to its density. If the width of the attenuating slab is u and the depth of penetration in the absorber is v, then z = u + v. If one recalls that in this case the absorber is still medium 1 but the attenuator is medium 2, then it is possible to write the beta bath rate of energy dissipation

$$I_B(z, E, \rho_1) = \frac{\rho_1}{\rho_2} I_C\left(u + \frac{\rho_1}{\rho_2} v, E, \rho_2\right) \tag{9}$$

Since the backscattering medium is now medium 3, I_C is given by

$$I_C = I\left(u + \frac{\rho_1}{\rho_2} v, E, \rho_2\right) \left[1 + \frac{J_p(E,-x,\rho_3) - J_p(E,-x,\rho_2)}{J_p(E,x,\rho_2)}\right], \quad (10)$$

where in this case x is given by

$$x = \frac{\rho_2}{r_o(\rho_2,E)}\left(u + \frac{\rho_1}{\rho_2} v\right) \quad (11)$$

The function I is the same as in Equation (4), with the appropriate value of the arguments. Finally, the disintegration rate multiplier is obviously

$$F_i(z) = \frac{c}{\rho_1 B_o} \int_o^{E_m} I_B\left(z,E,\rho_1\right) \frac{dN}{dE}\, dE \quad (12)$$

RESULTS

The integrals in Equations (4), (7), and (12) are not over functions expressible in closed form, and hence the integration must be done numerically. The computations have been programmed for the Stanford Research Institute Burroughs B-5500 computer. The U.S. Naval Radiological Defense Laboratory made available a copy of the output tape of their beta energy spectra, which gave the fractions of betas per disintegration emitted in energy increments of 0.02 Mev. These fractions were summed to provide the spectral function corresponding to the energy increments for which the dissipation functions had been stipulated. The numerical integration obviously is least accurate when the beta end point is very low so that only a few intervals contribute to the sum approximating the integral. However, those emitters with end point energies of only around one tenth of a Mev are certainly of

little importance in a normal fission product mixture, so that errors of this sort are of little importance.

A more serious difficulty can arise if the depth of penetration z is small in comparison with the range of the betas so that only one or two of the increments in x, of 0.025 each, contribute to the sum approximating the integral in (4). Hence some care must be made in interpreting the results for small z when the beta energy is relatively high.

The choice of depth in tissue or width of air gap for calculating the disintegration rate multipliers is somewhat arbitrary. It was not within the scope of this research to determine the depth at which sensitive tissue occurs in various species. On the basis that one sensitive tissue (the germinative layer of human skin) is at a depth of about 0.1 mm, the smallest z or v to be used should at least be smaller than this depth. It is also true that even betas of the higher energies are strongly attenuated by one cm of tissue; therefore the values of z and v used are 0.003, 0.01, 0.03, 0.1, 0.3, and 1.0 cm. Air gaps smaller than a few millimeters attenuate only the softest betas. If smaller gaps are indicated, the contact dose can be used as an approximation or the results for larger gaps extrapolated. At the other extreme, very few biological systems likely to be damaged by beta radiation have a mean height greater than one meter. Hence 0.1, 0.3, 1.0, 3.0, 10.0, 30.0, and 100.0 cm were chosen for the air gap u. Interpolations are made from semilogarithmic graphs of the results. Extrapolations for larger air gaps or depths in tissue are useful if the restriction on the maximum range is considered.

The results for all the beta emitting nuclides on the USNRDL tape are too lengthy to be presented here. Investigators who wish to use these results are referred to a more complete report.[8] A sample of these results is given in Table 1 for the radionuclide Ba 141. Although its decay scheme is not completely verified, it serves as a good example

because the decay schemes in current use show an energetic beta (2.833 Mev)[7] followed by an energetic gamma (0.7 Mev),[9] with no other transitions. The transition is allowed[7] with an average energy (1.158 Mev) comparable with the gamma energy. It is a fission product of reasonably high yield, although its half-life is only 18 minutes, making it dangerous in about the first hour or so after production. The units of the disintegration rate multipliers listed in Table 1 are Rad/(dis/cm^2).

Figure 2 shows the disintegration rate multiplier as a function of the depth in tissue for two of the cases indicated in Table 1, and compares them with beta and gamma multipliers as calculated by the simplified methods mentioned previously and described in Reference 8. Curve 1 is from the contact dose results of Table 1, whereas curve 2 is from the beta bath results for an air gap of 30 cm. The remaining three curves are all for the contact dose case. Curves 3 and 4 have been calculated from the simplified exponential and exponential integral models, respectively. The latter contains no correction for backscattering. The values of $1/3\mu_1$ (where μ is the linear absorption coefficient) and the maximum range R_m are indicated on these curves to indicate the maximum limits of validity that could possibly have been expected for these relations. The exponential is evidently a reasonable approximation between the lower limit and about one half of the range R_m. On the other hand, it might be possible to fit the shape of the computed curve 1 more nicely with an adjustment in one or more of the parameters (such as μ) of the exponential integral.

Curve 5 has been added to indicate roughly the gamma dose distribution from the same contamination of Ba 141. It has been calculated from the same set of physical and geometrical assumptions that went into the beta exponential integral model. It contains no corrections for backscattering or the buildup factor. Nevertheless, it clearly indicates that beta doses are much higher than gamma doses close to the

Table 1

Disintegration Rate Multipliers for Ba 141

F(u, cm)	0.003	0.010	0.030	0.100	0.300	1.000
Contact Dose z, cm						
F(0.0)	9.225×10^{-8}	6.585×10^{-8}	4.654×10^{-8}	2.550×10^{-8}	9.099×10^{-9}	2.075×10^{-11}
Beta Bath v, cm						
F(0.3)	9.378×10^{-8}	6.699×10^{-8}	4.627×10^{-8}	2.627×10^{-8}	9.214×10^{-9}	2.961×10^{-11}
F(1.0)	8.937×10^{-8}	6.525×10^{-8}	4.600×10^{-8}	2.608×10^{-8}	9.214×10^{-9}	2.961×10^{-11}
F(3.0)	8.113×10^{-8}	6.090×10^{-8}	4.536×10^{-8}	2.584×10^{-8}	8.831×10^{-9}	2.961×10^{-11}
F(10.0)	5.827×10^{-8}	5.200×10^{-8}	4.096×10^{-8}	2.408×10^{-8}	8.663×10^{-9}	2.961×10^{-11}
F(30.0)	4.278×10^{-8}	3.969×10^{-8}	3.363×10^{-8}	2.113×10^{-8}	7.730×10^{-9}	1.736×10^{-11}
F(100.0)	2.353×10^{-8}	2.260×10^{-8}	2.032×10^{-8}	1.394×10^{-8}	5.183×10^{-9}	4.843×10^{-12}

surface, but that the situation rapidly reverses itself as the depth into the tissue becomes greater.

Curves 1, 4, and 5 all have a difficulty near the origin because of the assumed infinitely thin source. Since a real source might be hundreds of microns (or tenths of millimeters) thick, the curves may be inaccurate for depths of that order of magnitude. There is also the problem of self-absorption in the emitter, which would reduce the entire disintegration rate multiplier curve, and would probably also change its shape somewhat because of the energy dependence. The gamma curve would be about fifty percent higher if the gamma energy had been identical with the average beta energy, but would still fall below any of the beta curves for depths of several millimeters.

Although the comparison for other beta-emitting radionuclides will not be specifically presented here, the conclusions would be similar. If the beta spectrum is composed of several allowed transitions, the disintegration rate multiplier curve is similar to the curve generated by adding the corresponding exponential curves in the proper proportions. A forbidden transition results in a curve that varies more from the exponential form than the one shown in Figure 2, but is still of the same general shape.

One feature of the calculation is that it is not particularly sensitive to the maximum beta energy or the shape of the spectrum, at least for near-surface doses. For illustration, the disintegration rate multipliers for one geometry (contact dose at depth of 0.01 cm) have been tabulated in Table 2 for a selected group of important fission products. This depth was chosen because it approximates the depth at which the germinative layer of human skin is found, and thus would give some idea of the hazard from fallout deposited directly on the body. Notice that most of the multipliers are within ±50% of 5×10^{-8} Rad/(dis/cm^2) and only a few depart by an order of magnitude. The uniformity is even more striking at z = 0.003 cm.

Table 2

Summary of Contact Dose Disintegration Rate Multipliers for Selected Radionuclides (in 10^{6} Rad/(dis/cm^2) for Depth of 0.01 cm in Tissue)

Nuclide	F_i	Nuclide	F_i	Nuclide	F_i	Nuclide	F_i
Zn-72	1.974	Nb-95	0.286	Sn-121	2.449	La-142	7.514
Ga-72	4.977	Nb-97	5.419	Sn-123	5.372	La-143	6.955
Ga-73	5.277	Mo-99	5.002	Sn-125	6.029	Ce-141	3.070
Ga-74	6.340	Mo-101	4.851	Sb-125	1.415	Ce-143	4.721
Ge-75	5.243	Mo-102	5.331	Sb-126	5.865	Ce-144	1.508
Ge-77	5.570	Tc-99	1.650	Sb-127	4.959	Ce-145	5.901
Ge-78	4.866	Tc-101	5.340	Sb-128	6.661	Ce-146	4.154
As-77	4.112	Tc-102	7.544	Sb-129	1.170	Pr-143	4.777
As-78	6.999	Tc-104	6.251	Te-127	4.139	Pr-144	6.670
As-79	6.199	Ru-103	0.796	Te-127A	0.068	Pr-145	5.785
Se-81	5.608	Ru-105	5.146	Te-129	5.399	Pr-146	6.758
Se-83A	6.971	Ru-106	0.000	Te-131	5.841	Nd-147	3.927
Br-83	4.948	Ru-107	7.288	Te-131A	2.570	Nd-149	4.689
Br-84	6.393	Ru-108	5.410	Te-132	4.879	Nd-151	5.602
Br-85	6.364	Rh-105	3.399	Te-133	6.222	Pm-147	0.850
Kr-85	4.440	Rh-106	7.009	Te-133A	4.846	Pm-149	5.003
Kr-85A	3.775	Rh-107	5.281	I-131	3.574	Pm-150	5.897
Kr-87	6.846	Pd-109	5.027	I-132	5.284	Pm-151	4.443
Kr-88	4.220	Pd-111	6.026	I-133	5.187	Pm-152	6.031
Rb-88	7.108	Pd-112	1.447	I-134	5.599	Pm-153	5.692
Rb-89	5.395	Ag-111	5.007	I-135	4.441	Sm-151	0.000
Rb-91A	6.795	Ag-112	6.920	Xe-133	2.078	Sm-153	4.030
Sr-89	5.631	Ag-115	6.675	Xe-135	4.733	Sm-155	5.594
Sr-90	4.043	Cd-115	4.664	Xe-137	7.173	Sm-156	3.427
Sr-91	5.591	Cd-115A	5.651	Xe-138	6.216	Eu-155	0.325
Sr-92	3.818	Cd-117A	4.966	Cs-137	3.891	Eu-156	4.020
Y-90	6.129	Cd-118	4.513	Cs-138	6.454	Eu-157	5.004
Y-91	5.667	In-115A	0.253	Cs-139	7.237	Eu-158	6.400
Y-92	7.042	In-117	4.349	Ba-139	6.124	Eu-159	6.025
Y-93	6.635	In-117A	4.583	Ba-140	4.414	Gd-159	4.606
Y-94	7.948	In-118	7.434	Ba-141	6.585	Gd-161	5.638
Fr-95	2.686	In-119	5.703	La-140	5.033	Tb-161	3.276
Fr-97	5.572	In-120	6.069	La-141	6.208		

A summation over radionuclide abundances was carried out for two lists representing the relative abundances of nuclides 10^4 (case 1) and 10^5 (case 2) seconds after U^{235} reactor runs of 20 and 600 seconds, respectively. These lists included only fission products, of course, but might fairly represent fallout from certain types of weapons. One can also compute an approximate standard intensity (one hour gamma air dose rate at three feet above the emitting plane) from these lists by determining the number of fissions, assuming an arbitrary area of contamination (10^8 cm^2), and using a rule-of-thumb conversion factor from fissions per unit area to standard intensity. Finally, the gamma dose rates at the times specified above can be estimated by using an assumed correction based on the $t^{-1.2}$ decay rule. The results of the calculation are shown in Table 3 for the three foot geometry for gammas and the contact dose geometry for betas, and a beta to gamma ratio is also given. This ratio is suggestive of the comparative doses from beta radiation to unprotected contaminated skin and from whole body gamma radiation for a human being, although exact equality of skin and ground surface contamination is unlikely and no statements are made about the relative sensitivity of tissues.

The cumulative absorbed beta dose with increasing depth in tissue can also be estimated by the mechanical integration of a curve like those in Figure 2. These results were compared with another calculation obtained by Monte Carlo techniques using the overall fission product beta spectrum of energies. The agreement is acceptable except at comparatively shallow depths, where the Monte Carlo representation is probably more accurate.*

*William H. Ellett, USNRDL, private communication.

Table 3

Beta and Gamma Dose Rates From Fission Product Contamination

Case 1		Case 2	
2.1×10^{17} fissions		2.1×10^{19} fissions	
1.95×10^{12} fissions/sq ft		1.95×10^{14} fissions/sq ft	
1.48	r/hr @ 1 hr	1.48×10^{2}	r/hr @ 1 hr
0.434	r/hr @ 10^{4} sec	2.74	r/hr @ 10^{5} sec

z	β Dose Rate	β/γ Ratio	β Dose Rate	β/γ Ratio
30 μ	18.33 rad/hr	42.	141.1 rad/hr	51.
100	12.12	28.	83.9	31.
300	7.71	18.	48.4	18.
1,000	3.75	8.6	17.7	6.5
3,000	1.21	2.8	3.4	1.2
10,000	0.06	0.1	0.0	0.0

CONCLUSIONS AND RECOMMENDATIONS

A study of the beta and gamma disintegration rate multipliers in Figure 2 leaves no other possible conclusion but that beta radiation can be a hazard in comparison with gamma radiation if there are unprotected radiosensitive tissues at shallow depths (of the order of millimeters or less) in the exposed organism. This is true whether or not an air gap separates the organism from the source, unless the air gap is very large or the beta radiation very soft. Research is currently under way to determine if insects and other low animal orders satisfy the above criteria for significant beta hazards.* It is recommended that additional research on the sensitivity of organisms to near-surface doses of beta radiation be carried out by capable investigators.

It would also be useful to study further the effect of self-absorption in the source on the results presented in this paper. In addition, the results last reported could easily be extended to any other mixture of radionuclides for which the disintegration rate multipliers have been calculated. This procedure, moreover, would be suitable for including the effects of fractionation as a function of time in a fission product and induced activities mixture.

ACKNOWLEDGMENTS

The subject of this study was suggested by Dr. Carl F. Miller, who also directed the research effort. Oliver S. Yu programmed the computations for the SRI Burroughs B-5500 computer. Paul E. Zigman, James L. Mackin, William H. Ellett, and Dr. S. Z. Mikhail of the U.S. Naval Radiological Defense Laboratory made many helpful suggestions, and Dr. Ora H. Hogan of that laboratory was kind enough to provide a copy of the output tape of her beta spectra calculations.

*Joseph D. Teresi, USNRDL, private communication.

REFERENCES

1. N.C.R.P., Exposure to Radiation in an Emergency, (University of Chicago, 1960)

2. I.C.R.P. Committee II, Health Phys. 3, 1 (1960)

3. Carl F. Miller and Stephen L. Brown, Report on SRI Project IMU-4021 (Stanford Research Institute, 1963)

4. The Effects of Nuclear Weapons, Samuel Glasstone, Ed. (USAEC, 1962)

5. A. Broido and J. D. Teresi, Health Phys. 5, 63 (1961)

6. L. V. Spencer, NBS Monograph 1 (Natl. Bu. Stds., 1959)

7. O. H. Hogan, P. E. Zigman, and J. L. Mackin, Report USNRDL-TR-802 (U.S. Naval Radiological Defense Laboratory, 1964)

8. Stephen L. Brown, Report on SRI Project MU-5116 (Stanford Research Institute, 1965)

9. C. F. Miller, Report USNRDL-TR-160 (U.S. Naval Radiological Defense Laboratory, 1957)

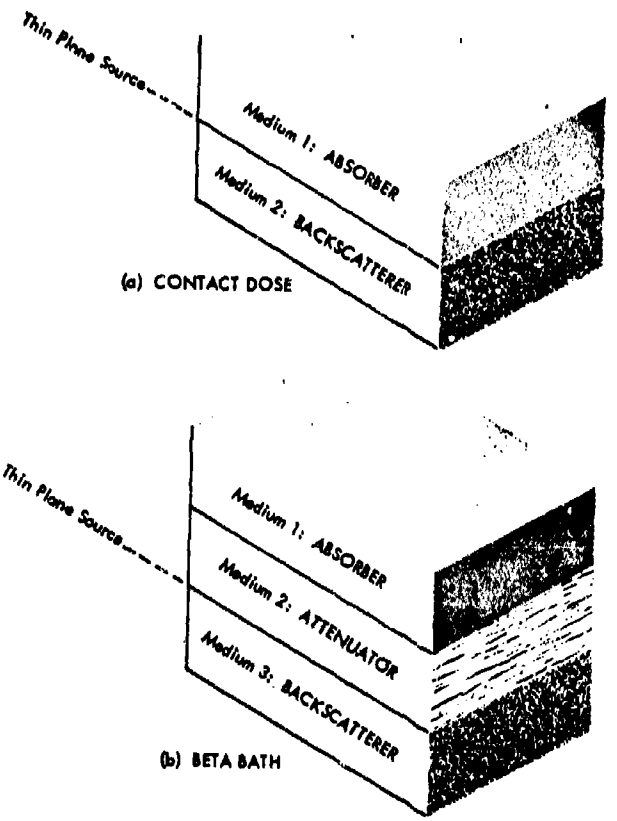

Fig. 1. Geometry for Beta Dose Calculations

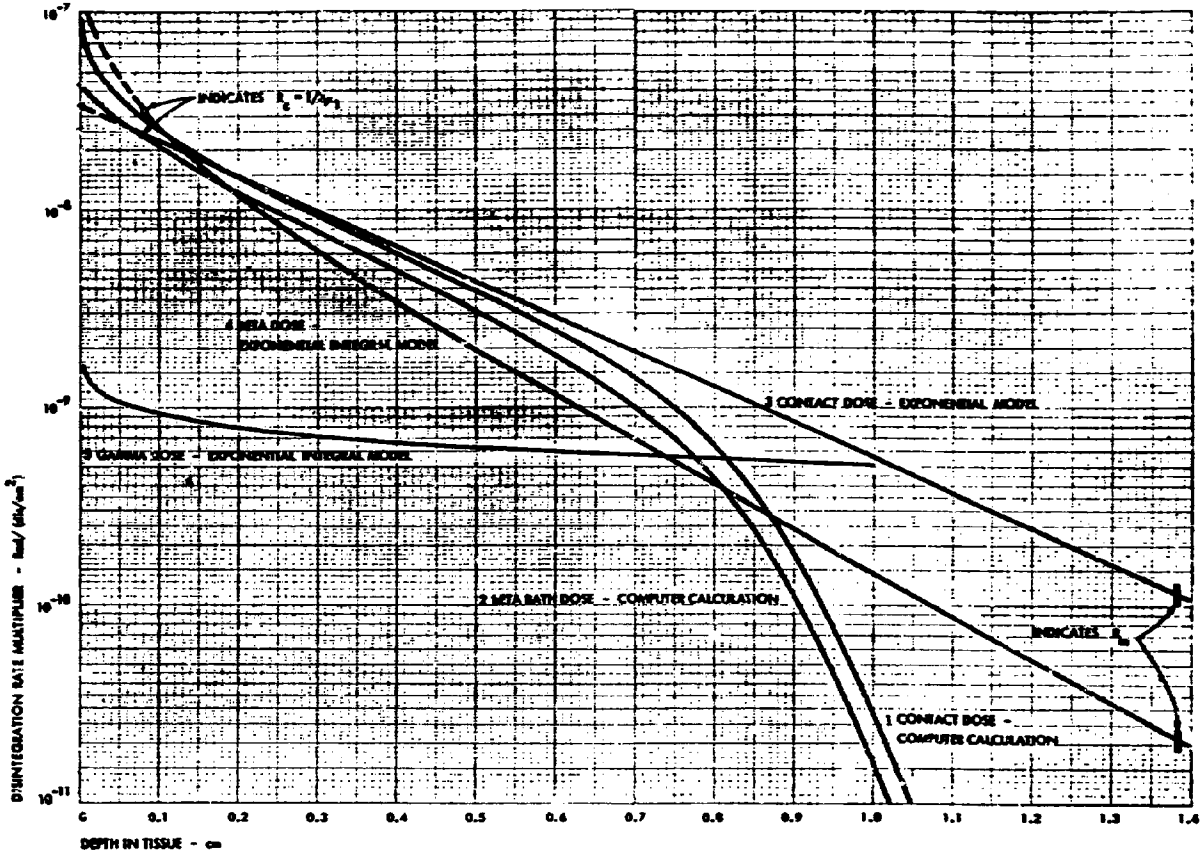

Fig. 2. Comparison of Disintegration Rate Multipliers for Ba-141

CHARACTERISTICS OF THE GAMMA-RAY ENVIRONMENT PRODUCED BY FALLOUT FIELDS

R. L. French
Radiation Research Associates, Inc.
Fort Worth, Texas

ABSTRACT

The gamma-ray environment produced near the air-ground interface by ground-deposited fallout must be known in considerable detail for the evaluation of the radiation protection afforded by structures and for other purposes such as the study of the effects of fallout on biological systems. Two characteristics of critical importance are the energy distribution and the angular distribution of the gamma rays because the fraction of the exterior, or free-field, dose which penetrates to the interior of a structure is highly dependent upon them. Similarly, the energy and angular distributions influence the fraction of the free-field dose which may penetrate to the critical organs of an exposed person.

A number of measurements and calculations of the energy and angular distributions above fallout have been made but all of the results have significant limitations. In the calculations, the problem is usually highly idealized by assumptions such as an infinite plane source on a smooth ground surface. Measurements, on the other hand, suffer from angular resolution, and to a lesser extent, energy resolution problems. They include the effects of ground roughness and other perturbations peculiar to the location of the measurement. New measurements are, of course, precluded by the Limited Test Ban Treaty.

Examination and comparison of various calculated and measured energy and angular distribution data show reasonable consistency and indicate a very strong peak of uncollided gamma rays from just below the horizon and a more diffuse scattered component which comprises on the order of 15 percent of the total dose. Recent applications of these data to shield penetration calculations, however, show that relatively minor differences in the energy and angular distributions can lead to large differences in the fraction of the dose which penetrates to the interior.

I. INTRODUCTION

During the past decade a number of experimental and theoretical investigations have been made of the characteristics of the gamma-ray environment produced by fallout deposited on the ground surface. These investigations have been concerned with such quantities as the specific dose rate and the gamma-ray energy and angular distribution above the fallout field and with the effects of type of fallout, fallout age, ground roughness, and size of the contaminated area upon those quantities. This paper describes the results of several such investigations by the author and his colleagues at Radiation Research Associates and relates them to some results of other workers.

Our work has consisted of theoretical investigations in the following areas:

(1) The determination of the gamma-ray energy and angular distribution above fallout.

(2) The simulation of fallout fields by means of artificial sources.

(3) The analysis of a shielding experiment performed in a real fallout field.

(4) The evaluation of several approaches for incorporating ground roughness effects in calculations of the fallout gamma-ray environment.

(5) The calculation of the gamma-ray depth dose patterns produced in a phantom by fallout and by simulated fallout.

(6) A Monte Carlo study of barrier attenuation factors for use in fallout shielding calculations.

The first two investigations were completed approximately two years ago. The second two were performed during the last year and the last two are currently in work. The following sections summarize the individual investigations and, where possible, give comparisons with the results of other investigators.

II. GAMMA-RAY ENERGY AND ANGULAR DISTRIBUTIONS*

In this investigation,[1] the L05 Monte Carlo Procedure[2] was used to calculate the energy and angular distribution of the photon flux 3 feet in air above infinite plane sources of monoenergetic gamma rays with energies of 0.10, 0.14, 0.25, 0.40, 0.67, 0.85, 1.25, 1.75, 2.50 and 3.50 MeV. The results of these individual calculations were weighted by the ^{235}U fission product decay spectra of Nelms and Cooper[3] and then combined to obtain data for fallout of several different ages.

The geometry of the calculations is shown in Figure 1. For each source, the direct-beam and scattered fluxes at the receiver were computed in each of ten energy intervals between 0.04 and 3.5 MeV and eighteen equal receiver angle (θ) intervals between 0° and 180°. In addition to the fluxes, the dose rate arriving through each ten-degree interval of receiver angle was computed. All results were integrated over azimuthal angle (ϕ) to reflect distribution in receiver angle only.

For the direct-beam calculations, exponential and inverse square attenuation were considered and an air composition of 22 percent (number density) oxygen and 78 percent nitrogen was assumed. Grodstein's gamma-ray cross sections[4] and an air density of 1.29×10^{-3} grams/cm^3 were used. The direct-beam calculations required an integration of the attenuation kernel over the surface of the infinite plane source. The receiver angle (θ) was selected as the variable of integration and, using a machine program, an increment $\Delta\theta$ of one minute was used in integrating over each ten-degree interval of receiver angle.

*Based on work sponsored by the Armed Forces Radiobiology Research Institute, Defense Atomic Support Agency, under Contract No. DA-49-146-XZ-254.

A ground composition corresponding to Nevada Test Site soil was used in the Monte Carlo calculation of the air- and ground-scattered fluxes. The LO5 program allowed essentially exact representation of the air-ground geometry and composition. The infinite plane source, which could not be treated directly by the program, was approximated by a set of 23 point isotropic sources, each of which represented an annular area on the infinite plane source. These point sources were carefully positioned to obtain a smooth integration and extended to a distance of 1600 feet from the receiver.

In a point isotropic source calculation, the LO5 Monte Carlo Program selects source emission directions at random and follows each photon through a path or random walk generated by random sampling from collision probability distributions and angular scattering distributions for the material being penetrated. Upon each collision, statistical estimation is applied to compute the probability that the scattered photon will go directly from the scattering center to the receiver without further interaction. These probabilities are scored at the receiver according to the photon's energy and the angle through which it arrives. An adequate number of photon paths or "histories" must be computed to insure a representative distribution of scattering events in the media about the source and receiver. The Monte Carlo estimate of the flux at the receiver is then the sum of the probabilities accumulated from all histories divided by the total number of histories.

A total of 2300 histories were run for each source energy. This number was generally adequate to keep the indicated standard deviation of the total fluxes below approximately 10 percent. Each photon history was terminated upon the 15th collision or upon the photon energy being degraded below 0.04 MeV. The full results of these calculations have been reported in the open literature[1] and they

have been used extensively in some of the other studies to be described. Thus we will confine the present description to some comparisons with other results.

The results of the monoenergetic plane source calculations may be conveniently summarized in terms of the dose buildup factor which is convenient for examining the relative importance of the direct-beam and the scattered dose. The buildup factor is defined as the ratio of the total dose to the direct-beam dose. As shown in Figure 2, it decreases rapidly with increasing energy up to approximately 1.0 MeV and then remains relatively constant. Buildup factors measured by Rexroad and Schmoke[5] for infinite plane sources simulated by ^{137}Cs and ^{60}Co point sources on the ground are within 5 to 10 percent of the corresponding Monte Carlo values. The buildup factor for ^{60}Co measured by Schlemn, et al.[6] is approximately 4 percent lower than the Monte Carlo value.

Since the original publication of these results, considerable attention has been given to the question of the exact values of the specific dose rate and the dose buildup factor for a receiver 3 feet above an infinite plane source (1.25 MeV).[7] In addition to the data from the above Monte Carlo calculations, the specific dose rate and the dose buildup factor are available, or may be inferred, from six or more different experimental investigations and from a lesser number of other calculations. Comparisons of the other results along with those shown in Figure 2 indicate inconsistencies on the order of 10 percent. Although some of these results were lower than the Monte Carlo results, the overall comparisons suggested that the Monte Carlo results could be too low.

Through the cooperation of Charles Garrett of the Armed Forces Radiobiology Research Institute, the Monte Carlo calculation for 1.25 MeV was extended to obtain results based on 19,320 histories

as compared to only 2300 for the original problem. The dose buildup factor increased from 1.153 to 1.171 but the indicated statistical deviation of the calculation remained at approximately 10 percent. The best value for the specific dose rate and the dose buildup factor for a receiver 3 feet above an infinite plane ^{60}Co source is still a matter of speculation.

The angular distribution of the gamma-ray dose rate three feet above a 1.12-hour fallout field, shown in Figure 3, is strongly peaked between 80 and 90° because most of the direct-beam radiation from the infinite plane source arrives in this angle interval. These data were obtained by folding the monoenergetic source data with the energy spectrum of the non-volatile fission products of ^{235}U as given by Nelms and Cooper.[3] Also shown in Figure 3 is the dose angular distribution 3.3 feet above a 1.12-hour fallout field as given by Spencer[8] who used the moments method and assumed an infinite water medium in performing calculations for the same source spectrum. The two angular distributions are in substantial overall agreement and, based on exploratory calculations performed with the L05 Monte Carlo Program, it appears that the differences which do exist for receiver angles greater than 90 degrees may possibly be attributed to the increased buildup within the infinite water medium assumed in the moments method calculation.

Mather, et al.[9] measured the energy and angular distribution one meter above a 9-day fallout field. His measurements included a source spectrum which differs considerably from the theoretical spectrum given by Nelms and Cooper. Hence a special calculation was made using Mather's source spectrum to weight the monoenergetic plane source data. The upper set of data in Figure 4 compare Mather's spectrum measured at 85 degrees to that calculated (using Mather's source spectrum) for the interval $80° < \theta < 90°$ and the lower set compares

the measured spectrum at 95 degrees to that calculated for $90° < \theta < 100°$. The measured and calculated spectra at 85° are comprised largely of direct-beam radiation and agree within approximately 25 percent in all energy groups above 0.10 MeV. The calculated and measured spectra for $90° < \theta < 100°$ agree almost equally well, although they are due entirely to scattered radiation.

III. SIMULATION OF FALLOUT FIELDS*

The simulation of fallout fields by artificial sources is of interest to the experimentalist who wishes to investigate the nature of the fallout gamma-ray environment, perform fallout shielding experiments, or study the radiobiological effects of fallout. Simulated fallout offers the advantage of controlled experimental conditions and avoids many of the obvious problems associated with real fallout. Our work in this area consisted of examining the extent to which the fallout gamma-ray environment can be simulated by three different approaches ranging from a very simple method to a very sophisticated method.[10]

Perhaps the simplest device for simulating fallout would be a single point source located a sufficient distance from the subject for the air- and ground-scattered components to provide some diffuseness in both energy and angular distribution. Accordingly, L05 Monte Carlo calculations were performed for a point ^{60}Co source located at horizontal separation distances of 100 to 800 feet from a receiver located 3 feet above the ground surface. Energy and angular distributions at the receiver were calculated in the manner described in the preceding section; the only difference was in the source definition.

* Based on work performed for the Armed Forces Radiobiology Research Institute, Defense Atomic Support Agency, under Contract No. DA-49-146-XZ-254.

Comparison of these energy and angular distributions with those above fallout indicated that the optimum separation distance was about 200 feet. Figure 5 shows an overall comparison of the energy and angular distribution at a receiver 3 feet above 1.12-hour fallout (center) and from the point ^{60}Co point source at a distance of 200 feet (right). The energy scale in Figure 5 is arranged in energy groups corresponding to those used in the Monte Carlo calculations. The logarithmic vertical scale gives the photon flux (in units of photons/cm^2-sec-steradian normalized to unit total dose rate as a function of angle in each energy group.

At receiver angles greater than 90 degrees, where all photons are from air scattering, the ^{60}Co point source data show considerable similarity to the fallout data except, of course, above the 1.0-1.5 MeV energy group in which the ^{60}Co source cannot contribute. Below 90 degrees there is little similarity due to the strong direct-beam component from the fallout source which is not present for the point source.

The next level of sophistication in simulating a fallout field consists of using a "pseudo-infinite" plane source of a single source material. This approach, which has been used in many experiments, is feasible because a finite plane source of reasonable dimensions is effectively an infinite source in terms of the radiation intensity 3 feet in air above the source. As an example, for a source energy of 1.25 MeV, 75 percent of the dose originates within 100 feet of the receiver.[11] Approximately 99 percent of the dose comes from within 1000 feet.

The simulation of fallout by pseudo-infinite plane sources of radioactive materials was investigated using the Monte Carlo data described in the previous section. The upper set of data in Figure 6 compares the energy distribution of the total photon flux 3 feet

above infinite plane sources of ^{137}Cs and ^{60}Co to that above a 1.12-hour fallout source. The ^{137}Cs and ^{60}Co data are normalized to give the same total dose rate as that above the fallout which is based on the fission products of one ^{238}U fission per cm^2. The ^{137}Cs and ^{60}Co spectra bear little resemblance to the fallout spectrum except for the degraded components below approximately 0.5 MeV. The principal deficiencies in the energy spectrum simulation occur above the maximum photon energies emitted by the two isotopes.

The lower set of data in Figure 6 shows how the differential energy spectrum above a mixed source of ^{144}Ce (~0.1 MeV), ^{137}Cs (~0.67 MeV) and ^{60}Co (~1.25 MeV) compares with the fallout spectrum. The amount of ^{144}Ce, ^{137}Cs, and ^{60}Co was selected to correspond with the fallout source strength for $E<0.25$ MeV, $0.25<E<1.00$ MeV and $E>1.00$ MeV, respectively. The spectrum from the mixed source shows stronger peaks and valleys (due to the direct-beam lines) but otherwise follows the fallout spectrum in general shape up to maximum energy provided by the mixed source.

Figure 7 shows a corresponding set of comparisons of the differential angular distribution of the total dose above the various sources. Both the ^{137}Cs and ^{60}Co sources are seen to provide good simulation of the fallout dose angular distributions except at very high angles at which only scattered photons may contribute to the dose. The deficiency at the high angles is essentially eliminated by the mixed source.

Included in Figure 5 is an overall comparison of the energy and angular distribution above the ^{144}Ce-^{137}Cs-^{60}Co source (left) and the 1.12-hour fallout source (center). The surfaces generated by the energy and angular distributions above the two sources are generally similar except for the absence of ^{144}Ce-^{137}Cs-^{60}Co photons in the energy groups above 1.50 MeV.

The most sophisticated fallout simulator which was evaluated was the so-called "compact" simulator proposed by the Armed Forces Radiobiology Research Institute.[12] Basically, the compact simulator consists of a 60-foot radius disc of ^{144}Ce, ^{137}Cs and ^{60}Co on the ground surface with a "rim" source of the same three isotopes at a height of 2.5 feet above the outer edge of the disc source. Six feet above the disc source is a thick slab of water, also with a radius of 60 feet. The philosophy behind the compact simulator is that within some usefully large volume about the center of the system, the rim source will be a virtual source for that portion of the infinite plane source not represented by that disc source, and that the water slab will act as a scattering medium for photons from both the disc and rim source to simulate skyshine from an infinite plane source.

The compact simulator was found to produce virtually the same gamma-ray energy and angular distribution as did the ^{144}Ce-^{137}Cs-^{60}Co infinite plane source.

IV. ANALYSIS OF FALLOUT SHIELDING EXPERIMENT*

Four multilayer enclosure shields were exposed to fallout 16,000 feet downwind from Shot Small Boy during Operation Sunbeam. The experiment,[13] designated Project 2.15, consisted of measuring the gamma-ray dose rates both inside and outside the enclosure shields for periods of 1 to 6 days following the detonation. The analysis consisted of calculating the dose transmission factors (inside dose rate divided by outside dose rate, D/D_o) of the enclosure shields on a theoretical basis and comparing with similar factors derived from the experimental results.[14] The purpose of the

*Based on work funded by the Office of Civil Defense through the Terminal Ballistics Laboratory, BRL, Aberdeen Proving Ground, Md., under contract DA-23-072-AMC-332(X).

experiment was to obtain information which would be useful in the development and evaluation of calculational methods for predicting the transmission of fallout gamma rays into shielded structures. Of particular interest was the investigation of the time-dependence of the dose transmission factors.

Two of the enclosure shields were cubical and consisted of a 4-inch inner layer and a 1-inch outer layer of iron separated by an 11-inch space which could be filled with water. One of the cubical shields, designated Shield 2 (see inset in Figure 8) had an inside dimension of 24 inches whereas the other cubical shield, designated Shield 3, had an inside dimension of only 6 inches. Both cubical shields were covered by a 1/8-inch layer of aluminum and a 1/4-inch layer of Boroxy. The other two enclosure shields were spherical and had an inside diameter of 24 inches. One spherical shield, Shield 4 (see Figure 9) had layer thicknesses similar to Shield 2. The other, Shield 5, consisted of two 1-inch layers of iron separated by a 2-inch space which could be filled with water. Both spherical shields were covered with a 1/4-inch layer of Boroxy.

Prior to the detonation, the shields were positioned with their geometric centers 50.5 inches above the ground and at 100-foot intervals along a line. G-M tubes were mounted at the center of each shield and at a corresponding height on each of ten free-field detector posts located in the vicinity of the shields. Film packs were also mounted at each detector location. Following the detonation, remote readings of the gamma-ray dose rate at each detector location were taken at frequent intervals until the dose rates inside the shields were too low to be measured accurately. The space between the inner and outer iron layers of each shield was filled with water which was drained by remote control at H+5 hours.

The calculations were divided into three steps; 1) specification of the time-dependent energy spectrum of the gamma rays emitted by the fallout, 2) determination of the energy and angular distribution of the gamma rays incident upon the shields, and 3) calculation of the penetration of the gamma rays into the shields. A variety of theoretical and measured data were used for the fallout emission spectra. The theoretical spectra were those of Nelms and Cooper[3] for the fission products from thermal-neutron fission of ^{235}U and those of Björnerstedt[15] for fission-neutron fission of ^{239}Pu and thermal-neutron fission of ^{235}U. The measured spectra included those of Tomnovec, et al.[16] for Small Boy fallout particles and Cook's composit spectra[17] based on fallout samples collected from a number of different weapons tests.

The energy and angular distribution of the scattered gamma rays above fallout with the above energy spectra were computed using the Monte Carlo data discussed in Section II. Analytic calculations were made of the energy and angular distribution of the direct-beam gamma rays above the fallout. Additional source term data were developed from the energy and angular distributions measured above Small Boy fallout by Huddleston, et al.[18] All of the source terms were processed into a consistent set of 10 energy groups and 18 angle groups for folding in with energy- and angle-dependent shield penetration data.

The shield penetration data were computed for each energy group and, for the cubical shields, each angle group. The direct-beam component was computed analytically. The shield-scattered component was computed with Wells' C1S Monte Carlo procedure[19] for the cubical shields and with Collins' L05 Monte Carlo procedure[2] for the spherical shields. The application of the resultant penetration

data in calculating the dose transmission factors of the enclosure shields is described by the general equation

$$D/D_o = \frac{\sum_E \sum_\theta N(E,\theta)g(E)A(E,\theta)}{\sum_E \sum_\theta N(E,\theta)g(E)}$$

where $N(E,\theta)$ is the free-field photon flux with energy E at angle θ,
$g(E)$ is the flux-to-dose conversion factor, and
$A(E,\theta)$ is the fraction of the dose from photons incident with energy E at angle θ which penetrates to a receiver at the center of the shield.

Calculations were performed for each shield as a function of time using each of the various theoretical and measured source terms. Most of the calculated dose transmission factors are summarized and compared with the measured data in Figures 8 and 9 for Shields 2 and 4, respectively. With few exceptions, the calculated dose transmission factors are higher than those measured. The extent of the overprediction depends upon the particular source term but it is typically 50 percent or more. Shield 2 (Figure 8) shows the best overall agreement between the calculations and the measurements. The calculated and measured factors for Shield 4 are noted to be consistently higher than those for Shield 2, the cubical shield of similar size and layer thicknesses. The measured and calculated transmission factors for the thin spherical shield (Shield 5), although much higher, have characteristics similar to those of Shield 4.

Of the calculations based on theoretical source terms, those using Björnerstedt's ^{239}Pu fission product gamma-ray spectra[15] agree best with the measured data. The use of Cook's composite measured spectra[17] gave dose transmission factors which agree better with the measured factors than any of the other source terms, either measured or

theoretical. The calculated factors based on the Small Boy fallout energy spectra measured by Tomnovec, et al.[16] show poor agreement with the measured factors. In the few cases where calculated factors based on the energy and angular distribution measured over Small Boy fallout by Huddleston, et al.[18] can be compared with measurements, they show little improvement over the other data.

Although the calculations generally overpredict the measurements, the time-dependence of the calculated dose transmission factors is reasonably consistent with that indicated by the measured factors. Both the calculations and measurements indicate that D/D_o was relatively constant during the first 5 hours (300 minutes) and, as would be expected, increased sharply when the water was drained. Peak values were reached between 5 and 8 hours followed by a decrease of as much as 50 percent during the remainder of the first day. All of the calculations indicate that D/D_o increases again after approximately 3 days.

The results of a simple calculation for Shield 2 based on current Civil Defense shielding technology are included in Figure 8. This calculation was performed with the method for simple above ground structures given on Page 4-6 of Reference 20. The bottom of the shield was neglected and it was assumed that the sides extended downward to the ground surface. The comparison shows that the simple calculation, which is based on Spencer's attenuation data[8] for a fixed energy spectrum (Nelms and Cooper, 1.12-hr ^{235}U), gives a reasonable estimate of D/D_o, particularly for the important early times.

It was concluded that the most critical factor in the calculations was the energy spectrum assumed for the fallout and that the tendency to over-predict D/D_o was probably the cumulative result of several factors. These factors include a possible deficiency of low energy gamma rays in the source terms, the use of idealized models of the

enclosure shields which neglected engineering detail, and the neglect of ground roughness effects on the energy and angular distribution of the gamma rays incident upon the enclosure shields. It was not possible to definitize the individual contributions of these factors to the discrepancies since no free-field measurements other than total dose rate were made at the exposure site.

V. GROUND ROUGHNESS EFFECTS*

The only detailed calculations of the gamma-ray energy and angular distributions above fallout which have been reported[1,8] employ the assumption that the radioactive material is uniformly distributed over a perfectly smooth surface. It is well known, however, that this assumption can lead to large overestimates of the radiation intensity, particularly at positions near the ground surface. A survey reported by Clifford[21] gives various estimates indicating that the dose rate one meter above rough ground may be only 10 to 70 percent of the corresponding dose rate over smooth ground.

A number of possible methods for incorporating the effects of ground roughness into fallout calculations have been suggested and explored to some extent.[21] However, their application has been limited to the direct-beam (uncollided) component with emphasis on the effect on radiation intensity rather than on energy and angular distribution. Experimental investigations have been limited largely to the effect on total dose. Exceptions are the field experiment performed by Huddleston, et al.[18] and current work by Shumway and co-workers at USNRDL.[22]

*Based on work funded by the Office of Civil Defense through the United States Naval Radiological Defense Laboratory under Contract No. N228(62479)68174.

The first phase of an investigation of possible methods for predicting the effects of ground roughness upon the energy and angular distribution above fallout is currently being completed at Radiation Research Associates.[23] The principle objectives of the investigation are; (1) to examine the effectiveness and practicality of several relatively simple methods of accounting for ground roughness effects, and (2) to gain additional insight on the nature and extent of ground roughness effects, particularly on the gamma-ray energy and angular distributions near the air/ground interface. Because of the overall complexity of the problem and the fact that there are a number of possible approaches to its solution, the first phase was limited primarily to the direct-beam and singly-scattered components (which contribute on the order of 90 percent of the total dose rate near the air/ground interface).

Of the various approaches which have been suggested for including the effects of ground roughness in calculating the radiation environment above fallout, four were selected for investigation:

1. Buried source model.
2. Mixed source model.
3. Collimated source model.
4. Furrowed surface model.

The buried source model is the most popular of the four. It has been discussed and investigated to various extents by several investigators.[18,24,25,26,27] In this approach, the degree of ground roughness is represented by the thickness of the soil layer beneath which the source is assumed to be buried. The mixed source model is similar to the buried source model in that the source material is assumed to be mixed with a thin layer of soil, the thickness of which is adjusted to simulate the desired degree of ground roughness.

The simplest model proposed thus far is the collimated source model conceived for the present investigation. In this model, the source is assumed to be uniformly deposited on a smooth ground surface. Rather than being allowed to emit gamma rays isotropically, however, the emission is constrained to angular sectors which are specified according to the degree of ground roughness.

The furrowed surface model has been investigated experimentally by Clifford,[21] but has not been used previously for calculations. It consists of a uniform array of furrows in the ground surface. The width, depth and spacing of the furrows, along with the division of source material among the regions of the furrows, control the degree of ground roughness.

Equations were formulated for the energy and angular distributions of the flux and dose rate from direct-beam and singly-scattered photons at an arbitrary height above a monoenergetic infinite plane source on a ground surface as represented by each of the four models. In each case, the single scattering was assumed to be affected by the ground roughness only through the effect on the distribution of the direct-beam flux in the air and ground (i.e., ground roughness was assumed to have a negligible effect on the path of the radiation after a collision occurs). Receiver energy and angle groups were selected to be consistent with those used in the previous Monte Carlo calculations.[1]

The most extensive calculations were performed with the buried source model. The energy and angular distribution of the flux and the angular distribution of the dose rate from direct-beam and singly-scattered gamma rays were computed three feet above the air-ground interface for sources buried in dry Nevada Test Site soil (ρ = 1.15 gm/cm^3) at depths of 0, 0.25, 0.50, 1.0, 1.5 and 2.0 inches and with source

energies of 0.10, 0.14, 0.25, 0.40, 0.67, 0.85, 1.25, 1.75, 2.5 and 3.5 MeV. The calculations for source energies of 0.67 and 1.25 MeV were extended to source depths of four inches.

Figure 10 illustrates the dependence of the angular distribution of the direct-beam and singly-scattered dose rates upon source depth for a source energy of 1.25 MeV. The shape of the direct-beam curve for $\theta>70°$ has a strong dependence upon source depth. The angular distribution of the singly-scattered dose rate is less sensitive to source depth, but it is noted that the dose rate from $\theta<90°$ increases at small depths. This increase overrides the decrease for $\theta>90°$ so that the total singly-scattered dose rate increases at small depths as is indicated in Figure 11 which shows the dose rates from the 0.67 MeV source versus source depth. Presumably, the increase in the scattered dose rate is due to the larger number of scattering events which occur between the source plane and the receiver.

Included in Figure 11 are the results of Clifford's measurements made 3 feet above a simulated plane Cs^{137} source 70 meters in radius with various thicknesses of expanded polystyrene covering the source.[26] To make a comparison with the calculated data, the polystyrene thicknesses were converted to mass-equivalent ground thicknesses. The measured dose rate for zero source depth is noted to be approximately 20 percent less than the calculated sum of the calculated direct-beam and singly-scattered dose rate. This difference is probably due to the experimental source extending to only 70 meters. Otherwise, the neglect of multiple scattering in the calculations should underpredict the measured dose rate. The other measured values for equivalent depths of 0.35 and 0.70 inches fall somewhat in line with the sum of the calculated direct-beam and singly-scattered dose rates. It is thought that the finite size of the experimental source does not reduce the

dose rate at these source depths because the contribution from points at greater distances on an infinite plane source would be limited by the large slant paths through the ground.

Results for fallout of several different ages were computed by weighting the monoenergetic source data according to the Nelms and Cooper energy spectra for non-volatile ^{235}U fission products[3] and summing over energy for each source depth. It was found that in terms of the total direct-beam and total singly-scattered dose rates, the 1.12-hour data has a source depth dependence which almost exactly matches that for the 1.25 MeV plane source. Similarly, the 23.8-hour fallout data matches the 0.85 MeV data and the 4.57-day fallout data matches the 0.67 MeV data.

Huddleston, et al.[18] measured the gamma-ray energy and angular distributions 3 feet above 28-hour fallout deposited on a dry lake bed and above 5.5-day fallout deposited on rough desert terrain. In order to make comparisons with the above mentioned calculations for 23.8-hour and 4.57-day fallout, the measured energy and angular distribution data were rearranged into the same energy and angle groups used for the calculations.

Comparisons of the measured dose angular distributions with those computed for buried fallout sources considering only the direct-beam and single scattering would not be meaningful since the effects of multiple scattering are included in the measured data. In order to make comparisons, two approaches for including an approximation of the multiple scattering were tried:

1) It was assumed that burying the source under the ground had no effect on the multiple scattering and that previously calculated multiple-scattering data for a source at the air-ground interface could be added to the direct beam from a buried source.

2) It was assumed that the total multiple-scattered dose for $\theta<90°$ was affected by source burial in the same manner as the singly-scattered dose but that the angular distribution within this interval is not changed. A corresponding assumption was made for the multiple scattering for $\theta>90°$.

These two approaches were used in a trial and error process to determine which approach and source depth led to the best approximation of the measured dose angular distributions.

Figure 12 shows a comparison of results obtained using the second approach with the measured results for the fallout deposited on a dry lake bed. The dose angular distribution calculated with the source buried at a depth of 0.5-inches agrees very well with the measured data except at very large angles. Included in Figure 12 is the dose angular distribution computed for fallout deposited on a smooth ground surface which is seen to differ considerably from the measured data. For the case of the fallout deposited on rough desert terrain, the best calculated results were obtained using the second approach and assuming the source to be buried at a depth of 1 inch.

The mixed source model may be treated as an extension of the buried source model inasmuch as buried source data may be weighted and combined to approximate mixed source results. Accordingly, the buried source results described in the previous paragraphs for monoenergetic and fallout sources were used to generate results for the case where the source is mixed uniformly with the soil to depths up to two inches.

The dependence of the direct-beam and singly-scattered dose rates upon the depth to which the source is mixed was found to be similar to that of buried source model, except that both components fall off less rapidly with increasing depth for the mixed source. The mixed source curves are flatter because a fraction of the source always remains near the ground surface and makes a relatively large contribution to the dose rate at the receiver. For the same reason, the

angular distribution of the direct beam from the mixed source differs significantly from that observed for the buried source. Even when mixed uniformly to a depth of 2 inches the mixed source direct beam has a strong peak as the receiver angle approaches 90 degrees. There was little difference between the singly-scattered dose rate angular distributions for the mixed and buried sources, however.

The collimated source model stems from the observation that one of the most apparent effects of ground roughness is a reduction in the strong direct-beam component from below the horizon caused by the large slant path through the surface materials lying above (but necessarily over) portions of the source (see Figure 13). If source particles are assumed to settle straight down into crevices and between lumps of soil, rocks, or other matter, the escape of uncollided radiation into the air is uninhibited at or near $\theta = 0°$ where θ is the angle measured with respect to the upward normal. As θ increases, however, the probability of penetrating ground material increases, approaching unity at $\theta = 90°$ for all but source particles lying on top of the highest surface features.

The collimated source model is based on the assumption that, for a given ground surface, there exists an effective cutoff angle θ' beyond which no leakage of uncollided radiation into the air can occur. The value of θ' depends on the nature and the degree of ground roughness. Leakage into the air is assumed to be uninhibited for $0° < \theta < \theta'$ and air scattering is assumed to be affected only through the effect of θ' on the uncollided flux distribution in air. Ground scattering is not affected by the model since the direct-beam leakage into the ground is uninhibited for $90° < \theta < 180°$.

The studies performed with the collimated source model were limited to a source energy of 1.25 MeV. Calculations were performed for several effective cutoff angles θ' ranging from 45 to 87.5 degrees. The direct-beam and singly-scattered dose rates versus cutoff angle are shown in Figure 14. The direct-beam curve is reminiscent of those computed with the buried source method; a relatively sharp initial decrease in the dose rate is followed by an approximately logarithmic gradual decrease. It should be noted, however, that if the curve was extended to small angles, it would have to turn steeply downward since the direct-beam dose rates for $\theta' = 0$ would be zero.

The singly-scattered dose rate curve bears no resemblance to that computed with the other methods. In particular, there is no initial buildup in scattered dose as the amount of ground roughness is increased (i.e., as θ' is decreased). Moreover, the singly-scattered dose rate curve does not tend to become parallel to the direct-beam curve. The singly-scattered component continuously increases in importance.

An interesting feature of the singly-scattered dose rate angular distribution curves computed with the collimated source model is that their shapes and magnitudes are nearly independent of θ' for receiver angles less than 90°. This behavior is a result of the strong contribution from ground scattering which is independent of θ'. The dependence of the singly-scattered dose upon θ' becomes progressively greater for receiver angles greater than 90°. The direct-beam angular distribution does not change in shape with θ'; it simply terminates.

The furrowed-surface ground roughness model is based on the assumption that the ground roughness can be represented by regular furrows or ridges in an otherwise smooth ground surface. The furrows may be either rectilinear or concentric. The concentric geometry was selected for the present study because the symmetry reduces the amount of calculational effort required. The geometry of the furrowed-surface model which was programmed is illustrated in Figure 15. The parameters L, W, X and Z may be adjusted to represent furrows of arbitrary profile.

The single-scattering calculation requires the assessment of the angular distribution of the direct-beam flux at a number of positions along the Z axis. The direct-beam flux at a given Z is then assumed to be independent of the radial position, and the presence of the furrows is neglected once the direct-beam distribution is computed. Hence, in the single-scattering calculations, the effect of the furrows is to modify the distribution of first collisions in the air and in the ground. Once a collision takes place, the path from the collision center to the receiver is assumed to be the same as if the ground surface had been smooth.

From the above it is seen that a physical interpretation of the model would be as follows: From any given point of observation, the ground surface has uniformly spaced furrows concentric about the vertical axis through the observation point insofar as the direct-beam component is concerned. The single-scattered component at the same observation point due to scattering in a particular dV is that which would result if the furrows were concentric about the axis on which that dV lies.

The machine time requirements for the furrowed-source calculations turned out to be quite large compared to the other models. The difficulty stems from the requirement for calculating the direct-beam at a large number of mesh points for use in the single-scattering calculation. For each such mesh point, the path through the furrows must be traced from many individual points on the furrowed surface in the process of integrating over the source distribution. Because of the large amounts of machine time required, only a few calculations were performed with the code. These calculations were designed to correspond to an experiment performed by Clifford.[21]

Clifford's experiment included measurements of the gamma-ray dose rate above rough ground simulated by a concentric sawtooth array with a radius of 70 meters and contaminated by ^{137}Cs sources (0.67 MeV).

The sawteeth were of concrete and had a 45° profile with a depth of 6 inches. Measurements were made at vertical heights of 1 to 19.3 meters above the center of the field with ^{137}Cs point sources positioned individually at various radii in the valleys, at the apex, and at the midpoint of each slope. Control measurements were made over a smooth concrete surface.

Calculations were performed for comparison with Clifford's results for the case where the sources were located at the midpoint of each shape and for the smooth surface case. Table I gives the measured and calculated results for a receiver 1 meter above the center of the concentric field, for both the smooth surface case and for the case where the sources are located at the mid-point of each slope. Since the measured dose rates include multiple scattering, it was necessary to include an estimate of the additional dose rate from higher orders of scattering in the calculations. This was done by assuming that the ratio of total scattering to single scattering for a receiver 3 feet above an infinite plane source of 0.67 MeV gamma rays on a smooth ground surface is applicable to the experimental geometry. This ratio was estimated from the single-scattering data from the buried source calculations for a source depth of zero and from the multiple scattering data given in reference 1.

From the preliminary studies of the four ground roughness models, it appears that the best choice for use in fallout calculations would be either the buried or the mixed source model. The buried source model, which may be regarded as a special case of the mixed source model, is the more convenient of the two to apply. The collimated source model, although easy to apply, does not appear to produce realistic results. The furrowed source model is attractive from the standpoint of physical realism, but it is exceedingly cumbersome to apply and, thus far, gives no indication of being better than the buried and mixed source models.

Table I

Dose Rates 1 Meter Above Center of ^{137}Cs Source
70 Meters in Radius

(rad(tissue)/hr per source photon/cm^2-sec)

Component	Calculated	Measured
	Furrowed Surface	
Direct-Beam	3.517×10^{-7}	
Singly-Scattered	1.466×10^{-7}	
Adjustment for Multiple Scattering	2.506×10^{-7}	
Total	7.489×10^{-7}	8.430×10^{-7}
	Smooth Surface	
Direct-Beam	2.248×10^{-6}	
Singly-Scattered	2.397×10^{-7}	
Adjustment for Multiple Scattering	4.090×10^{-7}	
Total	2.897×10^{-6}	2.399×10^{-6}

The results of the first phase of the theoretical ground roughness study led to the recommendation that the next phase consist of an investigation of the role of the multiply-scattered component and the correlation of buried and mixed source calculations with some of the more recent experimental studies. The ultimate objective should be the selection of a single model and the establishment of parameters such as source depth for different types of terrain.

VI. GAMMA-RAY DEPTH-DOSE PATTERNS IN PHANTOM*

The objective of this investigation, which was initiated only two months ago, is to determine the gamma-ray depth-dose patterns in a phantom representative of the human body when exposed to the radiation environment produced by fallout fields and by selected arrangements of radioactive sources. Of particular interest is the determination of the differences in the depth-dose patterns produced by fallout and by radioactive source configurations intended to simulate fallout.

The phantom consists of a tissue-equivalent vertical right cylinder 60 cm in height and 30 cm in diameter. The center of the phantom is assumed to be 111.8 cm above a ground surface uniformly contaminated by fallout. The energy and angular distribution of the fallout and simulated fallout gamma rays incident upon the phantoms are being taken from the Monte Carlo calculations described in Sections II and III.

The chief mathematical tool being used to compute the depth-dose patterns is the COHORT Monte Carlo procedure.[28] A special FORTRAN procedure was prepared to calculate the uncollided gamma-ray components analytically. Preliminary calculations indicate that a minimum of approximately 50 percent of the dose at any point in the phantom is from photons which have suffered no previous collisions in the phantom.

*Based on work sponsored by the Armed Forces Radiobiology Research Institute, Defense Atomic Support Agency, under Contract No. DA-49-146-XA-479.

VII. MONTE CARLO STUDY OF BARRIER ATTENUATION FACTORS*

Today's Civil Defense fallout shielding technology[20] is based largely on simplified methods[29] developed from the results of rigorous calculations[8] which, in turn, are based on idealizations of the actual problems. Although a considerable amount of experimental and theoretical work has been carried out in recent years toward the evaluation of some of the approximations, the evaluations themselves often involve idealizations. For example, essentially all experiments have employed finite arrays of artificial sources of monoenergetic gamma rays to simulate the gamma rays from infinite plane fallout sources. Consequently there has been little direct verification of the basic results from which the simplified methods were developed.

To provide a more direct evaluation of the barrier attenuation data in current use, Radiation Research Associates is computing some of the more important cases using Monte Carlo techniques[2,19,28] which avoid certain idealizations required in the previous calculations. The Monte Carlo calculations include two cases of fundamental importance; 1) vertical wall barrier and 2) cylindrical wall barrier. In each case the energy and angular distribution of direct-beam and scattered gamma rays incident upon the barrier walls due to an infinite plane source on the ground surface will be considered. The energy and angular distributions of the incident gamma rays are the results of previous Monte Carlo calculations[1] which consider the effect of the air/ground interface. Concrete will be used as the barrier material.

The vertical wall barrier attenuation data given in Reference 8 were computed with the moments method, a method which has been used with great success in infinite medium calculations. The restriction of the moments method to infinite medium problems, however, leads to possible shortcomings in the barrier attenuation data since the gamma

*Based on work funded by the Office of Civil Defense through the United States Naval Radiological Defense Laboratory under Contract No. N0022866C0910.

radiation transport (both in the air/ground medium before reaching the barrier and the transport in the barrier) required idealization of the problem. Implicit in the infinite medium treatment is the restriction to a single material. Water was used to represent both air and ground and the barrier material itself was taken to be water. Other simplifications in the calculations included the neglect of energy degradation prior to striking the barrier. Results for a cylindrical barrier are generated from the slab barrier results by a geometrical transformation given in Reference 29.

The Monte Carlo calculations incorporate the individual material compositions of the air, the ground and the barriers. Material interface effects are included in the calculations and no compromise is necessary in handling the energy and angular distribution of the radiation. The Monte Carlo approach allows direct generation of results for the cylindrical barrier so that use of a geometric transformation is required as was the case for the moments method calculations. Comparisons of the Monte Carlo results with the previous results for slab and cylindrical barriers should help provide a basis for deciding whether the Civil Defense fallout shielding technology should continue to build from the old basic calculations or whether new results should be generated.

VIII. SUMMARY

Recent and current research projects at Radiation Research Associates encompass many of the numerous radiation transport problems involved in the determination of the characteristics of the gamma-ray environment produced by fallout and in the consideration of these characteristics in fallout shielding and radiobiology studies. The important characteristics of the radiation field for most purposes are the energy and angular distributions of the gamma-ray. These distributions are particularly important if penetration through appreciable amounts of material is involved.

Although the energy and angular distributions produced by fallout are known, or can presently be calculated with what appears to be reasonable accuracy for idealized situations where the source energy spectrum is known and the ground surface is smooth, it must be acknowledged that the exact amount of uncertainty in such calculations has not been established. Even in terms of the total dose above a plane isotropic ^{60}Co source, there are discrepancies on the order of 10 percent among various measurements and calculations.

The best choice of a source energy spectrum for a particular case is not too clear. The analysis of the enclosure shield experiment, which involved penetrations on the order of 2 to 6 relaxation lengths, indicated that the results obtained using various theoretical and experimental energy spectra varied widely. Of particular importance was the observation that the Nelms and Cooper fission product decay spectra,[3] which is incorporated into most Civil Defense barrier attenuation data, were not among those spectra which seemed to produce the best overall results for the enclosure shields. Although the different spectra did not give consistent dose transmission factors for the shields, they were reasonably consistent in indicating the time dependence of the transmission factors.

The nature of ground roughness effects is being determined in some detail through current theoretical and experimental efforts and there are indications that these effects may be accounted for by relatively simple methods. Further study is required in this area, however, before the methods can be definitized.

Fallout simulation studies indicate that either extended or compact configurations of common radioactive sources can give good simulation of most aspects of the fallour gamma-ray environment except the energy distribution. Studies are currently underway to determine the extent to which the depth-dose patterns in phantoms are influenced by the discrepancies in the energy spectra.

REFERENCES

1. R. L. French, Health Physics 11, 369 (1965).

2. D. G. Collins, Utilization Instructions for General Application of the LO5 Monte Carlo Procedure, RRA-T44 (1964).

3. Ann T. Nelms and J. W. Cooper, Health Physics 1, 427 (1959).

4. Gladys White Grodstein, X-ray Attenuation Coefficients from 10 KeV to 100 MeV, National Bureau of Standards Circular 583 (1957) with supplement (159).

5. R. L. Rexroad and M. A. Schmoke, Scattered Radiation and Free-Field Dose Rates from Distributed Cobalt-60 and Cesium-137 Sources, NDL-TR-2 (1960).

6. C. L. Schlemn, et al., Scattered Gamma Radiation Measurements from a Co^{60} Contaminated Field, AFSWC-TN-59-6 (1959).

7. E. T. Clark, Scattering of Gamma Rays at an Air-Ground Interface, unpublished paper (1965).

8. L. V. Spencer, Structure Shielding Against Fallout Radiation from Nuclear Weapons, NBS Monograph 42 (1962).

9. R. L. Mather, et al., Health Physics 8, 245 (1962).

10. R. L. French, A Comparative Study of Radioactive Source Arrangements for Simulating Fallout Gamma Radiation Fields, RRA-T45 (1964).

11. R. L. French, Simulation of Fallout Gamma Radiation Fields by Monoenergetic Plane Isotropic Sources, RRA-M51 (1965).

12. Development of a Fallout Simulator, Armed Forces Radiobiology Research Institute, Physical Sciences Report 1-63 (1963).

13. C. M. Cialella, et al., "Shielding Effectiveness of Enclosure Shields in a Fallout Field," POR-2221 (1963). (Confidential)

14. R. L. French, et al., An Analysis of the Performance of Enclosure Shields in a Real Fallout Field, RRA-T55 (1965).

15. Rolf Björnerstedt, Arkiv for Fysik 16, 293-313 (1959).

16. F. M. Tomnovec, et al., The Effect of a Changing Gamma-Ray Fallout Spectrum on the Ground Roughness Factor, USNRDL-TR-915 (1965).

17. C. Sharp Cook, Health Physics 4, 42-51 (1960).

18. C. M. Huddleston, et al., Health Physics 11, 537-548 (1965).

19. M. B. Wells, Monte Carlo Multilayer Slab Geometry Shielding Code C-18, FZK-134-3 (1961).

20. Design and Review of Structures for Protection From Fallout Gamma Radiation, Department of Defense, Office of Civil Defense, PM-100-1 Interim Edition (1965).

21. C. E. Clifford, Effects of Ground Roughness on the γ Dose from Cs^{137} Contamination, DRCL Report No. 401 (1963).

22. B. W. Shumway, USNRDL, private communications (1965, 1966).

23. R. L. French and L. Olmedo, A Preliminary Investigation of Simplified Methods for Calculating the Effects of Ground Roughness on the Gamma-Ray Environment Above Fallout, RRA-T61 (to be published).

24. C. F. Ksanda, et al., Gamma Radiation from a Rough Infinite Plane, USNRDL-TR-108 (1956).

25. C. F. Ksanda, et al., Gamma Radiation from Contaminated Planes and Slabs, USNRDL-TM-27 (1955).

26. C. E. Clifford, Can. J. Phys. 42, 2373 (1964).

27. C. Eisenhauer, Health Physics 9, 503 (1963).

28. M. B. Wells and C. F. Malone, A Monte Carlo Procedure for Radiation Transport and Heating Studies, FZK-156 (1962).

29. C. Eisenhauer, An Engineering Method for Calculating Protection Afforded by Structures Against Fallout Radiation, NBS Monograph 76 (1964).

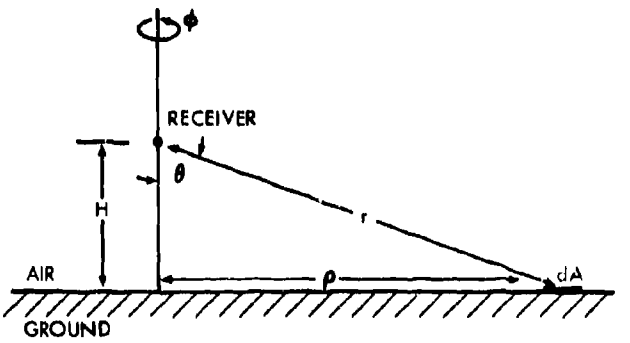

Fig. 1. Source and Receiver Geometry

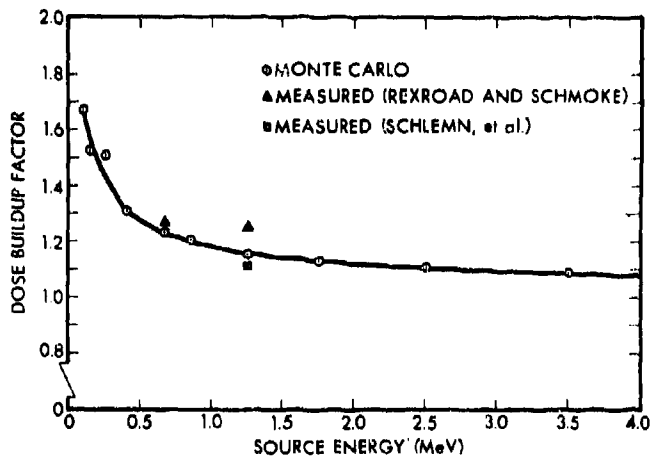

Fig. 2. Gamma Dose Buildup Factors for Receiver in Air 3 Feet Above Infinite Plane Isotropic Source on Ground

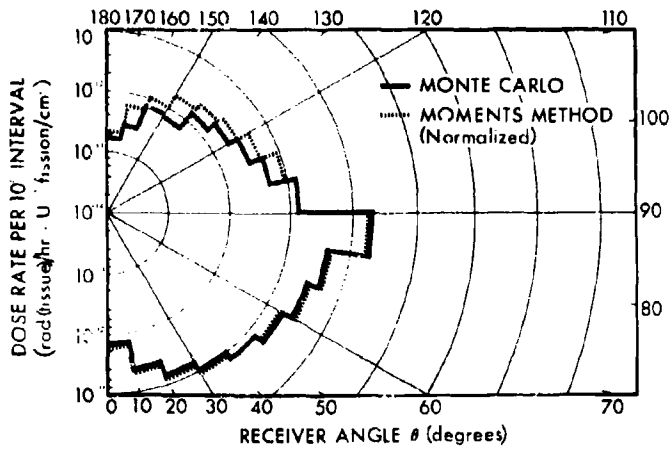

Fig. 3. Comparison of Monte Carlo and Moments Method Gamma-Ray Dose Rate Angular Distribution from 1.12 Hour Fallout

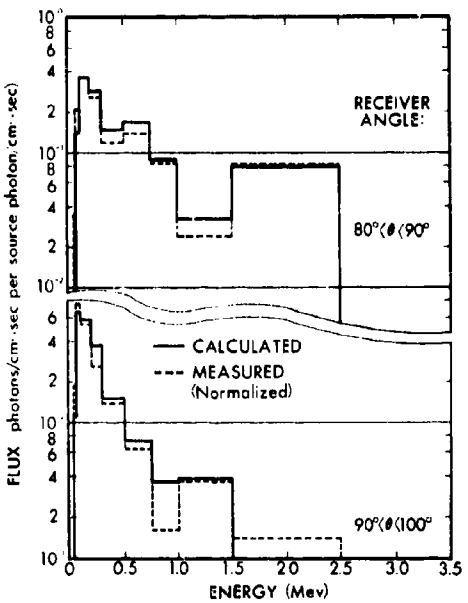

Fig. 4. Comparison of Calculated and Measured Gamma-Ray Energy Spectra 3 Feet Above 9 Day Fallout

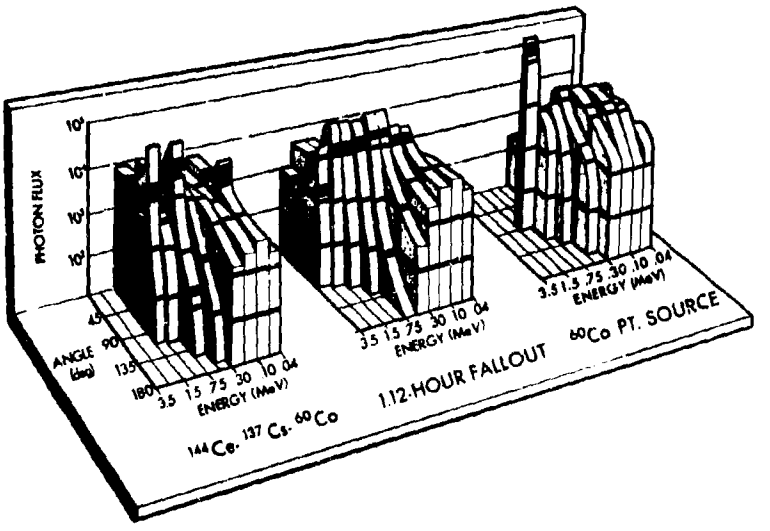

Fig. 5. Comparison of Flux Energy and Angular Distributions 3 Feet Above 1.12 Hour Fallout and Simulated Fallout

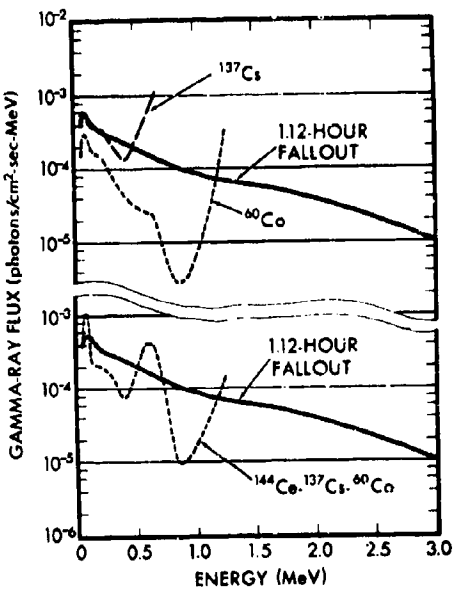

Fig. 6. Differential Energy Spectra 3 Feet Above Infinite Plane Source

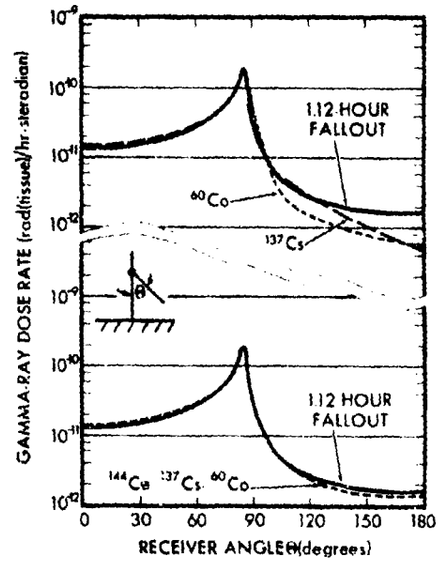

Fig. 7. Differential Dose Angular Distribution 3 Feet Above Infinite Plane Source

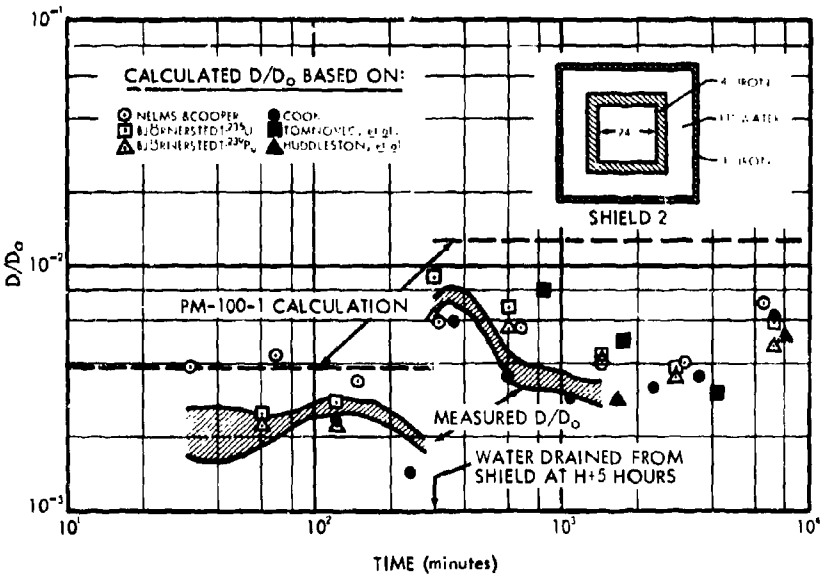

Fig. 8. Calculated and Measured Dose Transmission Factors for Cubical Enclosure Shield 2

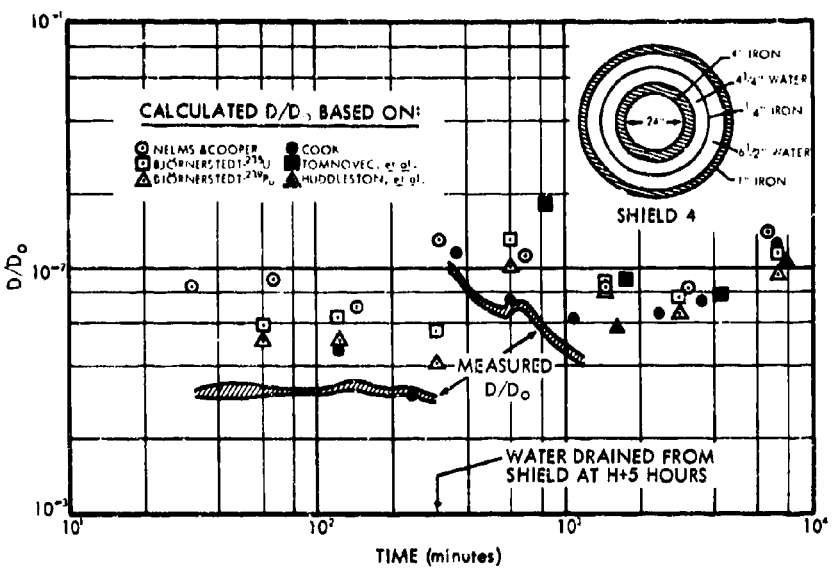

Fig. 9. Calculated and Measured Dose Transmission Factors for Spherical Enclosure Shield 4

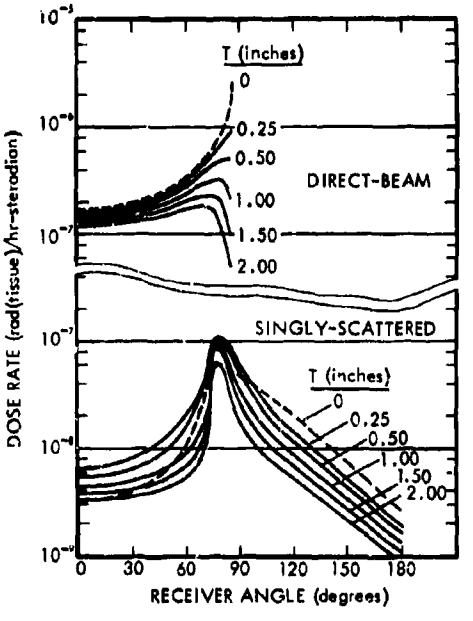

Fig. 10. Angular Distribution of Gamma-Ray Dose Rate 3 Feet Above 1.25 MeV Source at Depth T Below Ground Surface

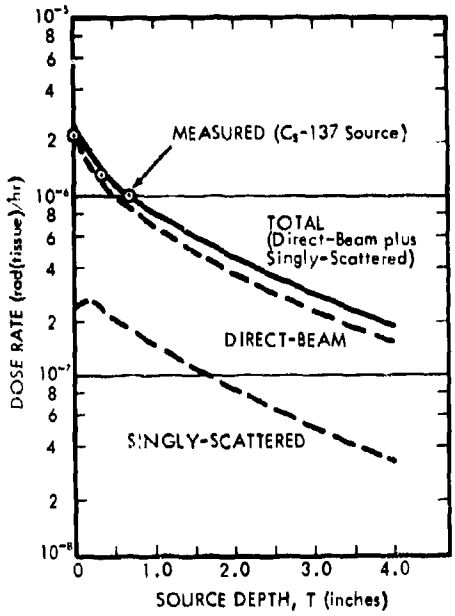

Fig. 11. Gamma-Ray Dose Rates 3 Feet Above 0.67 MeV Source at Depth T Below Ground Surface

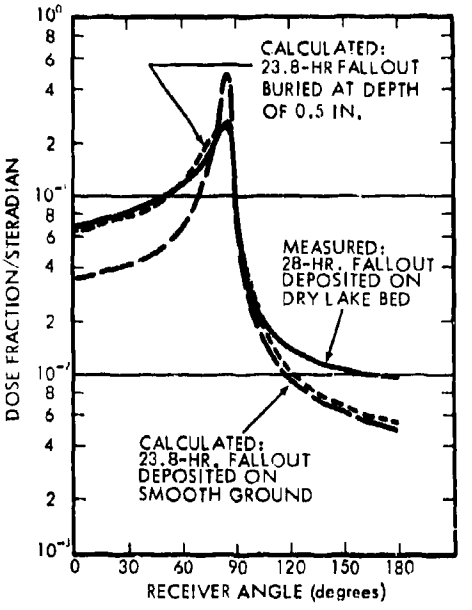

Fig. 12. Comparison of Measured and Calculated Dose Angular Distributions Above Fallout Deposited on a Dry Bed

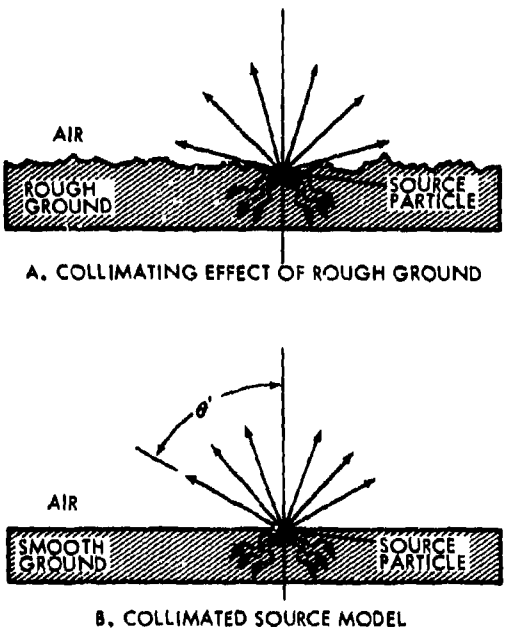

Fig. 13. Collimated Source Model for Simulating Ground Roughness Effects

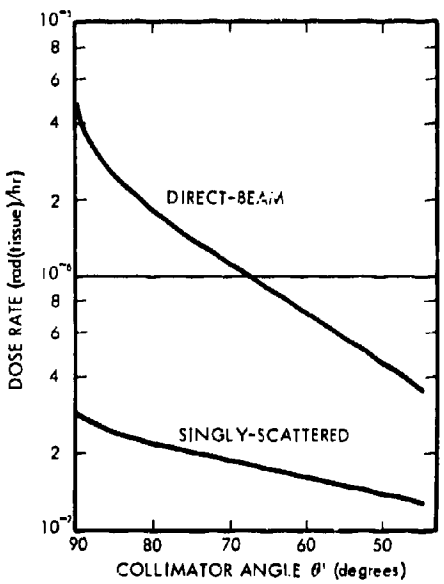

Fig. 14. Gamma-Ray Dose Rates 3 Feet Above Collimated 1.25 MeV Source

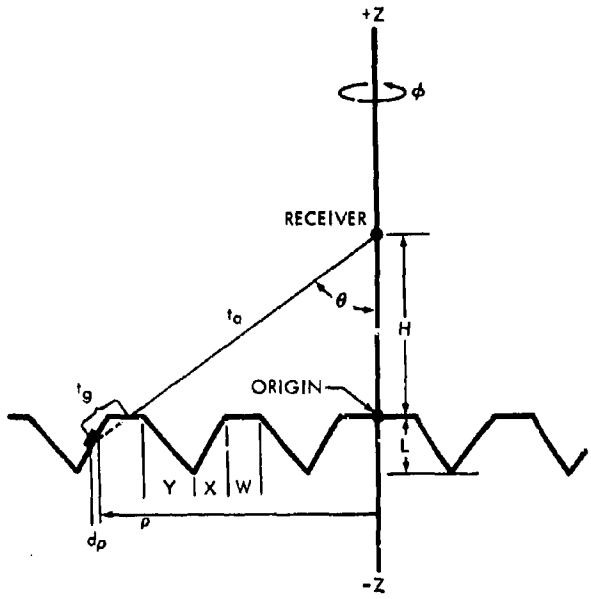

Fig. 15. Geometry of Furrowed-Surface Ground Roughness Model

INTENSITY--ACTIVITY RELATIONS FOR SHOT SMALL BOY

P. D. LaRiviere, S-K Yu and C. F. Miller

Stanford Research Institute
Menlo Park, California

ABSTRACT

An analysis of the relationship of gamma exposure rate to fission density and ionization activity of fallout samples from event Small Boy was made. The results indicate that, over the fallout region sampled, the fractionation of radionuclides was such that only ~30% of the gamma ionization strength per refractory fission of unfractionated fission products was exhibited. The combined effects of instrument response characteristics and terrain roughness were seen to further depress expected exposure rates at 1 hour after burst by an average factor of 0.72.

INTRODUCTION

The relationship between the radiation intensities observed in a fallout pattern and the amount of radioactivity deposited in the pattern has been studied for many years. The factor is of particular importance in attempting to evaluate the amount of radioactivity available for worldwide fallout, since the most common method employed relies on a subtraction of the amount in the local fallout from the theoretical total produced. In addition to this purpose, interpretation and correlation of radiation intensity and sample radioactivity at individual sampling locations requires some attention to the fundamentals of nuclear radiations and radiation sources.

The problem of relating fallout intensity to sample activity in general is complicated by several major factors: fractionation of radionuclides; the occurrence of non-fission product activities; the non-ideal response of gamma survey meters; and the departure of real terrain surfaces from the ideal mathematical plane. Of these, fractionation undoubtedly causes the greatest amount of confusion, especially when reference is made to "fraction of the device." Since each radioelement condenses to a different extent in the soil/weapon matrix particles, it is evident that a different fraction of each becomes associated with the fallout particles. Hence the term "fraction of device" is meaningless in the absence of a definition of "fraction."

In principle, radiochemical analysis of fallout samples could be made for any nuclide desired and, if enough samples were taken, the deposit density could be integrated over the fallout pattern to yield a precise fraction of that nuclide present. However, this procedure would

shed no light on the r/hr relation, in the absence of information on the relative abundances of all the other gamma-emitting nuclides present in the sample.

An alternative approach, if induced activities are not present in significant amounts, is to determine the fission density at a location by radiochemical analysis on one or more refractory fission product nuclides (or fission indicator, if available). The radiation intensity at the point is measured (conventionally at 3 feet above the ground) and, making due allowance for terrain shielding and instrument response, the measured intensity is compared with the theoretical intensity expected from the indicated fission density and unfractionated fission products on an infinite plane. The ratio obtained is a direct measure of the gross ionization fractionation, or fractionation number.

The fractionation number obtained directly from the measurements applies only to the time of measurement, but if an ionization decay rate is measured, then the fractionation number can also be determined as a function of time after detonation. The most satisfactory data would include radiochemical analyses for all the important nuclides, which would then allow computation of gamma decay rates in the field or in laboratory counters as desired.

The presence of induced products, originating in the device and its surroundings upon detonation, is not readily detected and the relative abundances cannot be determined without fairly complete radiochemistry on a variety of samples. In the past, this information was not usually available, so that the fractionation behavior of induced products could not be integrated, with the possible exception of a few uranium-derived products, especially Np-239. A current study at Stanford Research Institute however does include the capability of estimating for surface bursts the production and fractionation (with particle-size) of induced products from a variety of weapon/soil combinations.

The objective of this paper is to present an analysis of the ionization intensity--sample activity relations resulting from shot Small Boy, which took place at the Nevada Test Site. The principles mentioned above are applied and the gross fractionation numbers, terrain factors and instrument response factors are derived. The analysis closely parallels one previously presented[1] but differs in that more refined values of the input data were derived.

THEORY

It is generally known that the intensity-activity ratio can be defined for the intensity as observed at a given location or, as an average, for the whole fallout area. In the latter form, the ratio is sometimes called the intensity-area integral per unit fission yield. It is convenient in data analyses to express the surface density of the radioactivity in fissions per square foot rather than kilotons per square mile. Both representations of the surface density of radioactivity are independent of time after detonation. And, since the relation between the number of fissions and the energy released in fission is about the same for most common fissile materials, namely $(1.45 \pm 0.03) \times 10^{23}$ fissions per kiloton of fission yield, the two representations of the surface density of radioactivity are related by

$$A_f = 5.20 \times 10^{15} A_W \qquad (1)$$

where A_f is in fissions/sq ft and A_W is in KT/sq mi.

The intensity-activity ratio for a given location in a fallout region is defined by

$$K_o = I_s/A_f \qquad (2)$$

where I_s is the standard intensity, which is the intensity at 1 hr at a height of 3 feet above the ground, obtained from instrument readings on the completely deposited fallout, decay-corrected to 1 hr.

A_f is the fission density per square foot, based on refractory fission product analysis.

The ideal normalization factor, that is, the calculated value of the 1-hr intensity 3 feet above an infinite plane uniformly contaminated with unfractionated fission products of unit surface density (fiss/ft^2 or KT/mi^2), may be computed. However, the calculated values of K_o from observed values of I_s over real terrain for a given value of A_f (or A_w) are lower than those computed for the ideal plane due to attenuation of the gamma ray intensity by both small- and large-scale roughness of real terrain, to non-idealized responses of radiac instruments used in measuring the intensity, and to decreased contributions from the more volatile fission-product radionuclides whose relative concentrations in the fallout are decreased (i.e., the radioactive composition is altered or fractionated). The values of I_s, relative to those for the fission products, are increased by the production of induced radionuclides (usually through neutron capture) in both weapon components and nearby environmental materials. The representation of K_o, including consideration of the above four factors, is given by

$$K_o = Dq(r_{fp}k_{fp} + r_i k_i) \qquad (3)$$

in which D is the detector response factor for the assumed detector-radiation source geometry

q is the terrain attenuation factor

r_{fp} and r_i are the gross fractionation numbers for the fission and induced products, respectively

k_{fp} and k_i are the ideal normalization values of $\frac{\text{r/hr}}{\text{fiss/ft}^2}$ for fission and induced products, respectively, as computed for unfractionated fission products of uniform surface density on an infinite plane.

These quantities may be defined mathematically as shown below. It should be noted that the geometry assumed is a detector 3 feet above

a source uniformly distributed on real terrain or on a mathematical plane, as indicated, and that the intensity ratios are for the same time after fission.

The detector response factor is defined by

$$D = I_i/I_e \tag{4}$$

where I_i is the intensity indicated on the meter, and I_e is the intensity to which the meter is exposed.* D is therefore a ratio of two intensities which differ only because of non-ideal response of the detector. The usual causes of non-ideality are non-uniform directional response, due to self- and operator-shielding; non-linear energy response characteristics to gamma rays of different energies; and the relation of these to the manner in which the instrument is calibrated with a point source of radiation.

The terrain attenuation factor is defined by

$$q = \frac{I(x,t)}{I(x,p)} \tag{5}$$

where the parameter x represents any kind of fission and induced product mixture, fractionated or not, t denotes (real) terrain, and p indicates a mathematical plane. Thus, q is the ratio of two intensities which differ only because of the terrain characteristics upon which the source is distributed.

---

*D has been calculated[2] for the T1B survey meter as $D = I_i\,(u,p)/I(u,p)$ where $I_i\,(u,p)$ is the calculated reading a T1B instrument would indicate when exposed at a height of 3 feet to the unfractionated products of U-235 thermal fission distributed on a plane; I is the calculated true intensity under the same conditions.

The fractionation number is defined by

$$r_{fp} = \frac{I(f,s)}{I(u,s)} \tag{6}$$

where the parameter f denotes fractionated fission products, u denotes unfractionated fission products, and s denotes any kind of planar surface, rough or mathematically smooth. Hence, r_{fp} is the ratio of two intensities which differ only because of fractionation among the fission products. r_i is analogous to r_{fp} except that it refers to the summation of the induced products. Expressed another way, r_{fp} reflects the effects of fractionation among the gamma-emitting nuclides, or "ionization power" of the fractionated mixture relative to an unfractionated set of fission products. Pure beta emitters then, such as Sr-90, do not affect r_{fp} one way or the other.

Finally, the ideal normalization value is defined by

$$k_{fp} = \frac{I(u,p)}{A_f} \tag{7}$$

where u, p, and A_f are as defined previously.

If it is accepted that the radionuclide composition varies with the size of the fallout particles, the major factors in equation 3 that are dependent on particle diameter are r_{fp} and r_i. In more precise treatments, D and q also depend on the radionuclide composition because both of these parameters are functions of gamma energy which in turn depends on the relative abundance of the radionuclides in the fallout. It follows that each induced product also should be multiplied by its appropriate Dq rather than by an overall Dq value for the total assemblage of nuclides. So precise a treatment is not possible without a large amount of additional information.

Now, if induced products are of negligible importance, as was the case for the Small Boy fallout, equation 3 with rearrangement reduces to

$$Dq = \frac{K_o}{r_{fp} k_{fp}} \tag{8}$$

or using equation 2, to the equivalent,

$$Dq = \frac{I_s}{r_{fp} k_{fp} A_f} . \tag{9}$$

This equation may be evaluated by means of activity measurements on collected fallout samples. The computed response of the USNRDL 4π gamma ionization chamber, in ma/fiss, is closely proportional to k_{fp} from ~1 hr onward, for U-235 thermal fission products, as shown in Reference 2. Confidence in this calculated proportionality is supported by the excellent agreement Mackin has obtained between calculated and observed decay rates for unfractionated U-235 thermal fission products in this instrument.(3)

The quantity k_{fp} itself is not easily checked experimentally; however, the ion chamber results indicate that any error in k_{fp} must occur primarily in the conversion of flux to dose rate at 3 feet. The conversion used in Reference 2 is based on the Gates and Eisenhauer results as interpreted by Miller,(4) which are possibly accurate within $\sim \pm 10\%$, although no definite value can be assigned to this uncertainty.

Making the assumption that the ion chamber response is proportional to k_{fp} for all fissile-nuclide products, and, further, that the proportionality extends to fractionated products as well, then we may write

$$i_o \approx \text{const} \frac{I(f,p)}{A_f} = \text{const} \frac{r_{fp} I(u,p)}{A_f} \tag{10}$$

and

$$i_c = \text{const} \frac{I(u,p)}{A_f} \tag{11}$$

where i_o is the observed ma/fiss for a sample of fallout, and i_c is the calculated value of the ratio for unfractionated products. Dividing equation 10 by equation 11 results in

$$i_o/i_c = r_{fp} \tag{12}$$

which is to say the gross fractionation number for the fission products may be evaluated at any time desired simply by comparing the observed ma/fiss of a fallout sample to the calculated ma/fiss at that time. Substituting this result and the definition of k_{fp} from equation 7 into equation 9 results in

$$Dq = \frac{I_s/A_f i_o}{I(u,p)/A_f i_c} \tag{13}$$

Convenient units for $A_f i_o$ and $A_f i_c$ are fiss/ft^2 x ma/fiss = ma/ft^2 so that Dq is simply the ratio of $\frac{r/hr}{ma/ft^2}$ observed, to $\frac{r/hr}{ma/ft^2}$, computed.

Equation 13 is particularly convenient to use with field data since it allows determination of Dq without the necessity of a fission analysis of the sample. Once Dq is evaluated, equation 8 may be used to solve for r_{fp}.

Other parameters relevant to the analysis include the variation of i_o and r_{fp} with fallout particle size. Knowledge of the latter permits estimation of r_{fp} for a sample for which the size distribution alone is known.

TREATMENT OF THE DATA

Five kinds of measurements made in the fallout field and on fallout samples are necessary to this analysis: activity in the low-geometry scintillation counters, which were capable of accepting the unopened collector containing the entire fallout sample; [5,6] ionization

current in the 4π ion chamber on samples that were recovered from the collectors;[5,6] radiochemical fission analysis;[6] and radiation intensity measurements in the fallout field at the locations from which the fallout samples were taken.[5,7,8]

Sample Activity Relations

The results of the activity and fission analyses on samples recovered from the fallout collectors are shown in Table 1. Also included in the table is an examination of the consistency of the activities obtained, $\frac{c/m}{ma}$, and the ratios of these activities to the number of equivalent fissions in the samples. The corrections involved in calculating the activities listed in Table 1 are as follows:

Counter	Location, Use		Factor to Floor of CH-2 and CH-3	
CH-1	NTS, Project 2.9 off-site collections		0.578[5]	
CH-2,3	NTS, Project 2.9 on-site collections		1	
			Avg. from Samples	Cs-137 Std[6]
CH-4	NRDL, Project 2.10	Shelf 11	0.0314	0.0214
		Shelf 10	0.0908	0.0740
		Shelf 9	0.388	0.238

The average values of the shelf ratios for counter CH-4 to the floor of the reference counters were not used in the analysis except to verify proportionality to earlier counts obtained in counter CH-1. The ion chambers at NTS and NRDL were normalized to a standard response of 560×10^{-9} ma to a 105μg Radium Standard. A small residual discrepancy between the chambers, based on fallout sample counts in both chambers, was removed by multiplying the NRDL ion currents by 0.925.

The fission values reported in Reference 6 were derived from measurements made by Hazelton-Nuclear Science (H), Tracerlab, Western

Table 1

Activity Relationships for Recovered Fallout Samples

Station Number	Sample	$\frac{c/m}{ft^2} \times 10^{3}$	$\frac{mg}{ft^2} \times 10^{-3}$	$\frac{c/m}{mg} \times 10^{11}$	$\frac{fiss}{ft^2} \times 10^{12}$	$\frac{c/m}{fiss} \times 10^{9}$	$\frac{mg}{fiss} \times 10^{20}$
100	PC-1	214	217.6	1.021	217.6	1.003	0.9816
	PC-2	234	230	1.017	(235)	0.9937	0.9747
	PC-4	247	(235)	(1.051)	(239)	1.033	0.9853
	PC-5	205	232	0.8836	239	0.8577	0.9707
101	OC-1	2280	2170	1.097	2150	1.107	1.009
	AO-1	1990	-	-	(2000)	0.9950	-
	AO-4	1920	2070	0.9275	(1970)	0.9746	1.051
	AO-8	2000	1990	1.002	1966	1.017	1.015
103	AO-9	-	0.0970	-	2.710	-	0.03579
200	AO-9	10.89	11.34	0.9603	13.10	0.8311	0.8656
201	AO-4	714	837	0.8530	887	0.8053	0.9436
	AO-7	824	-	-	(827)	0.9964	-
	AO-8	837	(850)	0.9847	(800)	1.046	1.062
	AO-9	810	866	0.9353	812	0.9982	0.9496
	AO-10	840	884	0.9502	930	0.9032	0.9505
203	PC-18	242	246	0.9837	275.8	0.8848	0.8984
	PC-21	273	276	0.9920	(288)	0.9161	0.9329
	PC-22	284	(254)	1.118	(270)	1.052	0.9407
204	AO-9	-	0.006772	-	0.04178	-	0.1592
207	AO-9	-	0.01867	-	0.07228	-	0.2760
208	AO-9	-	0.02318	-	0.3290	-	0.0705
300	AO-9	2.189	2.306	0.9493	3.031	0.7222	0.7608
303	AO-9	[illegible]	676.8	1.109	87.02	8.545	7.706
306	AO-2	392.7	-	-	(477)	0.8233	-
	AO-3	810.6	472	2.109	472	1.929	0.9163
	AO-4	430.5	464	0.9282	481	0.8950	0.9439
	AO-8	438.8	448	0.9760	490	0.8806	0.9032
	AO-9	480	448	1.079	(490)	0.8796	0.9082
309	PC-16	-	0.1441	-	0.03186	-	4.523
311	AO-9	-	0.00999	-	0.07018	-	0.1423
400	AO-8	3.466	4.184	0.8284	4.703	0.5988	0.4808
401	OC	465	474	0.9810	527	0.8824	0.4994
	AO-9	474	462	1.026	539	0.8794	0.8590
403	OC	765	800	1.308	825	1.250	0.9564
	AO-1	595	(803)	0.9967	(813)	0.9732	0.9953
	AO-2	819	-	-	(840)	0.4964	-
	AO-4	593	814	0.9858	834	0.9534	0.9844
405	OC	204	220	0.9273	237	0.8608	0.9243
	AO-9	181	188	0.9628	(214)	0.8458	0.8745
407	AO-9	1.383	1.400	0.9879	1.94	0.7129	0.7216
413	AO-9	-	0.00316	-	0.1800	-	0.1842
501	AO-9	3.881	3.831	1.063	7.865	0.5037	0.4737
502	AO-9	-	0.01351	-	0.04938	-	0.2741
503	AO-8	172.9	161.3	1.089	254	0.6807	0.6429
505	AO-1	336	-	-	(311)	0.9973	-
	AO-2	337	323	1.043	302	1.116	1.070
	AO-3	190	344	0.8460	324	0.5864	1.074
	AO-4	361	(334)	1.038	(334)	1.038	1.000
	AO-8	344	336	1.027	312	1.103	1.074
507	PC-1	146	132	1.106	(133)	1.098	0.9925
	PC-2	141	(130)	1.085	(142)	0.9930	0.9158
	PC-4	140	147.6	1.098	120	1.167	1.068
	PC-5	140	136.3	0.8948	150	0.9333	1.043
509	AO-9	28.20	26.64	1.100	28.8	0.9792	0.4903
513	AO-9	-	0.006139	-	0.115	-	0.0534
601	AO-9	9.924	9.297	1.087	12.8	0.7878	0.7379

Table 1

Activity Relationships for Recovered Fallout Samples (Continued)

Station Number	Sample	$\frac{t/m^{a}}{ft^2} \times 10^{3}$		$\frac{ma}{ft^3} \times 10^{-5}$	$\frac{s/m}{ma} \times 10^{11}$	$\frac{fiss}{ft^2} \times 10^{12}$	$\frac{c/m}{fiss} \times 10^{-9}$	$\frac{ma}{fiss} \times 10^{-20}$
603	A0-1	150		164.5	1.094	148	1.216	1.111
	A0-2	174		187.5	1.106	148	1.176	1.064
	A0-3	174		(180)	1.112	(160)	1.112	1.000
	A0-4	186		-	-	(167)	1.102	-
606	A0-1	170		152	1.118	137	1.241	1.109
	A0-9	151		174	0.867[a]	160	0.943[a]	1.088
607	A0-9	10.74		11.47	0.9363	18.9	0.5682	0.6060
700	A0-9	-		0.1099	-	0.190	-	0.5744
701	A0-9	-		0.1375	-	0.304	-	0.4523
703	A0-9	416.87)		15.50	1.088	26.3	0.6414	0.5894
704	A0-9	-		0.0085	-	0.080		1.23,
705	A0[c]	28.94		34.74	0.832	-	-	-
707	A0-4	72.5		71.6	1.013	59.0	1.229	1.214
	A0-6	83.9		-	-	64.3	1.306	-
	A0-9	83.7		80.25	1.043	64.8	1.292	1.238
813	LaC	8.997		9.08	0.9930	6.005	1.498	-
814	18-11B	9.389		-	-	9.13	1.026	-
815	18-10B	8.231	(9.32m)[b]	-	-	9.38	0.8775	-
816	18-9B	8.537	(8.537)[b]	-	-	7.94	1.213	-
	27-1B	2.012	(3.308)[b]	-	-	0.100	20.12	-
	27-2A	2.202		-	-	0.00029	large	-
	27-2B	2.433	(2.464)[b]	-	-	1.80	1.350	-
	27-3B	2.604	(2.720)[b]	-	-	2.35	1.108	-
	27-4B	0.7468	(0.7486)[b]	-	-	0.115	6.494	-
	35-17B	0.3111	(0.2487)[b]	-	-	0.273	1.140	-
	35-18B	0.5780	(0.5397)[b]	-	-	0.379	1.525	-
	35-19B	1.010	(1.222)[b]	-	-	0.265	3.811	-
	35-20B	1.114	(0.9423)[b]	-	-	0.811	1.374	-
	58-11B	0.4774	(0.8604)[b]	-	-	0.215	2.220	-
	58-12B	0.5156	(0.6548)[b]	-	-	0.173	2.980	-
	58-14B	0.3023	(0.3315)[b]	-	-	0.1858	1.627	-
					Avg 1.015			

Notes to table

All activity values are for 100 hours after burst; estimated values are shown in parentheses

a Original GH and DH measurements were on entire contents of tray; Residual activity in tray has been subtracted off in this table to obtain activity of recovered sample

b Estimated from late counts on DH counter (44) at NRDL

c A0-1, 2, 3, 4, 6, 7, 9.

Division (T), and Nuclear Science and Engineering (N). The following adjustment factors were applied to the reported fission values:

Nuclide	(H)	(T)	(N)
Zr-95	1.307	1.140	0.9434
Mo-99	1.464	1.0	-
Ce-144	0.9761	0.9174	-

The factors shown for the contracting laboratories were obtained from a detailed examination[9] of the reported fission values; the factors shown convert the reported number of fissions for each laboratory-nuclide combination to equivalent fissions of Mo-99 as determined by Tracerlab, whose results were judged to be the most consistent and reliable. This judgement was based primarily on the finding that the variation in the ratio, ma/fiss at 100 hours, for each of eight fallout particle sizes, was least for the Tracerlab Mo-99 fission assays.

It may be seen in Table 1 that the counting was remarkably good, as evidenced by the generally steady values in the (c/m)/ma ratios; in these cases, therefore, when erratic values of either (c/m)/fiss or ma/fiss appear, it is clear that the fission analysis is in error. When (c/m)/ma is not available, it is not possible to determine whether the fission or the counting results are at fault.

The primary result of interest from Table 1 is the ma/fiss values on the recovered samples. Before these values can be used in conjunction with the r/hr intensities observed at the collection station, however, it is necessary to derive the best value of the ma/ft^2 for the station, which when divided by the sample ma/fiss, produces the best value of fiss/ft^2 for the station. Two factors are involved in the correction of sample values to station values; one is the recovery loss in removing the sample from the collector for analysis, and the other is the relation of the size of the sample analyzed to the average

obtained for all of the collectors exposed at the station. The latter correction, of course, is not possible for the stations at which multiple collectors were not exposed. A final correction is for radioactive decay to the 1-hour values, the time at which comparison is desired with the standard intensities.

Average Station Values. Table 2 lists the average fraction of sample recovered from the different kinds of collectors used, which are described in detail in Reference 5. The values are based on CH activities obtained on the collectors before and after removing the fallout sample. In the case of the GC collectors, the fraction is based on the CH activity of the fallout recovered from the granules, divided by the sum total activity of the processed samples. The latter value was variously somewhat more or less than the total before processing. The recovered fractions are plotted in Figure 1 versus r/hr @ 1 hour at the station, which was convenient to use as a rough indicator of sample size. The curve shown was used to estimate the recovery fraction for a few samples for which the fraction was unmeasured.

The average ma/ft^2 for each station was computed, using all available ion chamber measurements. When only a single reading was available from a station,* adjustment to the station average was made with the CH counter assays reported in Reference 4. When these were missing, no adjustment was possible. The resulting values are combined in Table 3 with the ma/fiss values previously obtained to produce the best estimate of the equivalent Mo-99 fiss/ft^2 deposited at the stations. It should be noted that the activities are evaluated at 100 hrs after burst, so that in order to compare these values with the standard intensity (1 hr after burst) a correction for decay to 1 hour is necessary.

*These cases include collector AO-9 from stations 300 303, 407, 601, and 703.

Table 2

Fraction of Sample Recovered from Collectors

Station Number		PCC	AOC	LAC	OC	LA	GC
100		~1.0					
101			~1.0		~1.0		
200			0.917		0.931		
201			~1.0				
203					~1.0		
300			0.856				
301			0.961				
303			0.979				
305			0.974				
307			-				
400			0.884				
401			0.967				
403			~1.0		0.962		
405			0.948		0.965		
407			-		0.945		
501			0.810				
503			~1.0		0.949		
505			~1.0				
507		0.945					
509			0.928				
601			0.934				
603			0.943				
605			0.974				
607			0.936				
705			0 921				
707			0.957				
810						0.550	
811						0.605	
812						0.830	
813						0.819	
814	(18-11B)					0.922	0.941
815	(18-10B)					0.926	0.894
816	(18-9B)					0.902	0.890
817						0.817	
818						0.922	
819						0.770	
820						0.881	
821						0.778	
822						0.764	
824						0.803	
27-1							~1.0
27-2							~1.0
27-3							0.941

Table 2

Fraction of Sample Recovered from Collectors (Continued)

Station Number	PCC	AOC	LAC	OC	LA	QC
27-4B						0.987
35-17B						0.706
35-18B						0.813
35-19B						0.980
35-20B						0.942
56-11B						0.621
56-13B						0.656
56-14B						0.472

Table 3

Activity Relationships for Fallout Collection Stations

Station Number	Station ma/ft^2 @ 100 x 10^{-8}	$\frac{ma}{flux}$ @ 100 hr x 10^{-20}	Station $flux/ft^2$ x 10^{12}
100	219.6	0.981	223.8
101	1888	1.02	1852
103	0.103	0.03579	2.878
300	12.7	0.8686	14.67
301	883	0.972	877.6
303	269	0.935	270.1
304	0.0115	0.1383	0.08315
307	0.0397	0.2750	0.1444
309	0.0484	0.07046	0.6868
300	2.65	0.760N	3.4N3
301	725	-	-
302	0.0533	-	-
303	621	0.7706[4]	806.9
305	470	0.929	506.9
309	0.174	4.523	0.0385
311	0.0130	0.1423	0.09135
400	5.20	0.4N0N	10.82
401	440	0.879	537.4
403	50N.5	0.969	52N.0
405	20N	0.931	223.4
407	2.0N4	0.7216	2.8NN
409	0.023[illegible]	-	-
413	0.0863	0.1N42	0.3595
501	12.9	0.4737	27.23
502	0.0270	0.2741	0.09850
503	169	0.6429	262.9
505	334	1.0N	308.3
507	141	1.02	138.2
509	27.6	0.8903	31.00
513	0.0123	0.0533N	0.2304
601	9.34	0.737N	12.66
603	172	1.07	160.7
605	169	1.10	153.6
607	13.1	0.6069	21.5N
700	0.220	0.5784	0.3804
701	0.276	0.4523	0.6080
703	16.5	0.5894	28.30
704	0.197	1.232	0.1599
705	37.7	-	-
707	79.3	1.22	65.0

Table 3

Activity Relationships for Fallout Collection Stations (Continued)

Station Number		Station nm/ft² @ 100 x 10^{-6}	NA flss @ 100 hr x 10^{-20}	Station flss/ft² x 10^{12}
810		-	-	-
811		-	-	-
812		-	-	-
813		9.86	1.51	8.530
814	(1A-11B)	9.83 LAC	0.949 (Col C)	8.74 (GC)
815	(1A-10B)	7.74	0.776	8.99 (GC)
816	(1A-9B)	5.68	0.683	8.29 (GC)
817		-	-	-
818		7.34	-	-
819		-	-	-
820		2.14	-	-
821		-	-	-
822		0.648	-	-
823		-	-	-
824		0.257	-	-
27-1		-	-	0.100
27-2		-	-	1.40
27-3		-	-	2.90
27-4		-	-	0.120
35-17		-	-	0.365
35-18		-	-	0.464
35-19		-	-	0.276
35-20		-	-	0.861
84-11		-	-	0.348
84-12		-	-	0.284
84-14		-	-	0.213

a Observed fissions increased by factor of 10.

Decay Corrections. In Reference 5, ion chamber measurements were corrected to 100 hours by means of a single composite decay curve determined from measurements on many samples. There were differences, of course, from sample to sample because the particle size distribution varied and, as is now quantitatively known, the radiochemical fractionation varied with particle size. Figure 2, take from Reference 9, shows the variation in ma/fiss, at 100 hours, when plotted against the average particle size retained on the sieves used in the separation. The variation with the average particle size for the entire fallout deposit at a station was not so pronounced because of the spectrum of sizes generally present in a collection.

Although it would be possible to use available ion chamber decay curves uniquely associated with some stations, many stations would be excluded through lack of these data and, in any event, none of the measured decay curves extends back as early as 1 hour. Hence in this treatment, the composite decay curve of Reference 5 has been used to correct ion chamber activities to 100 hours; further correction to 1 hour was possible only because of the fortuitous close similarity in decay rates exhibited between the composite curve and that observed by Miller at Operation Plumbbob, from Shot Diablo.[10] The Small Boy composite decay curve, and that observed for sample DS-1 which was the earliest obtained from Small Boy, have been normalized to Miller's* curve for comparison in Figure 3. The decay correction factor for the 4π ion chamber from 100 hours to 1 hour for Small Boy fallout samples is therefore taken as 350/1.45 = 241.4.

The ma/fiss for the unfractionated products resulting from fission-spectrum neutrons on Pu-239 is calculated to be 9.50×10^{-18} ma/fiss @ 1 hour. In this calculation, the chain yields were taken from Reference 11 and applied as correction factors on the U-235 thermal

*As slightly refined for inclusion in a report currently in preparation.

neutron yields calculated by Bolles and Ballou;[12] Reference 2 provided the response of the ion chamber to individual fission products. For the same conditions, the calculated value of the denominator of equation 13 is

$$\frac{6.538 \times 10^{-13} \text{ (r/hr)/(fiss/ft}^2\text{)}}{9.50 \times 10^{-18} \text{ ma/fiss}}^{*} = 0.6882 \times 10^{5} \text{ (r/hr)/(ma/ft}^2\text{)} \quad @ \text{ 1 hour.}$$

Standard Intensities. The results of the fallout intensity surveys for those stations at which ma/ft^2 or fiss/ft^2 data were measured are summarized in Table 4. The instruments used are indicated in the column headings. All are portable survey instruments with the exception of the NRDL GITR (Gamma-Intensity-Time Recorder) which is a continuously-recording instrument that was emplaced and started before zero time. The time (in hours after burst) at which the survey readings were made is noted in parentheses following the entries. The laboratory abbreviations indicated under Station Number have the following significance: NRDL refers to the on-site station number of Project 2.9;[5] UCLA, to the off-site stations of the same project, handled by UCLA;† and NDL refers to the Project 2.8 station numbers.[6] In two cases on the UCLA 27-mile arc, the NDL and UCLA station locations did not coincide; hence B-126/127, for example, means "between stations 126 and 127." Fortunately at this distance the intensity gradients are so small that little error is introduced by this approximation.

The 1-hour values entered in Table 4 are those reported in the source literature, in which decay constants ranged from $t^{-1.2}$ to $t^{-1.27}$.

*Which corresponds identically to 3400 (r/hr)/(KT/mi^2) reported in Reference 13.

†For purposes of correlation, the Indian Springs Valley sampling stations (800 and 18- series) were shared in common.

Table 4

Standard Intensities - r/hr @ 1 hr

Station Number			Proj. 2.8		Proj. 2.9		Proj. 2.11		Mean Value	Notes
			Reported time of observation (hrs after burst) given in parentheses							
NRDL	NDL	UCLA	NDL, 39A/27J		NRDL, 39A		NRDL, GITR	UCLA, CDV-700		
100	-				24	(5.25)	34	-	29	
101	T-40		330	(25)	320	(40.5)	350	-	350	Late readings omitted
103	T-39		1.4	(6.4)				-	1.4	
200	R-61		1.9	(3.0)	1.9	(4.6)	1.8	-	1.9	
201	R-51		120	(26)	78	(20.1)	100	-	100	Late readings omitted
203	R-41		34	(6.5)	30	(4.25)	27	-	30	
204	R-76		0.0028	(2.7)	-		-	-	0.0028	
300	P-76		0.58	(20.4)	0.72	(4.83)	-	-	0.66	
301	P-66		110	(26)	34	(4.59)	80	-	80	Proj. 2.8 and 2.9 readings omitted
302	P-87		0.022	(29.8)	-		-	-	0.022	
303	P-86		120	(26)	95	(29.2)	88	-	88	Proj. 2.8 and 2.9 readings omitted
305	P-46		95	(25)	30	(29.0)	56		06	Proj. 2.8 and 2.9 readings omitted
309	P-26		0.15	(50)	-		-	-	0.15	
311	P-16		0.068	(98.5)	-		-	-	0.068	
400	M-82		0.28	(2.7)	0.66	(24.7)	0.76	-	0.71	Proj. 2.8 reading omitted
401	M-67		35	(48.4)	60	(24.6)	58	-	59	
403	M-62		83	(48.7)	76	(24.4)	81	-	81	
405	M-37		28	(3.4)	19	(24.3)	23	-	24	
407	M-25		0.25	(3.4)	0.22	(24.2)	0.28	-	0.25	
409	M-10		0.006	(3.6)	-		-	-	0.005	
501	K-25		3.0	(48.2)	0.87	(53.3)	1.6	-	1.8	
503	K-31		26	(7.6)	34	(25.3)	21	-	27	
505	K-37		33	(7.9)	58	(25.6)	41	-	44	
507	K-43		17	(49.2)	12	(2.75)	17	-	15	
509	K-49		2.9	(49.5)	4.7	(49.0)	-	-	3.8	
601	I-17		0.81	(28.7)	1.6	(28.5)	-	-	1.2	
603	I-21		13	(28.8)	14	(28.3)	-	-	14	
605	I-25		14	(29.9)	13	(28.1)	-	-	14	
607	I-29		1.2	(30)	0.96	(28.0)	-	-	1.1	
703	G-21		1.2	(7.6)	1.7	(26.6)	-	-	1.4	
704	G-5		0.0355	(7.1)	-		-	-	0.0035	
705	G-25		3.9	(7.6)	5.1	(25.2)	3.2	-	4.1	
707	G-29		8.0	(7.7)	10	(24.8)	2.4	-	9.0	Proj. 2.11 reading omitted
810	E-64	18-15	0.013	(48.3)	0.034	(20)	0.014	0.015	0.014	Proj. 2.9 omitted
811	E-68	18-14	0.060	(30.8)	0.066	(24.8)	0.035	0.059	0.055	
812	E-72	18-13	0.14	(30.6)	0.099	(24.5)	0.085	0.12	0.11	
813	E-76	18-12	1.7	(30.4)	1.2	(24.2)	1.05	1.2	1.3	
814	E-80	18-11	1.4	(30.2)	0.96	(23.0)	1.0	1.0	1.1	
816	E-84	18-10	1.3	(30.0)	0.76	(27.8)	-	0.97	1.0	
816	E-88	18-9	1.1	(29.7)	0.76	(27.5)	0.74	0.96	0.89	
817	E-92	18-8	0.94	(50.3)	0.74	(27.2)	0.67	0.86	0.80	
818	E-96	18-7	0.80	(50.6)	0.71	(27.0)	-	0.74	0.76	
819	E-100	18-6	0.44	(50.8)	0.50	(26.8)	0.27	0.52	0.41	
820	E-104	18-5	0.15	(51.0)	0.17	(26.5)	0.18	0.24	0.18	
821	E-108	18-4	0.12	(51.2)	0.11	(26.2)	0.097	0.090	0.11	
822	E-112	18-3	-		0.059	(25.0)	-	0.065	0.062	
823	E-116	18-2	-		-		0.048	0.029	0.038	
824	E-120	18-1	-		-		0.028	0.015	0.022	
-	B-126/127	27-1	0.17	(47.1)				0.11	0.14	
-	B-124	27-2	0.18	(46.9)				0.13	0.16	
-	B-119	27-3	0.16	(46.7)				0.15	0.16	
-	B-119/111	27-4	0.09	(46.2)				0.058	0.074	
-	31.3[a]	35-17	0.024	(22.4)				0.074	0.049	
-	33.3[a]	35-18	0.074	(22.6)				0.113	0.094	
-	35.2[a]	35-19	0.050	(22.8)				0.164	0.11	
-	37.3[a]	35-20	0.075	(23.0)				0.162	0.12	
-	12.8[b]	55-11	0.074	(24)				0.116	0.095	
-	11.0[b]	55-12	0.037	(24)				0.097	0.067	
-	7.0[b]	55-14	0.024	(24)				0.053	0.038	

Notes to table

a Point AD to AE, miles
b Miles from Alamo, south, via US 93.

For some of the more distant stations 1-hour values were not computed by the investigators; in these cases an arbitrary decay function of $t^{-1.28}$ was applied.* There is no particular justification for this value, and in fact, it is fairly certain that some of the large discrepancies in the table arise from a general lack of knowledge of the proper decay corrections.

Another source of error, particularly for the high-intensity stations on the smooth lake-bed terrain, is the fact that the deposited fallout was continually being blown about and redistributed by winds. In such cases, surveys at late times cannot reconstruct the intensities as of 1 hour reliability, hence the GITR values were usually preferred. It should be pointed out, however, that some uncertainty is also present in the GITR readings since the calculated contribution of transit radiation (subtracted from the indicated 1-hour value) reported [8] was based on an imperfectly-known decay curve.

Aside from these sources of error, it was also noted that simultaneous readings with the 39A (TIB) and 27J instruments would sometimes differ by a factor of 2, which indicates the extent to which calibration procedure, instrument response, and operator technique can affect the readings. The last column of Table 4 lists the mean value of the standard intensity, which is an arithmetic mean of the values reported, unless otherwise noted.

Results of the Measurements

The measurements reported above are combined in Table 5. The standard intensities, I_s, are from Table 4; the station average ma/ft^2 is from Table 3, corrected to 1 hour after burst by the factor 241.4

*This factor was also used to correct the project 2.9 off-site surveys which were reported in terms of mr/hr at 12 hours.

Table 5

Terrain-Instrument Response Factor and Gross Fractionation Number at 1 hr After Burst

Station			Standard Intensity, I_s r/hr	$\frac{MeV}{ft^2} \times 10^{-5}$	$\frac{r/hr}{mR/hr} \times 10^{5}$	D_q	$\frac{fiss}{ft^2} \times 10^{12}$	$K_o = I_s A_f$		$\frac{K_o}{r_{fp} \cdot D_{qk} \cdot g_p}$	Terrain Type	d_{50} Meters
NRDL	UCLA	NDL						$\frac{10^{-13} r/hr}{fiss/ft^2}$	$\frac{r/hr}{kt \cdot mi^2}$			
100			28	53.0	0.547	0.795	224	1.29	671	0.249	1	540
101		T-48	350	456	0.769	1.12	1950	1.79	943	0.259	1	1050
103		T-33	1.4	0.0249	56.2	[illegible]	2.89	4.76	2530	0.0091	2	
200		R-61	1.9	3.07	0.619	0.899	14.7	1.29	671	0.219	3	230
201		R-51	180	286	0.635	0.705	870	1.14	593	0.247	3	670
203		R-41	30	60.7	0.494	0.714	270	1.11	577	0.236	3	630
204		R-76	0.0025	0.00278	1.91	1.47	0.0622	0.336	175	0.0350	3	
300		P-76	0.66	0.640	1.03	1.50	3.49	1.90	989	0.194	3	
301		P-66	80	175	0.457	0.664	-	-	-	-	3	810
302		P-57	0.022	0.0123	1.73	2.49	-	-	-	-	3	
303		P-56	64	150	0.587	0.853	$>04^{a}$	1.09	567	0.195	3	500
305		P-46	56	113	0.656	0.721	506	1.11	577	0.235	3	570
309		P-26	0.15	0.0420	3.57	5.16	0.0385	39.0	20,300	1.15	3	
311		P-15	0.068	0.00314	21.7	31.5	0.0914	7.44	3870	0.0361	3	
400		M-62	0.71	1.25	0.569	0.825	10.9	0.657	342	0.122	4	
401		M-57	59	108	0.546	0.793	567	1.16	603	0.224	4	600
403		M-52	61	147	0.551	0.801	624	1.29	536	0.246	4	305
405		M-37	24	50.1	0.479	0.696	222	1.04	562	0.237	4	330
407		M-29	0.25	0.503	0.497	0.722	2.99	0.965	341	0.193	3	
409		M-19	0.005	0.00553	0.904	1.31	-	-	-	-	3	
501		K-25	1.6	3.11	0.579	0.841	27.2	0.662	344	0.129	4	20
503		K-31	27	46.9	0.668	0.959	763	1.927	534	0.164	4	170
505		K-37	45	80.5	0.547	0.795	309	1.624	740	0.274	4	215
507		K-42	15	34.1	0.440	0.639	134	1.09	567	0.261	4	215
509		K-49	3.4	6.66	0.571	0.830	31.0	1.23	640	0.227	4	145
601		I-17	1.2	2.25	0.533	0.774	12.7	0.965	491	0.197	4	210
603		I-21	14	41.6	0.337	0.490	141	0.870	452	0.272	4	190
605		I-25	14	40.9	0.343	0.454	134	0.869	473	0.279	4	170
607		I-29	1.1	3.16	0.348	0.506	21.6	0.509	265	0.154	4	
703		G-21	1.6	3.74	0.374	0.543	26.3	0.532	277	0.150	4	
704		G-5	0.0035	0.0076	0.4735	0.107	0.160	219	114	0.313	4	
705		G-25	4.1	9.11	0.450	0.654	-	-	-	-	4	130
707		G-29	9.0	19.2	0.469	0.681	85.2	1.34	716	0.310	4	130
413	1--12	E-76	1.3	2.38	0.546	0.793	6.53	1.99	1030	0.394	3	86
414	1--11	E-80	1.1	2.23	0.495	0.716	9.76	1.13	584	0.241	3	74
415	1--10	E-84	1.0	1.86	0.538	0.782	9.99	1.00	520	0.198	3	74
416	1--9	E-6A	0.69	1.57	0.450	0.644	4.29	1.07	554	0.173	3	66
41-	1--7	E-96	0.75	1.77	0.424	0.616	-	-	-	-	3	63

Table 5

Terrain-Instrument Response Factor and Gross Fractionation Number at 1 hr After Burst (Continued)

Station			Standard Intensity, I_s r/hr	$\frac{ma}{ft^2} \times 10^{-5}$	$\frac{r/hr}{ma/ft^2} \times 10^{5}$	D_q	$\frac{fiss}{ft^2} \times 10^{12}$	$K_o - I_s/A_f$		$\frac{K_o}{r_{tp} \cdot Dq_{tp}}$	Terrain Type	δ_{50} Kilotons
NRDL	UCLA	NDL						$\frac{10^{-13} r/hr}{fiss/ft^2}$	$\frac{r \cdot hr}{kt \cdot ma^2}$			
420	18-5	E-104	0.18	0.515	0.[illegible]9	0.507	-	-	-	-	4	57
522	18-3	E-112	0.062	0.132	0.4[illegible]0	0.643	-	-	-	-	4	52
824	18-1	E-120	0.022	0.0621	0.354	0.514	-	-	-	-	4	51
-	27-1	B-126/127	0.14	0.693[d]	0.202	0.294	0.169	14.8	7240	7.2[illegible]		[illegible]
-	27-2	B-121	0.15	0.578[d]	0.260	0.379	1.80	0.[illegible]93	433	0.337		[illegible]
-	27-3	B-116	0.16	0.658[d]	0.243	0.353	2.50	9 640	323	9 277		63
-	27-4	B-110/111	0.074	0.156[d]	0.398	0.579	0.129	[illegible].17	3209	1.63		[illegible]
-	35-17	31.3[b]	0.049	0.104[d]	0.471	0.684	0.395	1.27	690	0.[illegible]2		[illegible]
-	35-18	33.3[b]	0.094	0.169[d]	0.556	0.804	0.466	2.02	1050	0.[illegible]2		[illegible]
-	35-19	35.2[b]	0.11	0.250[c,d]	0.440	0.639	0.276	3.99	2070	0.965		[illegible]
-	35-20	37.3[b]	0.12	0.241	0.427	0.620	0.961	1.38	723	0.342		34
-	56-11	12.6[c]	0.095	0.183[d]	0.519	0.754	0.346	2.75	1430	0.55[illegible]		[illegible]
-	56-12	11.0[c]	0.067	0.187[d]	0.358	0.520	0.264	2.54	1320	0.[illegible]6		[illegible]
-	56-14	7.0[c]	0.039	0.0825[d]	0.461	0.670	0.213	[illegible].74	926	0.406		[illegible]

Notes to table

a Obs. flux increased x 10
b Point AD to AE, miles
c Miles from Alamo, south, via US 93
d Estimated from CH counts

(see Decay Corrections); and Column 3, which is the numerator of equation 13, is the ratio of Column 1 to Column 2. Referring again to equation 13, Dq is obtained by dividing the values in Column 3 by I(u,p)/(ma/ft^2), which was evaluated previously as 0.6882 x 10^5 (r/hr)/(ma/ft^2) at 1 hour.

Column 5, fiss/ft^2, is taken from Table 3; K_o from equation 2 is the ratio of Columns 1 to 5; and, with Dq evaluated, r_{fp} in Column 7 is obtained from equation 8, rearranged. The terrain type[5] where known is also listed in Table 5, as well as the activity-median particle size of the fallout samples. The terrain types are described in Table 6. Notice that r_{fp} may also be obtained from equation 12 by the ratio of Column 2 to Column 3 (ma/fiss, observed) divided by ma/fiss for unfractionated Pu-239 fission products, evaluated previously as 9.50 x 10^{-18} ma/fiss at 1 hour.

It is evident that there is a good deal of fluctuation in the values of Dq and r_{fp}. In order to sort out the most reliable values, a review of the inputs to Dq (ma/ft^2, r/hr and station average) and r_{fp} (ma/ft^2 and fiss/ft^2) was made. The ma/ft^2 values were checked as reliable if the ratio (c/m)/ma was close to 1 x 10^{11} (see Table 1) or if there were replicate samples; fiss/ft^2 values were accepted if the ratios, ma/fiss or (c/m)/fiss, were near 10^{-20} and 10^{-9}, respectively, or if replicate fission analyses were available and were in reasonable agreement; r/hr averages were accepted if there was less than a factor of 2 among the readings; and the stations for which recovery losses were estimated were excluded. Table 7 recapitulates the surviving values of Dq and r_{fp}, i.e., those that merited a "check rating" on their appropriate inputs.

Table 6

Station Terrain Characteristics

Type 1. Dry lake bed of Frenchman Flat. Flat and smooth with no vegetation. Very dusty when wind was blowing or vehicular traffic nearby. Stations at ~ same elevation as ground zero.

Type 2. Near dry lake bed on flat, sandy terrain. Low growing sagebrush sparsely distributed around stations. Elevation ranged up to 77 feet above ground zero.

Type 3. The ground surface was covered with small rocks and a crust of soil. As long as the crust was not disturbed there was no dust except from traffic on roads. Vegetation heavier than Type 2, and Joshua trees from 6 to 8 feet high present. Elevation ranged from 30 to 230 feet above ground zero.

Type 4. Rough and rocky. Heavy vegetation consisting of sagebrush and cactus. Very little dust generated by winds. Elevations ranged from 280 to 1,480 feet above ground zero.

The value of Dq for station 300 is seen to exceed unity. This is unlikely physically, since D for most survey instruments is <1, and q for "plane-like" real terrain is always <1. Of course, the station terrain did not always resemble a plane, and in some instances was decidedly mountainous and rolling, but this was not the case for station 300. Hence, in view of the apparent quality of the input data, this value is not explainable at the present time.

The average variation of Dq with terrain type is as follows:

Table 7

Best Values of Terrain-Instrument Response Factor and Gross Fractionation Number at 1 Hour After Burst

Station Number	D_q	τ_{fp}
100	0.795	0.348
101	-	0.359
200	0.889	0.319
201	0.706	0.347
203	0.716	0.296
300	1.80[a]	-
302	0.863	-
305	-	0.226
401	0.793	0.284
403	0.801	0.246
405	0.696	0.227
407	-	0.163
503	0.869	-
505	0.795	0.274
507	0.639	0.261
509	-	0.227
601	-	0.187
603	0.490	0.272
605	0.498	0.279
607	0.506	-
705	0.654	-
707	-	0.310
813	0.793	0.384
814	0.716	0.341
815	0.782	0.196
818	0.616	-
27-2	-	0.327
27-3	-	0.277
35-17	-	0.184
35-18	-	0.382
35-20	-	0.343
56-11	-	0.858
56-12	-	0.747
56-14	-	0.406
	$\overline{D_q} = 0.721$	$\overline{\tau_{fp}} = 0.296$

a Omitted from average.

Type	Dq	No. of Stations
1	0.795	1
2	-	0
3	0.760	8
4	0.683	10

These results are in reasonable agreement with previous estimates of the terrain factor, although in the present case it is difficult to separate out D, since in many cases the standard intensity used was based on readings made with several different instruments.*

The average value of Dq for the 100-800 series of stations, shown in Table 7, is $\overline{Dq} = 0.721$, so that

$$\overline{K}_o = \overline{Dq}\, k_{fp}\, r_{fp} = 0.721 \times 3400\ (r/hr)/(KT/mi^2) r_{fp} = 2450\ r_{fp} \qquad (14)$$

The variation of r_{fp} with the activity-median particle size of the fallout samples is shown in Figure 4. The curve may be compared with that in Figure 2, which it follows approximately, although the data of Figure 4 are inherently less precise, since the median alone does not specify the distribution. It may be seen from the smooth curve drawn through the points in Figure 4 that r_{fp} varies from a minimum of 0.23 at $d_{50} = 300$ microns to 0.56 at 20 microns. The minimum value of r_{fp} corresponds roughly to the 0.19 to 0.30 range reported by Crocker for extremely fractionated fallout samples.(14)

The results for r_{fp} demonstrate the extreme effect that fractionation can exert on the expected value of r/hr for a given number of

*The GITR calibration procedure incorporated an appropriate point-source to plane-source correction factor, so that the readings reported(8) were for D = 1. D has been calculated(2) for the 39A (TIB) survey meter as 0.75. Values for the other insturments used in the Small Boy surveys are not known.

refractory fissions per square foot (or KT/mi^2). Also, in order to conserve activity produced in the explosion, it is necessary that r_{fp} (at 1 hour) continue to increase with decreasing particle size, as suggested in Figures 2 and 4, to values >1. The data also indicate that since $r_{fp} \simeq 30\%$ over the sampled region of the Small Boy fallout field, at least 70% of the gamma ionization potential as of 1 hour was not present in the fallout region sampled.

This missing activity must have been distributed among the rare gases, on particles in the vicinity of ground zero, or on those fine particles that comprised the intermediate and long-range fallout.

REFERENCES

1. Miller, C. F., and J. D. Sartor, Small Boy Shot Fallout Research Program in Radioactive Fallout From Nuclear Weapons Tests. Proceedings of the Second Conference, Germantown, Md., Nov. 3-6, 1964. Alfred W. Klement, Jr., Editor. AEC Symposium Series 5, Nov. 1965.

2. Miller, C. F., The Ionization Rate and Photon Pulse Decay of Fission Products from the Slow-Neutron Fission of U235. USNRDL-TR-247, U.S. Naval Radiological Defense Laboratory, Aug. 1958 (Unclassified).

3. Mackin, J. L., USNRDL, Private Communication, April 1966.

4. Miller, C. F., Analysis of Fallout Data, Part III. The Correlation of Some CASTLE Fallout Data from Shots 1, 2 and 3. USNRDL-TR-222, U.S. Naval Radiological Defense Laboratory, May 1958. (SECRET RESTRICTED DATA).

5. LaRiviere, P. D., J. D. Sartor, W. B. Lane, and K. H. Larson, Fallout Collection and Gross Sample Analysis (U), Project 2.9, Operation SUN BEAM, Shot Small Boy, POR-2215, U.S. Naval Radiological Defense Laboratory, Oct. 1964 (SECRET RESTRICTED DATA).

6. Freiling, E. C., L. R. Bunney, and F. K. Kawahara, Physicochemical and Radiochemical Analysis (U), Project 2.10, Operation SUN BEAM, Shot Small Boy, POR-2216, U.S. Naval Radiological Defense Laboratory, Oct. 1964 (SECRET RESTRICTED DATA).

7. Bouton, E. H., et al., Radiological Surveys (U), Project 2.8, Operation SUN BEAM, Shot Small Boy, POR-2266, U.S. Army Nuclear Defense Laboratory, Oct. 1964 (SECRET RESTRICTED DATA).

8. LaRiviere, P. D., H. Lee, and K. H. Larson, Ionization Rate Measurements (U), Project 2.11, Operation SUN BEAM, Shot Small Boy, POR-2217, U.S. Naval Radiological Defense Laboratory, undated (CONFIDENTIAL).

9. Yu, Oliver S-K, Study on the Mass Contour Ratio, SRI Project No. _____. Stanford Research Institute report in preparation.

10. Strope, W. E., Evaluation of Countermeasure System Components and Operational Procedures, Project 32.3, Operation PLUMBBOB, WT-1464, U.S. Naval Radiological Defense Laboratory, Sept. 1959 (Unclassified).

11. Miller, C. F., Biological and Radiological Effects of Fallout from Nuclear Explosions, Chapter 1: The Nature of Fallout. Chapter 2: Formation of Fallout Particles. SRI Project No. IMU-4536, Stanford Research Institute, March 1964 (Unclassified).

12. Bolles, R. C., and N. E. Ballou, Calculated Activities and Abundances of U235 Fission Products, USNRDL-456, U.S. Naval Radiological Defense Laboratory, Aug. 1956 (Unclassified).

13. Miller, C. F., Fallout and Radiological Countermeasures, Volume I, SRI Project No. IM-4021, Stanford Research Institute, Jan. 1963 (Unclassified).

14. Crocker, G. R., The Effect of Radionuclide Fractionation on the Normalization Factor for Fallout Fields, USNRDL-TR-892, U.S. Naval Radiological Defense Laboratory, Aug. 1965 (Unclassified).

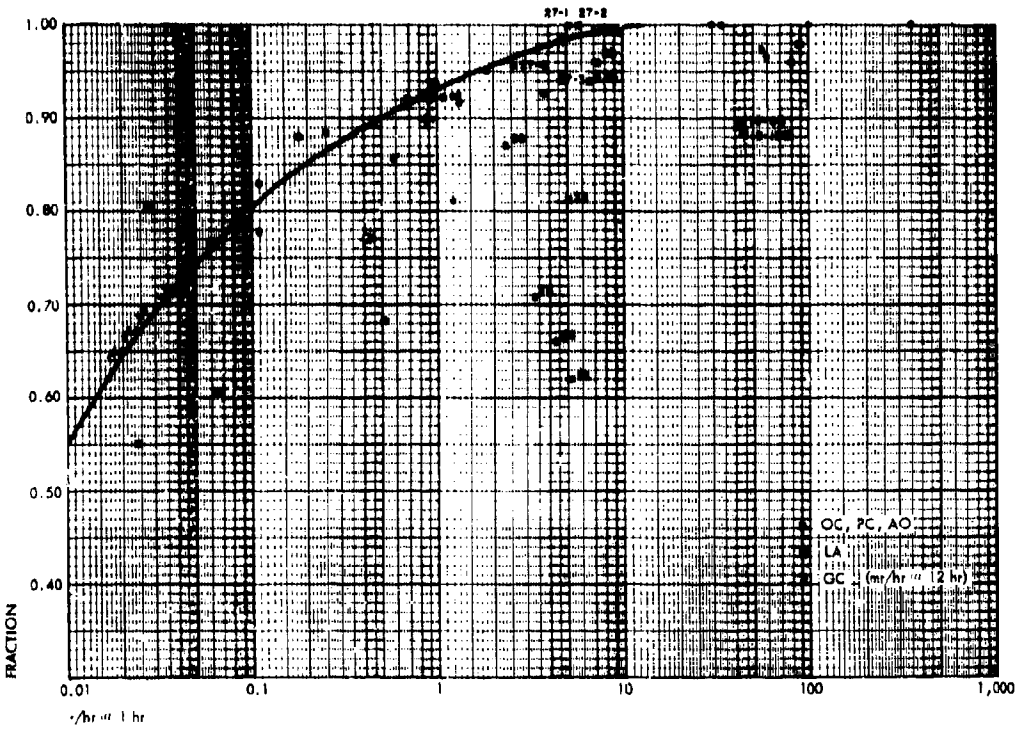

Fig. 1. Fraction of Sample Recovered from Project 2.9 Collectors

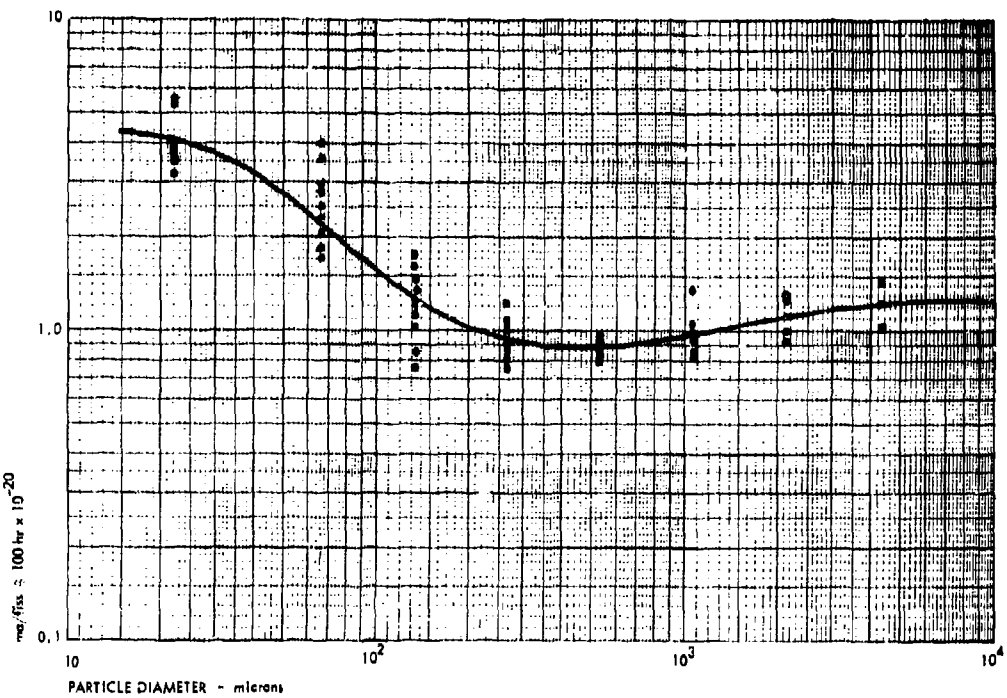

Fig. 2. Variation of ma/fission @ 100 hr with Particle Size

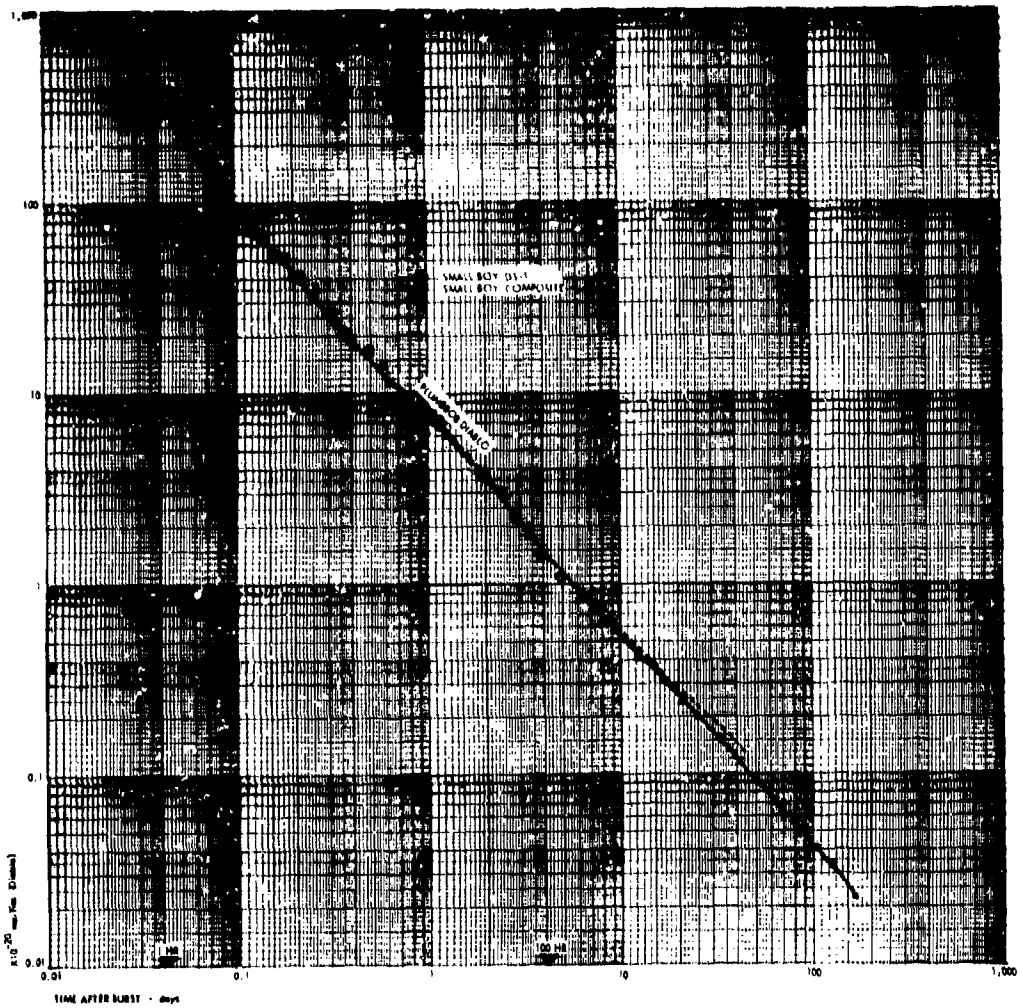

Fig. 3. Decay Rates of Diablo and Small Boy Samples in the 4 π Ion Chamber

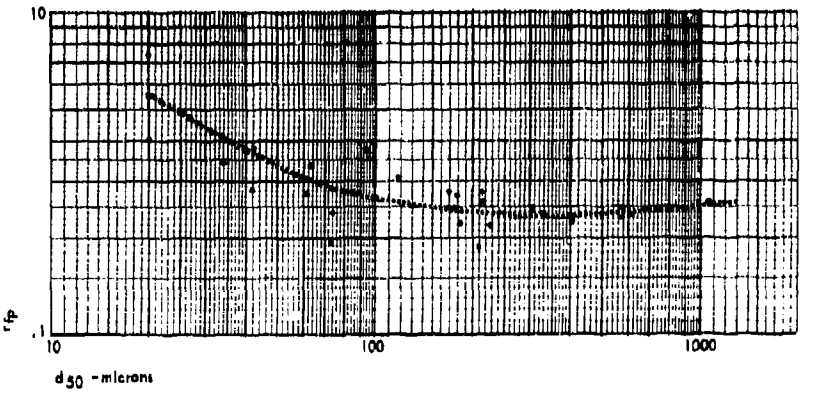

Fig. 4. Variation of Gross Fractionation Number with Median Size of Fallout Samples

INTRODUCTION TO LONG-TERM BIOLOGICAL EFFECTS OF NUCLEAR WAR

C. F. Miller and P. D. LaRiviere
Stanford Research Institute
Menlo Park, California

ABSTRACT

This report briefly summarizes the Stanford Research Institute radiological model assessment system, discusses model parameters related to radiation fields from fallout, and presents results of model computations as applications to civil defense problems that may be generated as a result of a nuclear war.

The general format of the currently available radiological model assessment system is presented in terms of its component submodels and the relations among these models. The inputs and outputs of these models with respect to interactions with civil defense functions and postattack operations is emphasized.

Parameters relating fallout deposition levels and radiation fields are presented. Several of the parameters, such as the terrain factor and radiation field K factor, are evaluated from measurements made on the fallout from Shot Small Boy and other similar measurements.

Input data and results of model calculations on the biological and ecological effects of a hypothetical nuclear attack are outlined and presented to indicate major effects and consequences in relation to resulting civil defense problems.

INTRODUCTION AND BACKGROUND

This paper is a brief summary of work presented in a larger report with the same title;[1] here, the nature of the study is outlined, and the conclusions from the study are reproduced.

The study was concerned with the state-of-knowledge and concepts about the reaction of biological systems to effects of nuclear weapons under nuclear war conditions, about the likely extent of damage to agricultural and wildlife ecosystems under nuclear war conditions, and about the factors involved in the long-term recovery potential of these systems after damage. In the study, an attempt was made to organize the available information for objective discussion of the subject, to outline the state-of-the-art regarding capabilities to use the information (as well as its availability), and to make estimates of effects using the available data and available (or new) computational methods. In the report,[1] only the radiological effects are discussed.

The subjects taken into consideration include:

1. The source of radiological injury or damage to biological species (i.e., local and worldwide fallout, its nature, its radiological properties, and methods used to estimate the distribution of fallout over the earth's surface and degree of the hazard from nuclear radiations emanating from fallout).

2. The external and internal contamination of exposed objects by fallout (i.e., the behavior of fallout particles during and after landing on urban configurations, on agricultural land, on wild land, and on lakes and rivers as well as on individual agriculturally important crop plants, on domestic animals, and on humans).

3. The pattern of radiological damage and recovery of biological species after exposure to nuclear radiations (i.e., the response of individual humans, animals, plants,

insects, and aquatic species to various exposure doses of nuclear radiation; also, the response and recovery patterns for simple ecosystems).

4. The development of operational recovery criteria for use in planning and carrying out civil defense operations under fallout conditions and for use in evaluating the feasibility of carrying out postattack recovery operations (i.e., the limits imposed on operations in terms of the hazard and the nature of the injury and natural patterns of recovery).

5. The long-term ecological consequences (i.e., secondary effects including interaction among species--mainly with respect to food chains and growth competition--, radionuclide cycling in food chains, and conditions that could lead to soil erosion).

Estimates of biological effects on agricultural production, food contamination and internal doses, and wildlife systems were made for two different assumed nuclear attacks. One was a counterforce city-avoidance type of attack with a total yield of about 6,000 megatons, and the other was a mixed military-city attack with a total yield of about 12,000 megatons. In each case, a counterattack of about 10,000 megatons was assumed. All attacks consisted of a mix of air and surface detonations. The computational system used is shown by the schematic diagram of Figure 1. The rectangular boxes in the figure indicate mathematical models, and the rounded boxes indicate either input or output parameters. The coordinate system was based on the location of counties since the county was the smallest unit of area for which agricultural input data is reported. In all cases, the computational systems and input data refer to the state-of-development and availability in 1963 (or before) when the study was made. Most of the models were developed as part of the continuing research program at Stanford Research Institute sponsored by the Office of Civil Defense; the adaptation of the model system to computer language, the computations for the two assumed attacks, and interpretation of the computational results were sponsored by the Director of Defense Research & Engineering.

SUMMARY

General

The analysis and evaluation of the effects of nuclear war on biological species and on their ecological systems depend upon the availability and organization of a great variety of data and information ranging from input information on weapon explosion phenomena and the initial interaction of these phenomena with biological species, wherever they may be, to information about the community behavior, the reproductive habits and cycles, and the recovery mechanisms of ecosystems.

The discussions in the text, with respect to the analyses and evaluations and the uncertainties involved in them, are separated into five subject areas for summary. These are (1) fallout deposition models, (2) radiation damage criteria, (3) second-order effects, (4) countermeasures, and (5) attack analysis findings.

Fallout Deposition Models

No fallout model exists that will reliably predict all the radiological hazards at a given geographical location, not to mention the combined exposure doses from beta and gamma radiation on plants, animals, insects, and humans. For example, of the several fallout models considered, the total area within the 100 r/hr at 1 hr contour varies by as much as a factor of 4. The simple fallout pattern scaling system developed by Miller[2] was used in this study because it was derived directly from selective analyses of evaluated weapons test data and because the output information from the model is applicable to evaluations of both the external gamma hazard and the internal hazard from radionuclide ingestion.

Some of the major unresolved problems include (1) definition of the fallout formation process (including fractionation and solubility), (2) radiological and physical properties of fallout from detonations on likely target environments, (3) meteorological prediction techniques, (4) foliar and plant-part contamination variables, (5) effect of local environments on deposition patterns and radiation fields, (6) beta radiation levels in selected contamination environments, and (7) influence of weather and environment on radiation fields, contamination of objects, and nuclide transfer processes.

One of the most important areas of future research for improving the fallout distribution models is continuation of studies which emphasize the specification of the particle source geometry during the period of fallout particle formation, as previously discussed. Continued research is needed on further development of predictive methods for weather data inputs to the models. Also, additional studies are needed on the appropriate operational use of early monitoring data by civil defense command and control centers and by damage assessment centers for evaluating the radiological hazard and for initiating transattack and postattack countermeasures. Because of the unreliability of prediction methods, it appears that these types of civil defense operations must be planned and scheduled on the basis of observed information.

Radiation Damage Criteria

The biological response, either to acute gamma radiation doses or to chronic doses (or both), is known for a few species, mainly the important higher vertebrate domestic animals. However, most of the information is for specific types of radiation source energies and exposure geometries that are not particularly representative of the conditions for exposure to radiation from fallout. The biological responses of all species to the pattern of exposure in nuclear war radiation environments such as a decaying source strength, intermittent exposures for different time periods,

and the rate of exposure dose received are not known, quantitatively; lack of information in this area is a major weakness in the current state-of-knowledge of biological effects from radiation exposure.

The mechanisms of biological recovery from radiation damage also are not known. But the principle of biological recovery from all types of injury is a firmly established concept for individual species as well as for ecosystems. The accepted description of the effects of acute gamma radiation doses on man have been deduced from scattered information, allowing for liberal use of technical judgement in lieu of factual information from carefully designed experimental investigations. Nevertheless, the recognition that a set of effects information must exist to establish damage criteria can be used to organize and categorize such information in terms of (1) the degree of injury from which recovery would be practically certain, (2) the degree of injury from which recovery would be practically impossible, and (3) the degree of injury from which recovery is uncertain, depending on small differences in the degree of injury, the state-of-health of the organism at the time, the amount of treatment available, and other factors.

For most species and ecosystems, because of many uncertainties in the application of the available data and incomplete coverage of the data, it is not yet possible to establish boundary conditions for injury categories. For the cases where the degree of injury can be categorized, damage assessment studies would require details about the third injury category given above. Information about the details of this injury category is least known for all species.

The use of damage criteria in civil defense system design can be shown to be associated with the definition of the first injury category (e.g., the degree of injury from which recovery would be practically certain). While this use is undoubtedly recognized and applied in the current civil defense programs, it is also apparent that the application more often has been in the form of misuse because the emphasis in the application has been only on one component of the system (i.e., shelter).

Some of the major unresolved problems include (1) radiobiological response of important species of the biota (at various stages of the reproductive cycle) to doses from gamma radiation characteristic in energy, geometry, and exposure patterns of that from fallout, (2) radiological response of selected species of animals, plants, and insects to beta radiation from fallout, and (3) injury recovery mechanisms and dependent variables.

Second-Order Effects

The second-order effects such as the movement of soluble radionuclides within the biosphere, the response of species to a combination of nonlethal doses of radiation, or the erosion of land areas denuded by high radiation doses and/or fire depend on many interrelated (and independent variables) and are poorly known. One main cause of existing controversies regarding the importance of the second-order biological effects stems from poor definition of the primary effects; another appears to arise from differences in interpretation of the efficiency of repair and recovery mechanisms of ecosystems.

Two major factors in the repair and recovery of biological communities appear to be important. The first is the time period over which the injury is sustained. The second is that the rate of the repair and recovery process, after injury, is usually slow, depending on the severity of the injury.

Plant species tend to dominate all important terrestrial ecosystems, and, since plants grow on nutrients in soils, the most serious type of injury to these ecosystems is one that leads to removal of the soil itself by erosion.

In the scale of injury that could result in a nuclear war, the cycling of radionuclides into the food chain of the higher animals appears to be a minor hazard. In the long term, it could be a general public health problem. Although the currently available plant and animal uptake data

are incomplete and of rather poor quality, and occasionally are reported in nonuseful units of measure, the conclusion that the scale of injury from internal contamination would be low is generally supported by these data.

The second-order effects from a fractionation of the degree of injury within the species of an ecosystem have not yet been thoroughly treated; the insect problem, secondary fires, invasion by weeds, and similar problems are of this class of second-order effects. Much applicable data is known to exist. The compilation, organization, and analysis of these data are needed before these second-order effects can be assessed.

At this time, all the second-order effects from a nuclear attack appear to be unresolved; some of the major ones are (1) damage leading to erosion and floods, (2) role of insects in ecosystem recovery processes, (3) ecological repair and recovery rates and dependent variables, (4) energy and matter flow in food chains, and (5) combined injury (long-term low-level) response of species.

Countermeasures

Man is a dominant factor in large segments of temporal ecosystems. While it is possible to state or enumerate the types of countermeasures and control that man could employ to aid in the recovery of the nation (including all types of contiguous ecosystems) after damage from a nuclear attack, it is not yet possible to establish the cost of preparations required to accomplish a desired level of recovery, the real need of the measures, or the capability of survivors to carry out any and all such conceived countermeasures. A better understanding of the nature and degree of the second-order effects is required before proposed countermeasures can be evaluated. At the present time, protective countermeasures against the immediate effects are more important.

Attack Analysis Finding

The following specific conclusions were reached with respect to the model computations carried out on the HM and MC attacks during the course of the study:

1. The nationwide recovery of the production potential of agriculture would be readily achieved, in spite of the radiological effects of the attack, if the farmers have, and utilize, protective shelters with a shielding protection factor of at least 10. The computed per capita production potential of most crops for the crop in the ground at the time of attack was approximately unity for both the case of existing shelter (PF = 10) and good shelter (PF = 1,000 for farmers and 100 psi blast shelters for urban population). However, for the good shelter case under the HM attack, the livestock availability is reduced to one-half of the preattack per capita level. The effect of other factors, such as the availability of power and fuel on the recovery of agriculture, was not considered in this part of the study.

2. The consumption of the foods and water contaminated by both local and worldwide fallout, without any special decontamination methods, would not produce absorbed doses to adult humans that would result in significant early or late biological effects. The same conclusion is applicable for infants that ingest foods contaminated to levels equivalent to those computed for the national median level. For foods contaminated to levels equivalent to those computed for the national 90 percentile level, some long-term effects to infants, from continuous ingestion, would be expected. The important sources of these effects are the assimilation of I-131 in the thyroid from early ingestion of water and milk and the concentration of Sr-89 and Sr-90 in the bone.

3. All crops contaminated to levels less than the 90 percentile level (national summary) of the harvestable crops would be edible, for both the existing shelter case and the good shelter case and for both attacks. The highest calculated absorbed dose to body organs from ingestion of contaminated food and water resulted from the deposition of small fallout particles on the aboveground plant parts and in exposed water sources. The absorbed doses from consumption of foods, in which the contamination of the edible parts of plants from uptake through the roots from both local and worldwide fallout deposited up to planting time and from foliar contamination by

worldwide fallout during the month of harvest, in the first postattack crop were less than those from consumption of the contamination on the crops in the ground at the time of attack.

4. No decontamination of agricultural land would be needed, and no quarantine of agricultural land is required because of contamination by Sr-90 and Cs-137. Green leafy crops (and others) grown on land which contributes to the foods contaminated to levels in excess of the 90 percentile contamination level could be fed to animals.

5. About 10 percent of the forest land (coniferous and deciduous) area would receive sufficiently high radiation doses so that recovery to preattack conditions within about 2 years is questionable. In a smaller fraction of the forest land area, all vegetation would be killed. About the same fractional areas were involved in both assumed attacks.

6. In the HM attack, the crops in 11 percent of the planted crop land (all types) were destroyed (i.e., about 2 percent of the area of the country); in the MC attack, the crops in about 3 percent of the planted crop land (all types) were destroyed. These estimates are probably somewhat low because the computations were presumably based on the response of mature plants, dose-effects data as a function of plant age being nonexistent, and because beta dose responses were not considered (no model and no response data being available).

7. A large fraction of the population has well-water sources available to them; these sources are not expected to be contaminated during an attack. (However, the availability of the water would depend on the availability of power for pumping.) The consumption of contaminated water from exposed sources in the early postattack period, neglecting natural and normal water treatment decontamination processes, would not be expected to produce serious somatic effects at the 90 percentile (nationwide) water source contamination level.

Within the reliability of the current information on the biological response of biological species to radiation exposures, the above results of the study lead to the conclusion that long-term biological and ecological effects would not be so severe as to inhibit or seriously delay the national recovery after a nuclear attack similar to one of those assumed in the study. Rather, the major problems of population and biological

resource survival are concluded as being associated with the short-term biological effects that would result from the exposure of all biological species to gamma radiation from fallout. The alleviation of these effects thus centers on the availability of shelter for the protection of the population and a local capability for organized efforts to recover food and water and other such resources that would be required to maintain the health of the survivors as a coherent work force in the early postattack period. This is the time period after attack when the need for knowledged leadership would be critical and when errors in recuperative actions would be the most likely to lead to secondary fatalities.

The effects of the radiation from fallout in some areas of the country could result in fatal doses to all higher forms of life in exposed conditions. A few percent of the total land area of the country would likely be denuded of vegetation for a short period of time. However, the location and extent of these areas, with respect to other aspects of resource damage and economic recovery problems, are such that the ecological consequences of the biological damage in these areas could have little or no influence on national recovery. Essentially all of the economically important agricultural land is recoverable within the first year after attack, even for the case of using existing shelters.

REFERENCES

1. Miller, Carl F., and Philip D. LaRiviere, Introduction to Long-Term Biological Effects of Nuclear War, Stanford Research Institute, Project No. MU-5779, April 1966.

2. Miller, Carl F., Fallout and Radiological Countermeasures, Volumes I and II, Stanford Research Institute, Project No. IMU-4021, January 1963.

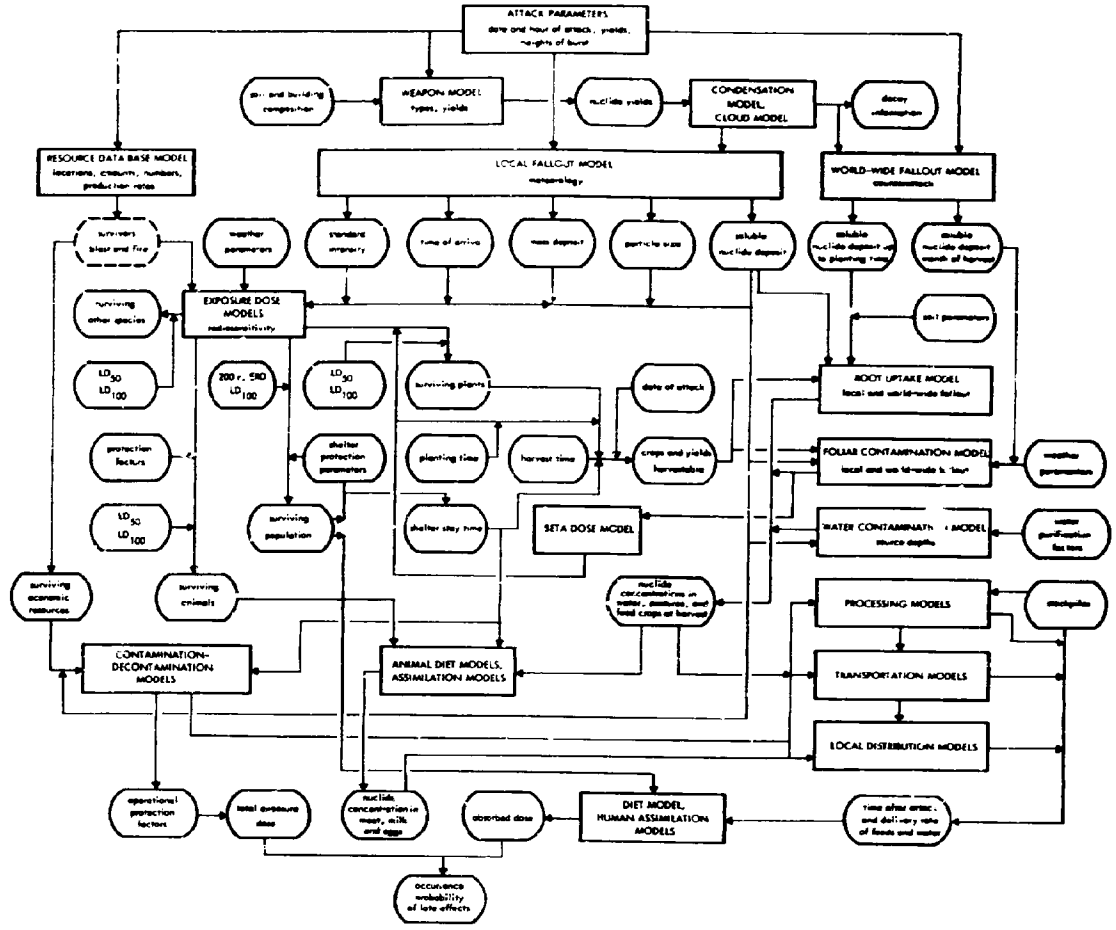

Fig. 1. Schematic Outline of Model Systems for Estimating Radiological Effects

SUMMARIES AND RECOMMENDATIONS

OF THE WORKING GROUPS

SESSION ONE - PARTICLE FORMATION

INTRODUCTION

The purpose of this report is to offer some comments on the state of the art with respect to the problem of particle formation as it pertains to land surface detonations of nuclear weapons in general and to the DOD Fallout Model in particular. The report is divided into three main sections: a statement of objectives; a non-comprehensive review of the main features of what is known and what is being studied; and a listing of some gaps in the state of knowledge and in our current research efforts.

The approach outlined above was accepted by the working group as a whole, and on this basis sections of the report were prepared by subgroups of 2 to 4 members. There was insufficient time for the subgroups to cross-review their contributions so that it cannot be assumed that each working group member necessarily agrees with all that is presented in this report. Furthermore, in the interest of conciseness, it has been necessary in many instances to paraphrase and condense. It is hoped that this has not done too great a violence to the ideas of the originators.

OBJECTIVES

An acceptable model of the particle formation process must satisfy two requirements.

(1) It must furnish, for a particular nuclear detonation, a detailed description of the distribution of particles as a function of size and mass or sedimentation rate. If the early distribution varies in an important way with location within the nuclear cloud, the nature and extent of the variation should be specified. Such information is essential as input to an effective transport calculation.

(2) It must furnish information regarding the particle size distribution of individual radionuclides and define the chemical and physical properties of the particle population in sufficient detail that the nature and extent of both external and internal radiation hazard can be determined for any specified time after detonation.

On this basis it is believed that the objective of the study of Particle Formation may be stated as follows: Given the yield, mass, and composition of a nuclear device and a description of the environment in which it is detonated, the Particle Formation model must predict, as a function of particle size, cloud dynamics, and early time, the chemical composition, isotopic composition and physical characteristics of the resulting radioactive particulates.

A SHORT REVIEW OF WHAT WE KNOW

Information relevant to the overall problem of Particle Formation may be sought by one of two main approaches -- Analysis of particles produced by nuclear detonations, or fundamental studies of the mechanism of synthesis of particles under conditions simulating those which prevail in a nuclear detonation. These approaches are essentially independent. However, results produced by the second must be consistent with the analytical data provided by the first. Some progress reports on examples of these two lines of investigation are discussed in the following paragraphs.

PARTICLE ANALYSIS. The underlying concept of the Particle Analysis approach is quite straightforward. Particle samples separated according to size or sedimentation rate are subjected to chemical, isotopic and physical analyses; the results of such analyses are expressed mathematically as distribution functions; and the variation of the parameters of the particle distribution functions with detonation conditions is studied with a view to arriving at a method of quantitative prediction. Under the general category of effort there are three principal lines of experimental endeavor -- analysis of particle samples separated by atmospheric processes; analysis of particle samples collected at early times and

separated in the laboratory according to size or sedimentation rate or density; and analysis of individual particles.

(1) Analyses of Particle Samples Separated by Atmospheric Processes. The internal isotopic ratios measured on particle samples collected on the ground and in the air at various times after detonation can be used to arrive at fractionation behavior relationships. Data of this type from airburst detonations were used by Freiling to arrive at his Radial Distribution Model. In I. J. Russell's paper, an application of this method to Johnnie Boy and Castle Bravo data was used to hypothesize the existence of a substantial population of very small particles. An extension of the approach to include induced activity data was presented by W. J. Auth. The consensus of contributors is that there exists a large body of experimental information which has not yet been subjected to the necessary detailed isotopic balance studies required for understanding the particle formation process. Data suitable for such analysis exists at the weapons laboratories and in the AFTAC laboratories. Other data exist at AERE and in foreign publications. In addition to the basic application of these data to the problem of particle formation, they should also be used to provide critical tests of the realism of fallout models, including the DOD model.

(2) Analysis of Particle Samples Separated in the Laboratory. One shortcoming of the particle samples that are separated by atmospheric processes is that the particles analyzed are grouped in an unsystematic fashion and in fact for any particular event, entire groups may not have been analyzed. The systematic separation of close-in aerial and fallout samples has been carried out in an attempt to provide particle sample sets which are evenly distributed and which represent the complete particle population. In addition to isotopic data, the analytical program provides particle mass data and information about the chemical composition and physical character of the various groups. R.E. Heft's paper describes the application of the method to two cratering events at Nevada. His findings

indicated a strong correlation between isotopic composition and chemical and physical nature of particles. Refractory isotopes were volume distributed in "glass" particles; volatiles were on the surface of crystalline particles. M. W. Nathan's paper gave some preliminary results from the application of the method to Johnnie Boy and appears to confirm and extend Russell's findings.

(3) Analysis of Individual Particles. A substantial backlog of data on the relationship between activity and size for individual particles has been built up over the years by various laboratories - NRDL and Tracerlab have been major contributors. In recent years this work has been extended to include measurements of individual radionuclides and the results of some of this work were summarized in Nathan's paper. Some interesting insights into the mechanism of particle formation are being provided by electron beam microprobe analyses of individual particles. J. H. Norman's paper provided some exceptional microprobe "photographs" of individual particles which showed examples of inclusions. He also reported the observation of radial concentration gradients in silicate particles which suggests the possibility of a process of diffusion-controlled absoprtion of fission products by these particles.

PARTICLE SYNTHESIS. In this category of investigation, we include all laboratory studies relating to the interaction of materials at high temperature which are aimed at improving our understanding of the condensation, absorption or agglomeration processes which contribute to the process of particle formation. An outline of the interaction of the various processes as conceived by the NRDL group is presented in the accompanying figure.

Laboratory studies pertinent to model description and determination include both thermodynamic and kinetic measurements. Of thermodynamic importance are solubility versus gas phase composition, gas phase composition, and energies involved in the transfer of materials between species or phases. Of possible kinetic importance are diffusivities in

the gas phase, diffusivities in the condensed phase, condensation coefficients, accretion and turbulence. In the thermodynamic representation, the important nuclear cloud parameters are condensed phase composition, gas phase composition including species, and temperature (possibly even electron temperature). For kinetic processes the important nuclear cloud specifications are cooling rate, particle size, and nucleation rate.

The synthesis work at General Atomic reported by Norman is concerned with measurements of Henry's Law constants for several fission products in silicates in the $CaO-Al_2O_3-SiO_2$ system. In these studies a considerable degree of nonideality has been observed. Ideal solution thermodynamics may be inadequate in describing solubility. For the particle sizes measured condensed state diffusion is the most reasonable candidate for the rate-controlling process for all but the calcium ferrite samples.

Studies at NRDL on molybdenum oxide, reported by E. Freiling, were aimed at determining whether gas phase diffusion, condensation, or condensed state diffusion are rate controlling in fission product absorption by the liquid state of calcium ferrite, $CaO-Al_2O_3-SiO_2$, clay, and sodium oxide-silica. For the particle sizes measured, condensed state diffusion is rate-determining for all but the calcium ferrite samples. In the latter case, condensed state diffusivities were quite large and gas phase diffusion was found to be rate governing.

Work at Lawrence Radiation Laboratory reported by G. T. Rynders was concerned with a study of physico-chemical processes taking place at high temperatures produced in an RF-induction plasma-torch. By passing particulate material through the torch and collecting the products, it is intended to investigate the interaction of liquid particles (as melted) with a gaseous environment, as well as the vaporization effects which also occur. The particulate material is subjected to short residence times at high temperature as well as short quench times which are of the order of tens of milliseconds. The particles do not reach plasma temperatures but are subjected to heating and cooling processes similar to

those which occur in a nuclear fireball. Future work will be concerned with the effects on condensation processes of environmental atmospheres, plasma temperatures, residence and quench times, and feed particle concentrations. For those particles that have been melted, the particle size distribution, fractionation effects, and particle morphology will be characterized. Some work will also be done on agglomeration effects which are observed to occur during condensation of vaporized material.

SOME GAPS IN THE STATE OF KNOWLEDGE

In connection with the overall problem of Particle Formation, there were a number of areas where essential input information was either lacking or very poorly substantiated and where there is no known effort to obtain improved data. In this section we have listed some of these areas.

(1) Effect of size distribution of particles in the pre-shot environment compared with final particle distributions. Condensed phase material introduced into the nuclear cloud has an important effect on the ultimate particle distribution. A need exists to better define the nature of this effect.

(2) Phase distribution of environmental material introduced into the nuclear cloud (vapor, liquid, solid). The DOD-Fallout Model appears to be tied to the assumption that 20% of the cloud mass is vaporized soil but this number is not well substantiated. There may be a possibility of considerably improving the quality of this input base. on detailed radiation-hydrodynamic calculations such as are carried out by the weapons laboratories. Such calculations could also better take into account the phenomenology which affects particle size distribution.

(3) Post-condensation agglomeration. Both aerial and fallout nuclear debris samples are probably subjected to artificial agglomeration by the presently used collection devices. There is need for measurements of particle size distributions as they exist in the cloud which are not subject to the limitations of sampling media. A completely representative sampling system should account for radioactive gases as well as radioactive products in particles.

(4) Height of burst effects on particle formation. Bursts on the ground or fifty feet above it would be classified as "land surface bursts" but the particle formation history might be substantially different. In this same connection, the effect on the distribution of particulate radioactivity by a base surge may be important. Neither variable is explicitly included in the DOD fallout model.

(5) There is a shortage of useful information on the space and time variation of the particle population within the cloud. Such information might be produced from possible future detonations if adequate sampling programs existed. There is no known work in the area of planning or implementing such a sampling program.

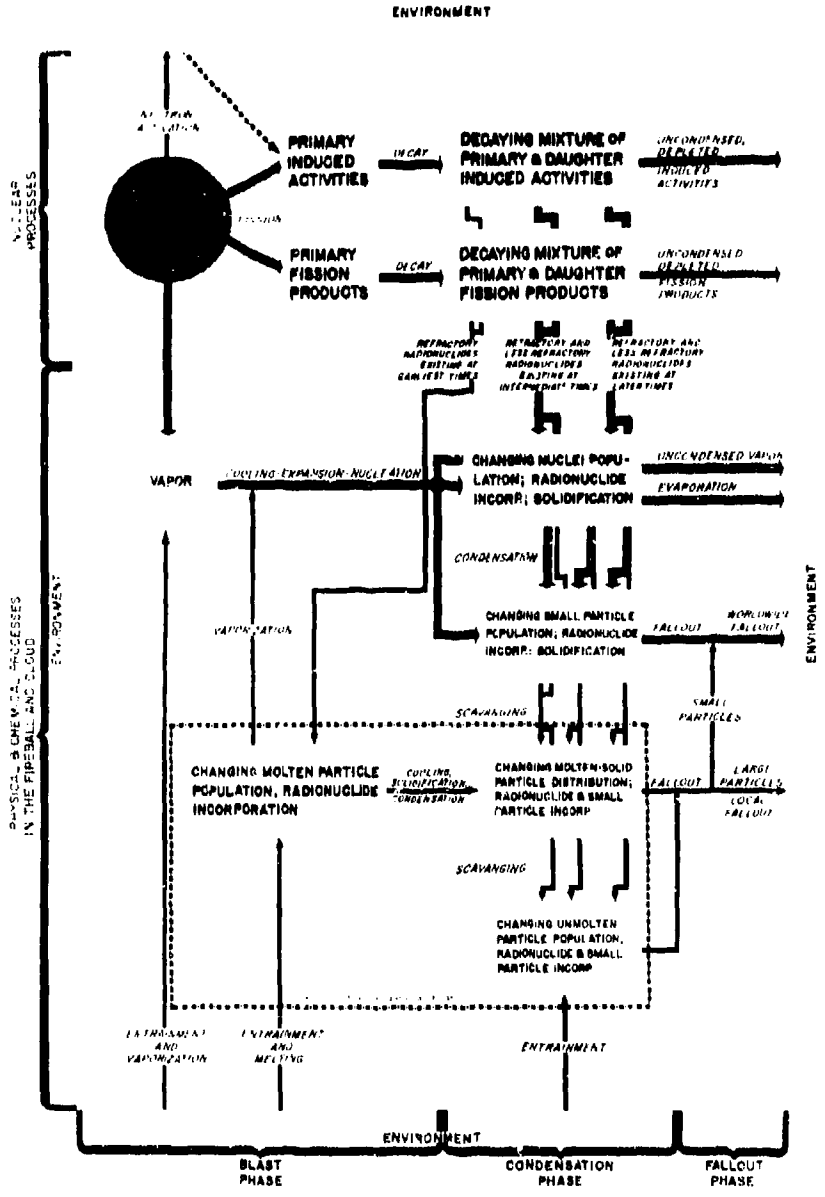

Fig. 1. Fallout Formation Processes in Air and Surface Bursts

SESSION TWO - CLOUD DEVELOPMENT, PARTICLE CIRCULATION

The working group considered the cloud rise problem from three different points of view; the information needed by the fallout model, the types of approaches available to provide this information, and suggested programs for advancing the state of the art.

The first essential is a measure of the cloud height. No matter what type of model is used, a measure of how high the particles are carried is of prime importance to the subsequent calculations. In order to consider the formation and dispersal of particles within the rising cloud it is necessary to know the time-temperature history and the velocity distribution within the rising cloud.

The degree of detail which is required of the temperature and velocity distributions within the cloud is dependent on the degree of sophistication of particle formation and coagulation models. At present an average temperature as a function of time and a gross partition of the internal kinetic energy between toroidal circulation and turbulent motions appears to be sufficient. Eventually we hope to gain greater understanding of the hydrodynamic history of the cloud rise.

To meet those needs we have available three levels of sophistication of cloud models. First is a strictly empirical analysis of the observed data, next is a one-dimensional parcel rise theory, and finally the fairly sophisticated two-dimensional hydrodynamic numerical methods.

The empirical methods range from a simple power law scaling with yield which ignores the possible variations produced by the atmosphere, to the fitting of more complicated equations which consider the gross lapse rate and/or the height of the tropopause.

The parcel rise methods have a long history starting with G. I. Taylor's analysis which was refined by Machta, Kellogg and many others. Most of these techniques suffered from the difficulties experienced by Normont, in that the predictions were quite unstable to small changes in the assumptions about entrainment, drag and the atmospheric conditions. Many of the difficulties with the parcel method have been overcome by the Huebsch who introduced a mechanism to account for the conservation of energy. A successful parcel method can, in addition to the height of stabilization, provide a curve of the mean parcel temperature as a function of time and can give a measure of the amounts of turbulent and thermal energy within the parcel. It should be noted, however, that no parcel method has ever been systematically tested against observed data.

Finally, there are the two-dimensional hydrodynamic methods which require rather powerful computing facilities for their use. There are quite a few simplified versions of these methods in the meteorological literature, but the simplifications involve the Boussinesq approximations and the assumptions of very small temperature differences, neither of which is applicable to nuclear clouds. The complete programs are rather horrendous in their complexity. Even with such apparently powerful tools, we must point out that the few calculations which have been made have not been tested against the observational data.

We suggest that work be pressed on all three approaches to cloud rise prediction. A continued search for improved empirical formulas for the height of stabilization, such as that presented by O.S-K. Yu, is essential to provide a standard against which all proposed improvements can be tested statistically.

A program for testing the accuracy of the parcel methods against the stabilization height is necessary to prove the validity of the postulated mechanisms. We suggest that a form of the energy conserving parcel method be tested against as many low air bursts as possible to determine how well it approximates the observations. We suggest low air bursts

in order to minimize the effects of soil loading on the one hand, and excessive atmospheric pressure gradients on the other. If we can produce evidence that those methods are useful in the most simple case, it will be easier to assess the effects of complex fire ball loading.

The search for analytic approximations to the problem of cloud rise should be pressed. We do not believe that these approximations will be useful in a model, but the insight they provide may show how the 2-dimensional aspects of the problem can be better parameterized into the parcel techniques. Such an approach is appealing because of the inordinate amount of time required for the rigorous 2-dimensional treatment.

Finally we suggest that a full scale 2-dimensional hydrodynamic problem be run with initial and boundary conditions which can be matched with a well documented, well behaved, low yield air burst. Again we suggest this work not as a possible program for a fallout model, but as a method for learning how the details of the flow can be parameterized into a simpler computing scheme.

We urge caution and deliberation in the adoption of any cloud rise model. The adoption of a physically appealing but untested approach could prevent us from finding obscure but important factors in the development of the cloud.

SESSION THREE - TRANSPORT AND DEPOSITION

Local Fallout

1. Computor capabilities exist that can simulate complex systems of particle transport.

2. Atmospheric parameters, including measurements of temperature, humidity and wind conditions, are generally available at locations spaced about 200 to 250 miles apart for time intervals of 6 to 12 hours in the U.S.A. For certain locations, such as the Nevada Test Site, capabilities exist, when necessary, for obtaining these atmospheric parameters at locations spaced tens of miles apart and at time intervals on the order of tens of minutes. However, persistence of the shot time ground zero winds, for the consideration of local fallout, is commonly considered the best particle transport mechanism in view of present wind forecasting capabilities.

3. The transport and deposition of "dry fallout," rather than scavenging of particles by precipitation, is considered most significant.

4. The theory for predicting the settling speed of individual particles given their size, shape and density is reasonably well agreed upon, but differences of opinion exist as to the physical particle characteristics to use in the theory.

5. The turbulent spread of free falling particles is not considered as important as wind shear effects in widening a fallout field.

6. We can handle transport in certain simplified wind circulations but not in air movements for the more real, complex circulation patterns.

Intermediate and World-wide Fallout

1. **We understand qualitatively but not quantitatively the transport, dispersion and deposition of intermediate fallout.**

2. **Empirical forecasting of fallout from stratospheric injections is considered quite reliable for the generalized time and space forecasts normally required.**

CURRENT LIMITATIONS

Local Fallout

1. We must find ways of running machine computed transport and deposition models faster and cheaper.

2. We need more reliable observations and forecasts of the three-dimensional field of motion (horizontal and vertical winds).

3. We need more information and better methods for adequately observing and forecasting the scavenging fields in the atmosphere (including scavenging efficiencies).

4. We suspect settling by processes other than by conventional formulas applied to isolated particles. The importance of either bulk subsidence of a cloud of particles or by agglomeration during free fall is still unkown.

5. We must know more about particle characteristics and their atmospheric interactions to be able to more accurately predict their deposition positions. This includes the possibility of water condensation and evaporation during descent.

6. We know little of the interaction of a nuclear cloud on the adjacent atmosphere insofar as the latter influences particle transport.

7. The influence of small scale (10-100 ft) objects on very localized fallout is known qualitatively - it should be known quantitatively.

8. The quantitative aspects of particle redistribution by winds and wash-off must be further studied and better understood.

9. We emphasize the crucial nature of the activity vs. altitude in applying transport factors to obtain fallout patterns.

Intermediate Fallout

1. We are limited to the more qualitative aspects of predicting intermediate fallout.

SUGGESTIONS

Local Fallout

1. Moral and financial help should be given to military and civilian groups to improve the observation and forecasting of air motions and precipitation scavenging regions.

2. Simulation (non-nuclear) experiments may be performed to better understand and verify the transport of falling particles.

3. Similarly, on a smaller scale, non-nuclear simulation can reveal patterns of fallout over and around small scale objects such as trees and buildings.

4. Settling speeds using actual collected particles from past events could be investigated in the laboratory.

5. It may be possible to simulate agglomeration and bulk settling of clouds of particles.

6. In general, it may be quite useful to undertake basic studies on the behaviour of existing (non-nuclear) atmospheric particulates applicable to fallout problems.

Intermediate Fallout

1. Investigations and studies related to existing data on past intermediate fallout may permit improved predictions of this fallout.

SESSION FOUR - RADIATION FIELDS

INTRODUCTORY COMMENTS

The problems of the fourth session of this symposium are perhaps better described as problems of residual radiation fields, rather than fallout radiation field problems. They include effects due to neutron-induced activity near ground zero.

The material of the session is conveniently divided into four major types of information:

(1) the spectra of radiation fields;

(2) the radiation field data for idealized configurations;

(3) effects due to the particular configuration of materials at the surface of the earth;

(4) a set of related topics which do not fit very well into these other three.

Let us also identify the main applications for the radiation field data. These are,

(1) for interpretation of field experiments;

(2) applications to shielding design and analysis problems;

(3) applications to problems of military tactics, as affected by nuclear weapons;

(4) the prediction of residual effects which result from nuclear explosions.

The following comments reflect many, but not all points of view expressed by participants in discussions held at the symposium, together with some afterthoughts; they are not the product of a systematic study.

SPECTRA

Probably it is in shielding that most use is made of this type of information at present; and the first category of information, that of spectra, is particularly important for shielding applications. Perhaps the single main requirement for the shielding applications is a sort of "coverall" spectrum. Most protection factor calculations are based on a spectrum due to Nelms and Cooper, which utilized the data on activities originally produced by Ballou and the data on spectral products tabulated by Carl Miller. This 1.12 hour spectrum is not particularly accurate; it was calculated very early to fill a serious informational gap and has served that purpose very well. There have since been advances in our ability to produce reliable fallout spectra; and this is an excellent time to replace the old one with something more accurate. There is no reason to preserve the odd time period of 1.12 hours. We should calculate a one hour spectrum, with fractionation appropriate to close-in fallout.

Because we know much more now about fractionation than formerly, as evidenced by Mr. LaRiviere's talk, the coverall spectrum should be complemented by perhaps as many as four additional types of spectra, all calculated as a function of time. These source spectra, identified as S_1, S_2, S_3, S_4, might be the following:

(1) $S_1(E,t)$ a close-in fallout spectrum; $S_1(E,1\ hr)$ would be the coverall spectrum we mentioned previously.

(2) $S_2(E,t)$ might be a spectrum for which fractionation is appropriate to fallout at substantial distances away from the burst.

(3) $S_3(E,t)$ might be appropriate to the world wide fallout.

(4) $S_4(E,t)$ would describe those induced activity components which appear in the fallout itself.

In connection with S_3 and S_4 particularly, and possibly for all spectra, it would be valuable to accompany the actual spectra with tables of data for specific nuclides as a function of time. In the induced

spectrum, for example, there are a few particularly important components; and tables of the activities and spectra for these nuclei would be especially useful for many purposes. On the other hand, the four spectra would serve as standard cases against which experiments and other calculations could be compared. To these gamma ray spectra we might add one more--a coverall spectrum for the beta rays. It would be advantageous to add to this a tabulation of beta ray data for the most important nuclides as a function of time. From this data other spectra could be constructed if and when desired; and for fallout at great distances, combined spectra are apt to be less important than spectra for specific nuclides.

It is our understanding that data for the chain yields are in much better state than for spectral yields, and that the decay schemes will be subject to revisions in the future, probably at a fairly low level of effort.

Fortunately, the group at NRDL with which Mr. Crocker has been working is now able to generate these spectra. We feel that the work of this group is especially important at this time, and that they should not stop short, nor should support for this work stop short, of a full coverage of these types of spectral information.

DISTRIBUTIONS FOR AN IDEAL PLANE

In regard to the second category of information, there are a number of types of data which clearly need to be obtained for all types of application. The simplest data are the source-to-field conversion factors, which give the exposure 3 feet (or 1 meter) above an ideal interface, for the spectra previously mentioned. The air-air interface, which is fundamentally simpler than the earth-air interface, lends itself better to these standard cases because it permits precision calculations. On the other hand, someone should once-for-all determine the difference in this conversion factor between the air-air case and the air-earth case; it

may be well below experimental observance and smaller than probable errors in the majority of computations.

In addition to the conversion factors there are a number of important types of distributions. Perhaps most useful would be the spatial distribution of the exposure as one moves away from the plane interface, as calculated for the coverall spectrum. We might call this D(z). Also needed are the angular distribution, $D(z,\cos\theta)$, of the exposure, and the spectral distribution, N(z,E), of the flux, both calculated for the coverall spectrum. The angular distributions, and also to some extent the actual space distribution of the total exposure, are comparatively insensitive to the spectrum. Hence it may not be necessary to do such calculations for all of the useful spectra. Because there is so much experimental work done with the Co^{60} and Cs^{137}, the three types of data just mentioned should also be obtained for these isotopes, as should the source-to-field conversion factor. All of these calculations should be of high precision.

Another type of data for which there has been a demand is the energy flux as a function of angle, say three feet above the plane interface, as calculated for a number of monoenergetic gamma ray components. Data of this type has been published by Mr. French. It is useful for determination of exposure distributions, for example in the human body.

In connection with the beta ray coverall spectrum already mentioned, it is clearly desirable to have a distribution for the beta ray exposure, calculated as a function of distance away from the plane interface. There are and will be applications of this data, probably more in the future than in the past. Dr. Brown's calculations are a useful reminder that beta rays are part of the radiation field and can be important under certain circumstances.

For the idealized configurations, properly done calculations may be an order of magnitude more accurate than experiments which might be designed specifically to check the calculations. Therefore, this type of

experiment should be closely scrutinized in regards to the information which it will produce, while it is at the stage of a proposal. A well-conceived, highly accurate experiment may have value for confirmation purposes, if errors are closely studied and understood.

CONFIGURATION EFFECTS

The third category of information relative to the radiation field is that of configuration effects. We subdivide this general topic into three subtopics,

(1) ground roughness,
(2) the special problem of shrubbery,
(3) terrain problems.

In all cases the irregularities affect mainly the strength of the direct component.

There exists a substantial amount of data for ground roughness; and the talk by Mr. Soule is an additional contribution. Mr. French's talk demonstrates again that we understand rather well what the physics of the roughness phenomena are. But the question of what happens to the fallout subsequent to arrival is not well known; and this means that we are only able to guess at the time variations of such effects. Perhaps the greatest need at present is for categorizing of types of ground surface, so as to be able to specify an appropriate roughness parameter. (There are at present a variety of opinions as to how this may be done and also as to the potential accuracy of such a procedure in any given application.)

In regard to the shrubbery problem, the data obtained in Costa Rica should, when published, provide information about fractional retention in various types of plants. In order to make this data usable, it will be necessary to make additional studies of the change in effectiveness due to source elevation. Clearly the effect can be an important one for below-grade shelter. There is an opportunity to do a certain amount of

modeling in both theoretical and experimental studies, using elevated plane and point sources to simulate radiation sources located in shrubs and trees. The attempt should be made to incorporate this type of information both into survey calculations and into PF calculations for specific structures.

The terrain category of configuration effects subdivides well into a set of problems for buildings in cities, and the way they shield one another, and a set of problems involving contour effects which occur, say, in the countryside. In general, the terrain effects can be estimated using only the unscattered radiation. Although more work has been done on the problem of mutual shielding by buildings in cities, it may be that if studies of contour effects in country localities were done first, the problems of mutual shielding in cities would be simplified. Perhaps what is currently needed is a combination of "terrain factor" with a logical categorization of different terrain types which gives appropriate weight to the distance from the detector to the visible elements of the source.

OTHER PROBLEMS

We will mention here some of the remaining problems without much discussion.

First is the problem of the redistribution of fallout after it has come down. Although there has been some study of this, there needs to be a great deal more, with considerable emphasis on what happens in cities with wind and rain washing. There is information, but more work needs to be done.

In connection with the beta ray problems, which have applications in ecological studies, there are problems of calculating beta ray exposures of small creatures, such as insects.

Another type of problem, that presented in our session by Dr. Ferguson, is that of neutron induced activity near ground zero. Perhaps what is most needed now is a study of induced activity in which both new and old devices are examined in some detail.

Finally, there are the long term problems, such as that of fallout on a worldwide scale, and the biological and ecological problems associated with external exposure as well as ingestion. If defense is broadly construed, these are defense problems; and there is a need for much more study of the complex and difficult consequences of massive and large-scale distribution of fallout. We hope that these longer range problems will not be by-passed.

CURRENT SITUATION

In conclusion we might generalize as follows:

(1) it is time that the accumulating information on fractionation were incorporated in a new series of source spectra, to replace those that have been used for the past 8 years or so;

(2) using this source data, precision calculations of radiation fields in idealized configurations should be carried out to replace older calculations of uncertain accuracy;

(3) the phase in which preliminary explorations of configuration effects are carried out should be replaced by attempts at systematization, accompanied by appropriate spot-check experiments;

(4) longer term effects should be included in the overall field of study in some manner.

BLANK PAGE

LIST OF ATTENDEES

Auth, W.J., Lt. Col., USAF	Chief, Laboratory Operations Section 1155 Technical Operations Squadron McClellan AFB, Calif. 95652
Ayres, Robert U., Dr.	Hudson Institute Quaker Ridge Road Harmon-On-Hudson New York 01520
Baker, Sherman A.	Resources Analyst Office of Civil Defense The Pentagon Washington, D.C. 20310
Bauer, Kenneth H., Lt., USN	U.S. Naval Postgraduate School Monterey, Calif.
Baum, Sanford	Operations Analyst Stanford Research Institute 333 Ravenswood Ave. Menlo Park, Calif. 94025
Beadle, Robert W.	Atmospheric Sampling Engineer Division of Biology and Medicine U.S. Atomic Energy Commission Washington, D.C. 20545
Bloore, Ernest W.	Chief, Physical Chemistry Branch U.S. Army Nuclear Defense Lab. Edgewood Arsenal, Maryland 21010
Bressee, James C., Dr.	Director, Civil Defense Research Project Oak Ridge National Laboratory Oak Ridge, Tennessee 37831
Brode, Harold L., Dr.	Physicist The RAND Corporation 1700 Main Street Santa Monica, Calif. 90406
Brown, Stephen L., Dr.	Physicist Stanford Research Institute 333 Ravenswood Ave. Menlo Park, Calif. 94025

Buchanan, James O., Dr.	Director, Shelter Research Division Office of Civil Defense The Pentagon Washington, D.C. 20310
Buskirk, Fred R., Dr.	Assoc. Prof., Physics U.S. Naval Postgraduate School Monterey, Calif. 93940
Cane, John W., LCDR, USN	Radiation Division Defense Atomic Support Agency The Pentagon Washington, D.C. 20310
Carlson, Buford A., CMDR, USN	U.S. Naval Postgraduate School Monterey, Calif. 93940
Cassidy, Samuel H.	Mathematician Military Evaluations Division U.S. Naval Radiological Defense Lab. San Francisco, Calif. 94135
Cattermole, George B., Capt.	Military Assistant to the Director Scientific Division Headquarters, Defense Atomic Support Agency The Pentagon Washington, D.C. 20310
Clarke, Eric T., Dr.	Vice President Technical Operations Research South Avenue Burlington, Massachusetts 01803
Cluff, Frank D.	Weather Bureau (ESSA) Washington, D.C. 20234
Cole, Richard, Dr.	Head, Chemical Technology Division U.S. Naval Radiological Defense Lab. San Francisco, Calif. 94135
Coleman, George H., Dr.	Chemistry Department Lawrence Radiation Laboratory Box 808 Livermore, Calif. 94551

Cowan, George A., Dr.	Los Alamos Scientific Lab. Los Alamos, New Mexico 87544
Crocker, Glenn R.	Physical Chemist Chemical Technology Division U.S. Naval Radiological Defense Lab. San Francisco, Calif. 94135
Curtis, Gale B.	Manager, Mathematics Department American Research Corporation 505 East Commonwealth Ave. Fullerton, Calif. 92632
Dardis, John G., Dr.	Technical Management Office U.S. Naval Radiological Defense Lab. San Francisco, Calif. 94135
Day, Walter C.	U.S. Army Engineering Nuclear Cratering Group Lawrence Radiation Laboratory Box 808 Livermore, Calif. 94551
Dieckhoner, James E., Capt., USAF	Nuclear Research Officer Air Force Weapons Laboratory (WLRB-1) Kirtland AFB, New Mexico 87117
Dyer, John N., Dr.	Assoc. Prof., Physics U.S. Naval Postgraduate School Monterey, Calif. 93940
Eldridge, Ralph G.	The MITRE Corporation Box 208 Bedford, Mass. 01730
Evans, E.C., III, Dr.	Head, Weapons Capabilities Branch Military Evaluations Division U.S. Naval Radiological Defense Lab. San Francisco, Calif. 94135
Ferguson, James M., Dr.	Nucleonics Division U.S. Naval Radiological Defense Lab. San Francisco, Calif. 94135
Freiling, Edward C., Dr.	Head, Physical Chemistry Branch Chemical Technology Division U.S. Naval Radiological Defense Lab. San Francisco, Calif. 94135

French, R.L., Dr.	Staff Physicist Radiation Research Associates, Inc. 1506 W. Terrell Ave. Fort Worth, Texas 76104
Fuquay, James J.	Battelle - Northwest Box 999 Richland, Washington
Gagliano, Ross A., Capt., USA	U.S. Naval Postgraduate School Monterey, Calif. 93940
Garrett, Charles W.	Defense Atomic Support Agency (AFRRI) The Pentagon Washington, D.C. 20310
Garvey, Daniel P., Lt., USNR	U.S. Naval Postgraduate School Monterey, Calif. 93940
Gibson, Tomas A., Jr.	Plowshare Division Lawrence Radiation Laboratory Box 808 Livermore, Calif. 94551
Greene, Jack C.	Director Postattack Research Division Office of Civil Defense The Pentagon Washington, D.C. 20310
Haltiner, George J., Dr.	Prof., Met. and Ocean. U.S. Naval Postgraduate School Monterey, Calif. 93940
Hardin, Luther M.	Chief Evaluations Division (AMXND-E) U.S. Army Nuclear Defense Lab. Edgewood Arsenal, Maryland 21010
Harris, L.E., Capt., USN	Chief General War Division Joint War Games Agency (OJCS) The Pentagon Washington, D.C. 20310

Hedman, Fritz A., Dr.	Physicist Defense Communications Agency National Military Command System Support Center (NMCSSC) 4319 East-West Highway Bethesda, Maryland
Heffter, Jerome L.	Weather Bureau (ESSA) Washington, D.C. 20235
Heft, Robert E., Dr.	Lawrence Radiation Lab. Box 808 Livermore, Calif. 94551
Hicks, H.G.	Lawrence Radiation Lab. Box 808 Livermore, Calif. 94551
Hollister, Hal L.	Chief, Tech. Analysis Branch Division of Biology and Medicine U.S. Atomic Energy Commission Washington, D.C. 20545
Home, William M., Lt. Col.	Support Systems Division Office of Civil Defense (Research) The Pentagon Washington, D.C. 20310
Huebsch, Ian O.	Military Evaluations Branch U.S. Naval Radiological Defense Lab. San Francisco, Calif. 94135
Johnson, John P. III, Capt., USA	U.S. Naval Postgraduate School Monterey, Calif. 93940
Jones, James T., Col.	Chief McClellan Central Laboratory 1155 Technical Operations Squadron McClellan AFB, Calif. 95652
Keith, James E.	Staff Member Sandia Corporation P.O. Box 500 Sandia Base Albuquerque, New Mexico 87115

Knapp, Myron W., Dr.	Test Division, L-45 Lawrence Radiation Lab. P.O. Box 808 Livermore, Calif. 94550
Knox, Joseph B., Dr.	Group Leader, Plowshare Division Lawrence Radiation Lab. P.O. Box 808 Livermore, Calif. 94550
Ksanda, Charles F.	Head, Operational Requirements Office U.S. Naval Radiological Defense Lab. San Francisco, Calif. 94135
Lacy, William J.	Research Analyst Postattack Research Division Office of Civil Defense The Pentagon Washington, D.C. 20310
Lane, William B.	Stanford Research Institute 333 Ravenswood Ave. Menlo Park, Calif. 94025
LaRiviere, Philip D.	Operations Analyst Stanford Research Institute 333 Ravenswood Ave. Menlo Park, Calif. 94025
Larson, Kermit, Dr.	Research Associate Atmospheric Sciences Section Environmental and Radiological Sciences Dept. Battelle-Northwest P.O. Box 999 Richland, Washington 99352
Laurino, Richard D.	Stanford Research Institute 333 Ravenswood Ave. Menlo Park, Calif. 94025
Leies, Gerard M., Dr.	Headquarters, USAF(AFTAC)/TC-6 Washington, D.C. 20333

Leventhal, Leon	Manager, Technical Services Tracorlab Div. of LFE Inc. 2030 Wright Ave. Richmond, Calif. 94804
Machta, Lester, Dr.	Director, Air Resources Lab. Institute of Atmospheric Sciences Environmental Science Services Administration Department of Commerce Washington, D.C. 20235
Mackin, James L.	Technical Management Office U.S. Naval Radiological Defense Lab. San Francisco, Calif. 94135
Maloney, Joseph C.	Chief, Radiation Protection Branch Nuclear Engineering Division U.S. Army Nuclear Defense Lab. Edgewood Arsenal, Maryland 21010
Martin, Richard T., Capt., USAF	McClellan Central Laboratory 1155 Technical Operations Squadron McClellan AFB, Calif. 95652
McKee, John W., Dr.	Project Manager General Electric - Tempo P.O. Dwr. QQ Santa Barbara, Calif.
Menneken, Carl E.	Prof., Elec. Engr. Dean Res. Admin. U.S. Naval Postgraduate School Monterey, Calif. 93940
Merritt, Melvin L., Dr.	Division Supervisor Sandia Corporation P.O. Box 5800 Sandia Base Albuquerque, New Mexico 87115
Mikhail, S.Z., Dr.	Technical Management Office U.S. Naval Radiological Defense Lab. San Francisco, Calif. 94135

Miller, Carl F., Dr.	Director, Operations Evaluation Programs Stanford Research Institute 333 Ravenswood Ave. Menlo Park, Calif. 94025
Miskel, John A., Dr.	Chemistry Department Lawrence Radiation Lab. Box 808 Livermore, Calif. 94551
Morris, George A., Capt.	U.S. Army Engineer Nuclear Cratering Group Lawrence Radiation Laboratory Box 808 Livermore, Calif 94551
Nathans, Marcel W.	Project Leader Tracerlab, Div. of LFE Inc. 2030 Wright Ave. Richmond, Calif. 94804
Norman, John H., Dr.	General Atomic Division of General Dynamics Corp. P.O. Box 608 San Diego, Calif. 92112
Norment, Hillyer G., Dr.	Project Leader Technical Operations Research South Avenue Burlington, Massachusetts 01803
O'Donnell E.J., RADM, USN	Superintendent, U.S. Naval Postgraduate School Monterey, Calif. 93940
Petonke, Richard H.	Supervisory Mathematician Mathematics and Computation Lab. NREC/OEP Executive Office of the President Washington, D.C. 20504
Polan, Marvin	Project Supervisor Ford Instruments Company Division of Sperry Rand Corp. 31-10 Thomson Ave. Long Island City New York 11101

Pugh, George E., Dr.	Lambda Corp. 1401 Wilson Blvd. Arlington, Virginia
Rapp, Dr. Robert R.	The RAND Corporation 1700 Main Street Santa Monica, Calif. 90406
Read, Robert R., Dr.	Assoc. Prof., Opn. Analy. U.S. Naval Postgraduate School Monterey, Calif. 93940
Reed, Jack W.	Staff Member Sandia Corporation P.O. Box 5800 Sandia Base Albuquerque, New Mexico 87115
Rigotti, David L.	Chief, Nuclear Engineering Division (AMXND-NE) U.S. Army Nuclear Defense Lab. Edgewood Arsenal, Maryland 21010
Rowland, David W.	Chief, Systems Analysis Division National Civil Defense Computer Facility P.O. Box 256 Olney, Maryland 20832
Rowland, Richard H.	Information Analysis General Electric - Tempo P.O. Dwr. QQ Santa Barbara, Calif.
Russell, Irving J., Dr.	Professor Chemistry Department Boston College Chestnut Hill, Mass.
Rynders, Gerald J., Dr.	Chemist Lawrence Radiation Lab. P.O. Box 808 Livermore, Calif. 94550
Schwenke, Theodore W.	Analyst Technical Operations Research, Inc. South Ave. Burlington, Mass. 01803

Shafer, Charles K.	Staff Director Emergency Operations Division Office of Civil Defense Washington, D.C. 20310
Shaw, Harold E., Lt. Col., USA	Commanding Officer U.S. Army Nuclear Defense Lab. Edgewood Arsenal, Maryland 21010
Smiley, Ronald H., Maj., USA	U.S. Naval Postgraduate School Monterey, Calif. 93940
Soule, Richard R.	Reconnaissance Task Group U.S. Naval Radiological Defense Lab. San Francisco, Calif. 94135
Spencer, Lewis V., Dr.	Mathematician - Physicist National Bureau of Standards Professor, Physics Dept. Ottawa University 1147 S. Hickory Street Ottawa, Kansas 66067
Strope, Walmer E.	Assistant Director of Civil Defense (Research) The Pentagon Washington, D.C. 20310
Tewes, Howard A.	Plowshare Division Lawrence Radiation Lab. P.O. Box 808 Livermore, Calif. 94551
Tompkins, Edward R., Dr.	Associate Scientific Director U.S. Naval Radiological Defense Lab. San Francisco, Calif. 94135
Tompkins, Paul C., Dr.	Executive Director Federal Radiation Council 1800 G. Street N.W. Washington, D.C. 20449
Tompkins, Robert C.	Chief, Nuclear Studies Branch Evaluations Division (AMXND-E) U.S. Army Nuclear Defense Lab. Edgewood Arsenal, Maryland 21010

Urban, Doyle V.	Air Resources Field Research Office Environmental Science Services Administration AEC Bldg., 2753 South Highland Las Vegas, Nevada
Whitten, Henry P.	Physicist U.S. Army Combat Developments Command Chemical - Biological - Radiological Agency Fort McClellan, Alabama 36201
Wilsey, Edward F.	Physical Scientist Evaluations Division (AMXND-E) U.S. Army Nuclear Defense Lab. Edgewood Arsenal, Maryland 21010
Winchell, Perrin	General Atomic Div. of General Dynamics Corp. P.O. Box 608 San Diego, Calif. 92112
Woolf, Stanley NMN	Physicist Technical Operations Research South Ave. Burlington, Massachusetts 01803
Yoder, Robert E., Dr.	Hazards Control Department Lawrence Radiation Laboratory Box 808 Livermore, Calif. 94551
Yu, Oliver S-K.	Operations Analyst Stanford Research Institute 333 Ravenswood Ave. Menlo Park, Calif. 94025
Zigman, Paul E.	Head, Technical Management Office U.S. Naval Radiological Defense Lab. San Francisco, Calif. 94135

UNCLASSIFIED
Security Classification

DOCUMENT CONTROL DATA - R&D
(Security classification of title, body of abstract and indexing annotation must be entered when the overall report is classified)

1. ORIGINATING ACTIVITY (Corporate author) U. S. Naval Radiological Defense Laboratory San Francisco, California 94135	2a. REPORT SECURITY CLASSIFICATION UNCLASSIFIED 2b. GROUP

3. REPORT TITLE
FALLOUT PHENOMENA SYMPOSIUM PROCEEDINGS - PART I

4. DESCRIPTIVE NOTES (Type of report and inclusive dates)

5. AUTHOR(S) (Last name, first name, initial)
Mikhail, Saad Z., Editor

6. REPORT DATE	7a. TOTAL NO. OF PAGES	7b. NO. OF REFS
	501	--

8a. CONTRACT OR GRANT NO.	9a. ORIGINATOR'S REPORT NUMBER(S)
b. PROJECT NO.	USNRDL-R&L-177
c.	9b. OTHER REPORT NO(S) (Any other numbers that may be assigned this report)
d.	

10. AVAILABILITY/LIMITATION NOTICES
Each transmittal of this document outside the agencies of the U. S. Government must have prior approval of the Office of Civil Defense, Office of the Secretary of the Army, Division for Research, Washington, D. C. 20310.

11. SUPPLEMENTARY NOTES	12. SPONSORING MILITARY ACTIVITY
	Office of Civil Defense, Washington, D. C. Defense Atomic Support Agency, Washington, D. C. 20301

13. ABSTRACT

By agreement between the Department of the Navy and the Office of Civil Defense, the U. S. Naval Radiological Defense Laboratory provides technical advisory services for specific areas of the OCD research program. In addition to recommending annual research programs, monitoring and reviewing research progress, and evaluating research proposals, such technical advisory services include efforts to promote the exchange and examination of pertinent information and consequently, includes development of appropriate scientific symposia. It is in this capacity that the USNRDL assisted in the planning and development of the OCD/DASA Fallout Phenomena Symposium.

DD FORM 1 JAN 64 1473

UNCLASSIFIED
Security Classification

UNCLASSIFIED
Security Classification

14. KEY WORDS	LINK A		LINK B		LINK C	
	ROLE	WT	ROLE	WT	ROLE	WT

INSTRUCTIONS

1. **ORIGINATING ACTIVITY:** Enter the name and address of the contractor, subcontractor, grantee, Department of Defense activity or other organization *(corporate author)* issuing the report.

2a. **REPORT SECURITY CLASSIFICATION:** Enter the overall security classification of the report. Indicate whether "Restricted Data" is included. Marking is to be in accordance with appropriate security regulations.

2b. **GROUP:** Automatic downgrading is specified in DoD Directive 5200.10 and Armed Forces Industrial Manual. Enter the group number. Also, when applicable, show that optional markings have been used for Group 3 and Group 4 as authorized.

3. **REPORT TITLE:** Enter the complete report title in all capital letters. Titles in all cases should be unclassified. If a meaningful title cannot be selected without classification, show title classification in all capitals in parenthesis immediately following the title.

4. **DESCRIPTIVE NOTES:** If appropriate, enter the type of report, e.g., interim, progress, summary, annual, or final. Give the inclusive dates when a specific reporting period is covered.

5. **AUTHOR(S):** Enter the name(s) of author(s) as shown on or in the report. Enter last name, first name, middle initial. If military, show rank and branch of service. The name of the principal author is an absolute minimum requirement.

6. **REPORT DATE:** Enter the date of the report as day, month, year; or month, year. If more than one date appears on the report, use date of publication.

7a. **TOTAL NUMBER OF PAGES:** The total page count should follow normal pagination procedures, i.e., enter the number of pages containing information.

7b. **NUMBER OF REFERENCES:** Enter the total number of references cited in the report.

8a. **CONTRACT OR GRANT NUMBER:** If appropriate, enter the applicable number of the contract or grant under which the report was written.

8b, 8c, & 8d. **PROJECT NUMBER:** Enter the appropriate military department identification, such as project number, subproject number, system numbers, task number, etc.

9a. **ORIGINATOR'S REPORT NUMBER(S):** Enter the official report number by which the document will be identified and controlled by the originating activity. This number must be unique to this report.

9b. **OTHER REPORT NUMBER(S):** If the report has been assigned any other report numbers *(either by the originator or by the sponsor)*, also enter this number(s).

10. **AVAILABILITY/LIMITATION NOTICES:** Enter any limitations on further dissemination of the report, other than those imposed by security classification, using standard statements such as:

(1) "Qualified requesters may obtain copies of this report from DDC."

(2) "Foreign announcement and dissemination of this report by DDC is not authorized."

(3) "U. S. Government agencies may obtain copies of this report directly from DDC. Other qualified DDC users shall request through _____."

(4) "U. S. military agencies may obtain copies of this report directly from DDC. Other qualified users shall request through _____."

(5) "All distribution of this report is controlled. Qualified DDC users shall request through _____."

If the report has been furnished to the Office of Technical Services, Department of Commerce, for sale to the public, indicate this fact and enter the price, if known.

11. **SUPPLEMENTARY NOTES:** Use for additional explanatory notes.

12. **SPONSORING MILITARY ACTIVITY:** Enter the name of the departmental project office or laboratory sponsoring *(paying for)* the research and development. Include address.

13. **ABSTRACT:** Enter an abstract giving a brief and factual summary of the document indicative of the report, even though it may also appear elsewhere in the body of the technical report. If additional space is required, a continuation sheet shall be attached.

It is highly desirable that the abstract of classified reports be unclassified. Each paragraph of the abstract shall end with an indication of the military security classification of the information in the paragraph, represented as *(TS), (S), (C), or (U)*.

There is no limitation on the length of the abstract. However, the suggested length is from 150 to 225 words.

14. **KEY WORDS:** Key words are technically meaningful terms or short phrases that characterize a report and may be used as index entries for cataloging the report. Key words must be selected so that no security classification is required. Identifiers, such as equipment model designation, trade name, military project code name, geographic location, may be used as key words but will be followed by an indication of technical context. The assignment of links, roles, and weights is optional.